CHANNEL MEANDER MIGRATION IN LARGE-SCALE PHYSICAL MODEL STUDY

A Dissertation

by

PO-HUNG YEH

Submitted to the Office of Graduate Studies of
Texas A&M University
in partial fulfillment of the requirements for the degree of

DOCTOR OF PHILOSOPHY

August 2009

Major Subject: Ocean Engineering

CHANNEL MEANDER MIGRATION IN LARGE-SCALE PHYSICAL MODEL STUDY

A Dissertation

by

PO-HUNG YEH

Submitted to the Office of Graduate Studies of
Texas A&M University
in partial fulfillment of the requirements for the degree of

DOCTOR OF PHILOSOPHY

Approved by:

Chair of Committee,	Kuang-An Chang
Committee Members,	Jean-Louis Briaud
	Hamn-Ching Chen
	Douglas J. Sherman
Head of Department,	David V. Rosowsky

August 2009

Major Subject: Ocean Engineering

ABSTRACT

Channel Meander Migration in Large-scale Physical Model Study.

(August 2009)

Po-Hung Yeh, B.S., Tamkang University, Taipei, Taiwan;

M.S., National Chung Hsing University, Taichung, Taiwan

Chair of Advisory Committee: Dr. Kuang-An Chang

A set of large-scale laboratory experiments were conducted to study channel meander migration. Factors affecting the migration of banklines, including the ratio of curvature to channel width, bend angle, and the Froude number were tested in the experiments. The effect of each factor on the evolution of channel plan form was evaluated and quantified. The channel bankline displacement was modeled by a hyperbolic function with the inclusion of an initial migration rate and a maximum migration distance. It is found that both the initial migration rate and maximum migration distance exhibit a Gaussian distribution along a channel bend. Correlations between the distributions and the controlling parameters were then studied. Two sets of equations were developed for predicting the initial migration rate and the maximum migration distance. With the initial migration rate and maximum migration distance being developed as a function of geometric and flow parameters, a hyperbolic-function model can be applied to estimate the bankline migration distance.

The prediction of channel centerline migration was also developed in this study. The channel centerline was represented with a combination of several circular curves and straight lines. Each curve with the radius of curvature and bend angle was used to describe the channel bend geometry. HEC-RAS was applied to estimate the flow hydraulic properties along the

channel by adjusting the channel bed slope. The intersections of two consecutive centerlines were found to be the inflection points of the centerline migration rate. Phase lag to the bend entrance was measured and correlated with the bend length and water depth. The migration rate between two successive inflection points demonstrated a growth and decay cycle. A sine function was used to model the centerline migration rate with regression analysis of the measurement data. The method was applied to four sites of four natural rivers in Texas. The results showed that the prediction equation provides agreeable results to the centerline migration of natural rivers.

DEDICATION

To my parents

ACKNOWLEDGEMENTS

I would like to express my utmost gratitude to my advisor, Professor Kuang-An Chang, for providing me this great opportunity to work on this very intriguing and challenging topic. Over the years, his inspiration, guidance and generous understanding have been invaluable.

I would like to thank Professor Jean-Louis Briaud and Professor Hamn-Ching Chen of the Civil Engineering Department for their valuable advice and opinions. Much appreciation should be given to Professor Chen for his generosity in allowing me the opportunity to learn and use his numerical model. I would also like to thank Professor Douglas Sherman of the Department of Geography for serving as my committee member. The large-scale experiments were only possible through the collaborative efforts with Dr. Namgyu Park.

A special thanks to Professor Billy Edge of Ocean Engineering and Hanes Coastal Laboratory. The experience of working in the laboratory is precious and significant. It has extended the width and depth in my study. I also wish to thank Professor Robert Randall, Mr. Jonnie Reed and Ms. Pam Fambro of Ocean Engineering for their help and encouragement.

I wish to thank my parents, brothers and sister, and all my family members for their endless love and support from my home country Taiwan. This long journey of self-discovery was not possible without their support and patience.

TABLE OF CONTENTS

CHAPTER Page

LIST OF TABLES

LIST OF FIGURES

FIGURE Page

FIGURE Page

FIGURE Page

FIGURE Page

CHAPTER I

INTRODUCTION

1.1 Channel Meander Migration

Channel meander migration and the associated bank erosion have long been intriguing to scientists and engineers. A river may continuously erode its banklines and rework the floodplains. Different plan forms and flowing routes are gradually established by time. It largely affects the human activities and property safety, such as near bank structures, waterway navigation, flood control, and land use. Usually, channel meander migration is a long-term and incremental process. Its effects and threats to a structure are not obvious in the planning and designing stage, and may not become evident even after the structures are constructed. The ability to foresee or predict channel migration will reduce the cost for protecting the affected structures and installation of the associated countermeasures. Guidelines to account for possible changes of river morphology are therefore needed in order for dealing with possible consequences of stream instability. An effective and accurate method to evaluate the potential migration distance of a meander channel has become crucial for engineers in many areas, such as hydraulic, transportation, construction, and water resources engineering. However, since the temporal and spatial variations of channel migration, the evolution of a river's course and plan form encompasses different scales of variance. The time scale of this phenomenon spans from the geological, geographic and engineering time scales. These very different aspects of time scale make the channel meander migration very complicated and difficult in incorporating all the knowledge from different research fields (Hickin 1983). From the engineering point of view, the

---

This dissertation follows the style of *Journal of Hydraulic Engineering*.

ability in estimating the channel migration rate and its resulting migration distance is needed at least for the design life of an existing or future structure. An efficient and accurate prediction of channel morphologic changes will be the basis for the construction regulation and following maintenance.

A meander channel is featured of a pair of loops in opposite directions. Its movement or migration is affected by the flow inertia, channel geometry conditions, boundary material properties and sediment transport (Hickin and Nanson 1984). When the flow enters a curved bend, it is affected by the centrifugal acceleration from channel curvature. In order to counterbalance the outward momentum, the flow responds with water elevation difference between the outer and inner banks (superelevation). Hydraulic pressure is intensified on the bottom of the water column and drives the flow moving laterally from the outer to the inner bank. As a result of mass conservation, outward surface current and inward near bed current form a transverse circulation in the cross-stream direction. Along with the effect of the primary flow, the flow within a curved bend exhibits a helical motion. The secondary circulation carves down the channel outer banks and moves the sediment towards the inner banks. The primary flow transports the sediment to the downstream and consequently, a series of point bars and pools form along the channel bank.

The stream primary and secondary flow not only play the main and important roles in eroding and carving channel bed and bank. Its strength to the resistance of the channel boundary material largely decides the onset of erosion and bank retreat. This helical flow is also the media to transport the sediment longitudinally and transversely. The alternate sand bars and pools, which are the resultant of erosion and sediment transport, cause the thalweg which usually accompanies with larger shear stress (Ippen and Drinker 1962) to display sinuously of deep pools separated by shallow crossings. Its inherent asymmetry and out-of-phase to the channel

plan form directly lead to the asymmetry of channel plan form (Carson and Lapointe 1983). As a channel continuously erodes its banks and changes its morphologic features, the flow field inside is in turn largely determined by the channel plan form and bed topography (Dietrich and Smith 1983).

1.2 Literature Review

Meander migration is the progressing displacement of a channel changing its course as the flow continuously erodes the banks. Sediment transport and deposition also take place during the process. It is not only the movement in space, but the re-establishment in state. Over the past few decades, many researchers have been attempting to discuss and analyze this very intriguing and challenging topic. Numerous studies from different aspects can be found in literature. Prediction models with different assumptions and of certain degrees of simplifications are proposed. These models, from simple empirical formulae to complicated numerical simulations, comprise the variability and complexity of the phenomena. Generally, studies of channel meander migration can be divided into three broad categories: field investigations, analytical derivations and numerical simulations, and laboratory physical model studies.

Natural rivers provide the best sources to investigate the channel meander migration. Field measurements, historical maps and aerial photos all provide abundant evidences and direct materials. In the empirical approach, the channel migration rate is usually correlated with the channel properties. Keady and Priest (1977) related the channel downstream migration rate with the channel free surface slope. Hooke (1980) analyzed the magnitudes and distributions of channel migration rate from field measurements and historical maps of several streams in Southeast Devon, England. A formula stating that the mean erosion rate of a river is proportional to the square root of its catchment area was proposed. Brice (1982) collected a large data set, including aerial photos, maps, and bankline records of about 200 streams across

the United States, and found that the erosion rate of channel bankline increases with increasing in the channel width.

The most profound and widely mentioned field study is the empirical formula by Hickin and Nanson (1975). An estimation of annual channel migration rate was derived from the dendrochronology surveys on the Beatton River, Canada recorded by Hickin (1974). The normal channel migration rate is a function of the local channel radius of curvature to width ratio, R/W; it decreases as the ratio increases. A maximum value of the rate occurs when $2.0 < R/W < 3.0$. In tight curvatures ($R/W < 2.0$), the migration rate decreases rapidly and reaches zero when $R/W = 1.0$. This model was revised in Hickin and Nanson (1984) and Nanson and Hickin (1986) by adding new data to the original analysis. Nonetheless, the relationship between channel migration rate and the radius of curvature to width ratio is still centered in these following studies. Ferguson (1983) developed a simple kinematic model to simulate channel meander migration and plan form evolutions. The migration rate in this model is purely a quadratic function of radius to width ratio. The results show that this methodology is capable of simulating realistic deformation of a channel, from an initially symmetric plan form deforms into a sinuous, asymmetric multiple lobes meandering channel. It was also concluded in this study that channel asymmetry depends on a spatial lag in the kinematic relationship between the migration rate and its curvature. Howard and Knutson (1984) developed a simulation model in which the channel migration rate is also a function of channel curvature, which increases as the channel curvature increases and reaches a maximum value at $R/W = 3$. In sharper bends, the migration rate decreases in accord with the investigations of Hickin and Nanson (1984). Different from Nanson and Hickin's empirical approach, the model added a weighting function to the migration rate in order to include the effects from channel upstream. Local migration rate is the weighted average of the nominal migration rate (the same with Hickin and Nanson) and a

weighted upstream migration rates. The model includes previsions for neck cutoffs and may be used to forecast future patterns of channel migration in meandering streams. However, the weighting parameters and the upstream weighting function all need to be specified before applying it to a natural river migration. Although channel curvature alone causes different distributions of shear stress on the channel bank, other factors, such as flow velocity, bend angle, and soil property, were not included. A more dynamic consideration including the interaction between flow and channel bank was developed in the later studies.

The migration rate of Hickin and Nanson (1975) is empirical in nature, with the lack of considering the flow to bank interactions. Iketa et al. (1981) developed a "bend theory" to calculate the lateral distribution of the depth-averaged primary flow velocity along a curved channel. Analogous to the flow shear stress, the channel bank erosion rate is assumed to be proportional to the lateral velocity gradient of flow which equals the excessive bank velocity which is the difference between the near-bank depth-averaged mean velocity and the cross sectional mean velocity. Parker (1983) derived a convolution equation relating the excess near-bank velocity with R/W. For a long bend of $R/W > 3$, the predicted bank erosion rate is linearly proportional to the channel radius of curvature to width ratio and the results agree well with Hickin and Nanson (1975). However, the deviation becomes progressively increasing in tight. Except the flow velocities, other factors that affect bank erosion are all included and represented implicitly in the erosion constant. Hasegawa (1989) proposed a universal bank erosion coefficient which was proposed to be related to the channel cross sectional mean velocity and validated with data from several alluvial channels in Japan. Although several later models adapting this concept were reported (e.g., Parker et al. 1982; Odgaard 1987, 1989; Johannesson and Parker, 1989), the site specific erosion coefficient that needs to be calibrated before applied limits their applications. Also, the channel bank erosion rate has been correlated to the resultant

of the flow hydraulic strength to the bank material geotechnical properties (Nanson and Hickin 1983; Osman and Thorne 1988). Another approach including the bank material properties needs to be considered.

The analytical meander path model by Chang (1984) is based on the streamwise distribution of flow transverse velocity. In a curved channel, the transverse velocity is governed by the centrifugal acceleration, transverse water surface and flow internal shear stress as investigated by Rozovskii (1957). The meander path, where the transverse velocity has zero net discharge, was derived from the equation of motion for the flow transverse velocity. The phase lag, which is defined as the phase difference between the two inflection points of channel centerline and meander path respectively, is obtained by trial-and-error. It is found that the phase lag in regular meander path is about one-fifth of the distance between the channel apex and its next crossover. It is also found that the meander arc length, which is measured between repeating points (inflection points) along the path, is a function of the depth and channel roughness and independent of channel curvature or arc angle.

Numerical simulations incorporating three elements: fluid flow, sediment transport, and bank erosion to simulate the bank erosion and channel meander migration are developed rapidly. Most fluid flow models solve Navier-Stokes equation with different assumptions and neglects. Sediment transport theories, bed topography, transverse bed slope, channel bed degradation/aggradation and grain-size sorting are usually included in the other module of the simulation. Bank erosion processes include weathering, fluvial erosion and geotechnical instability are the main mechanism for the channel bankline retreat or advance. Several recent developments are briefly discussed in this section. Nagata et al. (2000) developed a numerical model to investigate the channel bed deformation and bankline shift. A two-dimensional depth-averaged Navier-Stokes equation was applied to solve the flow field in a moving boundary-fitted

coordinate system. The fluid model was coupled with the theory of non-equilibrium sediment transport of Nakagawa and Tsujimoto (1980). In the bank erosion submodel, a simplified model of noncohesive material proposed by Hasegawa (1981) was used.

Darby et al. (2002) coupled a two-dimensional depth-averaged fluid flow model with an erosion submodel from a mechanistic approach proposed by Osman and Thorne (1988) to simulate the river morphology for meander bends with erodible cohesive banks. This mechanistic approach is capable of simulating bank stability conditions resulting from deformation of the bank profile caused by direct fluvial shear erosion of the bank materials and near-bank bed degradation. It also featured with the deposition of bank material debris on the bed of the channel after mass failure, and its subsequent removal by the flow. Duan and Julien (2005) developed a two-dimensional, depth-averaged flow model to simulate the formation process of meander channels. Sediment transport equations including the effects of secondary flow and transverse bed slope were coupled. The model described the channel bankline retreat or advance by calculating the near-bank sediment mass conservation as the bank material from basal erosion and bank failure is also included.

Physical models in laboratory flumes have also been studied to simulate channel meander migration (e.g., Friedkin 1945; Rozovskii 1957; Ippen and Drinker 1962; Yen and Yen 1971; Odgaard 1989). Most studies included only single curved bend to investigate the shear stress distribution or validate the flow field inside a curved channel. Among all these researches, Ippen and Drinker (1962) investigated the distribution and the magnitudes of boundary shear stresses in curved bends of smooth trapezoidal channels. Several tests were conducted to determine the effects in discharge and bend geometry on the shear stress pattern. It is found that the maximum shear stress is generally with the flow highest velocity. And the distribution and the relative magnitudes of the local boundary shear stresses is a function of channel geometry for

subcritical flow. Dietrich and Smith (1983) used the experimental results of Yen and Yen (1971) and field measurements in Muddy Creek to investigate the influence of the point bar on flow through curved channels. Shear stress on the channel boundary increases along the outer bank in the bend downstream, while decreasing from the upstream part of the bend to the downstream end on the inner bank. Dramatic change in channel curvature will cause large force due to flow spiral motion. Friedkin (1945) performed flume tests to study the behaviors of self-formed meandering rivers in a large-scale flume that had dimensions of 36 m (120 ft) in length and 11.4 m (38 ft) in width. A series of cases under different conditions such as discharge, angle of attack, bed slope, initial cross section, sediment supply and bed material was conducted. The investigations are very valuable and informative although only qualitative descriptions were reported.

1.3 Objectives

The ultimate goal of this research is to establish guidance for soil properties-based prediction of meandering migration. In order to achieve this goal, the following objectives are of this study:

1) conduct large-scale physical models to simulate channel meander migration;
2) evaluate the factors that affect meander migration, which include channel geometry configurations, soil properties, and flow hydraulic conditions;
3) apply a hyperbolic function to the bankline migration distance, a soil erosion model also included;
4) develop a prediction method to estimate the channel centerline migration rate;
5) validate the model with laboratory data as well as field measurements

In this dissertation, several existing models, from empirical formulae, analytical derivations, numerical simulations to physical model studies, of channel meander migration are introduced and reviewed in Chapter I. In Chapter II, a set of large-scale physical model

experiments are presented. The experiment conducts sand channels in a large-scale basin with 13 different tests. Dimensional analysis and the experimental setup are performed in this chapter. Test observations and results are discussed in Chapter III. Bankline and centerline migration in a meandering channel are also studied in this chapter. In Chapter IV, a hyperbolic function is proposed for the channel bankline migration distance. The initial migration rate and maximum migration distance in the hyperbolic process are also introduced in this chapter. A dual-modal Gaussian distribution function is proposed to model the channel maximum migration distance. Chapter V develops a prediction equation of the channel centerline migration rate. Inflection points, phase lag and the migration rate are all discussed in this chapter. The approach is applied to the laboratory tests and four natural rivers. Chapter VI gives the conclusions and future studies of this research.

CHAPTER II

DIMENSIONAL ANALYSIS AND EXPERIMENT SETUP

2.1 Dimensional Analysis

Factors that affect channel migration distance m, and channel migration rate $\dot{m}$ can be divided into four categories: (1) channel plan form geometry, (2) flow hydraulic parameters, (3) channel bank/bed soil property and (4) others not included in the first three categories. The channel plan form geometry are the channel planimetric features such as channel width W, radius of curvature of a channel bend R, angle of a channel bend Φ, and channel bed slope s. The flow hydraulic parameters include fluid density ρ_w, fluid viscosity μ_w, cross sectional mean velocity U, and water depth h. The soil property is the soil resistance to flow tractive force, in a relationship between soil erosion rate $\dot{z}$ and flow shear stress τ. Usually, the critical shear stress τ_c of soil is used to indicate the threshold of flow strength to initiate soil erosion. The soil erosion rate $\dot{z}$ is then a function of the "excess" shear stress τ-τ_c. The other factors not in the first three categories include external forcings, vegetation condition, human impacts, and artificial structures etc. In this study, only the first three categories and the gravitational acceleration g were considered in the dimensional analysis and the two functional relationships can be expressed as

$$m = f_1(W, R, \Phi, s, \rho_w, \mu_w, U, h, \tau_c, g) \tag{1}$$

$$\dot{m} = f_2(W, R, \Phi, s, \rho_w, \mu_w, U, h, \tau_c, g) \tag{2}$$

The dimensionless relationships of m and $\dot{m}$ with all the variables can be further derived as

$$\frac{m}{W} = f_3\left(\frac{R}{W}, \Phi, s, Re, Fr, \frac{h}{W}, \frac{\tau_c}{\rho_w U^2}\right) \tag{3}$$

$$\frac{\dot{m}}{U} = f_4\left(\frac{R}{W}, \Phi, s, Re, Fr, \frac{h}{W}, \frac{\tau_c}{\rho_w U^2}\right) \quad (4)$$

where $Re = \rho_w Uh/\mu_w$ and $Fr = U/(gh)^{1/2}$ are the Reynolds number and the Froude number, respectively. According to the standard one-dimensional fixed bed open-channel flow theory, water depth h depends on flowrate Q and channel slope s. An expected h (and therefore also U) can be obtained through adjusting s under a constant Q and constant channel cross sectional condition in the experiments. This means that s, in turn, is a dependent variable of U and h and thus is crossed out in the dimensionless relationships. The Reynolds number Re in the present study is between 1.5×10^4 and 2.2×10^4, which is greater than 15,000, falling in the range of turbulent flow in open channels (e.g., Munson et al. 2006). Therefore, the effect of fluid viscosity may be considered as small and negligible.

Flow shear stress τ is the primary tractive force destabilizing soil particles and hence changes channel cross sectional profiles and banklines. Its difference from the soil critical shear stress, τ-τ_c, is the excess shear stress and indicates the flow strength to soil erosion. The channel migration distance m and migration rate $\dot{m}$ are influenced by the bed and bank material properties (Hickin and Nanson 1975, 1984; Nanson and Hickin 1983), and are usually are thought to be proportional to τ-τ_c (Osman and Thorne 1988). τ_c is the critical value of shear stress to begin the inception motion of soil and can be obtained from Shields diagram. From the Shields diagram, it is seen that τ_c is a soil property related to its grain size. However, from geotechnical point of view, the grain size of any cohesive soil has no impact on its critical shear stress and thus makes the use of the Shields parameter questionable. In order to describe the soil erodibility in a more general way and be consistent between coarse-grained (e.g., gravel and sand) and fine-grained (e.g., clay and silt) soils, the flow erosive strength in this study is presented by using an "excess velocity" U-U_c which is the difference between the flow velocity

U and a critical velocity U_c. The critical velocity U_c, sometimes called permissible velocity (Chang 1988), is defined as the maximum flow velocity which will not cause erosion on the channel boundaries. It usually refers to the minimum flow velocity to arise the soil particle's incipient motion and can be found in many published researches (Fortier and Scobey 1926; Hjulstrom 1935; Mavis and Laushey 1949; Carstens 1966; Neill 1967; The ASCE Task Committee 1993).

The channel average shear stress τ in a uniform flow condition can be expressed as

$$\tau = \rho_w ghs = \rho_w gn^2 h^{-1/3} U^2 \tag{5}$$

where n is the Manning's coefficient and the hydraulic radius is assumed approximately equal to h in a wide open channel. From Eq. (5), U and U_c are related to τ and τ_c, and can be written as

$$U = \frac{(\tau/\rho_w)^{1/2}}{(gn^2 h^{-1/3})^{1/2}} = \frac{u_*}{(gn^2 h^{-1/3})^{1/2}} \tag{6}$$

$$U_c = \frac{(\tau_c/\rho_w)^{1/2}}{(gn^2 h^{-1/3})^{1/2}} = \frac{u_{*c}}{(gn^2 h^{-1/3})^{1/2}} \tag{7}$$

where u_* and u_{*c} are shear and critical shear velocities. In this way, the correlation between the channel migration distance m (also $\dot{m}$) and the excess shear stress τ-τ_c can be translated into the excess velocity U-U_c in a channel cross section. This study measures U_c by testing a soil sample with an erosion function apparatus (EFA, Briaud et al. 1999). The test results are shown in the next section.

In a curved channel, the local shear stress on the outer bank is usually greater than the average value due to its local flow velocity is larger than U (Ippen and Drinker 1962). If taking this local maximum velocity into account, a parameter β which is the ratio of maximum velocity U_{max} to cross sectional mean velocity U is defined (i.e., $\beta = U_{max}/U$). Thus, the local maximum velocity in a channel bend can be expressed as βU, and the excess velocity of flow erosive

strength noted above is modified as βU-U_c. The Corps of Engineers (1970) analyzed the maximum boundary shear stress τ_{max} in four smooth and one rough curved channels against the effect of channel curvature. The ratio of maximum boundary shear stress τ_{max} to channel mean shear stress τ clearly presents a functional relationship with the channel curvature to width ratio R/W as shown in Fig. 1. The solid line in the figure is the regression formula from the four smooth channels, in which the shear stress ratio is inversely proportional to the square root of R/W. In order to include the extreme situation (straight channels) in the equation, the data of the four smooth channels were curve-fitted with a modified equation in this study. The resultant equation is written as Eq. (8) and plotted in Fig. 2(a)

$$\frac{\tau_{max}}{\tau} = \left(\frac{5.73}{R/W} + 1.0 \right)^{1/2} \tag{8}$$

in which the constant 1.0 is the value of the ratio in straight channels when $R/W \rightarrow \infty$. Based on the dimensional analysis, flow velocity is proportional to the square root of shear stress. By simply taking the square root of Eq. (8), the value of β with variations of channel R/W is then determined by Eq. (9) and plotted in Fig. 2(b).

$$\beta = \frac{U_{max}}{U} = \left(\frac{5.73}{R/W} + 1.0 \right)^{1/4} \tag{9}$$

In the above equation, $\beta = 1.0$ is for a straight channel ($R/W \rightarrow \infty$).

For a single type of soil, the critical shear stress (also the Shields parameter) is constant regardless the flow condition, whereas the critical velocity is varied as a function of the water depth (Mehrota 1983). For different water depths, shear stress is different because of different velocity profiles, even if their mean velocities are the same. This dependence on water depth is considered in the excess velocity aforementioned and a new non-dimensional term is used in the functional relationship as

$$\frac{\beta U - U_c}{\sqrt{gh}} = \frac{\beta U}{\sqrt{gh}} - \frac{U_c}{\sqrt{gh}} = \beta Fr - Frc \tag{10}$$

where *Frc*, which has a similar form as *Fr*, is the Froude number at which the flow shear stress and velocity at a given water depth are equal to the critical values. In Eq. (10), βFr-*Frc* is derived to express the ability of flow to erode the channel bankline and is denoted as the excessive Froude number. Ikeda et al. (1981) in their bend theory assumed that channel bankline migration rate is linearly proportional to the difference between the near-bank depth-averaged mean velocity and the channel cross sectional mean velocity. This study, on the other hand, derived that $\dot{m}$ (also m) is proportional to βU-U_c from dimensional analysis. In addition, since the critical velocity is dependent on the ambient water depth, an excess Froude number βFr-*Frc* results in the final equations of the functional relationship.

Note here although the flow Froude number is seldom used as an erosion parameter in the research of sediment transport, the use of the critical Froude number, instead of the critical Shields parameter, is still based on the critical shear stress of a type of soil. The approach of the excess Froude number is analogous to the excess shear stress. The advantage is to express soil erodibility in a more general way, yet to be consistent with that of fine-grained soils such as clay. For cohesive soils, the median grain diameter d_{50} used in the Shields parameter has no impact on the critical shear stress, therefore, the Shields parameter may not be used for fine-grained soils. On the other hand, βFr-*Frc* is the difference between the flow inertial force and the soil resistant force, which diverts the debate on the use of soil grain diameter. In practical applications, once the critical velocity U_c and the ambient water depth h are obtained, the flow erosive strength in cohesive/cohesionless (fine-/coarse-grained) soils can be determined. According to the discussions above, Eq. (3) and (4) are now simplified to

$$\frac{m}{W} = f_5(\frac{R}{W}, \Phi, \frac{h}{W}, \beta Fr - Frc) \tag{11}$$

$$\frac{\dot{m}}{U} = f_6(\frac{R}{W}, \Phi, \frac{h}{W}, \beta Fr - Frc) \tag{12}$$

in which, m/W and $\dot{m}/U$ are the channel dimensionless migration distance and rate; R/W, Φ, h/W and βFr-Frc are radius-to-width ratio, bend angle, depth-to-width ratio and the excess Froude number, respectively.

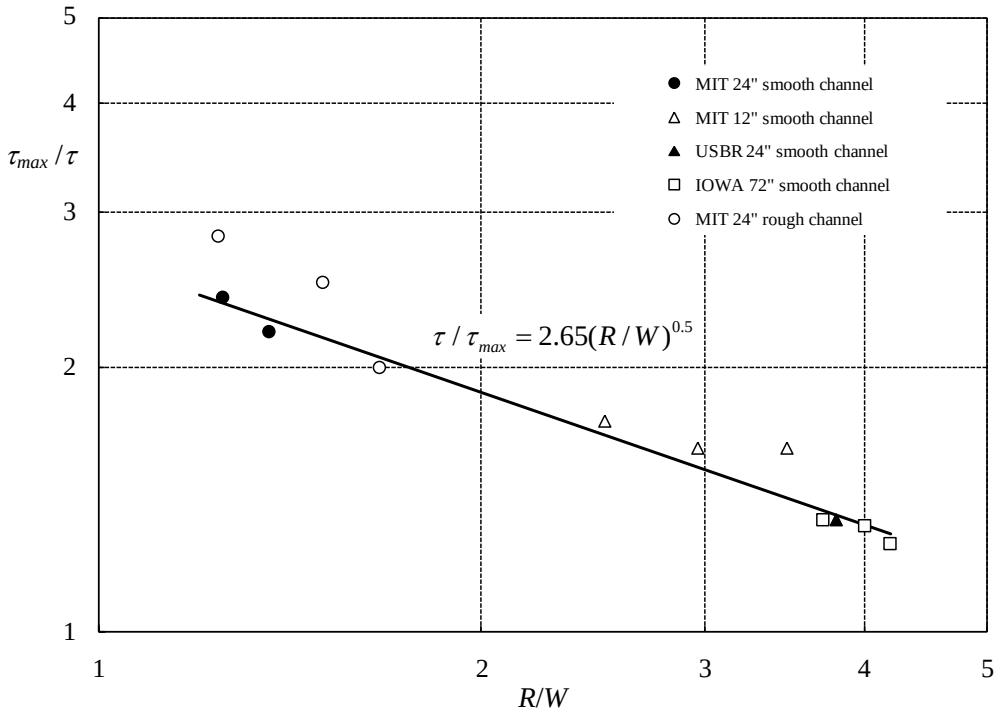

Fig. 1. Test results of τ_{max}/τ with different R/W, ━ regression formula of smooth channels (after Corps of Engineers 1970)

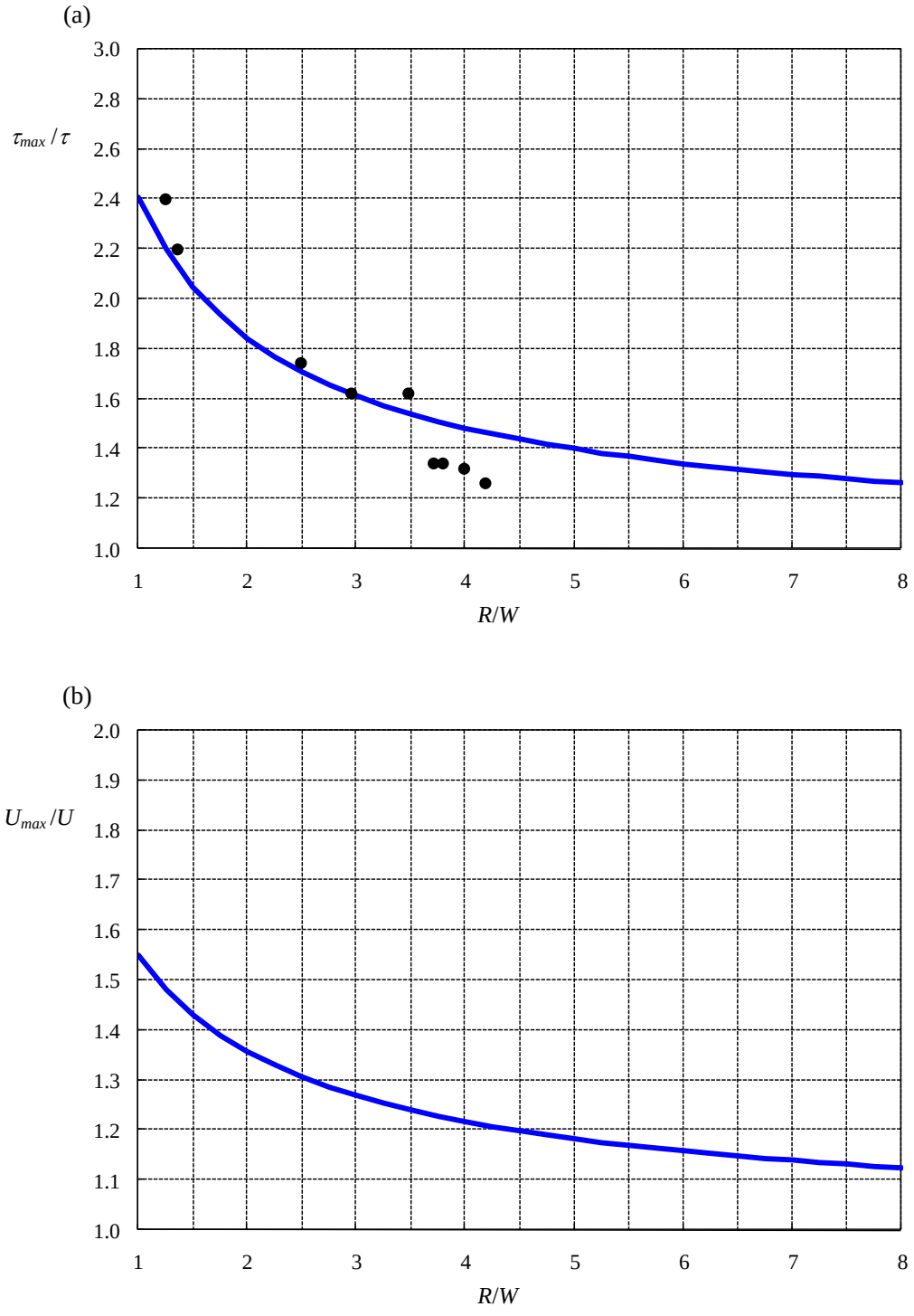

Fig. 2. (a) τ_{max}/τ; (b) U_{max}/U (= β) versus R/W, ● experimental data; ━ curve fitted results

2.2 Experiment Setup

The experiments were conducted in a large basin which is 36.6 m (120 feet) long, 20.9 m (75 feet) wide, and 1.5 m (5 feet) deep located in the Haynes Coastal Engineering Laboratory at Texas A&M University. The test area was 27.4 m long, 13.7 m wide, and 0.30 m deep inside the basin and filled with sand. Curved channels were molded on the sand bed to simulate channel meander migration of natural rivers. A constant-head tank and built reservoir were connected to the entrance of the sand channel to discharge a designed flowrate. A flowmeter was used to monitor and adjust the flowrate. At the end of the test area, an adjustable weir was installed to control the water depth in the channel. The aerial view of the test area and experimental setup is shown in Fig. 3.

Fig. 3. Experimental setup

The initial plan form of the sand channel was comprised with several successive curved bends. A channel bend is defined as a circular curved bend between two inflection points on the channel centerline. The bend radius of curvature R is the radius of the fitted circle and the bend angle Φ is the angle between the initial and end inflection points. An angular variable θ, which varies from zero to Φ in each bend, represents a position angle of each point on the bend centerline. The channel width W is defined as the top width on the flow free surface. Each bend is preceded and followed by an identical bend with opposite direction. A definition sketch of two channel bends is shown in Fig. 4.

Fig. 5 shows the dimensions of the channel initial cross section. For simplicity, the channel has a uniform initial cross section in the form of a trapezoid. The cross section has a bottom width of 40.0 cm, top width of 74.6 cm, bank slope of 30 degree, and depth of 15.6 cm. Although the cross section was trapezoidal in the beginning of each test, it is observed that it deformed immediately right after the channel migration started and continued to transform into a natural shape. Also from the findings of Friedkin (1945), it is proved that a river will shape its cross sections irrespective of its initial cross sections. The water depth in the beginning of each test was set as 10 cm to keep the relative measuring error (1 cm/10 cm) within a certain percentage. The initial channel slope was carefully controlled by adjusting the slope of the sand bed to maintain a constant initial water depth along the channel with a maximum discrepancy less than 1.0 cm (10% of the design depth) in the beginning of each test.

(a)

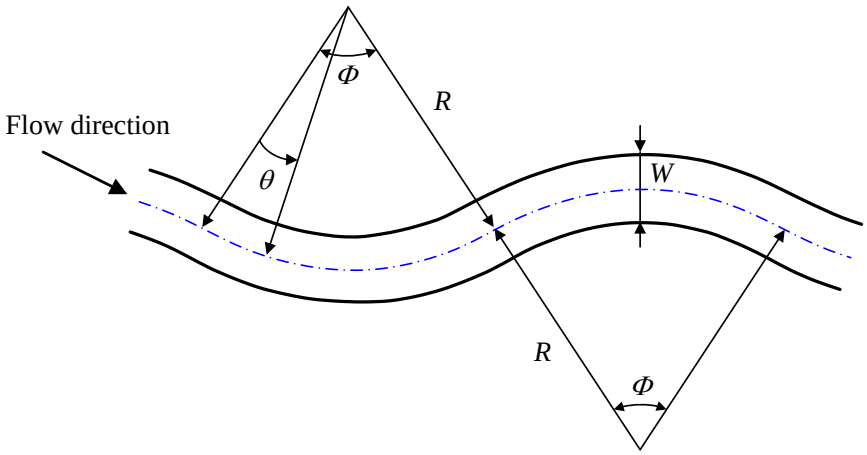

(b)

Fig. 4. Definition sketch of the channel bends

(a)

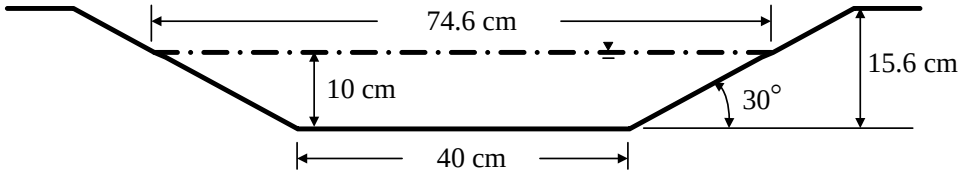

(b)

Fig. 5. Dimensions of the channel initial cross section

Sand with a median grain diameter d_{50} = 0.32 mm was used in the tests because it is uniform, inexpensive, plentiful, and, most importantly, its critical velocity U_c to the incipient motion is within the right range in the use of pumping system in the laboratory. The grain size distribution curve obtained from the sieve analysis of the soil sample is shown in Fig. 6. As discussed in the previous section, this study used the critical velocity instead of critical Shields parameter to quantify the resistance of soil to its initiation of motion. The critical velocity U_c was measured from the EFA (Erosion Function Apparatus) which was developed to measure the erodibility of a soil sample in order for the scour depth at bridge piers (Briaud et al. 1999). The test results include the soil erosion rate $\dot{z}$ to the flow mean velocity U and shear stress τ shown in Fig. 7. From these two curves, the critical velocity U_c of the sand was estimated as 0.08 m/s, which is the minimum flow velocity to initiate channel bankline erosion in the tests.

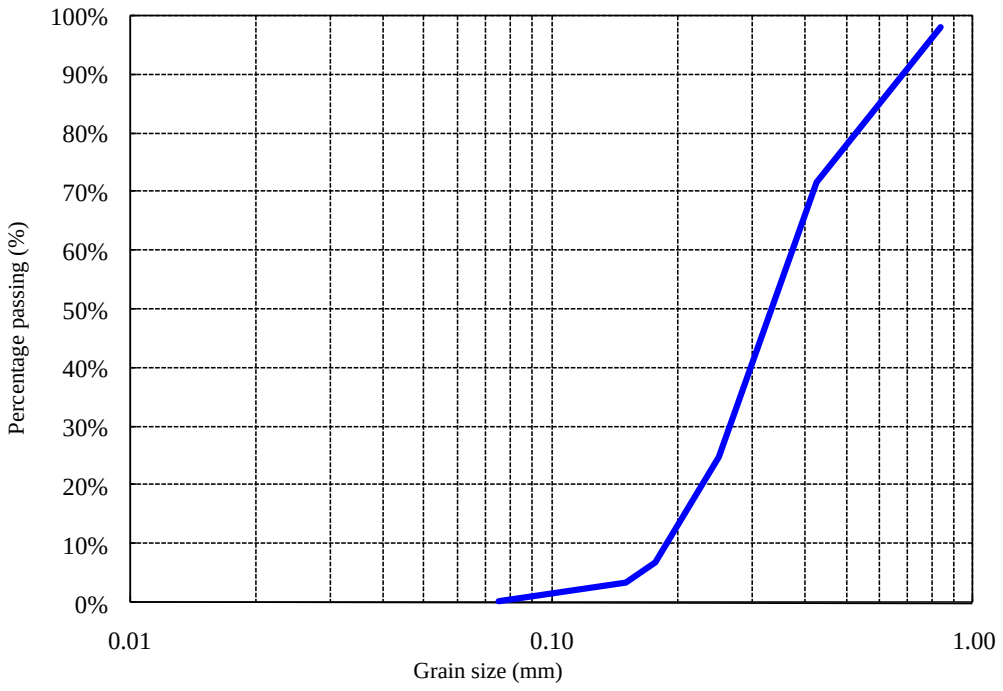

Fig. 6. Grain size distribution of the sand

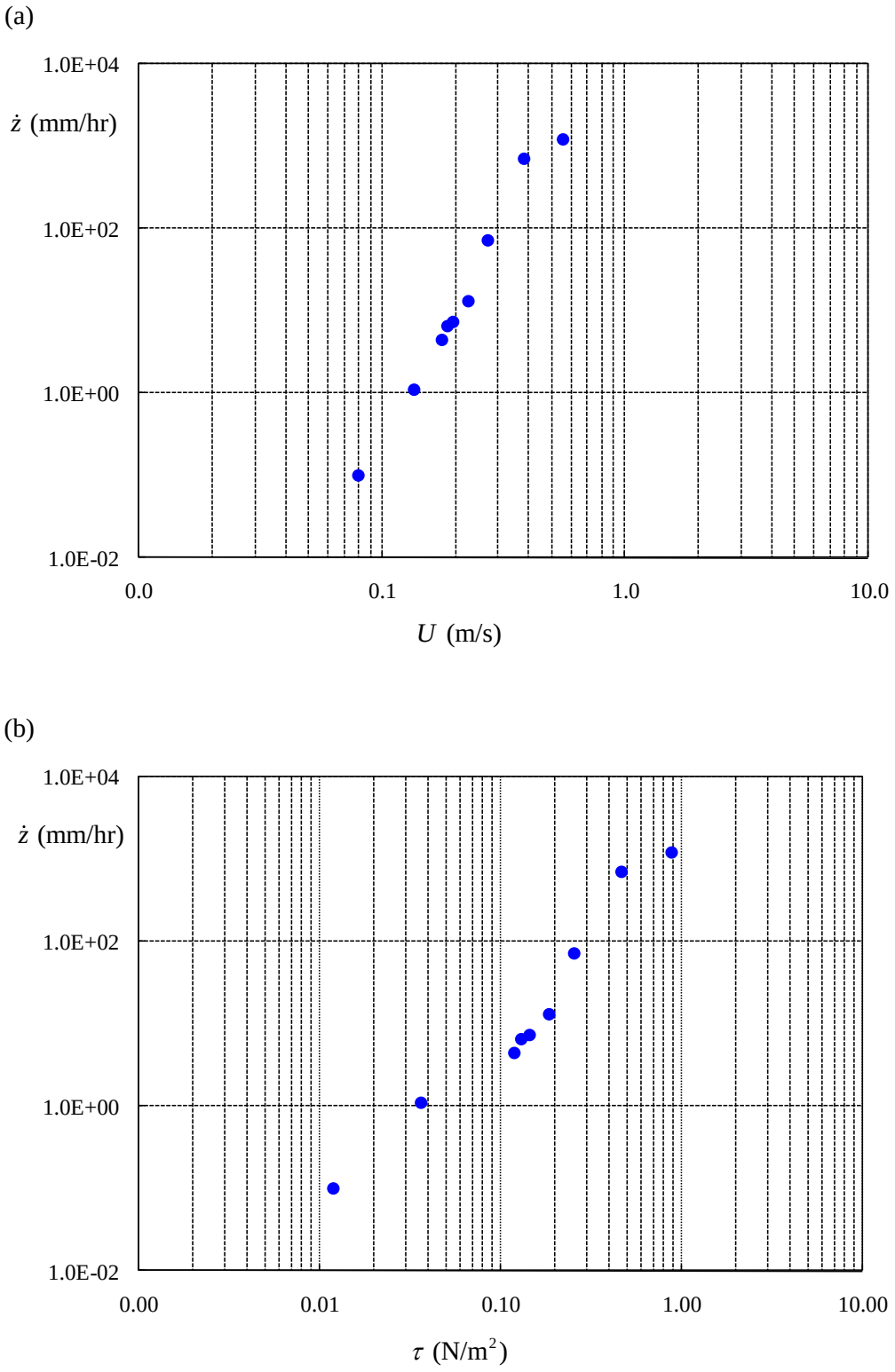

Fig. 7. EFA test results: soil erosion rate $\dot{z}$ with (a) mean velocity U; (b) shear stress τ

By varying the geometry parameters, five different R/W ratios and four different Φ angles were tested in the experiment. In order to reduce the scale effect, the channel was designed to maximize the scale but also be able to fit in the test area with at least three successive curved bends. Straight channels were preceded and followed to each end of the curved channel with two half Φ angle transitions. These two straight channels were kept long enough so the flow became fully-developed before it entered the first curved bend. Since a channel has larger erosion rates in high flowrate (Leopold 1994), the hydraulic conditions in the experiment were all set under high flowrates. Four different flowrates, and therefore four different values of initial Froude number Fr, all in the subcritical flow range, were applied. The experimental setup and test matrix with different geometry and hydraulic conditions are shown in Table 1 and Fig. 8, respectively. The parameters in Table 1 refer to the initial test conditions only and do not reflect the later changes during the tests. Among the test cases, case 12 was performed with the same test conditions as case 03 to test the repeatability of experimental results. Each test was run with a 10 cm initial water depth and 5.6 cm free board on the channel bank. The initial water depth to channel width ratio h/W was kept constant (h/W = 1/7.5) in all tests with h being approximately one order of magnitude smaller than W. Such a condition is close to that of a nature channel while compromising with the limit of physical dimensions in the tests (even though the modeling scale is one of the largest in its kind).

An initially straight channel (case 13) was also conducted in the experiment to investigate the growth and propagation of channel meander migration. The channel starts with a 45° entrance, and follows with a smooth curved bend to form an upstream disturbance. Successive to the curved bend, the channel turns straight gradually and continues to the exit of the test area. Fig. 9 shows the initial channel plan form of case 13. The initial cross sectional geometry and soil type are the same with the first 12 cases, whereas the initial water depth is

slightly reduced to 9.5 cm to facilitate bank erosion. The flowrate was varied in this case to simulate a simple hydrograph. Table 1 also lists the flow conditions of case 13.

The channel bankline was defined and measured at the water-bank interface, and recorded several times during the test. Measurements were taken within relatively short time steps in the early stage of the test to resolve the intensive early movements of the bankline. In addition to the measurements of bankline, several cross sections were chosen along the channel with the bed profiles mapped. Each profile was mapped every 5 cm laterally along the direction perpendicular to the initial channel bank. Water elevations were also measured at the middle of these cross sections. Each test case was run continuously until the bankline movement was less than 1.0 cm between two consecutive measurements, because the measurement error would be in the same magnitude as the bankline migration. The test was also stopped when overflow occurred at any reach of the channel before surface runoff alters the flow field and affects the bank erosion. The test duration of each case, depending on its test condition, varies from 18 to 147 hours as shown in Table 1.

There was no sediment supply at the channel upstream head. Friedkin (1945) investigated in their experiments that the lack of sand feeding at the upstream head does not prevent the channel from meandering. The immediate and direct effect of this shortage is only locally in the upstream section. This study took measurements after the channel second bend, which is behind a significant distance from the channel entrance with a straight section, a transitional curved bend, and the first bend in between. The sediment transported within a channel bend is mostly from the nearby outer banks. It is therefore concluded that the lack of sand feeding at the upstream head of the channel would have an insignificant effect on the migration downstream from the second bend. This may also be better than performing the same

experiments with feeding sand because of the uncertainty and difficulty in feeding sand with a right amount and uniformity.

TABLE 1. Experiment conditions

Case No.	Q (cms)	R/W	Φ	Fr	βFr-Frc	Duration (hrs)
01	0.014	2	65°	0.30	0.34	18
02	0.014	3	65°	0.30	0.31	42
03	0.014	4	65°	0.30	0.29	39
04	0.014	6	65°	0.30	0.27	45
05	0.014	8	65°	0.30	0.26	66
06	0.014	4	120°	0.30	0.29	30
07	0.014	4	180°	0.30	0.29	86
08	0.014	4	220°	0.30	0.29	147
09	0.012	4	120°	0.25	0.23	56
10	0.017	4	120°	0.35	0.34	39
11	0.018	4	120°	0.37	0.37	23
12	0.014	4	65°	0.30	0.29	33
13-1	0.016	∞	∞	0.36	0.28	9
13-2	0.014					3
13-3	0.016					6
13-4	0.014					10

(a)

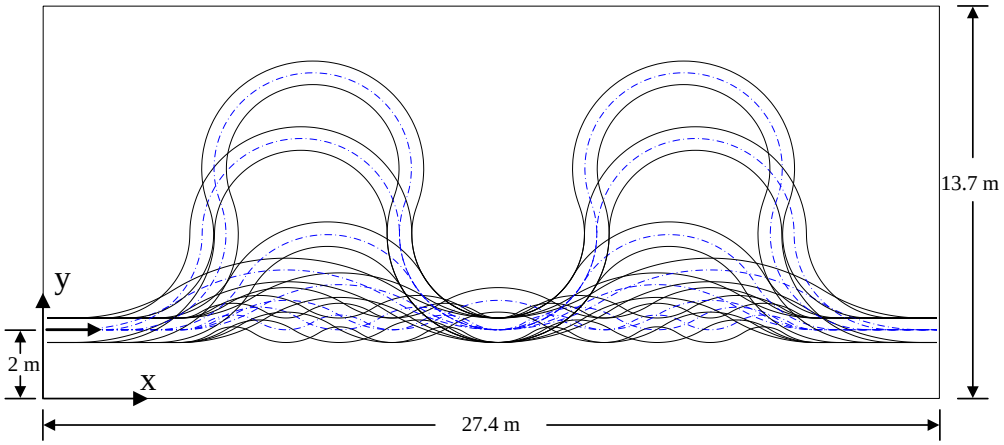

(b)

Fig. 8. (a) Initial channel plan forms of all cases; (b) initial channel of case 08

(a)

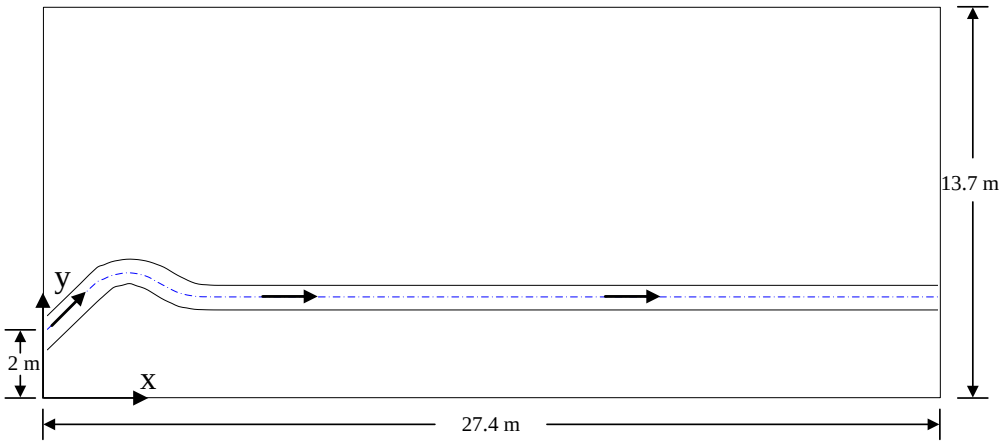

(b)

Fig. 9. Initial channel plan form of case 13

CHAPTER III

FLUME TEST RESULTS

3.1 Channel Meander Migration

The morphological behavior of a curved channel with a constant flowrate is examined from both the spatial and temporal aspects in this study. The following discussion uses case 03 of the experiment as an example to illustrate the channel meander migration of a curved channel. Fig. 10 shows the plan form variations of the second and third bends at several different time steps. On the right bank of the channel, the bankline has relatively small migration distances in both the first half of the leading outer bank (concave, $0.0 < \theta/\Phi < 0.5$) and the second half of the following inner bank (convex, $1.5 < \theta/\Phi < 2.0$). A large displacement occurs beyond the apex of the second bend ($\theta/\Phi = 0.5$) and around the inflection point ($\theta/\Phi = 1.0$). The migration of the second bend persists some considerable distances downstream and intrudes the third bend which has an opposite curvature to the preceded bend. A phase lag exists between the bankline erosion and the channel configuration, resulting in the development of an asymmetric channel plan form. From this spatial aspect, it can be said that the channel plan form expands laterally and translates downstream. Hence, the bankline migration contains two components: the cross-valley (lateral) expansion and the down-valley (downstream) translation. The cross-valley expansion increases channel meander width/belt, whereas the downstream translation stretches channel length and makes the channel become asymmetric. Since each case in the experiment starts (the first twelve curved cases) from symmetric meander loops and homogeneous material, both banks of the channel undergoes a similar but alternate migration pattern.

The temporal variations of the bankline movements shown Fig. 10 had a relatively large migration distance within a short time at the beginning of the test. The bankline migration rate is

high at this stage and the channel sinuosity which is defined as the ratio of channel length to valley length also increases rapidly. The migration rate then decreases gradually as the test proceeds. Small displacement takes place between two consecutive measurements. At the end of the test, the bankline ceases to shift and the channel plan form attains a stable and equilibrium state.

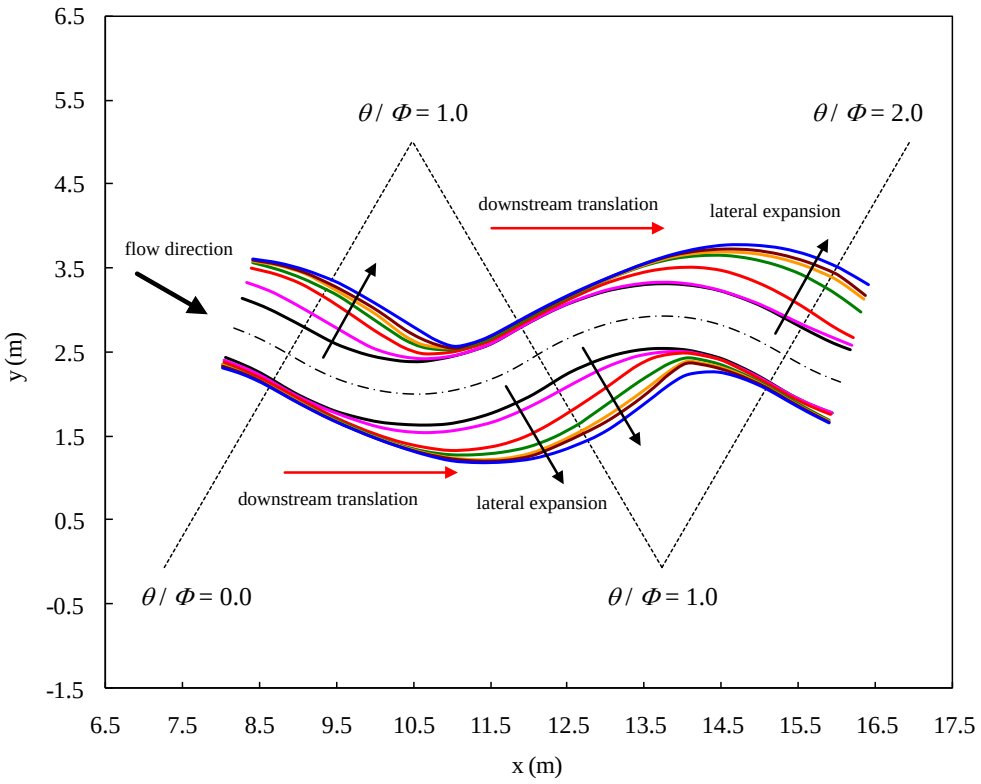

Fig. 10. Channel bankline migration of case 03: — 0 hr; — 3 hr; — 6 hr; — 9 hr; — 15 hr; — 21 hr; — 39 hr

Since high flowrate was used in the experiment, it is clearly demonstrated that both banks of the channel move outwards and the channel get widened accordingly. The banklines on

both sides of the channel had a similar but alternate migration pattern. However, because of different migration rates between the two banks, the channel centerline shows a smaller but more sinuous migration compared to the channel bankline. Fig. 11 illustrates the channel centerline migration of case 03. The migration swings between the two banks and oscillates along the initial channel centerline. The channel centerline translates downstream with time, as the intersections (crossovers) of two consecutive measurements move in the downstream direction. On these intersections, the centerline has zero migration distance and thus a zero migration rate. In a curved bend, the centerline moves towards the center of curvature (centripetal direction) from the bend entrance to the intersection; whereas, beyond the intersection to the exit of the bend, the migration reverses its direction and moves away from the center of curvature (centrifugal direction).

3.2 Channel Cross Sectional Profiles

This study mapped the cross sectional profiles at several selected cross sections along the channel. The profile was measured every 5.0 cm distance across the cross section by using a point gauge. Fig. 12 is a plot of the seven cross sectional profiles of case 03; among these, five cross sections (A-A', B-B', D-D', F-F' and G-G') are located around the initial bend apexes and the other two (C-C' and E-E') are at the bend crossings (inflection points). It is seen that all the five apex cross sections have deep pools in front of the toes of their outer banks (A', B, D', F and G') and sand deposited as point bars along the inner banks (A, B', D, F' and G). Bank slope is steep on the outer banks, while larger bank retreat occurs on the inner banks. On the other hand, the two crossing cross sections are much flatter and shallower in shape, with sand bars develop close to the middle of the cross section. The two banks of these two cross sections have very different erosion distance; on the banks preceded with an outer bank (C and E'), bank retreat is much larger than the banks following an inner bank on the opposite side (C' and E). Over all the

cross sections, sediment coming from the nearby upstream and from the collapse of the banks contributes to the increase in bed elevation and in transverse slope across the cross section.

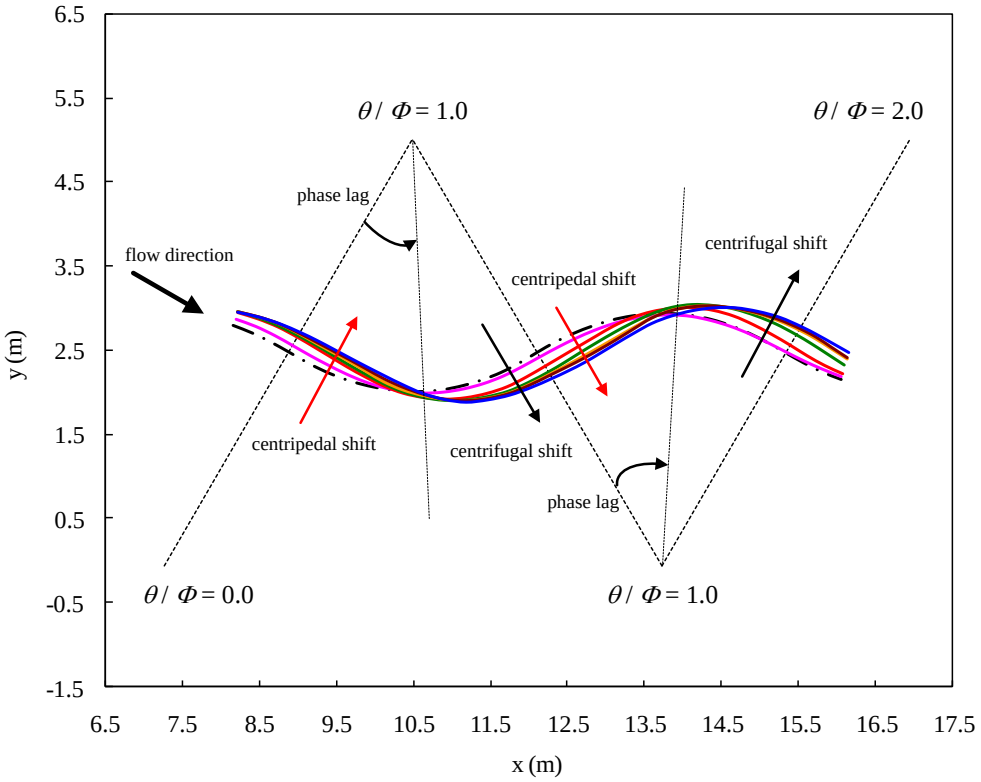

Fig. 11. Channel centerline migration of case 03: — 0 hr; — 3 hr; — 6 hr; — 9 hr; — 15 hr; — 21 hr; — 39 hr

It is believed that the secondary flow is the main mechanism for the lateral sediment transport in a curved bend (Dietrich and Smith 1983). Higher velocities on the upper surface layer move from the inner bank to the outer bank and slower velocities on the channel bottom move in the opposite direction. The outer bank downwelling and near-bottom velocity scour the outer bank and channel bottom. Sediment is then transported as bed load towards the inner bank.

This explains why the curved channel has a deeper depth and steep slope at the outer bank and sediment deposits as a point bar along the inner bank as shown in Fig. 12. Similar flow patterns and cross sectional profiles have also been reported by field studies of natural rivers (e.g., Thorne et al. 1985).

From these profiles, it is seen that the deep pools are formed alternately at the channel outer banks, and point bars are developed in the channel crossings between two curved bends. The thalweg moves sinuously in a path deep in the bends separated by shallow crossings. As shown in Fig. 12, large erosion doesn't occur on the apex of an outer bank (e.g., B and D'), instead the inner bank around the adjacent downstream crossing (e.g., C and E') undergoes larger bank retreat. When the flow enters a curved bend, higher primary velocity flanks along the inner bank in conformity with free vertex flow (Ippen and Drinker 1962). After crossing over the bend, the thalweg impinges on the channel bank and causes large erosion. Due to the phase lag of the thalweg to the channel curvature, the bank erosion and bankline migration also have a phase lag to the channel plan form (Carson and Lapointe 1983). This explains why the downstream crossings have larger bank migration than the preceded outer bank apexes. In this way, the phase lag of the thalweg would be translated into an asymmetry in the channel plan form.

One thing needs to note here is since high flowrates were used in this study (similar to having a flood lasting for months), the banklines on both sides of the bend moved outward and widened the channel width. If the flowrates were reduced in the tests after having high flowrate flow for certain amount of time, such as in the dry season for a natural channel, the water would have flow in the deeper paths in the channel and the water-bank interfaces would have shifted toward the outer banks exposing the sand bars along the inner banks. Moreover, vegetation may grow and strengthen the soil above the water line in the channel during the dry season in nature

and make it harder to erode in the next wet season. The width of the river therefore may not widen as much as it showed in the experiment. This is a feature that the experiment of this study did not reproduce.

3.3 Cross Sectional Flow Properties Measurements

In the experiment, four flow properties at these selected cross sections were also estimated in each time step. The cross sectional mean velocity was calculated as $U = Q / A$, with A being the wetted cross section area as shown in Fig. 12. A point gauge was used to measure the water elevation Zw at the middle of each cross section. The hydraulic water depth h and the Froude number Fr were then estimated as $h = A / W$ and $Fr = U / \sqrt{gh}$. The temporal variations of these flow properties at all the cross sections of case 03 are shown in Fig. 13. Fig. 13(a) shows that the mean velocity of each cross section decreased with time and its value gradually reached a constant as the test continued. Sediment transported from the nearby upstream and bank collapse (primary as bedload) caused aggradation and, as a result, increased the water elevation in Fig. 13(b). The hydraulic water depth in Fig. 13(c) decreased in the beginning of the test and increased to a constant value in the later time steps. The variations of the Froude number (Fig. 13(d)) and channel width were influenced by the mean velocity and hydraulic water depth. Both increased in the early stage of the test due to a shallow water depth, and reached constant as the variations of the mean velocity decreased.

From the temporal variations of these cross sectional properties, it can be summarized that the channel began eroding their banks with a larger rate. The bank retreat and sediment deposition caused the cross sections become wide and shallow. As a result, the velocity and energy slope were so reduced that the bank erosion stopped and the channel meander reached an equilibrium state.

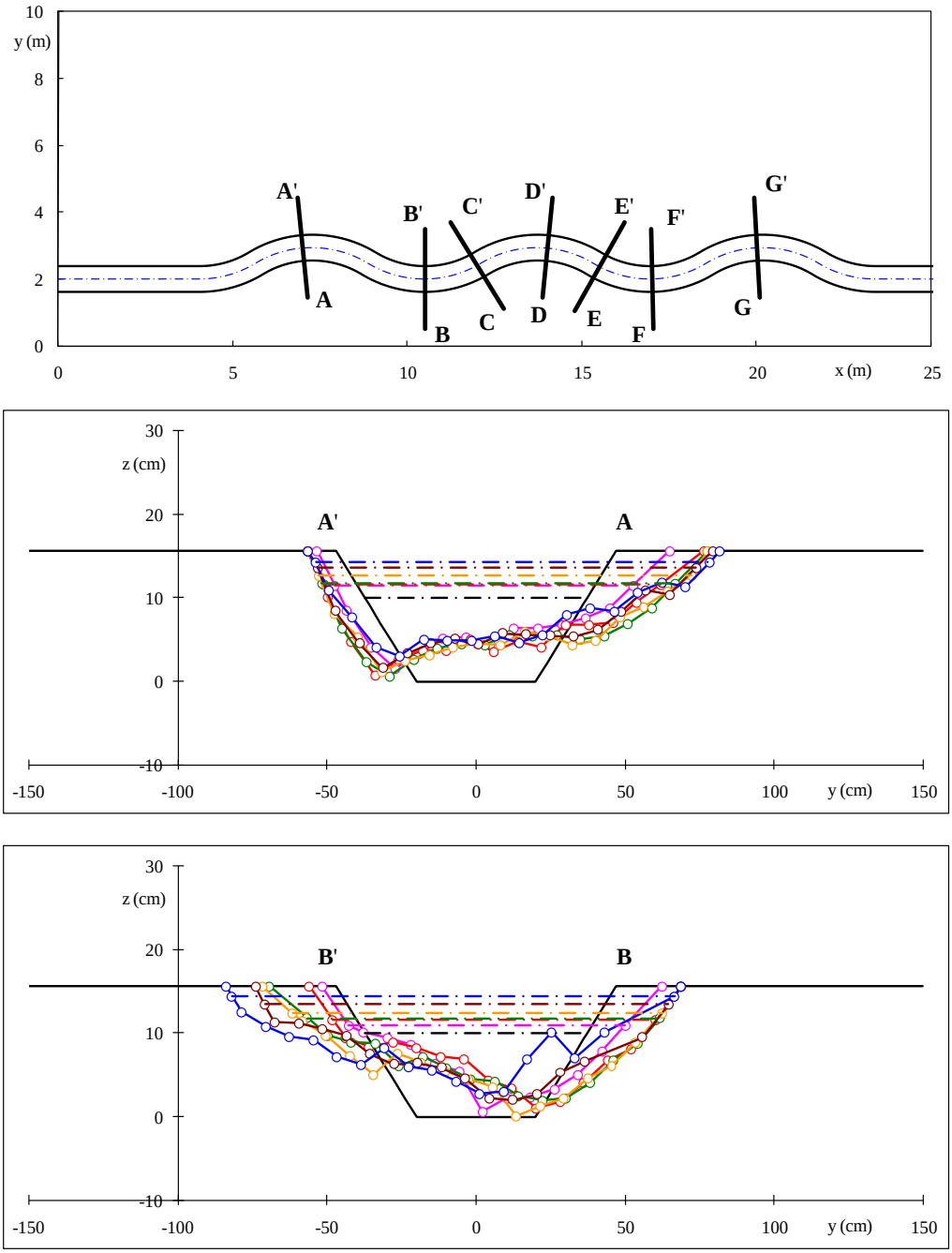

Fig. 12. Downstream look cross section profiles of case 03: ○ measurements; — 0 hr; — 3 hr; — 6 hr; — 9 hr; — 15 hr; — 21 hr; — 39 hr

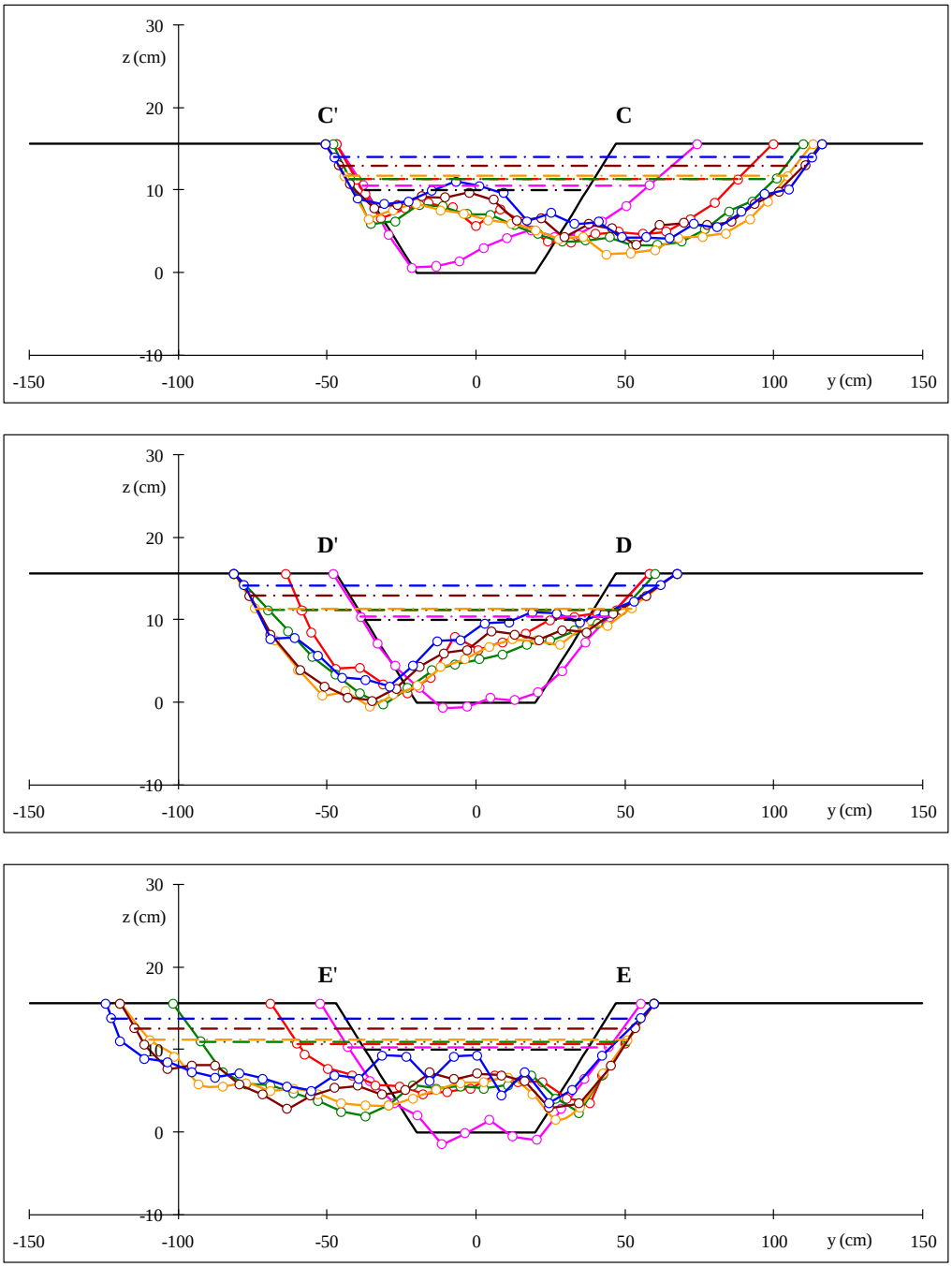

Fig. 12. (Continued)

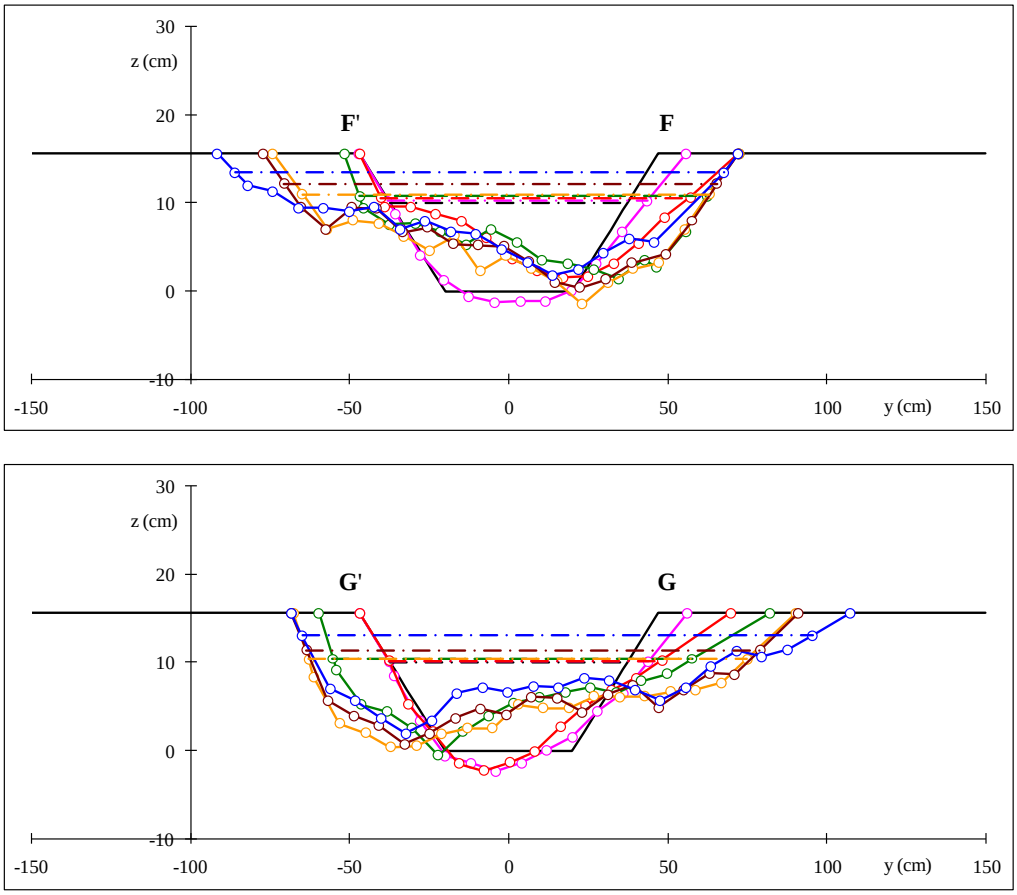

Fig. 12. (Continued)

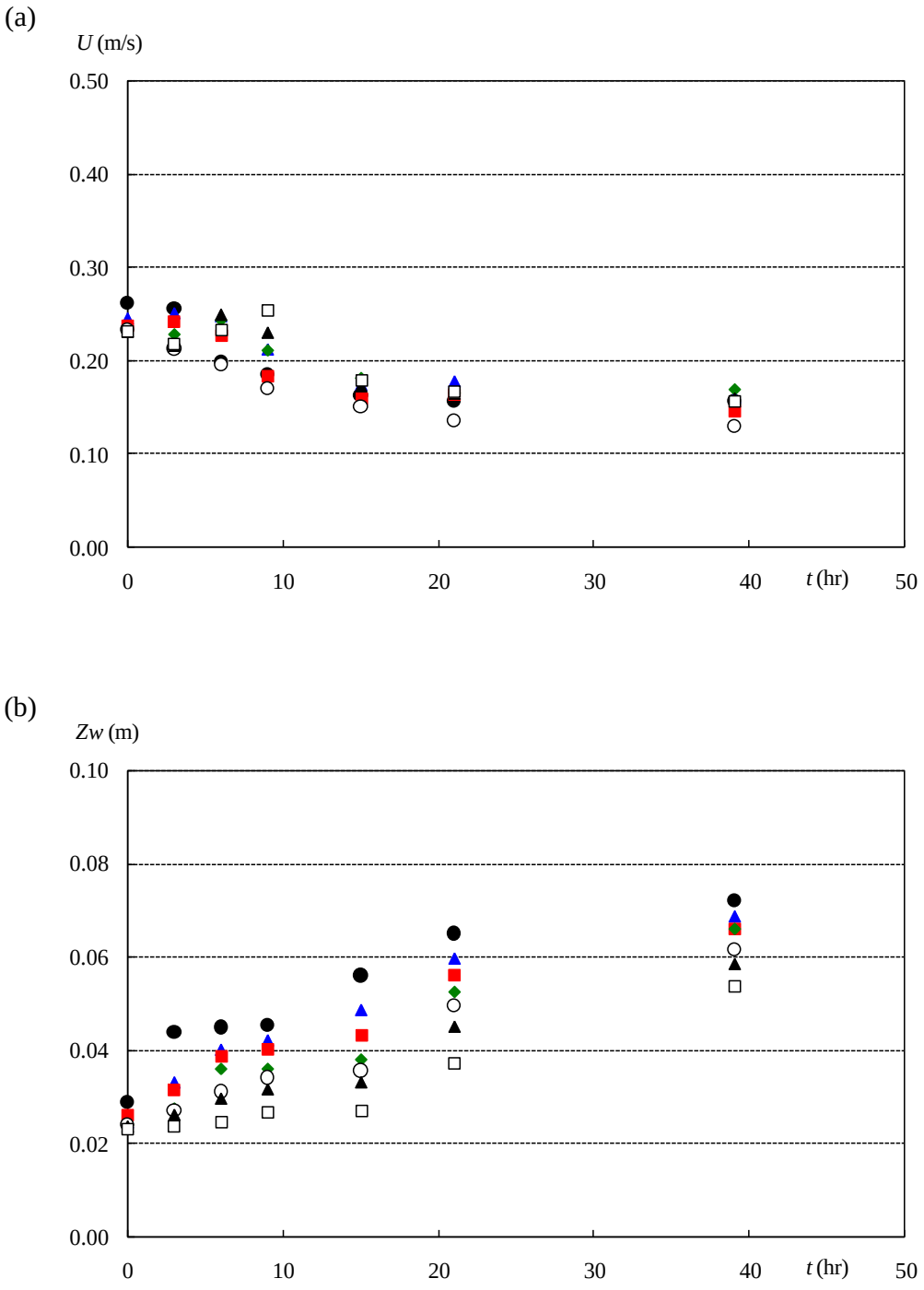

Fig. 13. (a) Mean velocity *U*; (b) water elevation *Zw*; (c) water depth *h*; (d) Froude number *Fr* measurements of case 03, ● section A; ▲ section B; ■ section C; ♦ section D; ○ section E; ▲ section F; □ section G

(c)

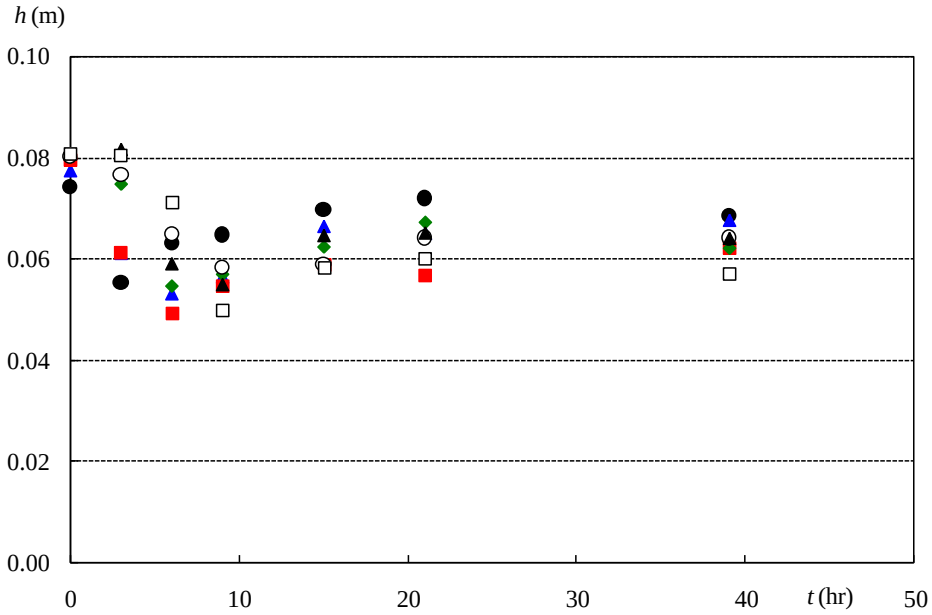

(d)

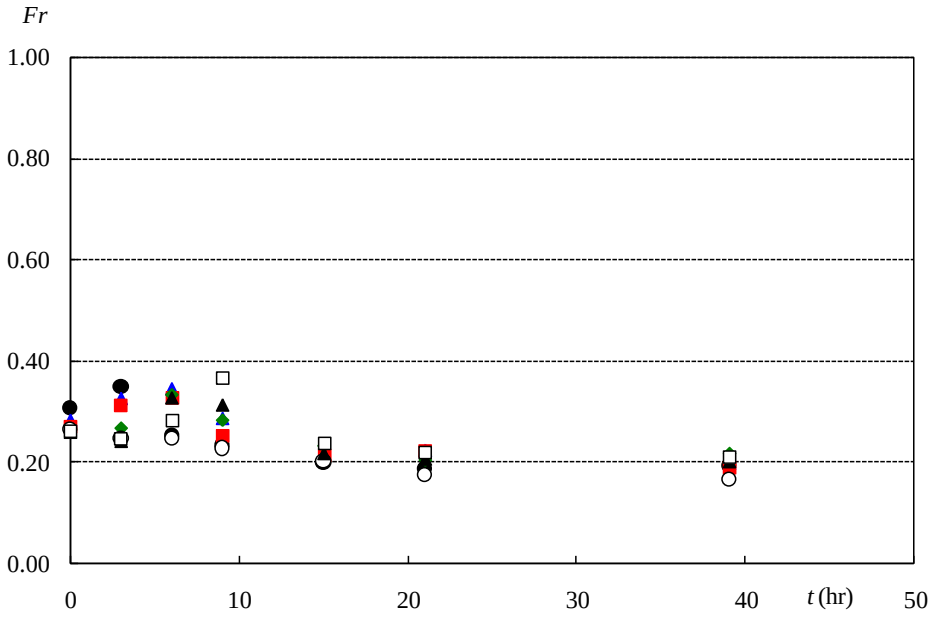

Fig. 13. (continued)

3.4 Channel Plan Form Variations

Fig. 14 shows the channel plan form variations of four other cases with different R/W values, corresponding to cases 01, 02, 04, and 05 in Table 1. The other two parameters Φ and Fr were kept constant in these cases. In the first two cases (R/W = 2 and 3), the erosion mostly occurs on the inner (convex) bank and the bankline moves in the down-valley direction. The bankline migration has a great phase lag to the channel curvature. According to Ippen and Drinker (1962), high velocity and shear stress occurs on the inner bank of a curved bend with small R/W. Channel bankline appears strengthened and the sinuosity reduces. On the other hand, the channel bankline in the larger R/W cases (R/W = 6 and 8) migrated in both the cross- and down-valley directions. Large migration distance can be found on the outer bank, consistent with the increased stresses. The channel still remains a sinuous course in the end of the test. Among these four cases and case 03 (Fig. 10), case 03 has a largest migration distance and the location of this migration distance moves downstream as R/W decreases. The maximum migration distance occurs on the inner bank ($\theta/\Phi > 1$) in cases 01 and 02 and on the outer bank in 04 and 05 ($\theta/\Phi < 1$).

The bend angle Φ is another important parameter to describe the channel geometry. If R/W is the same, the channel with a greater bend angle Φ has a longer channel length. Fig. 15 shows the bankline movement of four different bend angles with same initial R/W and Fr (cases 03, 06, 07, and 08 in Table 1). The results show that the final plan form of case 03 (smallest Φ) is straightening and asymmetric as the test proceeded. In the two large Φ cases (case 07 and 08), two places of larger migration appear along the bend. The channel has a greater migration distance and phase lag to the channel curvature as Φ decreases. Fig. 16 compares the channel plan form variations among four different initial Froude numbers with constant initial R/W and Φ (cases 09, 06, 10, and 11 in Table 1). R/W and Φ of these four cases are 4 and 120°, respectively.

Since the channel initial conditions and bed/bank material are the same, these four Froude numbers directly result from four different flowrates. The result shows that the final plan forms of these four cases are very similar, except the bankline migration rate increases with the increase of the Froude number (flowrate). All these cases remain a very symmetric plan form at the end of the test. A greater migration distance on the right bank occurs around the outer bank apex (θ/Φ = 0.5), and a smaller value is found on the downstream convex bank (θ/Φ = 1.5). It also can be seen in the figure that an increase in the initial Froude number results in increasing the size (amplitude) of the curved bends.

3.5 Meander Migration of a Straight Channel

In the experiment of this study, case 13 is a straight channel except with an initial upstream curved bend. The initial channel plan form starts with a 45° straight segment and connects with a curve bend. The channel then gradually turns to a horizontally straight channel to the outlet of the test area. The initial cross section and channel bed and bank material are the same with the first 12 cases, except the initial water depth reduces slightly to 9.5 cm in order to facilitate the bank erosion. Two different flowrates are used alternatively in this case to simulate a simple hydrograph. Fig. 17 shows the results of bankline and centerline migration in this case. It is seen that erosion takes place throughout the whole channel right after the test starts. Large bank retreat occurs on the inner bank adjacent the curved bend and persists beyond the connection with the downstream straight reach. Both banks of the channel have a significant amount of shifting in three hours. A series of uniform and sinuous bends are developed, with bend widths (amplitudes) and lengths increase as the test proceeds. At the last one time step (after 38 hours), the channel has turned into a stable and fully-developed meander loop of which the meander length is about 7.0 m. On the other hand, the channel centerline migration exhibits a “wave propagation” pattern in Fig. 17(b). The centerline oscillates from a straight line to a sinuous

curve in space, and the increase in its amplitude transmits from upstream towards downstream. The amplitude stops increasing and becomes uniform when the channel meander reaches equilibrium. The wavelength of the centerline wave form is about half of the meander length of the channel bank.

Fig. 18 shows the temporal variations of cross sections in case 13. It can be seen that the curved bends develop as a result of the flow impingement and deflection from the channel banks, and deposition of sand inside the channel. The channel is deeper on the concave side of the bend (e.g., B) and shallower in the crossing between two bends (e.g., B'). Alternate bars appear beside both banks in the straight reach and move downstream with increase of the bar height. The downstream shifting of these bars then slows down and eventually ceases as the flow continues to rework the channel boundaries. After the build-up of alternate bars, flow path and its impinge angle to the channel bank become stationary. Erosion therefore occurs on the front face of each alternate bar, and gradually transforms it into a point bar. The flow in turn is confined and swings between these sand bars. Following this interaction between the flow and sediment, channel meander has been initiated and the development of curved bends becomes appreciable. The channel is then deeper on the concave side of the bend (e.g., B) and shallower in the crossing between two bends (e.g., B'). Finally, the thalweg along the meander channel showed a contrast formation of deep pools separated by shallow crossings.

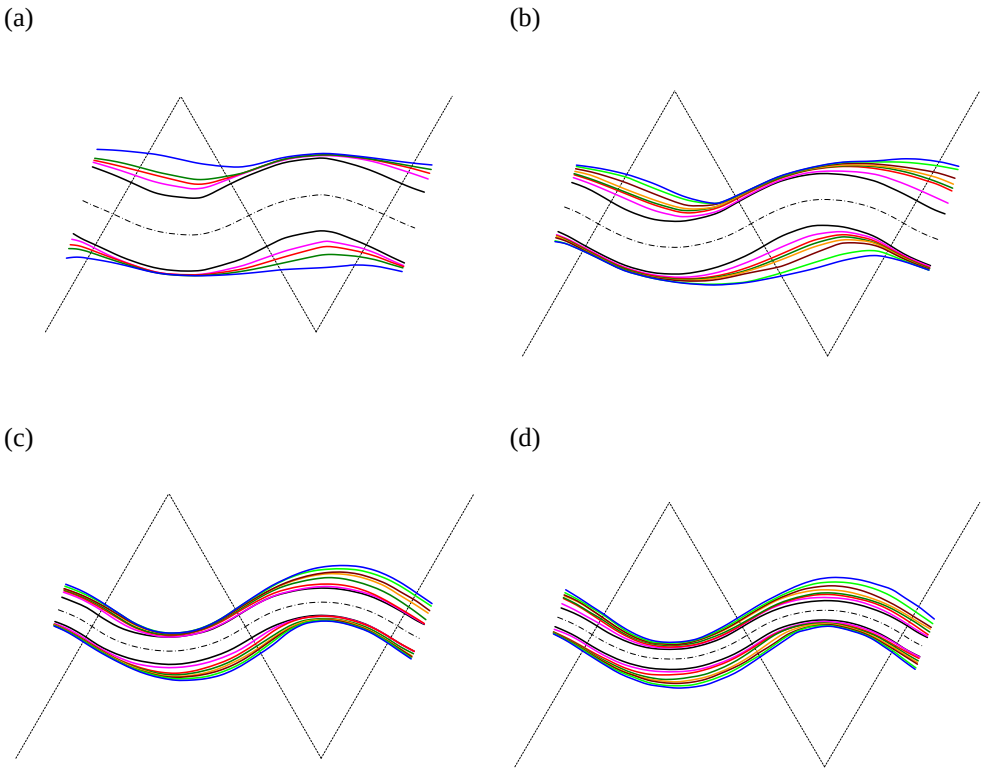

Fig. 14. Channel plan form variations in different *R*/*W*: (a) case 01 (18 hrs); (b) case 02 (42 hrs); (c) case 04 (45 hrs); (d) case 05 (66 hrs)

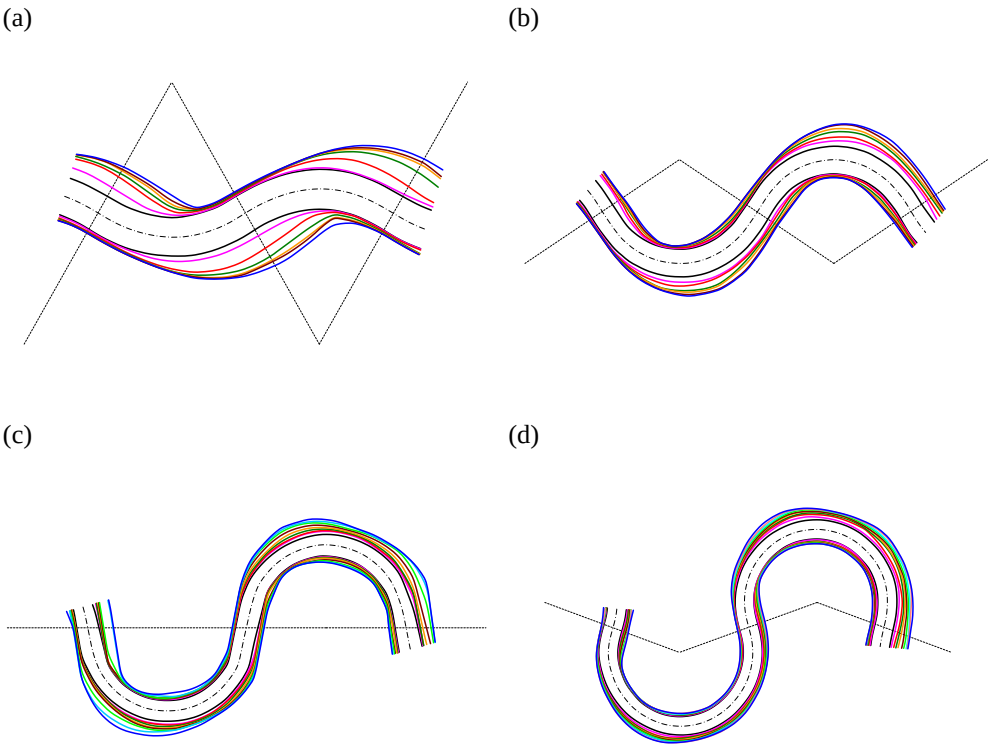

Fig. 15. Channel plan form variations in different Φ: (a) case 03 (39hrs); (b) case 06 (30 hrs); (c) case 07 (86 hrs); (d) case 08 (147 hrs)

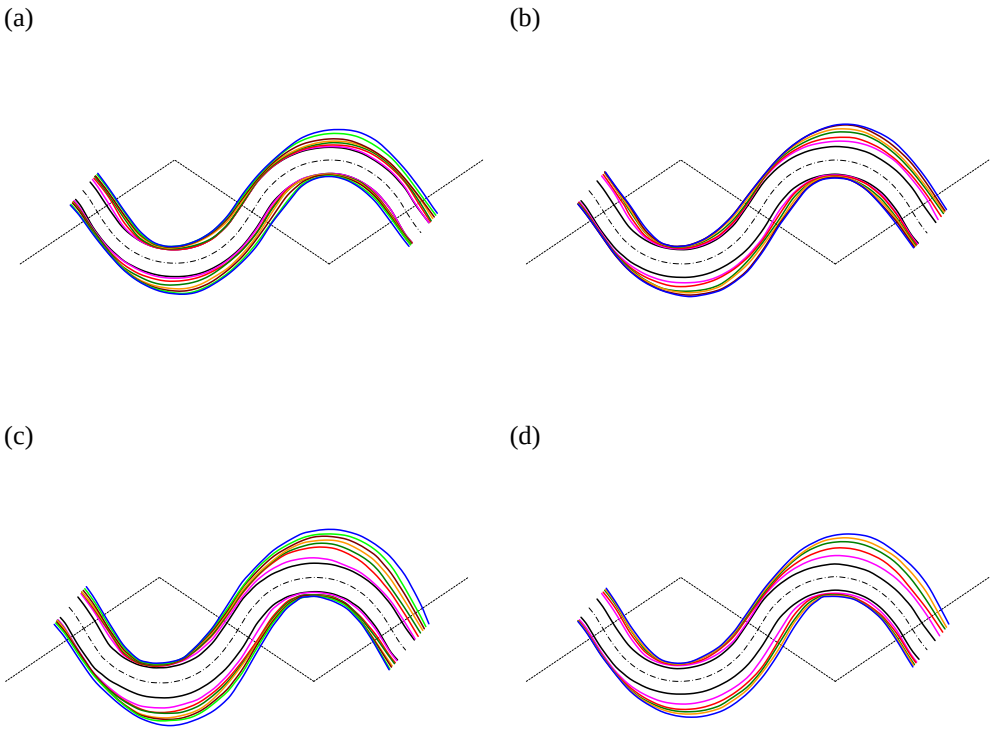

Fig. 16. Channel plan form variations in different *Fr*: (a) case 09 (56 hrs); (b) case 06 (30 hrs); (c) case 10 (39 hrs); (d) case 11 (23hrs)

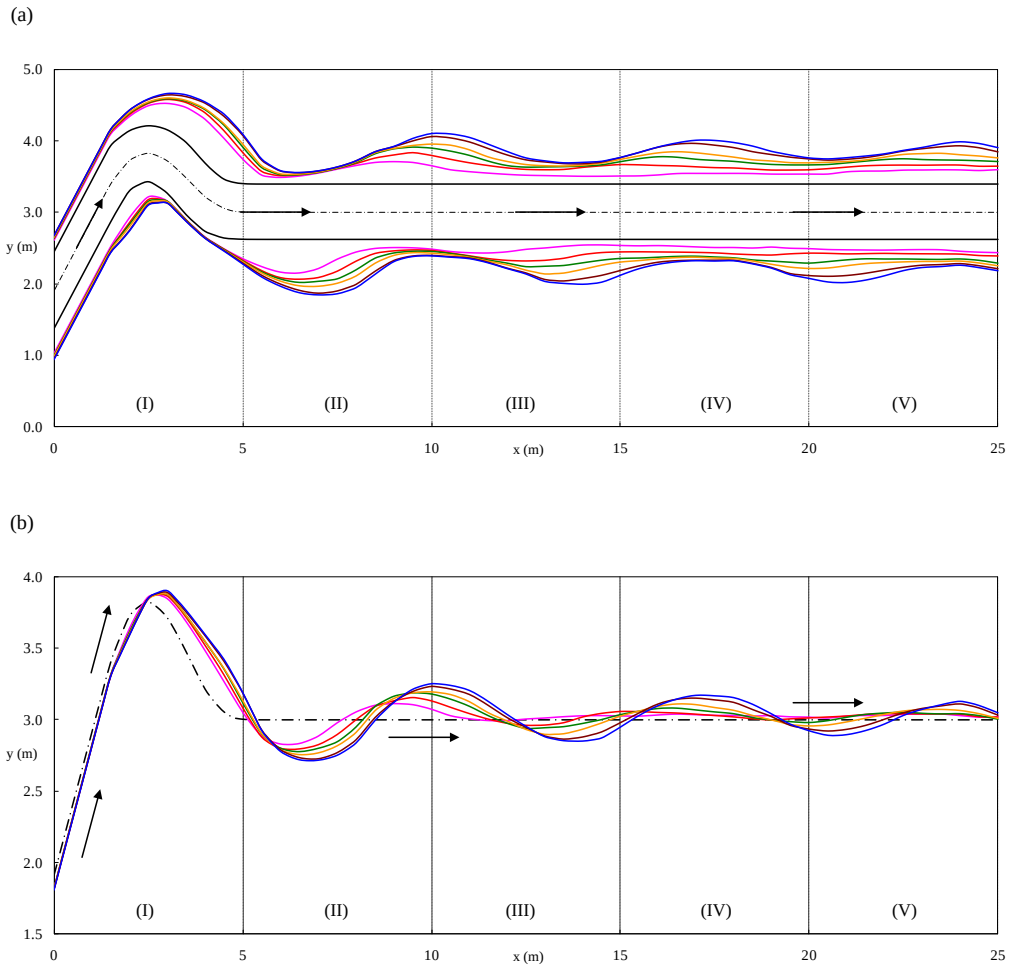

Fig. 17. Channel (a) bankline; (b) centerline migration of case 13: — 0 hr; — 3 hr; — 6 hr; — 12 hr; — 18 hr; — 28 hr; — 38 hr

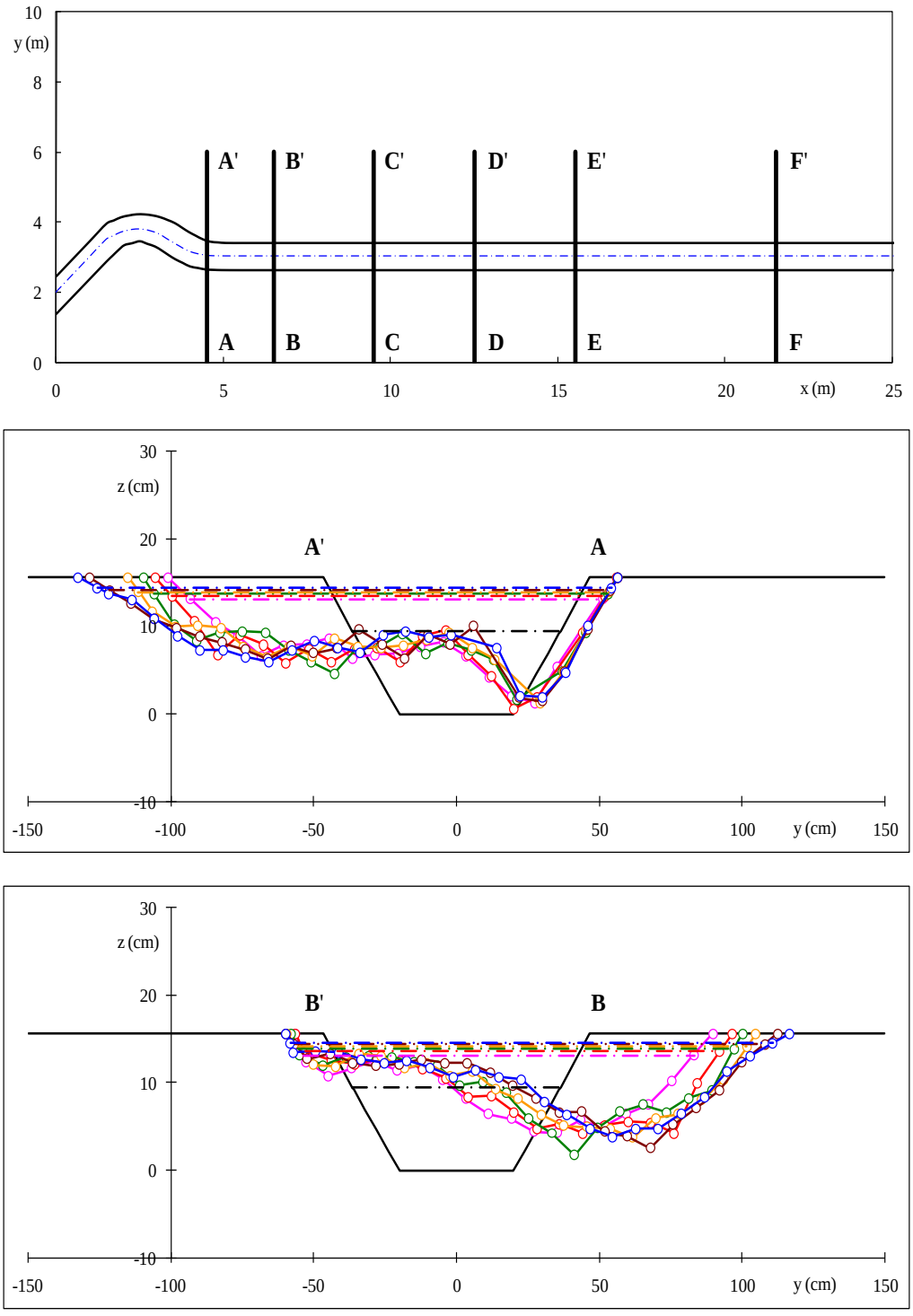

Fig. 18. Downstream look cross section profiles of case 13: ○ measurements; — 0 hr; — 3 hr; — 6 hr; — 12 hr; — 18 hr; — 28 hr; — 38 hr

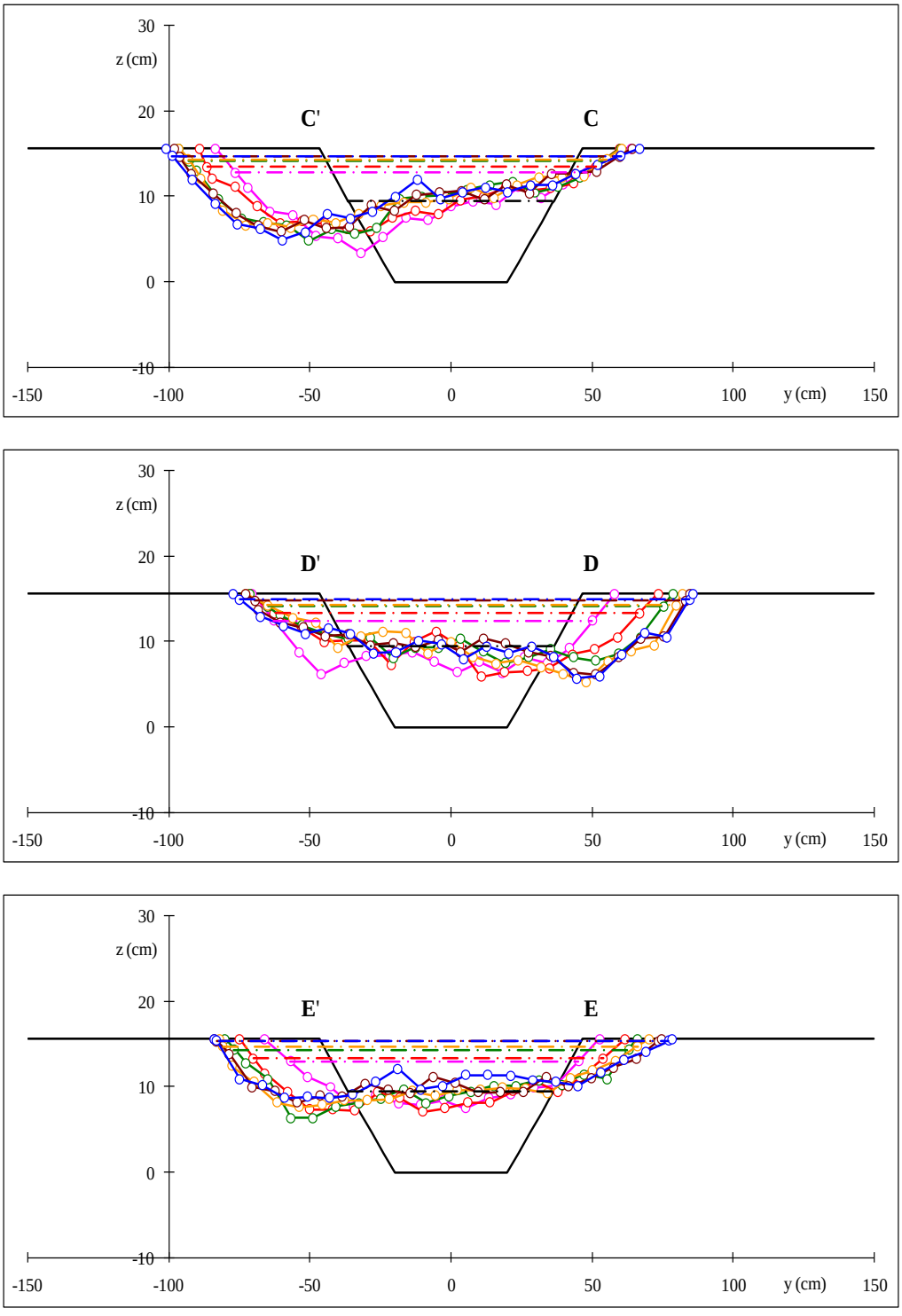

Fig. 18. (Continued)

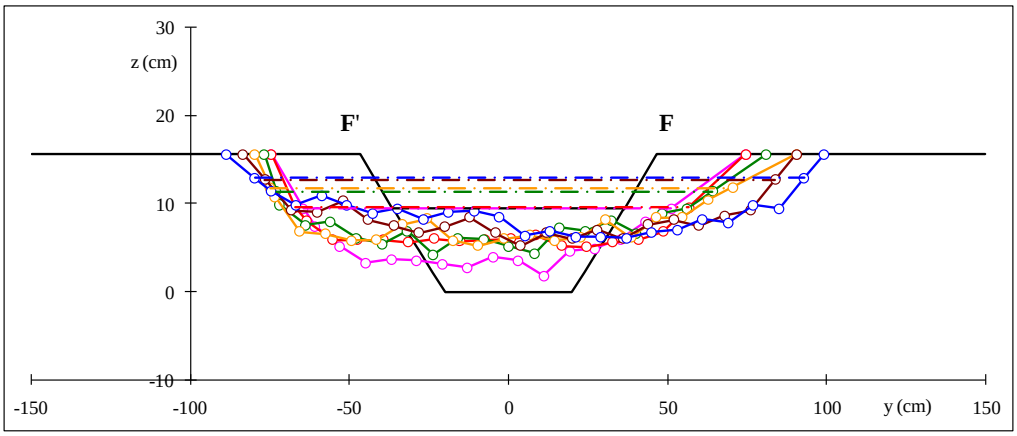

Fig. 18. (Continued)

CHAPTER IV

CHANNEL BANKLINE MEANDER MIGRATION DISTANCE

4.1 Channel Bankline Migration Distance and Hyperbolic Process

The channel bankline migration distance m is defined as the bankline displacement to the initial channel, in the direction perpendicular to the initial bank. In this study, the measurements of m were taken along the channel at every five degree increment, from the beginning of the second bend (defined as $\theta/\Phi = 0.0$) to the end of the third bend (defined as $\theta/\Phi = 2.0$). Using case 03 in Fig. 10 as an example, the migration distance at five different angles on the channel right bank is shown in Fig. 19. It is seen that the channel bankline migration has a greater rate $\dot{m}$ (slope) at the early stage of the test, meaning that m increases rapidly within a short period of time. As the flow continues to erode the channel bankline, $\dot{m}$ decreases continuously and gradually. A maximum value of m then is expected when the bankline migration reaches an equilibrium state at $t \to \infty$. The figure also shows that the bankline underwent different migration rates in different angles and the maximum value of migration distance ranged from 0.1 m to 1.0 m, which is approximately 0.13 to 1.30 times the initial channel width W. Note that $1.0 \leq \theta/\Phi \leq 2.0$ in the subfigure denotes a position on the right bank of the downstream inner bend. The increment of m at each cross section in Fig. 19 clearly exhibits a hyperbolic function of time, which gives a good approximation in estimating the bankline migration distance. The function is of the form

$$m = \frac{t}{a + bt} \tag{14}$$

where m is the channel bankline migration distance, t is time, and a, b are constants. The reciprocals of the two constants in the hyperbolic function are the initial slope at $t = 0$ ($1/a$) and the asymptotic value of the hyperbolic curve at $t \to \infty$ ($1/b$).

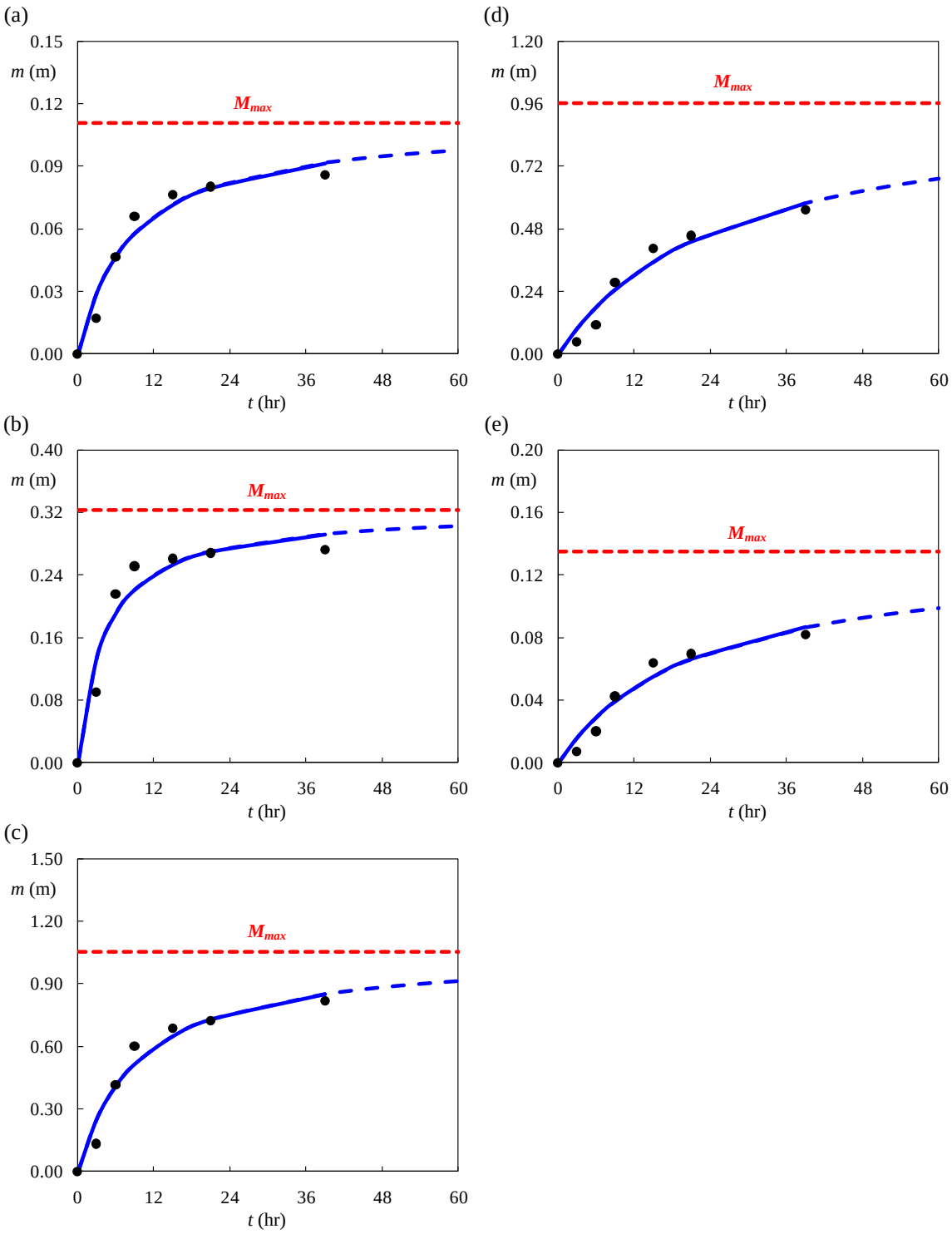

Fig. 19. Bankline migration distance at five different cross sections in case 03: (a) $\theta/\Phi = 0.0$; (b) $\theta/\Phi = 0.5$; (c) $\theta/\Phi = 1.0$; (d) $\theta/\Phi = 1.5$; (e) $\theta/\Phi = 2.0$, ● measurement; — hyperbolic fit

The hyperbolic process uses two constant parameters to model the bankline migration distance at a cross section along the channel. The function can be re-written in another form

$$\lim_{t\to 0}\frac{t}{m}=\lim_{t\to 0}(a+bt)=a=\frac{1}{\dot{M}_i} \tag{15}$$

$$\lim_{t\to \infty}\frac{1}{m}=\lim_{t\to \infty}(a/t+b)=b=\frac{1}{M_{max}} \tag{16}$$

in which a linearly functional relationship is between t/m and t. The inception (a) and slope (b) of this straight line represent the reciprocals of the bankline migration rate at the beginning of the process (t = 0) and the bankline migration distance at the asymptotic state ($t \to \infty$). Therefore, the initial migration rate $\dot{M}_i$ and the maximum migration distance M_{max} at a given cross section can be expressed as $\dot{M}_i = 1/a$ and $M_{max} = 1/b$. Fig. 20 shows an example for the estimations of $\dot{M}_i$ and M_{max} at a cross section under the hyperbolic process. The values were obtained through non-linear regression of m or linear regression of t/m with a least-square-errors method to the measurement data.

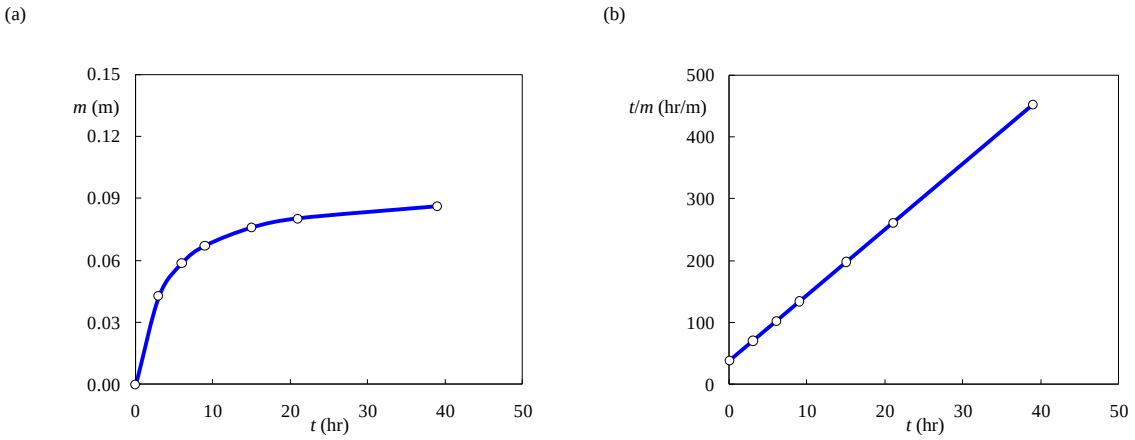

Fig. 20. Estimations of $\dot{M}_i$ and M_{max} under the hyperbolic process, ○ measurements; ━ hyperbolic fit

In this study, the data from the second outer bank of the channel and the following third inner bank were used, only to ensure that a fully-developed secondary flow in the channel was accounted for and the back water effect from the channel exit was negligible. The non-dimensional results of $\dot{M}_i$ and M_{max} of case 03 are shown in Fig. 21, in which $\dot{M}_i$ and M_{max} were normalized by the initial channel mean velocity *U* and channel top width *W*, respectively. It is seen that both $\dot{M}_i$ and M_{max} along the channel have a peak value behind the channel apex (θ/Φ = 0.5) and a phase lag to the channel curvature. Both distributions increase with the increase of the position angle (θ) and reach a maximum value behind the apex of the channel outer bank. The maximum value of $\dot{M}_i$ occurs at θ/Φ = 0.92 (θ = 60°), while the maximum value of M_{max} occurs further downstream at θ/Φ = 1.15 (θ = 70°) which is in the downstream inner bank. The distributions decrease from the maximum value to the exit of the downstream bend (θ/Φ = 2.0). The migration in the leading side of the outer bank ($0.0 < \theta/\Phi < 0.5$) was apparently affected and interfered by the preceding bend (first bend of the channel). Since the experiment used a larger flowrate, the initial flow mean velocity was larger than the soil critical velocity. As a result, there is no "zero migration" point in both distributions. Figs. 22-25 are the distributions of $\dot{M}_i$ and M_{max} in other four cases whose bend angles Φ are all 65 degree. After comparing these cases, it can be seen that case 03 (R/W = 4) has a largest peak value in $\dot{M}_i$ and M_{max} among these five cases. The value difference to other four cases in $\dot{M}_i$ is greater than the value difference in M_{max}. The peak value decreases as R/W increases or decreases from 4. The position angles of the peak values in both $\dot{M}_i$ and M_{max} shift to the downstream inner bend in small R/W cases. The standard deviations of these two distributions are very close among the cases, while case 03 has a smallest value in $\dot{M}_i$ and case 01 has a largest value in M_{max}.

(a)

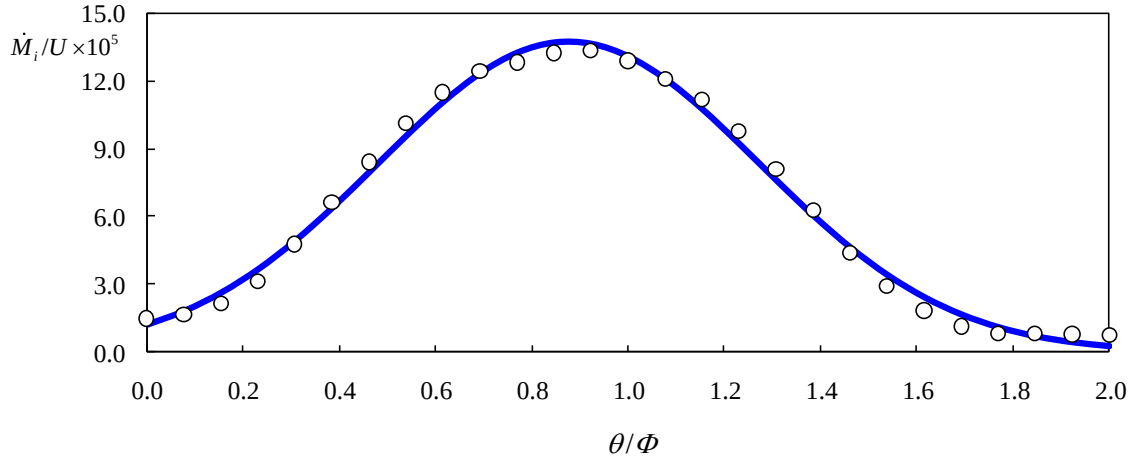

(b)

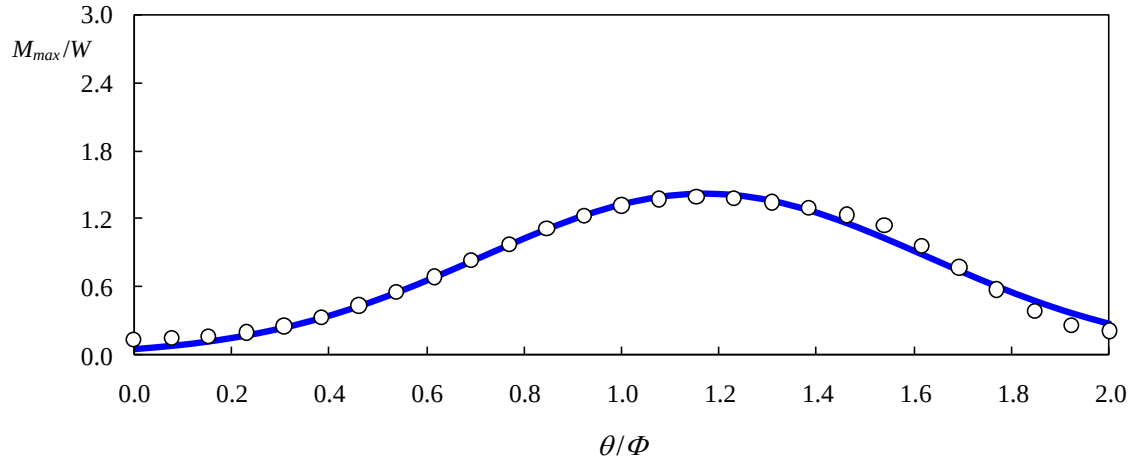

Fig. 21. Normalized $\dot{M}_i$ and M_{max} of case 03, ○ measurements; — Gaussian distribution function fit

(a)

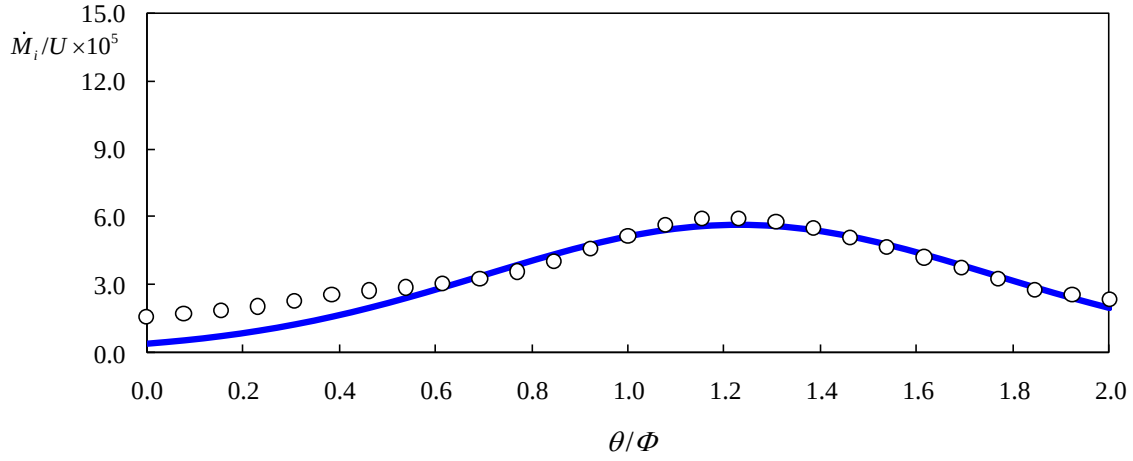

(b)

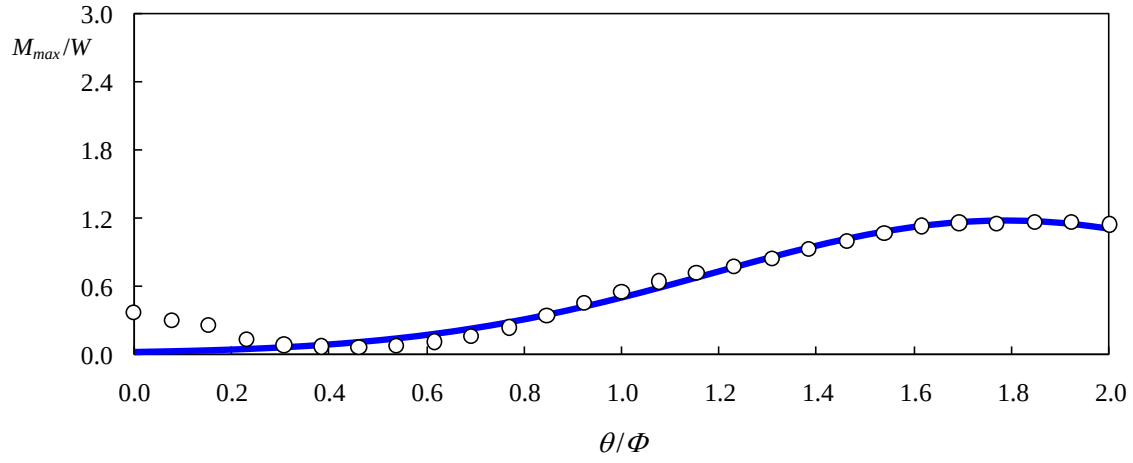

Fig. 22. Normalized $\dot{M}_i$ and M_{max} of case 01, ○ measurements; ━ Gaussian distribution function fit

(a)

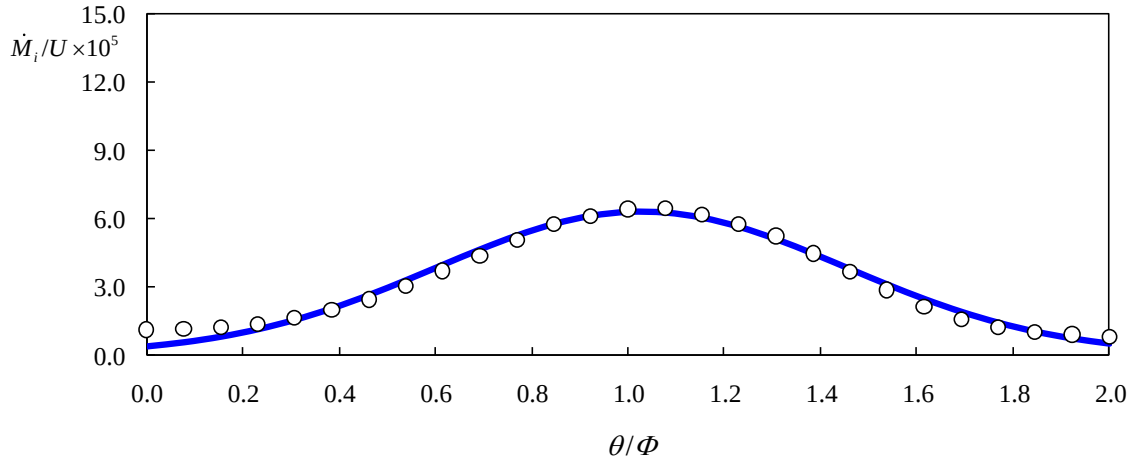

(b)

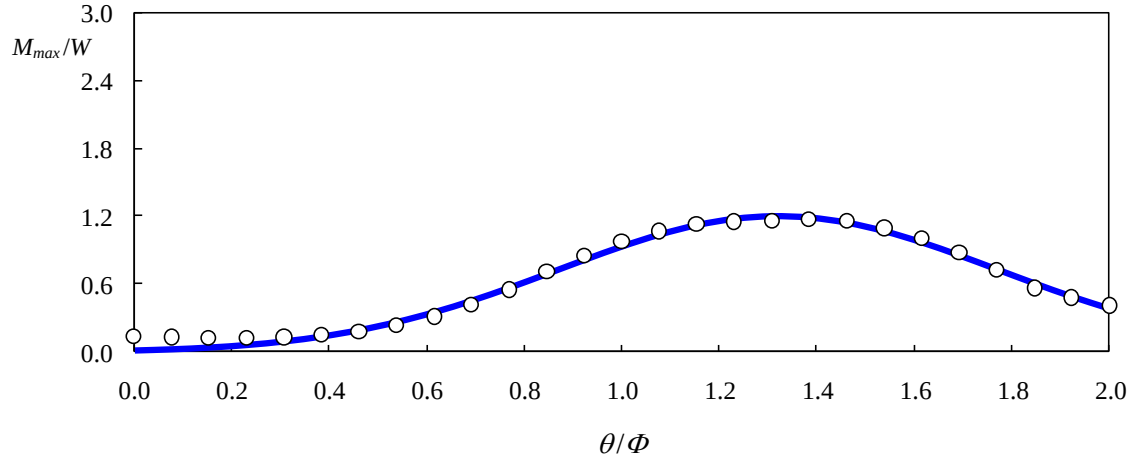

Fig. 23. Normalized $\dot{M}_i$ and M_{max} of case 02, ○ measurements; — Gaussian distribution function fit

(a)

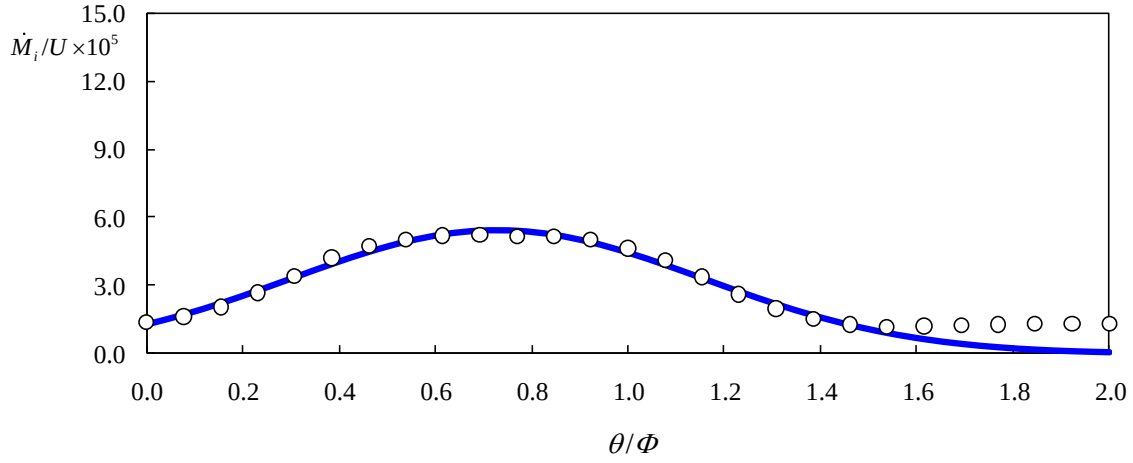

(b)

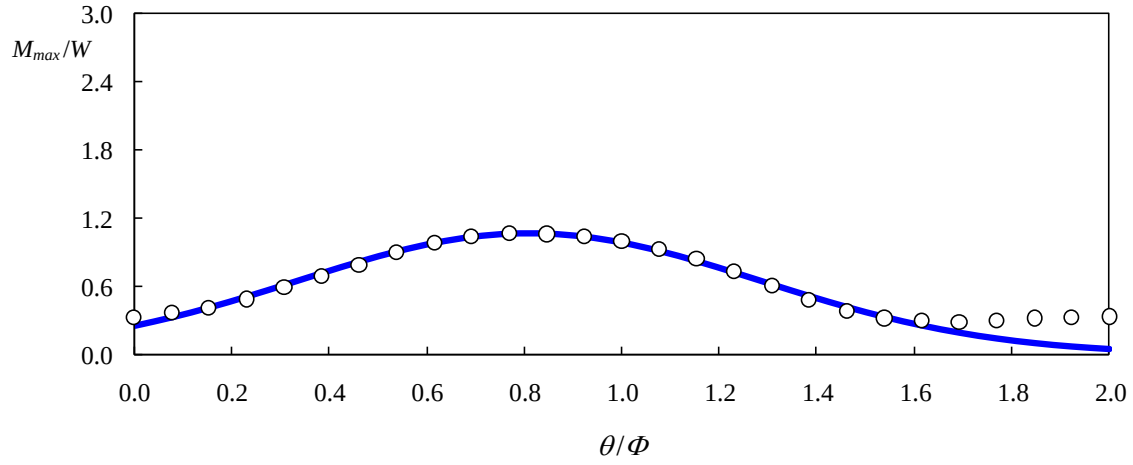

Fig. 24. Normalized $\dot{M}_i$ and M_{max} of case 04, ○ measurements; — Gaussian distribution function fit

(a)

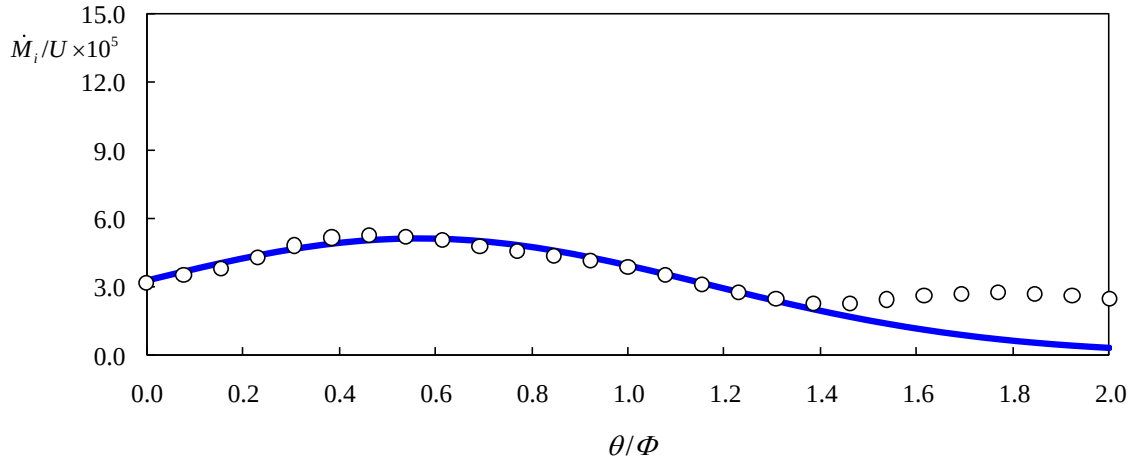

(b)

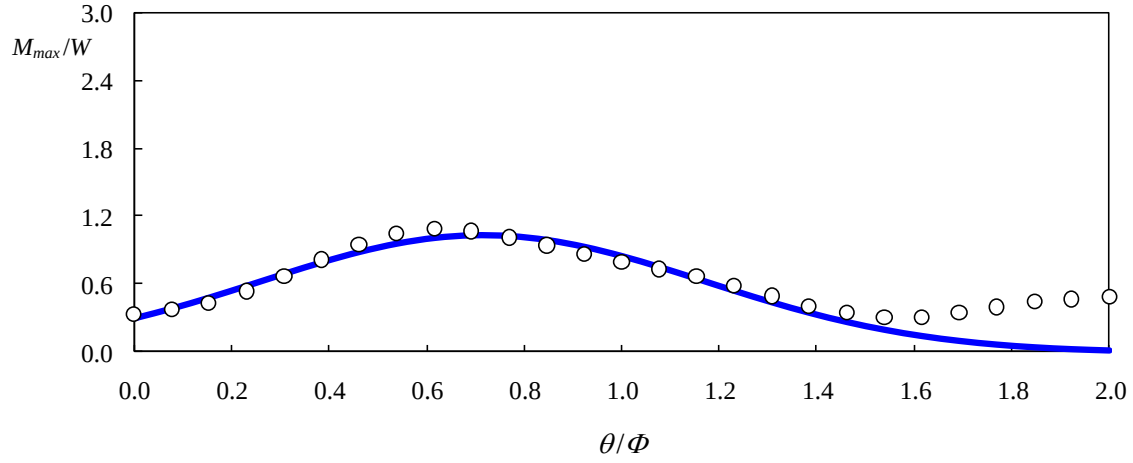

Fig. 25. Normalized $\dot{M}_i$ and M_{max} of case 05, ○ measurements; — Gaussian distribution function fit

Since both $\dot{M}_i$ and M_{max} of the five cases display a Gaussian distribution, a Gaussian distribution function was used to model the magnitudes of $\dot{M}_i$ and M_{max} along a complete meander channel bend:

$$\frac{\dot{M}_i}{U} = A_i \exp\left[-0.5\left(\frac{\theta/\Phi - \mu_i}{\sigma_i}\right)^2\right] \tag{17}$$

$$\frac{M_{max}}{W} = A_m \exp\left[-0.5\left(\frac{\theta/\Phi - \mu_m}{\sigma_m}\right)^2\right] \tag{18}$$

where A_i and A_m are the maximum values of the distributions, μ_i and μ_m are the locations of the maximum values, σ_i and σ_m are the standard deviations of the distributions, and θ/Φ is the normalized position angle. Note that θ/Φ ranges from 0.0 to 2.0 and $\theta/\Phi > 1$ denotes a location in the downstream inner bank beyond the leading outer bank. Regression analysis with a least-square-errors method was again applied to the results in Figs. 21-25, and the three parameters of each distribution (A_i , μ_i , and σ_i of $\dot{M}_i$ distribution; A_m , μ_m , and σ_m of M_{max} distribution) were obtained for each case. Solid lines in Figs. 21-25 are the results of the Gaussian distribution function fit.

One case (case 03) was repeated (case 12) to test the repeatability of the tests. The values of $\dot{M}_i$ and M_{max} of these two cases were compared in Fig. 26. The differences for $\dot{M}_i$ and M_{max} are: 0.7% for A_i , 2.2% for μ_i , and 4.7% for σ_i ; 0.7% for A_m , 2.2% for μ_m , and 4.7% for σ_m . The relatively small differences between these two cases demonstrate that the experiment are capable of duplication and the methodology using the hyperbolic function in channel bankline migration and Gaussian distribution functions for $\dot{M}_i$ and M_{max} along two successive curved bends is suitable.

(a)

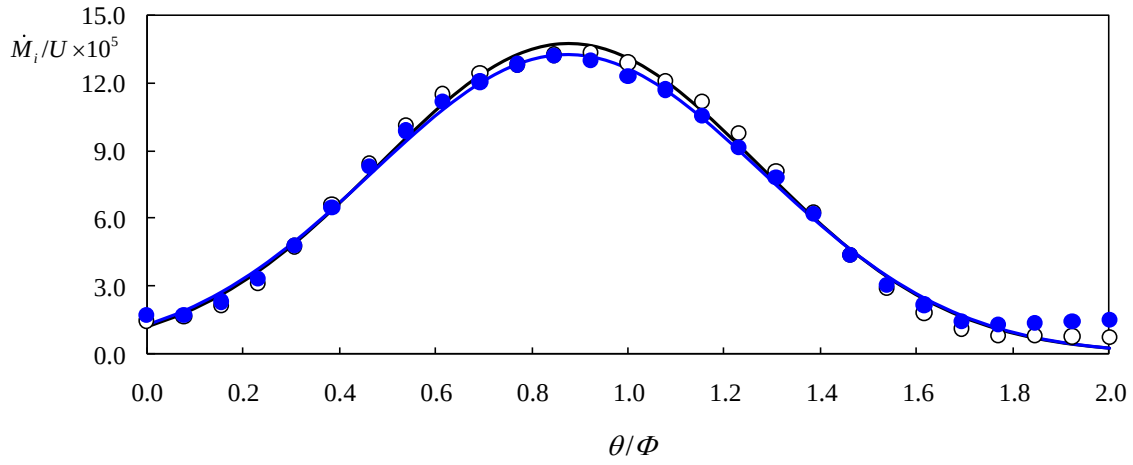

(b)

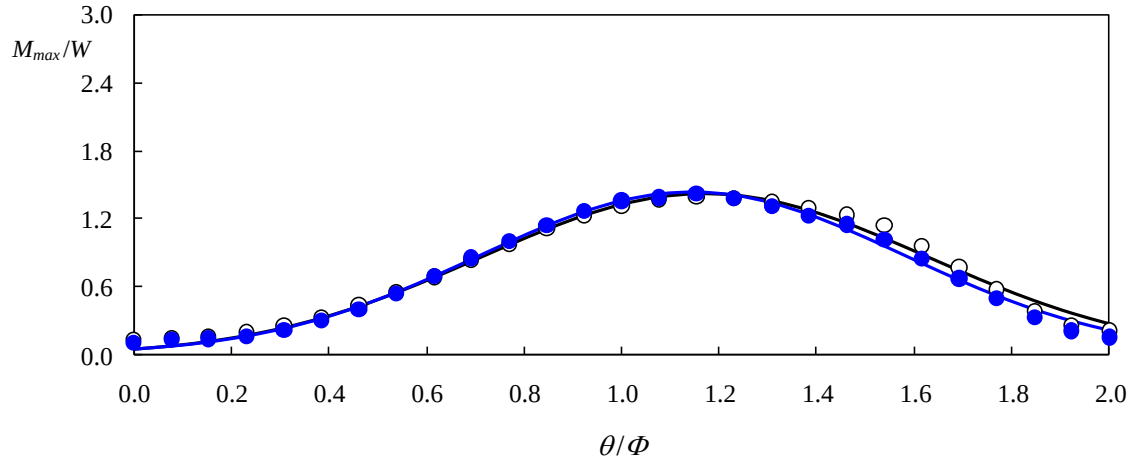

Fig. 26. Repeatability comparison of the normalized $\dot{M}_i$ and M_{max} of case 03 and case 12, ○ case 03; ● case 12; ━ Gaussian fit of case 03; ━ Gaussian fit of case 12

For a large bend angle, both $\dot{M}_i$ and M_{max} along the curved bend show a "bi-modal" distribution. There are two high value zones for the initial migrate rate and the maximum migration distance in the leading outer bank ($0.0 \leq \theta/\Phi \leq 1.0$) and the following inner bend ($1.0 \leq \theta/\Phi \leq 2.0$) as shown in Figs. 27-32. The dual zones of $\dot{M}_i$ and M_{max} only appear in the cases with a bend angle equal to 120 degree or greater; the second peak is not apparent for the 65 degree bend angle cases (Figs. 21-25). When the flow enters a curved bend, the primary and secondary flows create high shear stresses when the secondary flow is fully developed. If the bend angle is large enough (the bend length is long enough), the induced helical flow first dissipates its energy and then has enough time and room to regain energy before the flow enters next bend. After the flow passes the inflection point, the curvature of the following bend induces the centrifugal acceleration in the opposite direction and results in a momentum exchange. This strong momentum exchange makes the flow in the channel have a second zone of high shear stress. In this second zone of high shear stress, bank scour occurs with a relative smaller magnitude compared to the first high shear zone. However, in the two longest cases (case 07 and 08), the re-growing secondary flow reached fully developed again before entering next bend. The values of $\dot{M}_i$ in the second zone are almost the same as in the first zone.

The distributions of $\dot{M}_i$ and M_{max} in a large bend angle bend also show smaller magnitudes and phase lags. In a curved bend with mild change of curvature, the flow path is more in line with the channel curvature. Flow separation has less chance to occur in the bend. Also, the longer bend length provides larger friction as the flow passes through the channel. As a result, the peak values in $\dot{M}_i$ and M_{max} of these four cases decrease with the increase of bend angle.

(a)

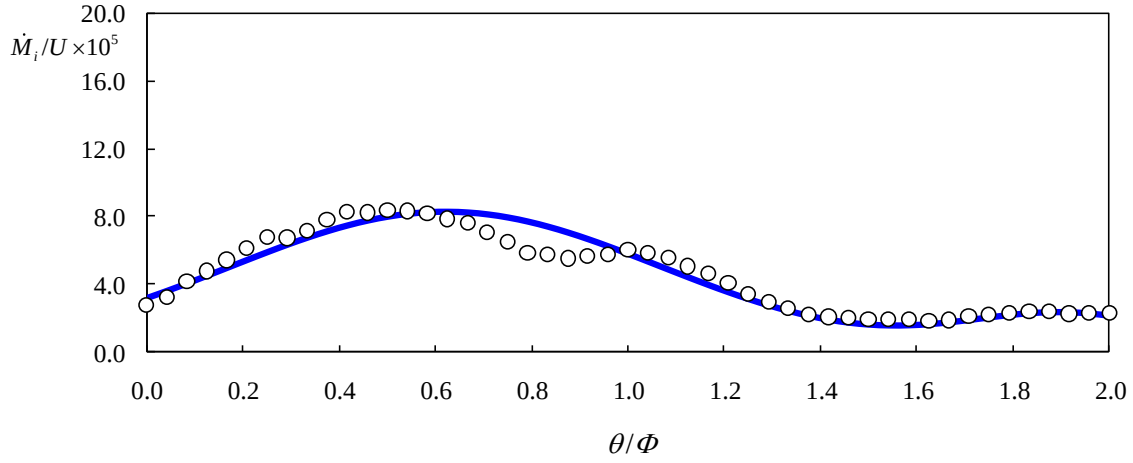

(b)

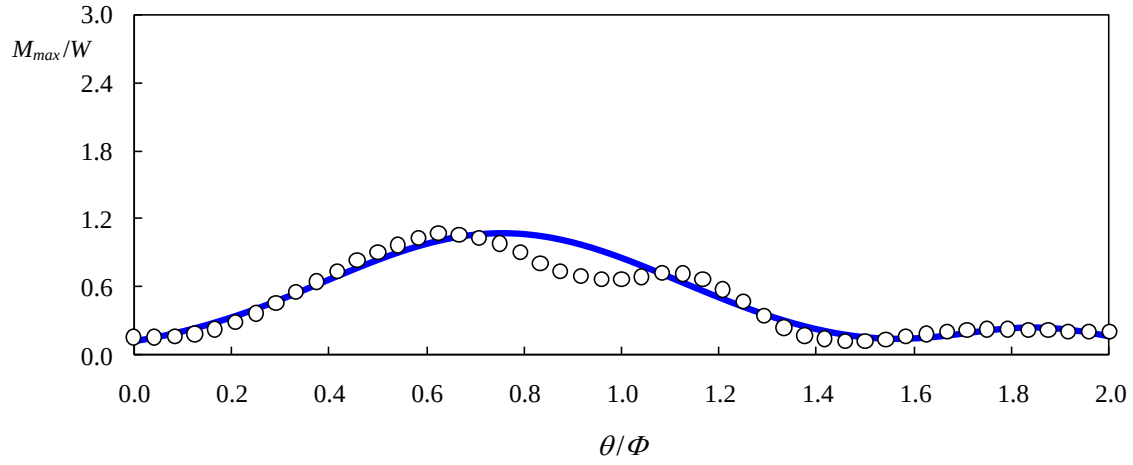

Fig. 27. Normalized $\dot{M}_i$ and M_{max} of case 06, ○ measurements; — Gaussian distribution function fit

(a)

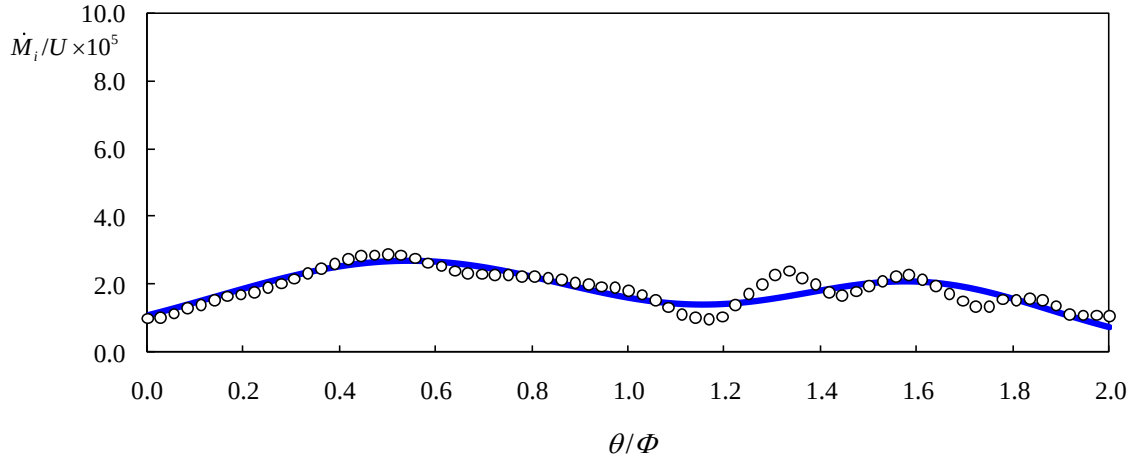

(b)

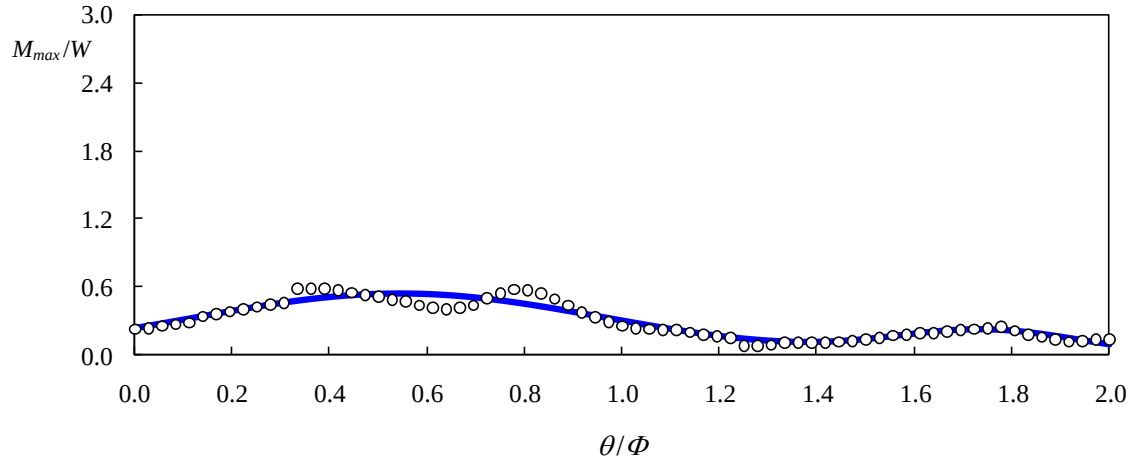

Fig. 28. Normalized $\dot{M}_i$ and M_{max} of case 07, ○ measurements; — Gaussian distribution function fit

(a)

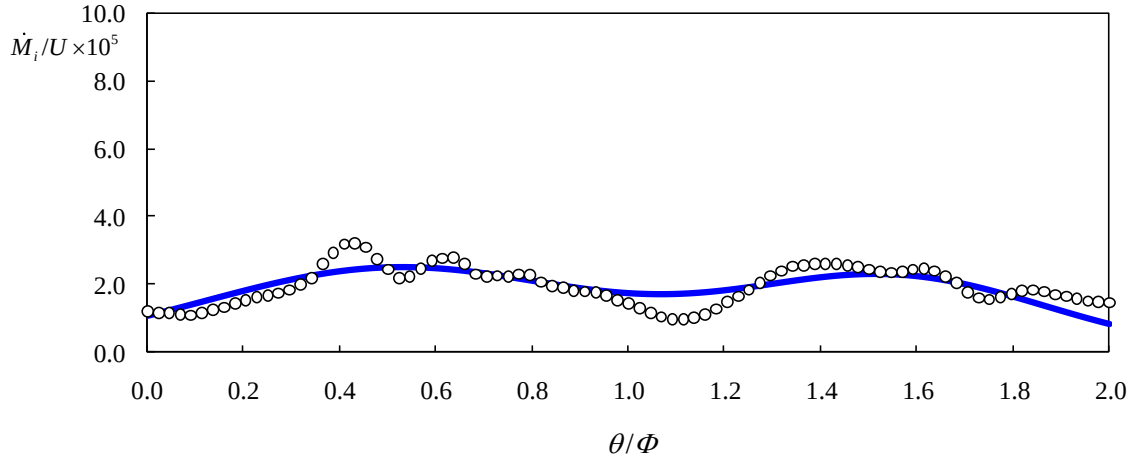

(b)

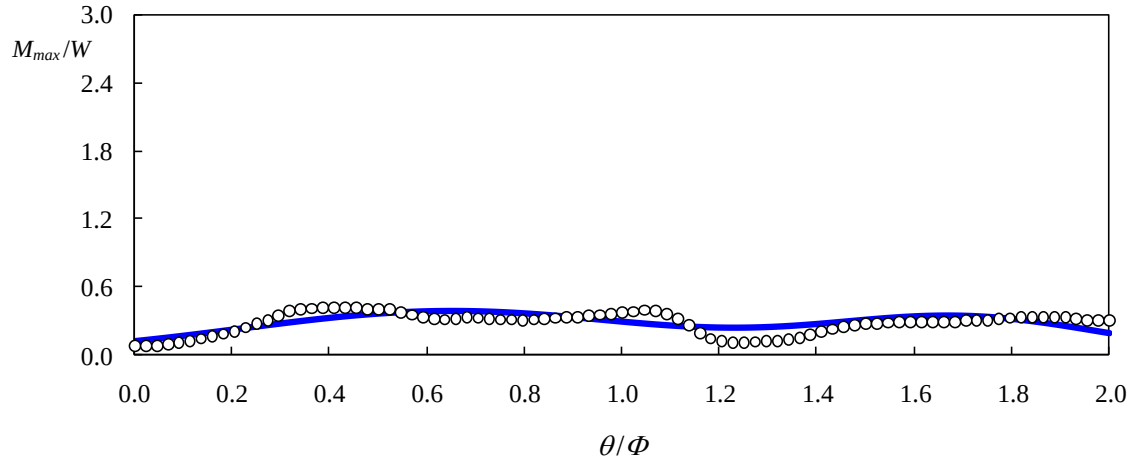

Fig. 29. Normalized $\dot{M}_i$ and M_{max} of case 08, ○ measurements; — Gaussian distribution function fit

(a)

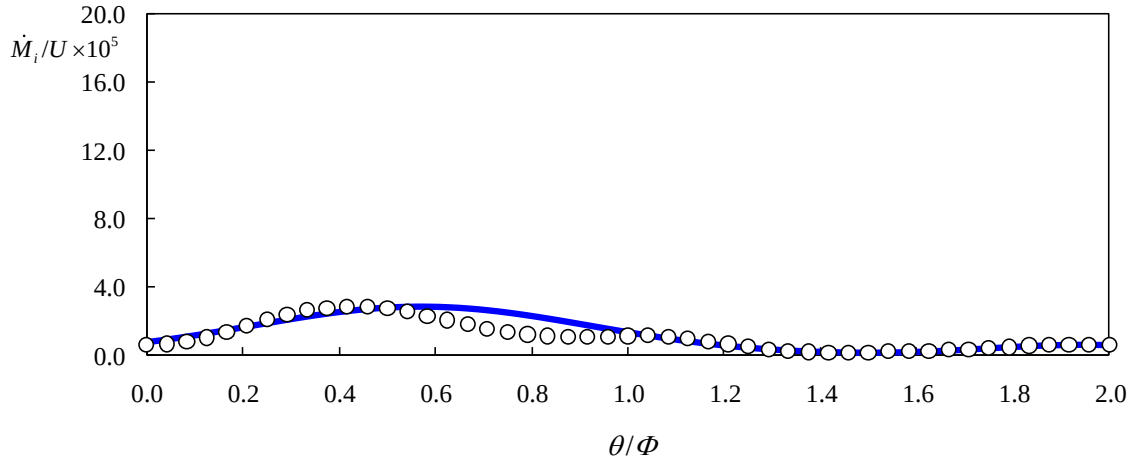

(b)

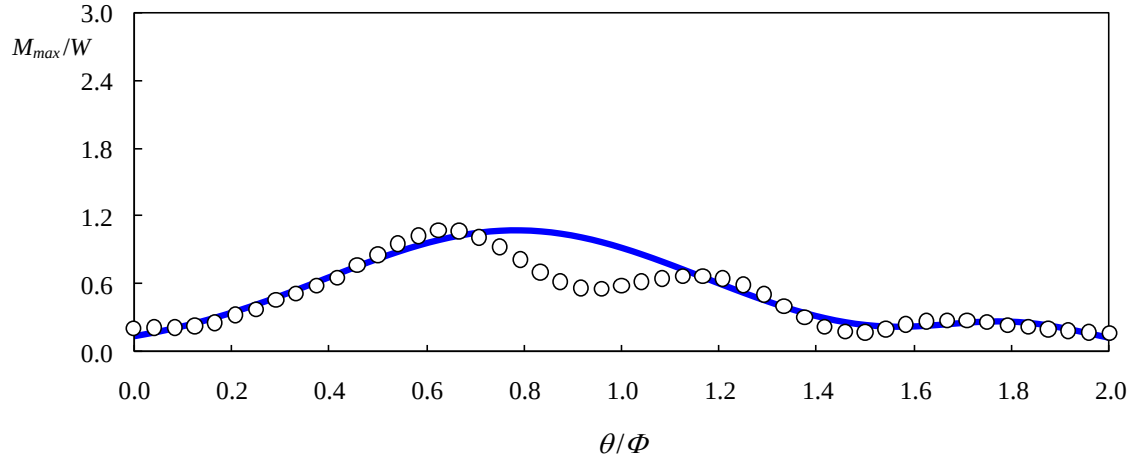

Fig. 30. Normalized $\dot{M}_i$ and M_{max} of case 09, ○ measurements; — Gaussian distribution function fit

(a)

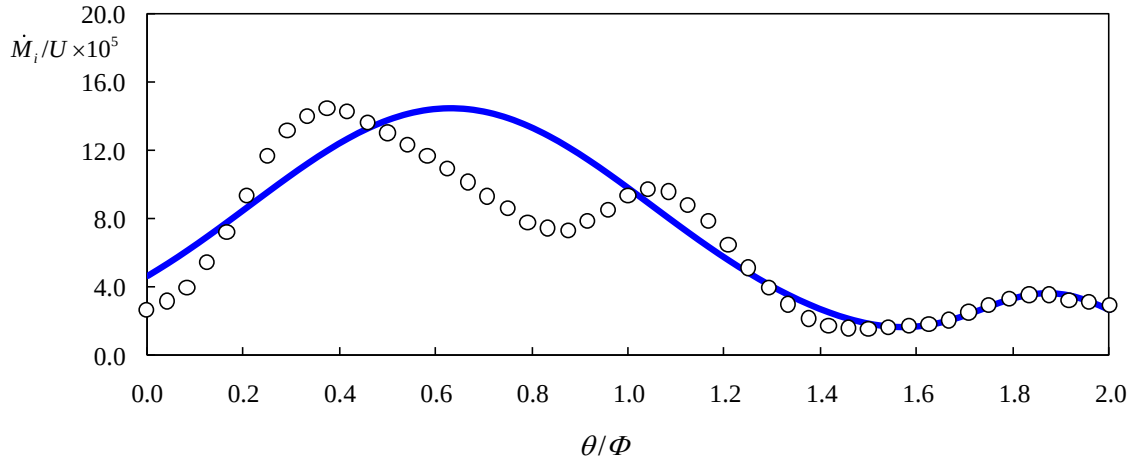

(b)

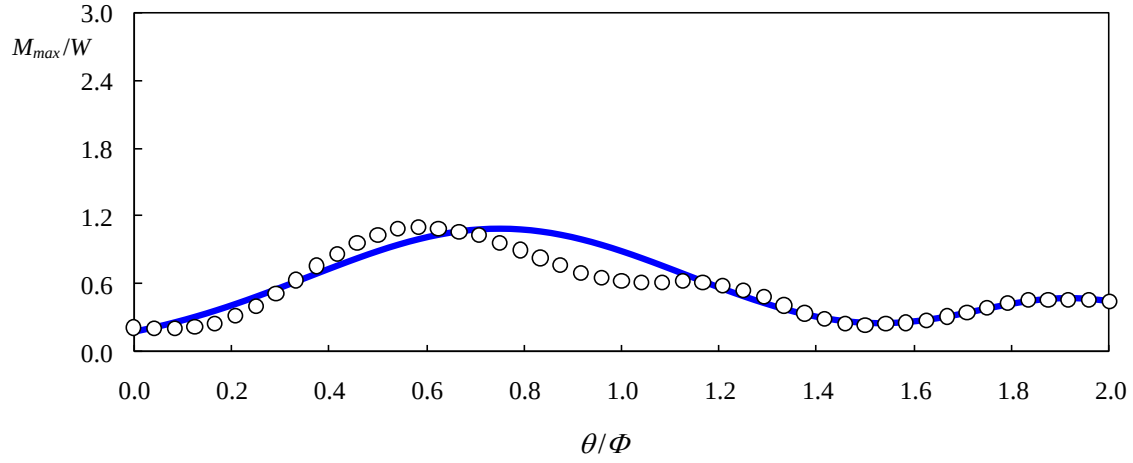

Fig. 31. Normalized $\dot{M}_i$ and M_{max} of case 10, ○ measurements; — Gaussian distribution function fit

(a)

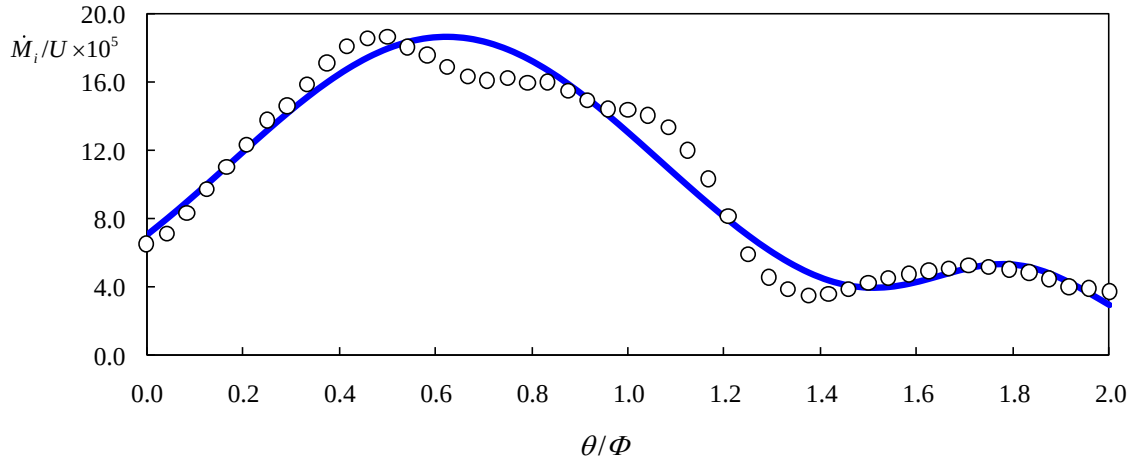

(b)

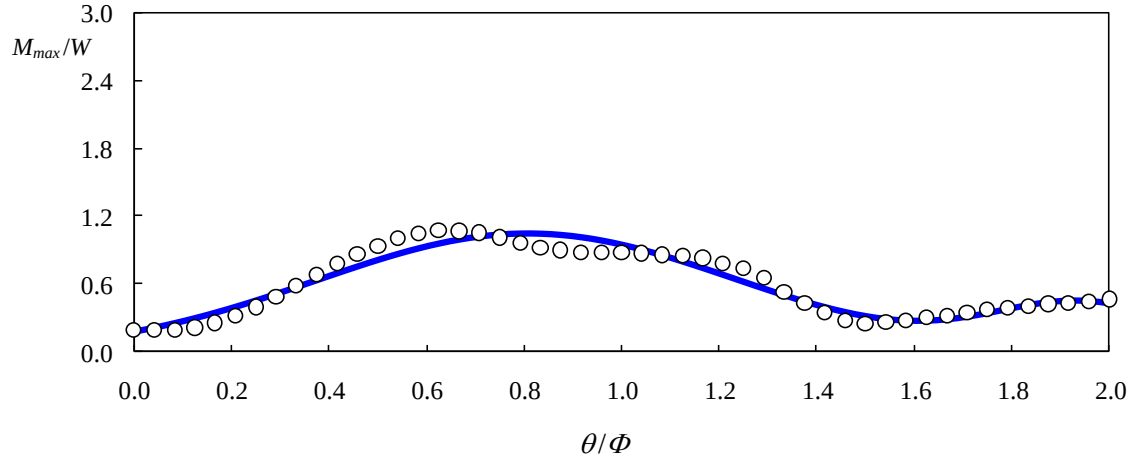

Fig. 32. Normalized $\dot{M}_i$ and M_{max} of case 11, ○ measurements; — Gaussian distribution function fit

In order to model the bi-modal behavior, a superposition of two Gaussian distribution functions was used to fit the values of $\dot{M}_i$ and M_{max}. The formulae can be expressed as

$$\frac{\dot{M}_i}{U} = A_{i1}\exp\left[-0.5\left(\frac{\theta/\Phi-\mu_{i1}}{\sigma_{i1}}\right)^2\right] + A_{i2}\exp\left[-0.5\left(\frac{\theta/\Phi-\mu_{i2}}{\sigma_{i2}}\right)^2\right] \quad (17)$$

$$\frac{M_{max}}{W} = A_{m1}\exp\left[-0.5\left(\frac{\theta/\Phi-\mu_{m1}}{\sigma_{m1}}\right)^2\right] + A_{m2}\exp\left[-0.5\left(\frac{\theta/\Phi-\mu_{m2}}{\sigma_{m2}}\right)^2\right] \quad (18)$$

Similar to the single Gaussian distribution, the coefficients of the above equations were also estimated by using a least-square-errors regression method. Solid lines in Figs. 27-32 are the results of the Gaussian distribution function fit.

4.2 Channel Bankline Initial Migration Rate

For each cross section, $\dot{M}_i$ and M_{max} were estimated using regression analysis of the measurements as shown in Fig. 19. Since the initial cross section is artificially trapezoidal, the flow system will require some time to come to stable. The interpretation of any initial transient behavior then becomes complicated. Fig. 33 shows an example of the migration distance in an arbitrary cross section. In the early stage of the test, the channel cross section transformed from an artificial trapezoidal geometry to a natural shape. Bank erosion rate was very unstable and irregular. In order to reduce the sensitivity of the initial measurement, the initial transient data were then skipped while only the data in the later stages were included in the regression. These data represent the migration distances under channel free meandering. $\dot{M}_i$ is thus the initial migration rate of the hyperbolic process rather the incipient motion of bank material.

There are six undetermined coefficients in the $\dot{M}_i$ equation (Eq. (17)) and each one was then correlated with the three controlling parameters: R/W, Φ, and $\beta Fr\text{-}Frc$. Fig. 34 shows the correlations among the coefficients and R/W. Since the cases with different R/W are all 65

degree, the amplitudes of the second Gaussian function are zero. The results show that $\dot{M}_i$ has a maximum value (A_{i1}) at R/W = 4 and decreases in either smaller or larger R/W values. The location of the peak value (μ_{i1}) shifts to the downstream as R/W decreases. The influence on $\dot{M}_i$ by the channel bend angle Φ is shown in Fig. 35. As Φ increases, the value for the first peak (A_{i1}) decreases and the locations of the peak (μ_{i1} and μ_{i2}) move upstream toward the front of the outer bank. The second Gaussian distributions for all bend angles have relatively small and nearly constant peak values in $\dot{M}_i$ except for the Φ = 65 degree case in which the peak values are zero. The ratio of second peak to first peak demonstrates a linear increasing trend with respect to the bend angle. The standard deviations (σ_{i1}, σ_{i2}) remain somewhat constant. The effect of βFr-Frc on $\dot{M}_i$ is shown in Fig. 36. The two peak values (A_{i1}, A_{i2}) are proportional to the excess Froude number. This study used the excess Froude number to express the flow strength to initiate erosion. βFr-Frc has little effect on the peak locations (μ_{i1}, μ_{i2}) and standard deviations (σ_{i1}, σ_{i2}) of the $\dot{M}_i$ distribution.

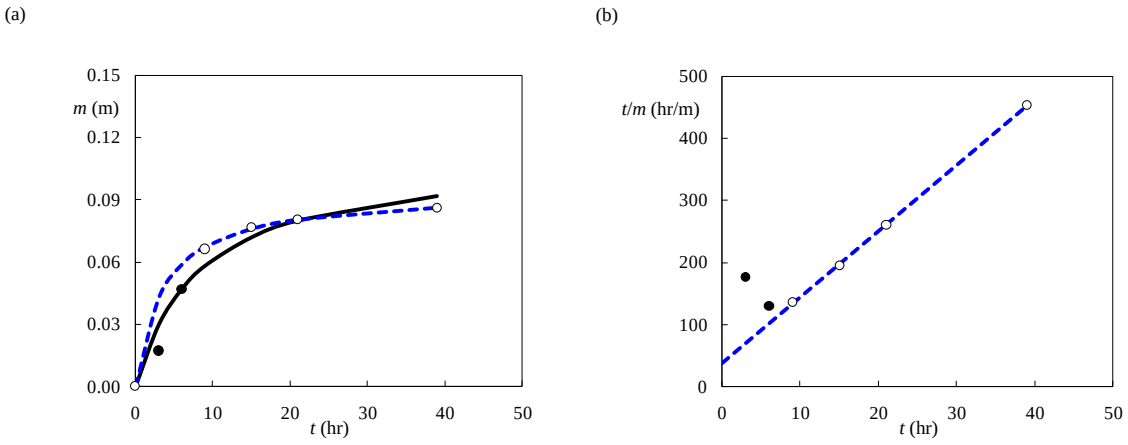

Fig. 33. Estimation of $\dot{M}_i$ in the hyperbolic model, ○, ● measurements; ━ hyperbolic fit; ━ adjusted hyperbolic fit (skip the first two measurements)

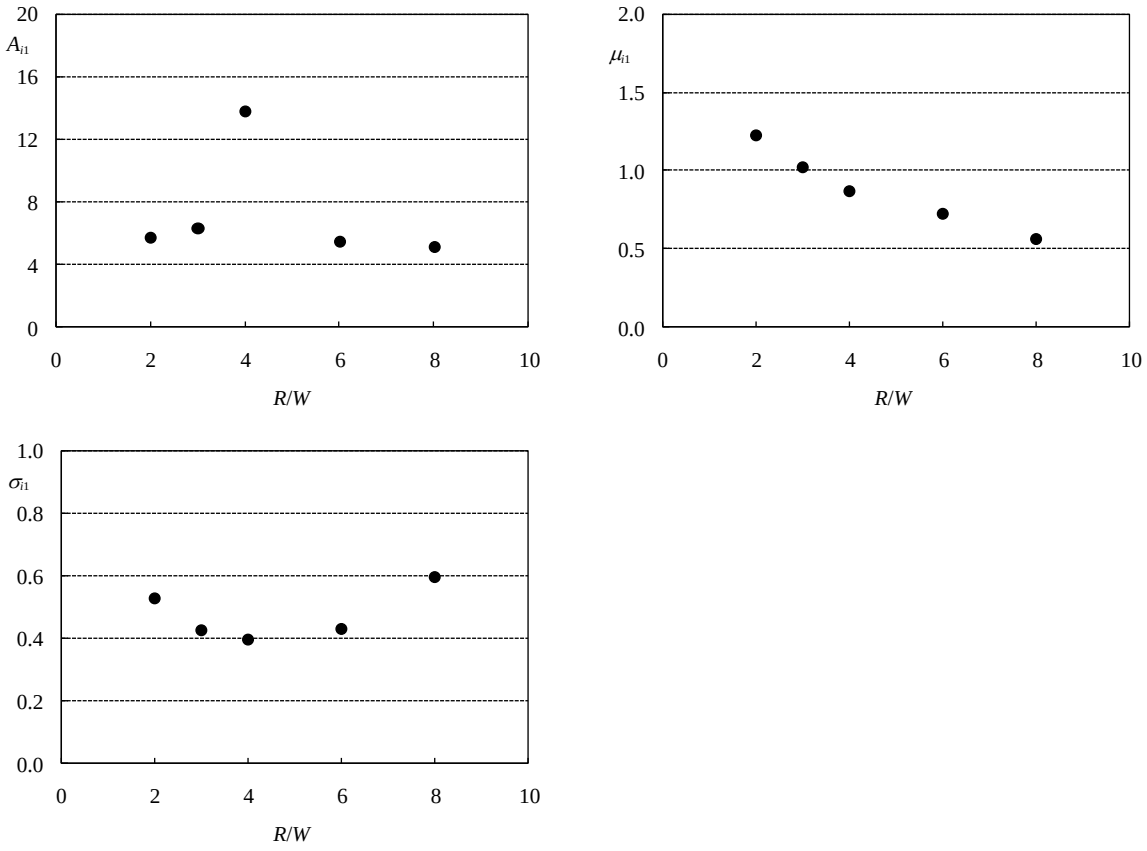

Fig. 34. Gaussian distribution coefficients of $\dot{M}_i$ with different *R*/*W* (the coefficients of the second Gaussian distribution are all zero in these five cases)

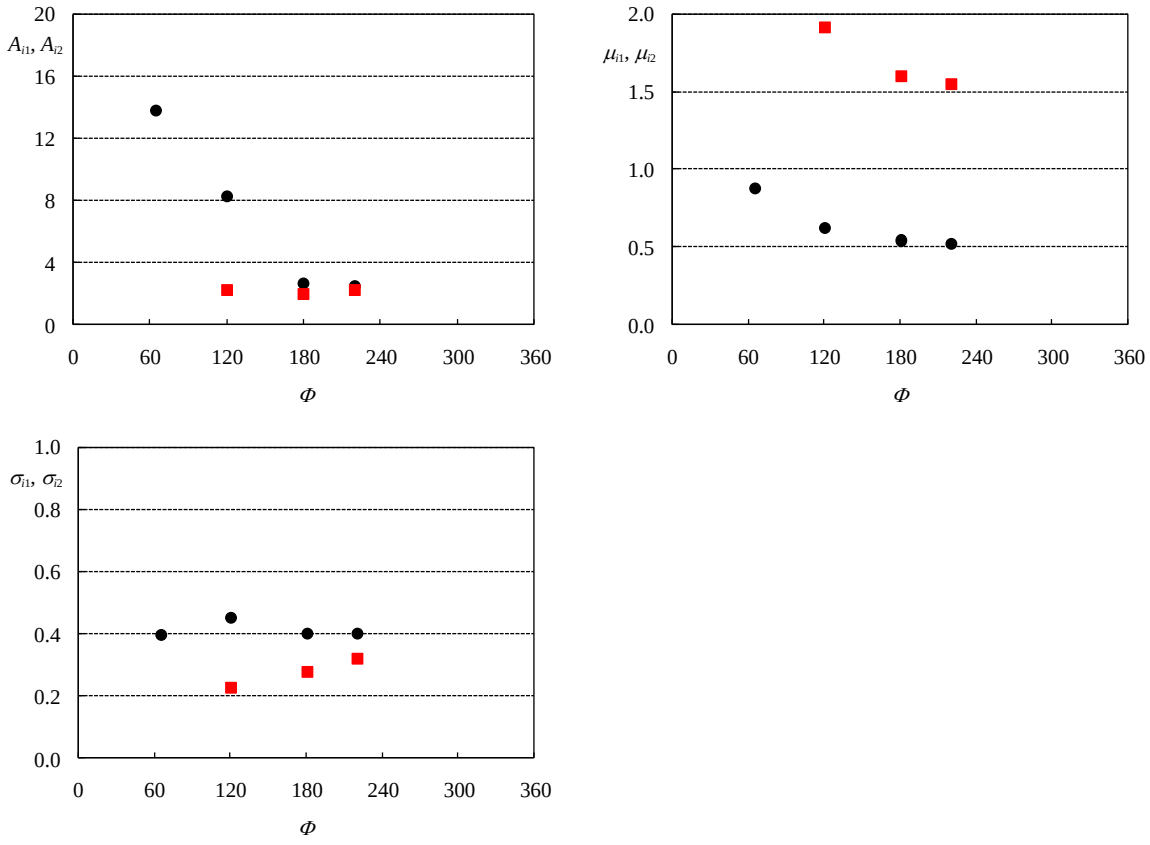

Fig. 35. Gaussian distribution coefficients of $\dot{M}_i$ with different Φ, ● first Gaussian distribution; ■ second Gaussian distribution

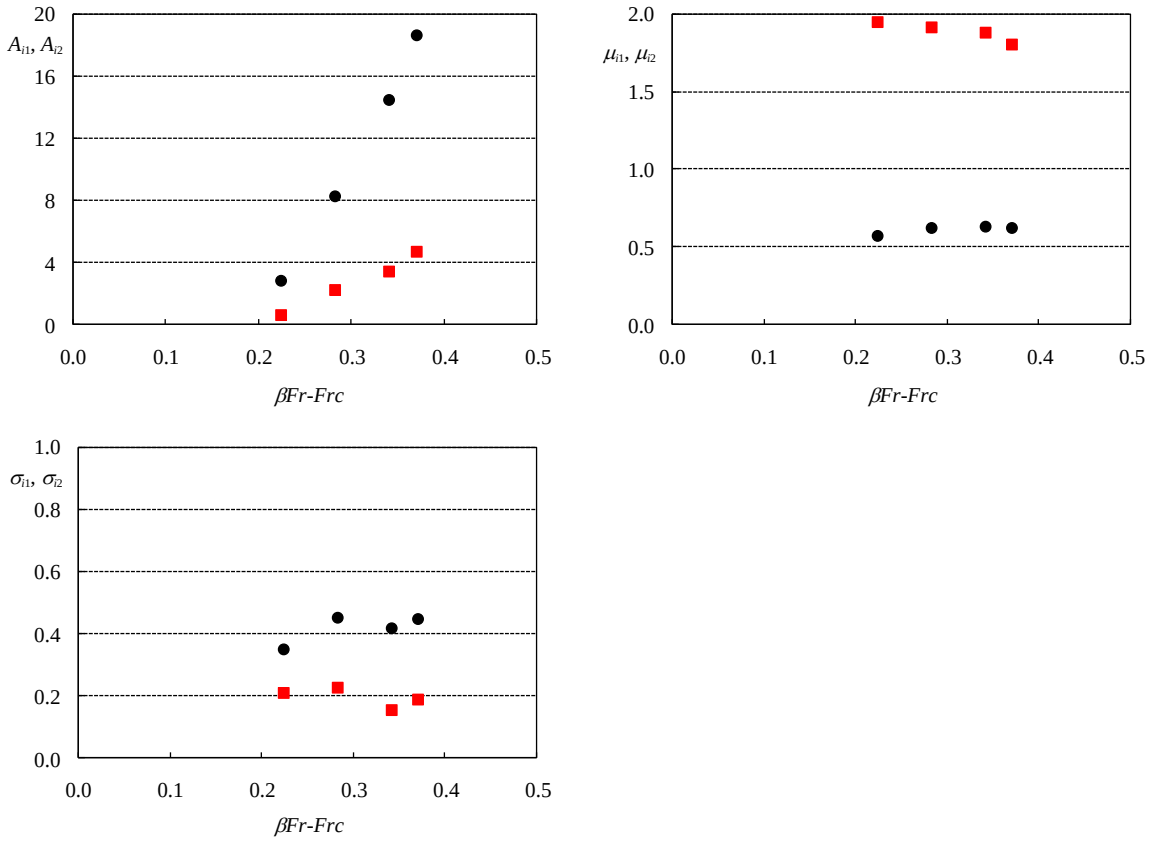

Fig. 36. Gaussian distribution coefficients of $\dot{M}_i$ with different *βFr-Frc*, ● first Gaussian distribution; ■ second Gaussian distribution

4.3 Channel Bankline Maximum Migration Distance

In the experiments, the initial channel geometry of each case was pre-determined with a pair of R/W and Φ as listed in Table 1, and the time of the hyperbolic process starting from this initial condition is set as the initial time (t = 0). Natural rivers migrate with existing plan form and geometry; the current geometric and hydraulic conditions to the hyperbolic process might need to be identified. From the experiments, it is observed that the channel initial cross section immediately (within minutes) evolves into a "nature" shape, and the rate of channel migration gradually slows down along with the decrease of flow velocity. Fig. 37 shows the hyperbolic processes with different initial times at the same five cross sections in Fig. 19. The figures show the bankline migration follows the hyperbolic process regardless what initial time was chosen. The solid lines in each subfigure are the results of curve fitting with each data point chosen as the "initial" time. It is found that the summation of the maximum migration distance of each time step and the migration distance accumulated at each time step will reach very close values at the asymptotic state ($t \rightarrow \infty$). As long as the flowrate keeps constant, the hyperbolic process and the value of M_{max} are independent of the initial time arbitrary chosen.

The six undetermined coefficients in the M_{max} equation (Eq. (18)) were also correlated with the three controlling parameters, R/W, Φ, and $\beta Fr\text{-}Frc$. Fig. 38 shows the correlations among the coefficients and R/W. The results show M_{max} also has a maximum value (A_{m1}) at R/W = 4 and decreases as R/W deviates from this value (Fig. 38(a)). Note that the migration direction in the present study is defined as the cross sectional direction from the center of curvature and perpendicular to the *initial* channel bankline. The displacement at a given point on the channel bankline contains two components: the lateral expansion (the y-direction displacement in the experiment) and the down-valley translation (the x-direction displacement in the experiment). For channels with a small R/W (such as R/W = 2), the channel bankline

displacement is dominated by the down-valley translation with little lateral expansion. As a result, *m* remains small as the channel bankline continues to straighten. A similar straightening phenomenon for small *R*/*W* cases was observed for the location of the peak (μ_{m1}) in Fig. 38(b). The location of the peak moves downstream as *R*/*W* decreases, indicating that the following inner bend may have a large migration rate and migration distance. The standard deviation (σ_{m1}) has a relatively small variation in all the cases in Fig. 38(c). The average values are close to 0.44.

The distribution of M_{max} is also influenced by the channel bend angle Φ as shown in Fig. 39. As Φ increases, the values for the first peak (A_{m1}) for M_{max} decreases; the location of the peak (μ_{m1}) moves upstream toward the front of the outer bank. The second Gaussian distribution for all bend angles has a relatively small and nearly constant peak value in M_{max} except for the Φ = 65 degree case in which the peak value is zero. The ratio of second peak to first peak demonstrates a linear increasing trend with respect to the bend angle. Similar to the results in Fig. 38, the standard deviation (σ_{m1}) remains somewhat constant. For large bend angles (Φ = 120˚, 180˚, and 220˚), μ_{m2} values for the second Gaussian distribution are less than 2.0, indicating that the second peak is within the same channel bend. The location of second peak moves upstream with a slight increase in standard deviation when the channel bend angle increases. As the effect from the second peak gets more obvious, the bankline displacement becomes more uniform and symmetric. Fig. 39 shows the effects of βFr-Frc on the coefficients in the M_{max} equation. Different from the results in $\dot{M}_i$, the excess Froude number has an insignificant effect on M_{max}. This indicates that the initial flow condition has a weak influence on M_{max}. The geometric condition, not the initial hydraulic condition, dominates M_{max}. This finding is consistent with that found in bridge pier scour in Briaud et al. (1999).

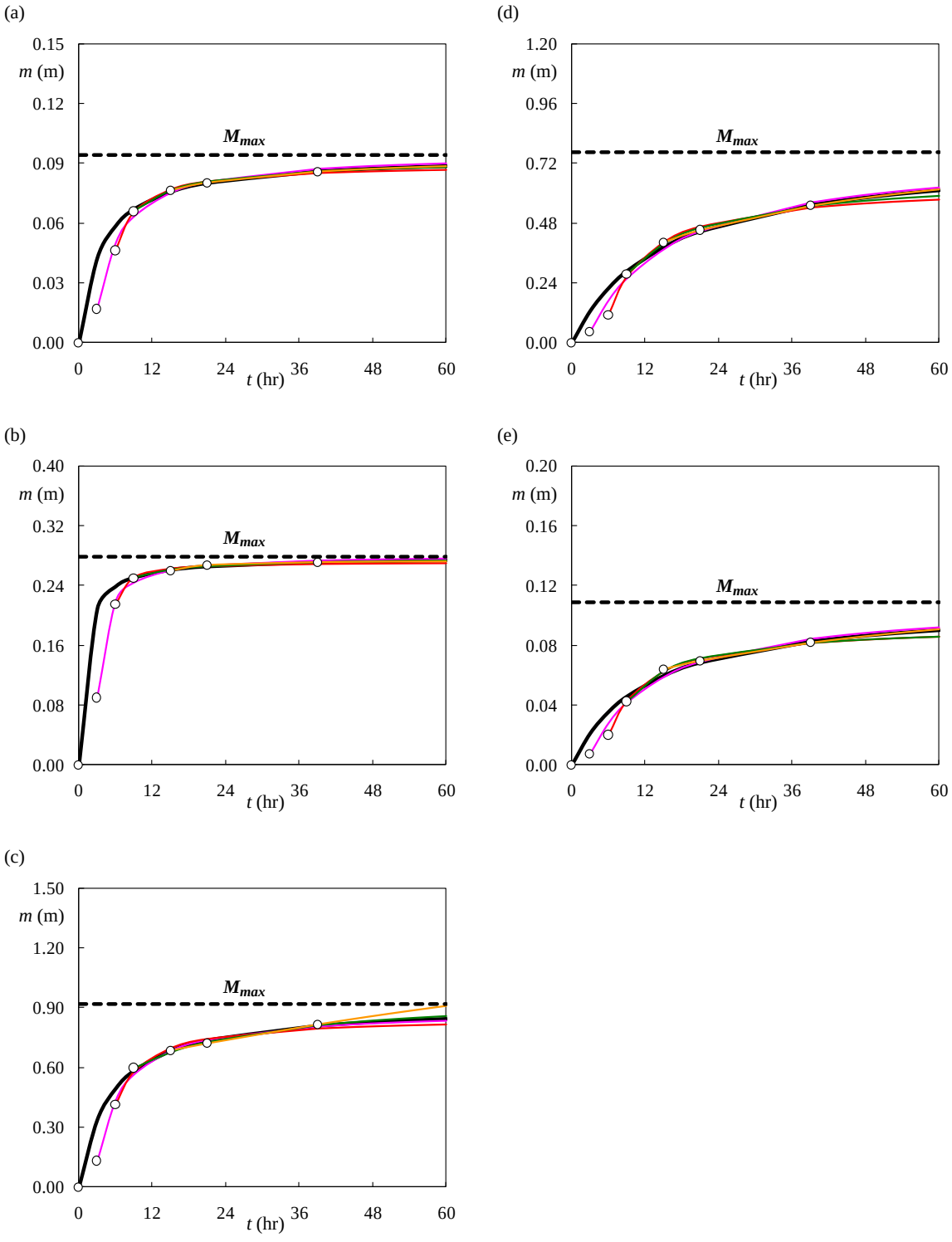

Fig. 37. Hyperbolic processes with different initial time, ○ measurements; — 0 hr; — 3 hr; — 6 hr; — 9 hr; — 15 hr after the test was started

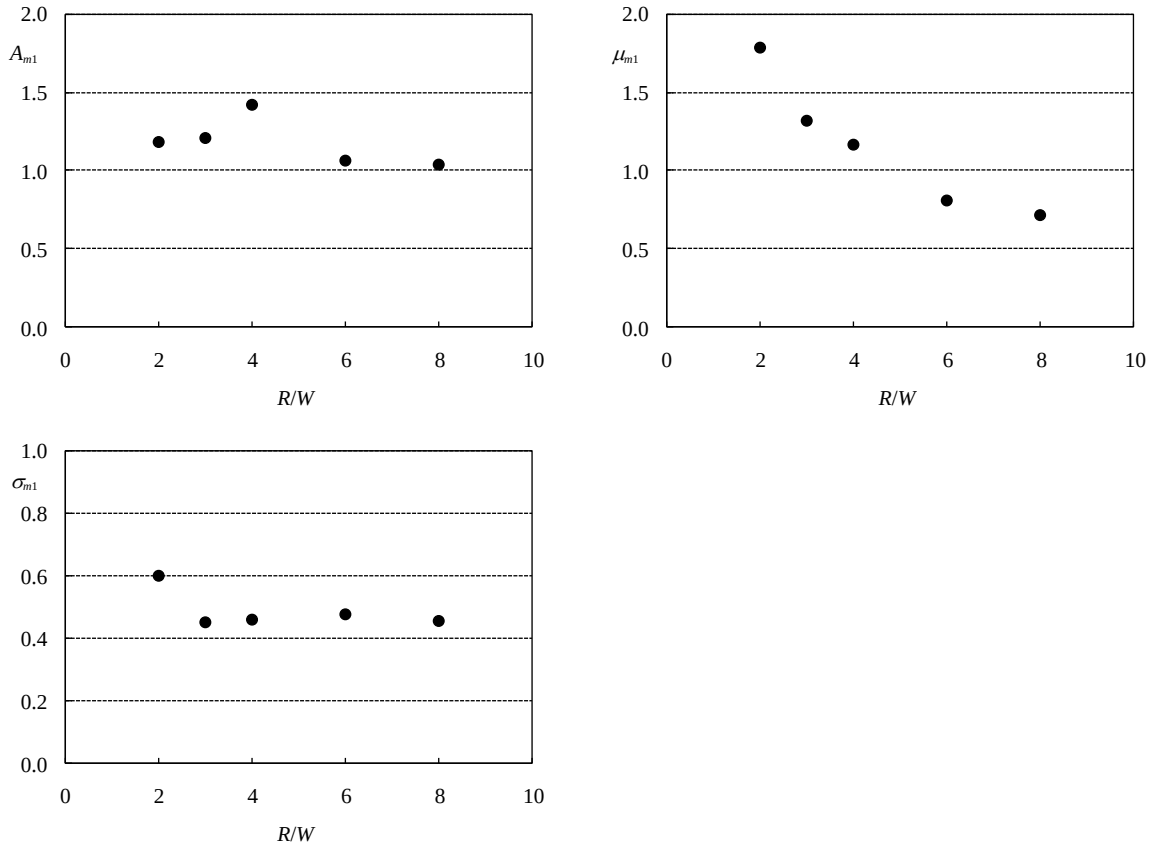

Fig. 38. Gaussian distribution coefficients of M_{max} with different R/W (the coefficients of the second Gaussian distribution are all zero in these five cases)

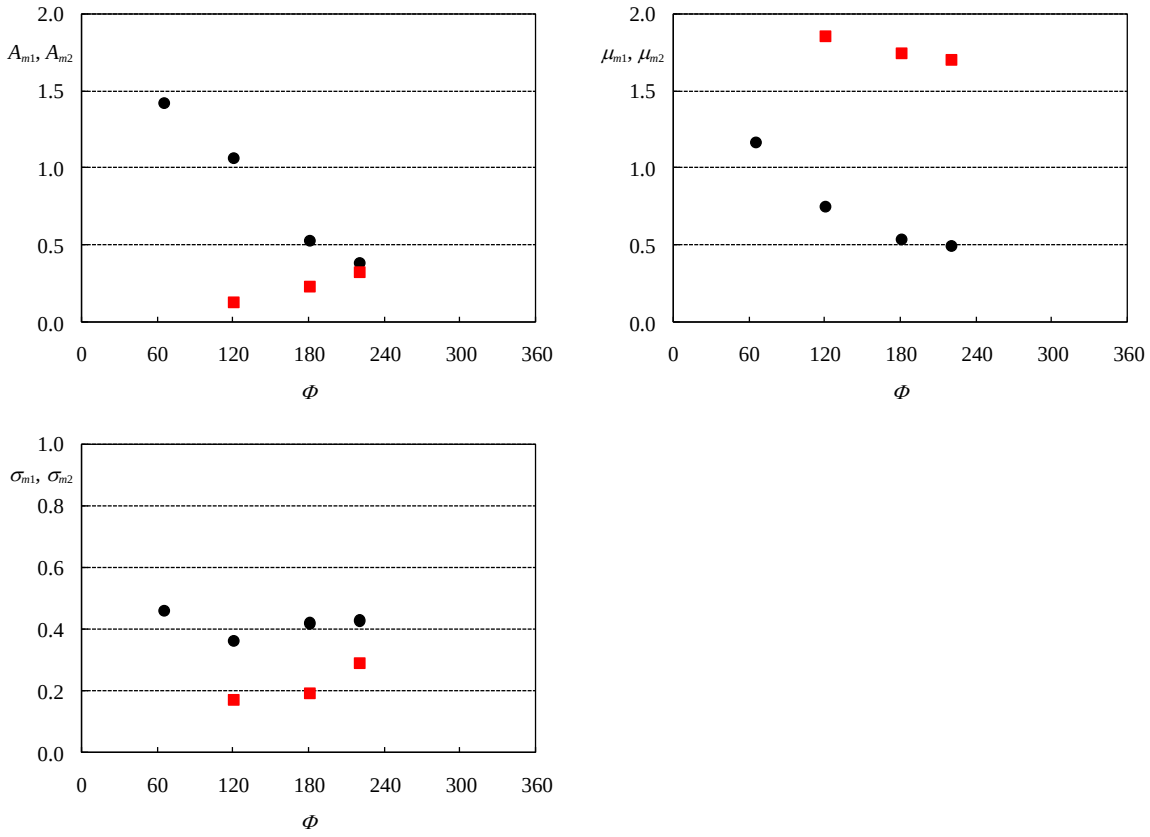

Fig. 39. Gaussian distribution coefficients of M_{max} with different Φ, ● first Gaussian distribution; ■ second Gaussian distribution

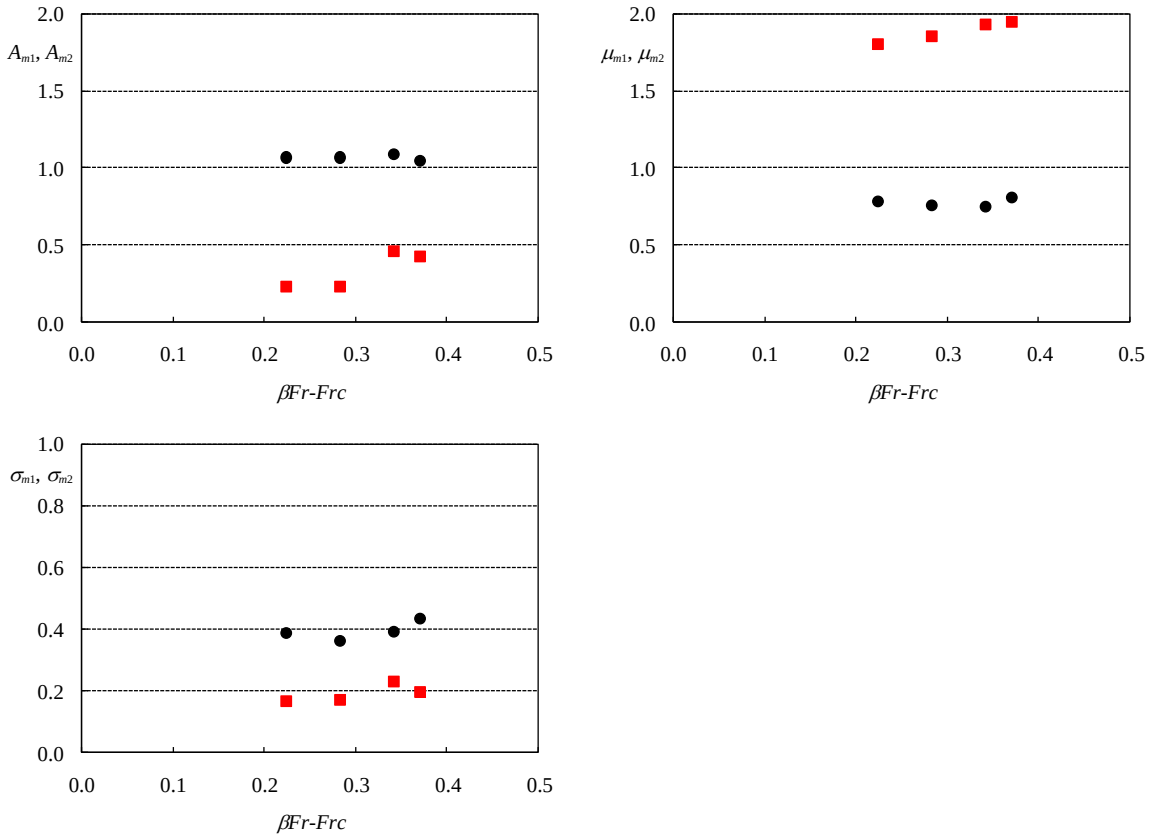

Fig. 40. Gaussian distribution coefficients of M_{max} with different *βFr-Frc*, ● first Gaussian distribution; ■ second Gaussian distribution

Based on the results in Figs. 34-36 and 38-40, each one of the six coefficients for the $\dot{M}_i$ and M_{max} equations (Eq. (17) and (18)) is a function of R/W, Φ, and $\beta Fr\text{-}Frc$, and can be obtained by using regression analysis with all the data measured in the experiments. The final equations for these coefficients in the Gaussian distribution functions are expressed as

$\dot{M}_i$:

$$
\begin{aligned}
&A_{i1} = 5.88\times10^{4}(R/W)^{2.71}(\Phi)^{16.24}(\beta Fr\text{-}Frc)^{44.73} \quad \text{for } 2 \le R/W \le 4;\\
&A_{i1} = 4.69\times10^{6}(R/W)^{-1.76}(\Phi)^{-1.10}(\beta Fr\text{-}Frc)^{3.20} \quad \text{for } 4 \le R/W \le 8;\\
&\mu_{i1} = 14.04(R/W)^{-0.53}(\Phi)^{-0.49};\\
&\sigma_{i1} = 0.44;\\
&A_{i2} / A_{i1} = -0.36;\\
&\mu_{i2} = 8.90(\Phi)^{-0.36}(\beta Fr\text{-}Frc)^{-0.10};\\
&\sigma_{i2} = 0.22;
\end{aligned}
\tag{19}
$$

M_{max} :

$$
\begin{aligned}
&A_{m1} = 5.88\times10^{4}(R/W)^{0.57}(\Phi)^{16.45}(\beta Fr\text{-}Frc)^{44.87} \quad \text{for } 2 \le R/W \le 4;\\
&A_{m1} = 4.69\times10^{6}(R/W)^{-0.68}(\Phi)^{-1.89}(\beta Fr\text{-}Frc)^{3.47} \quad \text{for } 4 \le R/W \le 8;\\
&\mu_{m1} = 41.27(R/W)^{-0.67}(\Phi)^{-0.64};\\
&\sigma_{m1} = 0.44;\\
&A_{m2} / A_{m1} = -0.32;\\
&\mu_{m2} = 5.15(\Phi)^{-0.17}(\beta Fr\text{-}Frc)^{0.12};\\
&\sigma_{m2} = 0.22;
\end{aligned}
\tag{20}
$$

CHAPTER V

CHANNEL CENTERLINE MEANDER MIGRATION RATE

5.1 Introduction

A prediction method to estimate the channel migration distance without any pre-described process is developed in this chapter. Unlike the channel bankline migration distance and the resulting hyperbolic function in the previous chapter, the channel centerline migration of each time step in the experiments is analyzed herein. Laboratory results (discussed in Chapter III) are still used as the basis in investigating the centerline meander migration. The channel centerline of each time step in the test is curve fitted with a combination of several circular curves and straight lines. A least-square-error circular fitting method developed by Moura and Kitney (1991) is applied to the centerline measurements of the entire channel. Fig. 41 shows the curve fitting results and the geometry conditions of case 03 and case 13 at t = 0 hr. Inflection points at which the channel changes its curvature are firstly identified along the centerline (e.g., a, b, c,…). In order to reduce the noises and errors from the centerline depiction, criteria are set in the process of curve fitting. A minimum curve length $R\Phi$ and a maximum radius of curvature R criteria are applied (Carson and Lapointe 1983). Minimum curve length of one channel width, i.e. $R\Phi/W$ = 1, and maximum radius of curvature of 25 channel widths, i.e. R/W = 25, are used in such that shorter curve lengths and larger values of radius of curvature are all approximated as straight lines.

Each circular curve between two successive inflection points from curve fitting represents a curved bend with a radius of curvature R and a bend angle Φ. The radius of curvature R is the radius of the fitted circle, while the bend angle Φ is the angle between the leading and end inflection points. In addition, each bend is also given a sign to its curvature; a

bend (curve) is defined as positive if the curvature to the flow direction is counter-clockwise. For each point in the bend, its position angle θ is the circular angle in relation to the leading inflection point. Thus, the non-dimensional angle θ/Φ ranges from 0 to 1 in each bend. The curve fitting is applied to the centerline of each time step in the tests.

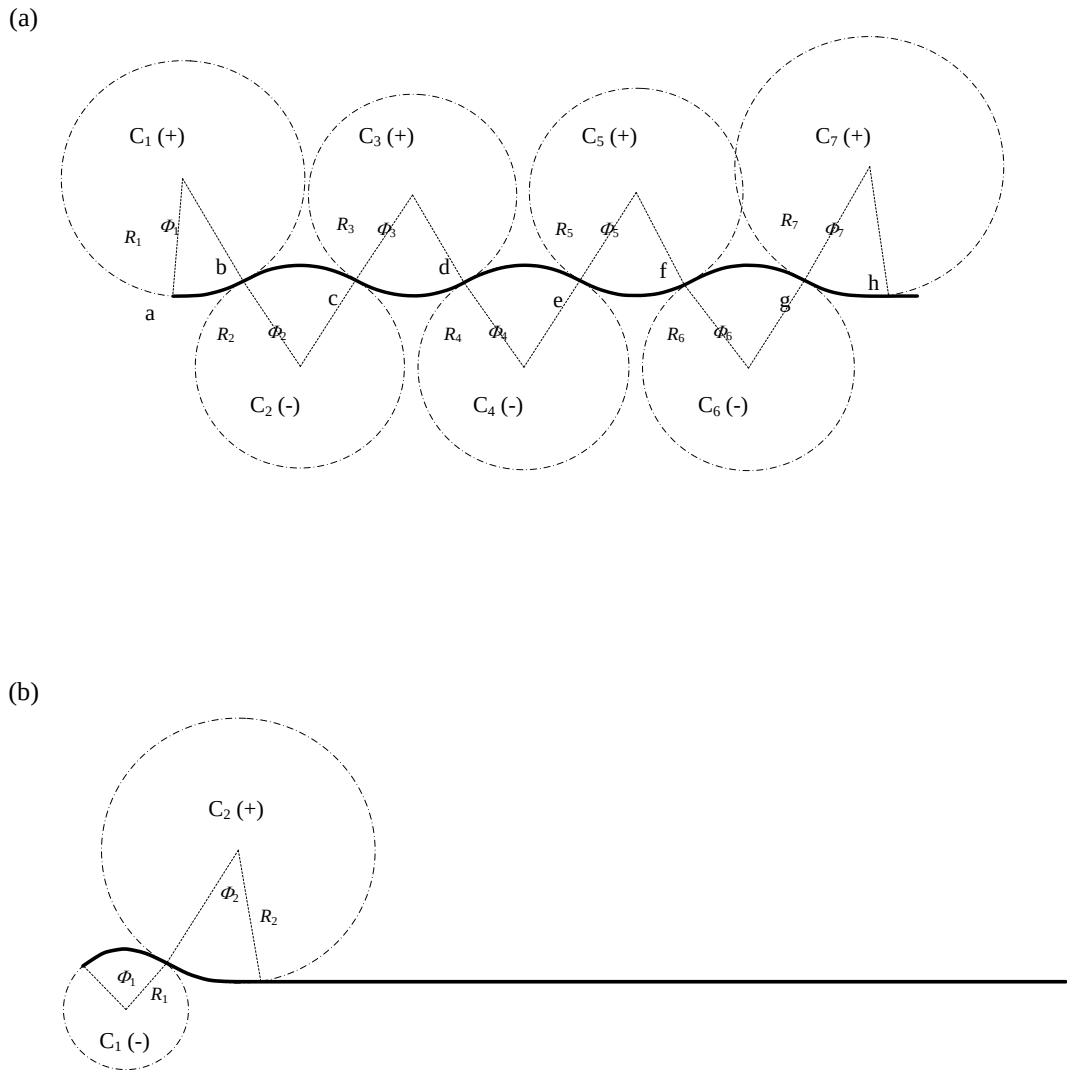

Fig. 41. Curve fitting on the centerline of case 03 and case 13 at t = 0 hr

As discussed in Chapter III, several cross sections were selected in each case to measure the cross sectional mean velocities and map the profiles as shown in Fig. 12. The streamwise distributions of the cross sectional mean velocities and other hydraulic properties associated with the fitted centerline were estimated by using HEC-RAS. Flowrate, channel plan form and mapped cross sectional profiles of each time step are used as initial conditions in each time step. A constant slope throughout the entire channel is assumed as the trial channel slope. The estimations of the mean velocities and other properties (hydraulic water depth, cross section top width, and the Froude number) from HEC-RAS are then compared with the measurements in the selected cross sections. If the results do not match the measurements, the channel bed slope between each two successive cross sections is then adjusted by trial-and-error. Starting from the last cross section downstream, the procedure is proceed towards the channel upstream until all the properties are all compatible with the measurements. Flow properties upstream from the first and downstream from the last mapped cross section are assumed uniform. With the use of HEC-RAS, the flow hydraulic properties of each point along the centerline are obtained for all the time steps. Example results of case 03 are shown in Fig. 42 in which s is the channel length from the channel upstream head.

5.2 Channel Centerline Migration Rate

The centerline migration of two consecutive measurements of case 03 and case 13 are analyzed as shown in Fig. 43. Several intersections (crossovers) of these two centerlines exist along the channel (e.g., b', c' and d'), where the migration distance m and the migration rates $\dot{m}$ are zero. As discussed in the previous chapter (Chapter III), the centerline migration of a curved bend moves in a direction opposite to the bend curvature (centripetal direction) from the bend entrance (e.g., b, c, d) to the intersection, but moves in the same direction with the bend curvature (centrifugal direction) beyond the intersection to the bend exit (e.g., c, d). Relative to the center

of curvature, the migration rate then can be assumed as negative or positive for the front part (before intersection point) or the back part (after intersection point) of the bend, respectively. The migration rate changes its direction (also sign) on the intersection. With the use of the sign in the migration direction, these intersections are the inflection points of migration rate, apart from the inflection points of channel curvature (e.g., b, c, d).

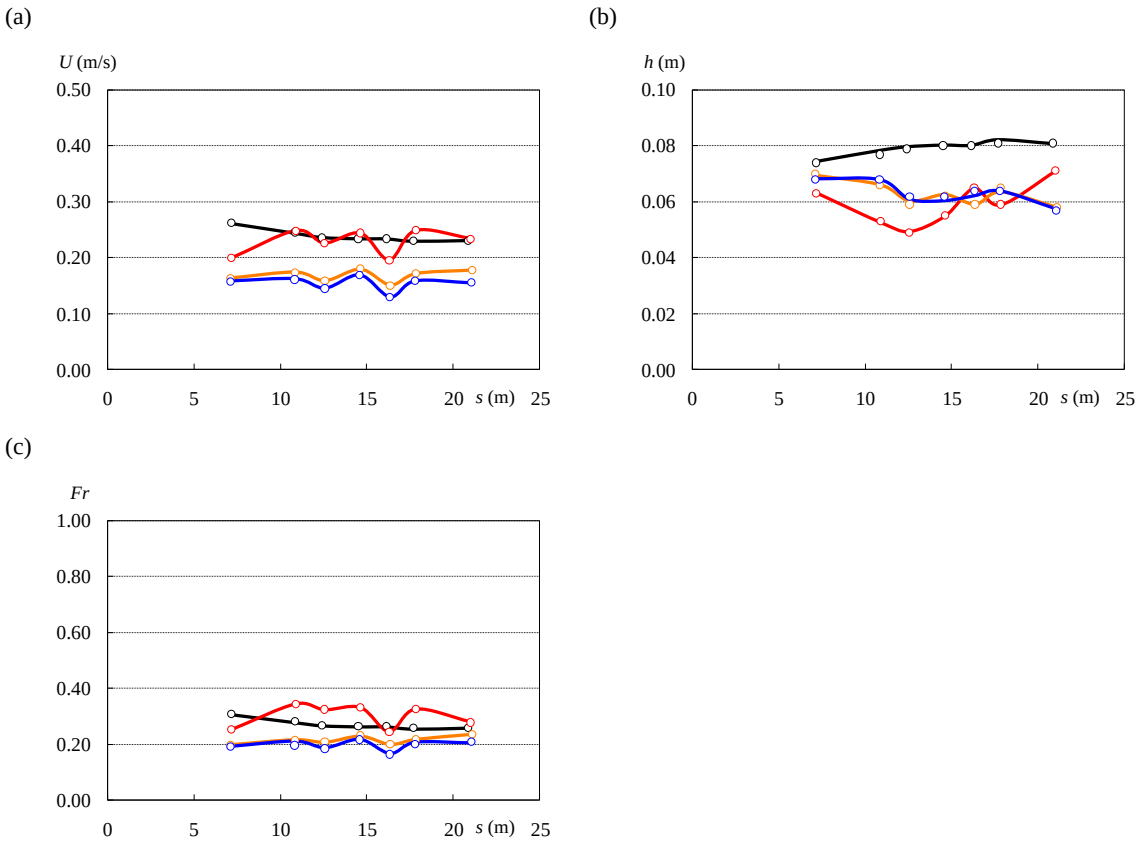

Fig. 42. (a) Mean velocity *U*; (b) water depth *h*; (c) Froude number *Fr* of case 03 by using HEC-RAS, ○ measurements; — 0 hr; — 6 hr; — 15 hr; — 39 hr

A phase lag θ_m exits between each inflection point of migration rate (b', c' and d') and its bend entrance (b, c and d) which is the centerline geometric inflection point from curve fitting. Carson and Lapointe (1983) conducted a comprehensive study about the inherent asymmetry of meander channel, stating that the delayed crossover of the thalweg to the channel centerline would be the starting point for the channel meander asymmetry. Also, as in the regular meander path model by Chang (1984), the discharge centerline (flow path), which has zero transverse discharge, is out of phase to the channel centerline (channel path), attributed from the channel's response to the flow. The intersections of two centerlines here are somewhat the outcome of the channel plan form to the asymmetric migration rate in a curved bend, and the phase lag θ_m denotes the translation and rotation in channel morphologic change. Similar to the findings of Chang (1984), θ_m is found to be independent of bend curvature and bend angle. Fig. 44 shows the variation of θ_m in different bend length $R\Phi$. It is seen that shorter bends with small curvature have large ratio of θ_m/Φ, indicating the tendency of channel straightening, and θ_m/Φ decreases as the bend length increases. After including the influence from water depth, a regression equation of the phase lag in a curved bend is then obtained as

$$\frac{\theta_m}{\Phi} = 9.18 \times \left(\frac{h}{W}\right)^{0.67} \left(\frac{R\Phi}{W}\right)^{-0.92} \tag{21}$$

where R is the radius of curvature, Φ is the bend angle, h is the water depth and W is the channel width. In Eq. (21), all the parameters are bend-averaged. The migration curve length λ, which is the distance between two successive inflection points along the channel centerline, is also compared with the length of the leading curved bend in Fig. 45. The results show that λ is very close to the bend length $R\Phi$. For most curved bends in the experiment, moderate curvature doesn't cause large plan form change within a short time step, so that λ is very close to the bend length $R\Phi$ at any time step. However, for small curvature like case 01, the channel straightens

very quickly so that θ_m usually exceeds the bend angle. If the curvature change is too dramatic as the connection between the curved and straight reach of case 13 in Fig. 43(b), large migration would also make λ larger than the bend length.

(a)

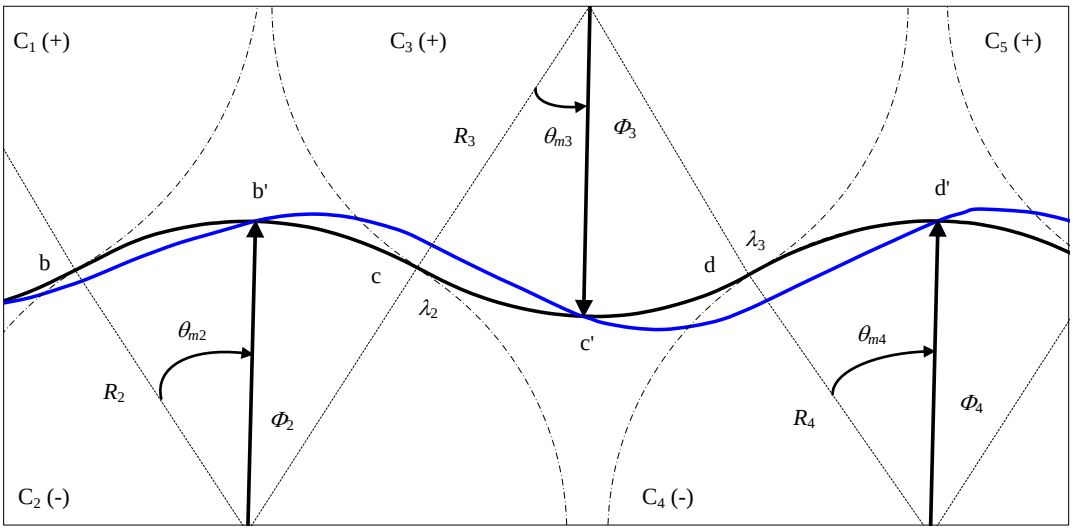

(b)

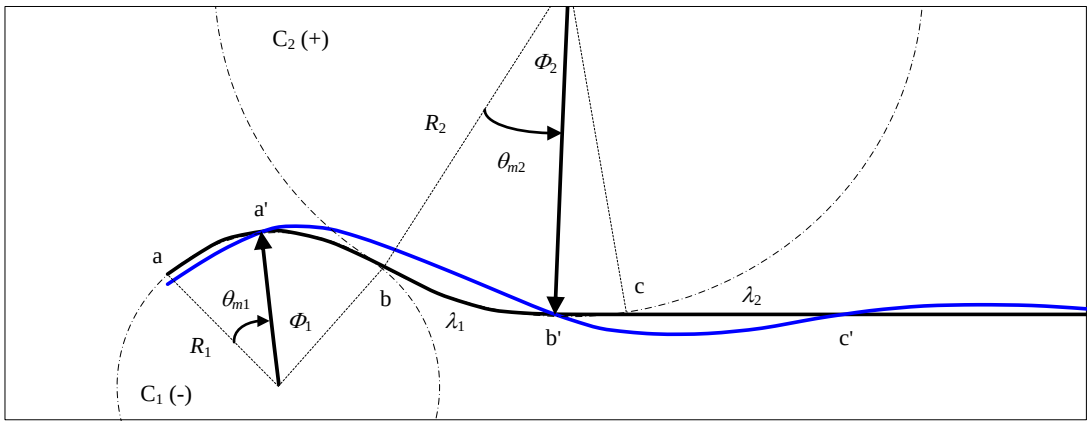

Fig. 43. Centerline migration and phase lag of each curved bend in case 03 and case 13

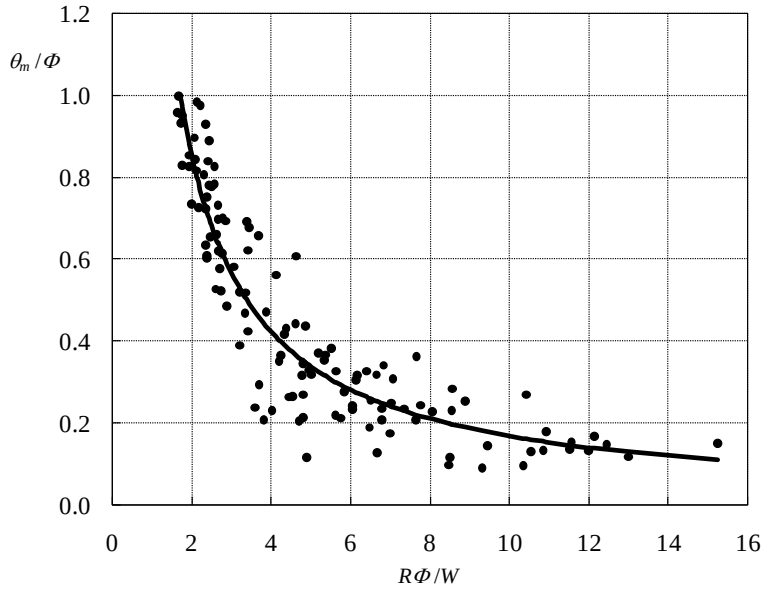

Fig. 44. Phase lag θ_m in different bend length $R\Phi$

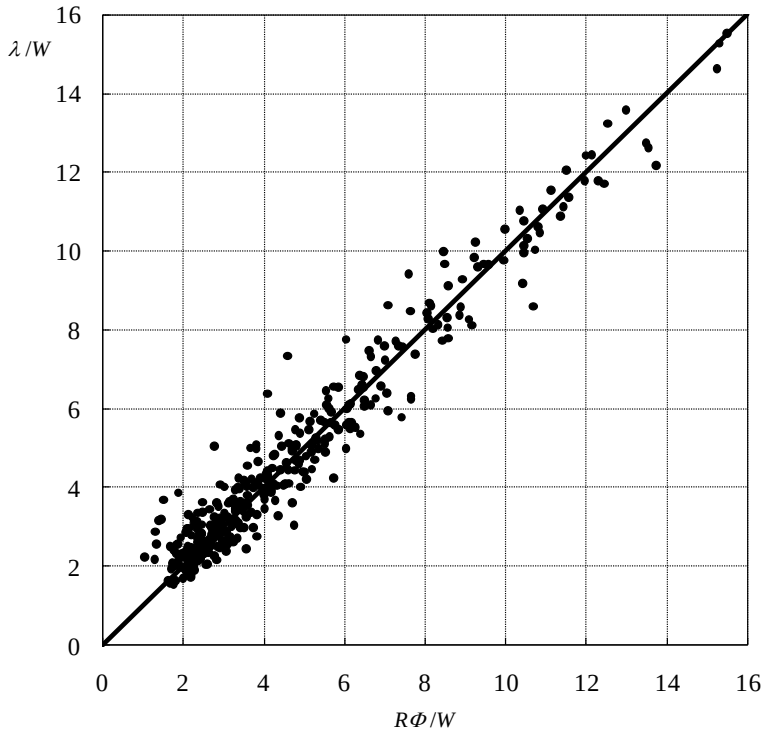

Fig. 45. Migration curve length λ in different bend length $R\Phi$

Along the curved channel, the centerline migration rate $\dot{m}_c$ of each point is estimated on the direction normal to the centerline and normalized by the longitudinal mean velocity U estimated from HEC-RAS. Its sign is given as the product of curvature and movement directions. For a bend with a positive curvature (+), i.e., C_3 in case 03, the migration rate is negative (-) before the inflection point (c') due to the centripetal movement (-), and is positive (+) beyond the inflection point for the centrifugal movement (+). On the other hand, for the following bend C_4 which has a negative curvature, the signs of the migration rate before and beyond the inflection point (d') are reverse from C_3. Fig. 46 shows the migration rates of case 03 and case 13 in the first three hours (t = 0 hr ~ t = 3 hr). It is seen that the migration rate is zero on the inflection points and exhibits a growth and decay pattern between two successive inflection points. Using the sign noted above, the migration rate shows a wave form with alternate amplitudes similar to the velocity contrast of the thalweg along a channel course. A large amplitude of migration rate exists in the second bend and the amplitude decreases to the outlet of the channel in case 03 (Fig. 46(a)). On the other hand, case 13 (Fig. 46(b)) has an even larger migration rate in the initial curved bend, and two additional wave forms are developed successively in the front part of the straight reach. In the downstream of the straight reach, the centerline migration rate is small although both banks undergo significant retreat. The migration rate in case 13 shows a "propagation" phenomenon. The propagation of the wave form from the upstream curved bend transmits "faster" than the channel curvature; two curved bends create four migration rate waves in three hours. Since the curvature changes from a curved bend to the straight reach, flow separation and vortices caused by flow spiral motion creates large migration rate in the curved bend and persists for some distance on the straight reach (c' in Fig. 43(b)). The amplitude then drops rapidly on the two additional wave forms.

The migration rates in other time steps of case 03 and case 13 are plotted in Figs. 47 and 48, respectively. Note here that the migration rate is estimated between two consecutive measurements and the centerline geometry is curve fitted at each time step. Case 03 (Fig. 47) shows a surge of large migration rate propagating towards downstream. The migration rate attenuates after the surge passes to the next bend and gradually ceased. Since the curved channel is designed to turn back to a straight channel which is in line with the channel entrance, lateral movement is not constrained in the channel downstream. The channel downstream would adjust its plan form according to the changes from upstream. As a result, a large migration rate transmits from upstream to downstream as the test proceeds. After the passage of the large migration, the migration rate attenuates following a wider channel width and flatter bed slope. Mean velocity and the energy slope are reduced to stop bank erosion. On the other hand, the migration rate remains a developing status in case 13 (Fig. 48). Additional loops of the migration rate develop in the straight reach towards downstream. Except in the first time step (t = 0 hr ~ t = 3 hr), the peak value of the additional loops decays sequentially from the latest loop of the curved bend with an average 20 % ratio. The migration rate gradually decreases to a uniform state after the whole channel becomes sinuous. As discussed in Fig. 17, several curved bends with uniform bend widths and lengths are developed in the end of the test.

With all the measurements of flume test in this study, a sine function is used to estimate the centerline migration rate between two migration inflection points

$$\frac{\dot{m}_c}{U} = A_m \sin\left(\lambda' \times \pi\right) \tag{22}$$

in which A_m is the amplitude of the sine function and λ' is the distance fraction between two successive inflection points of migration rate. The results show that the sine function represents the migration rate between two inflection points pretty well. A_m is then further correlated with the bend geometric and hydraulic conditions and a prediction equation is expressed as

$$A_m = 0.01 \times \left(R/W\right)^{-0.39} \left(\Phi\right)^{-0.36} \left(h/W\right)^{0.79} \left(\beta Fr\text{-}Frc\right)^{2.77} \tag{23}$$

where R and Φ are of the leading curved bend, and W, h, and $\beta Fr\text{-}Frc$ are the average value between two inflection points. Once θ_m is determined for each bend, the migration rate between two inflection points (zero points) can be obtained.

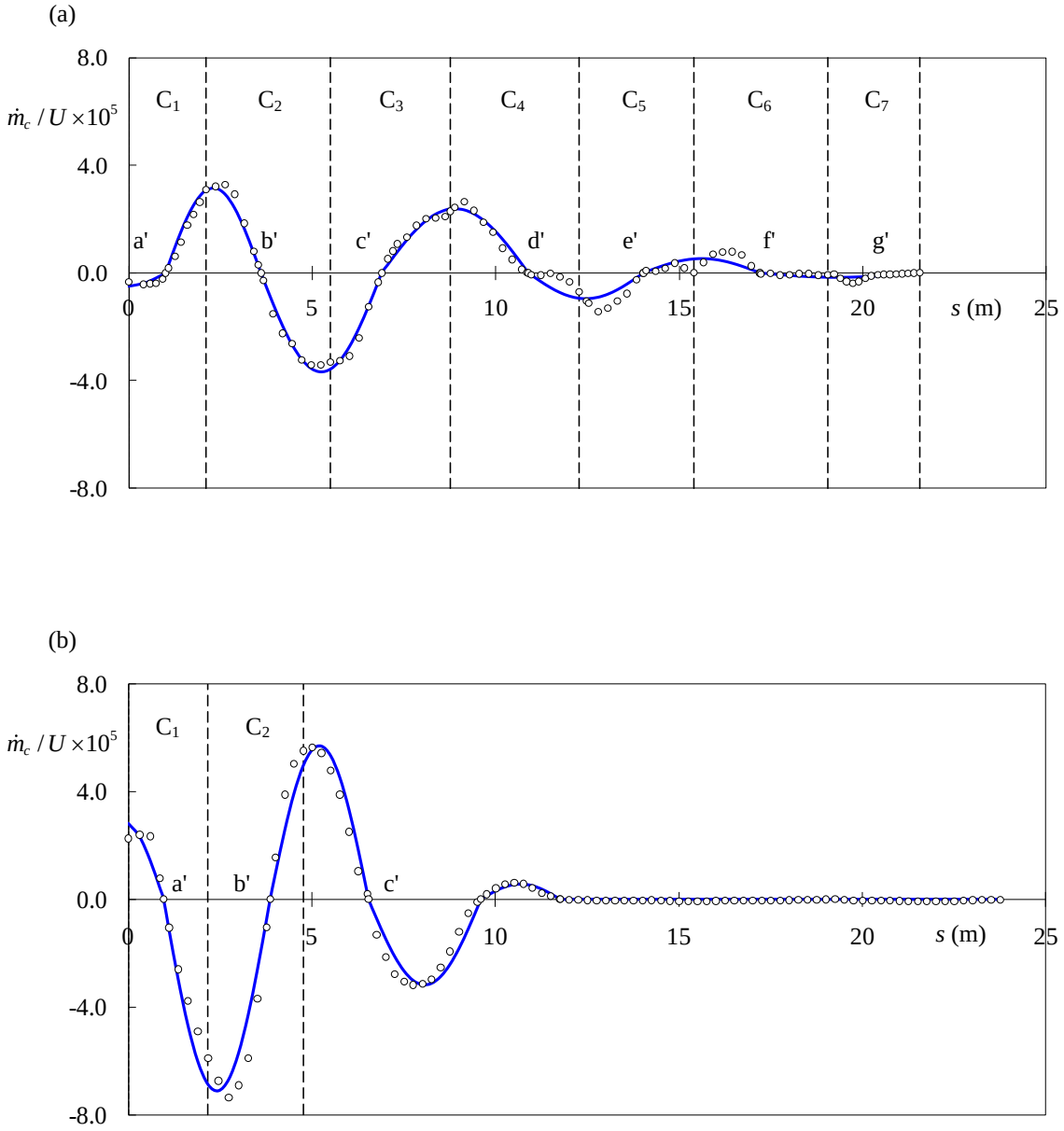

Fig. 46. Normalized centerline migration rates of case 03 and case 13, ○ measurements; ━ sine function fit

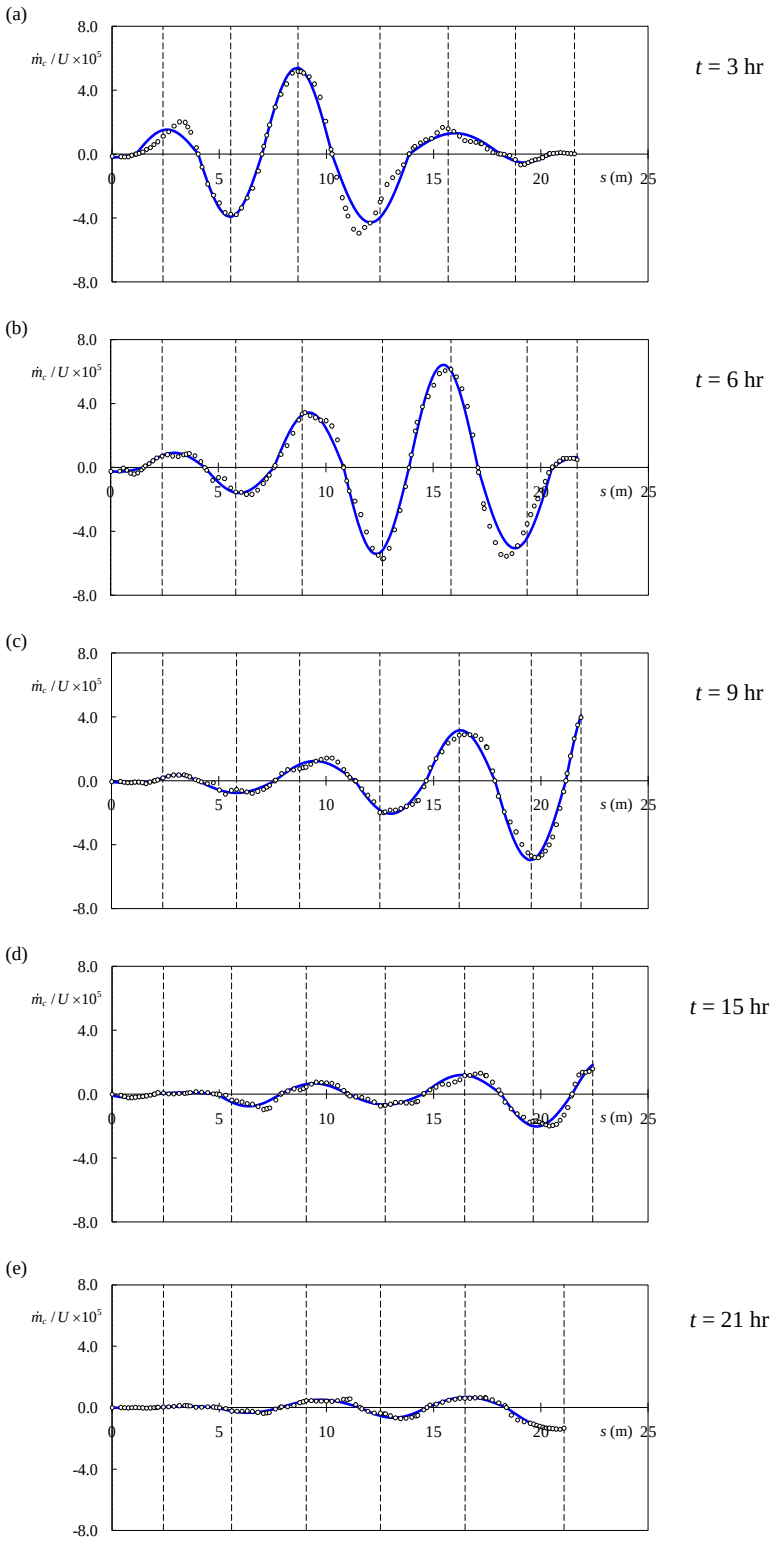

Fig. 47. Normalized centerline migration rate of case 03, ○ measurements; ━ sine function fit

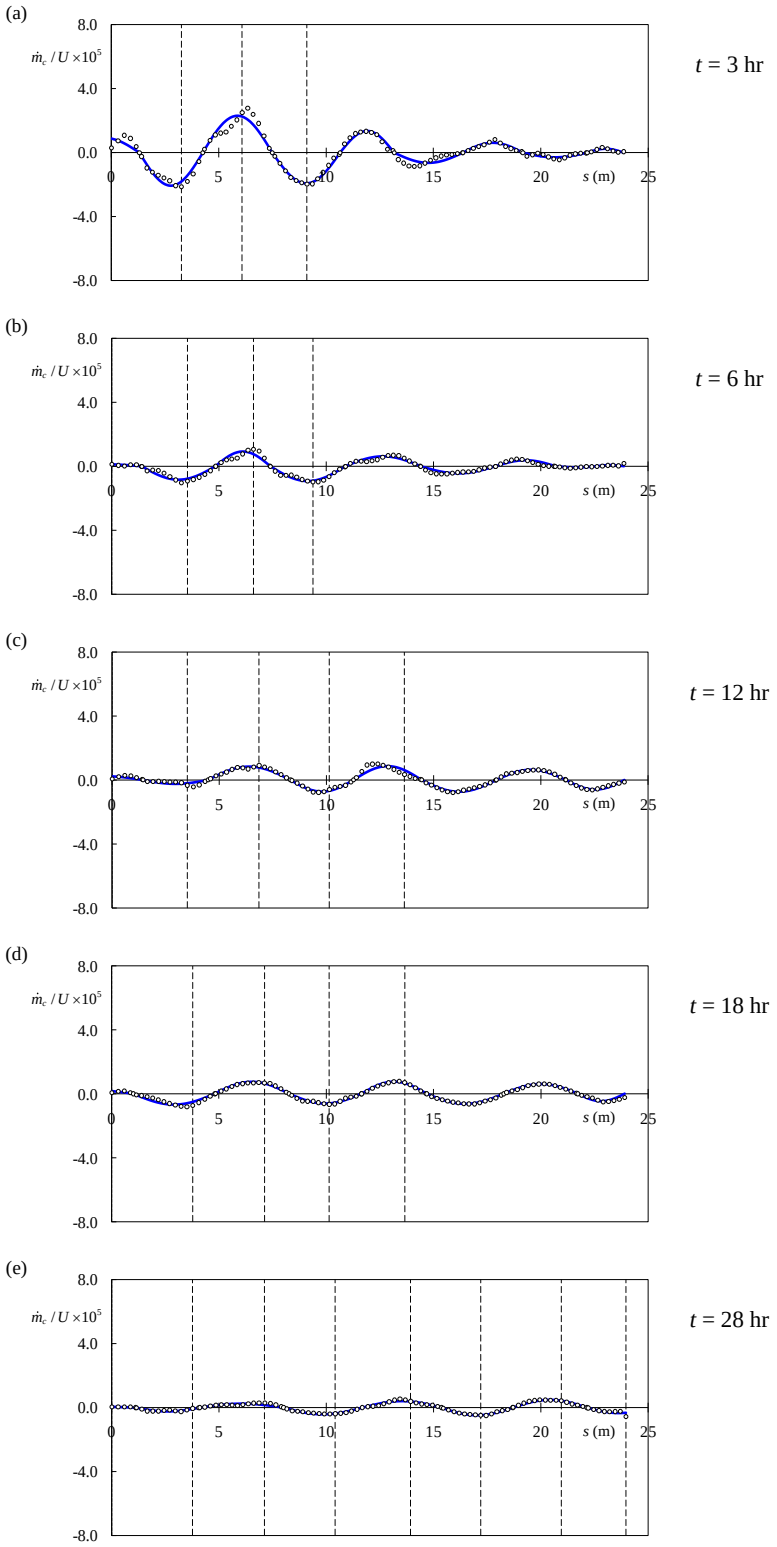

Fig. 48. Normalized centerline migration rate of case 13, ○ measurements; ━ sine function fit

5.3 Channel Centerline Migration Distance

The channel centerline migration distance and its evolutions with time are computed with the equations (Eqs. (21)-(23)) developed in the previous sections. The measured and calculated centerlines in each time step are compared in Figs. 49 (case 03) and 50 (case 13). Both cases start from the initial symmetric centerline of the test (t = 0), and proceed to the next time step. In each time step, the centerline is re-curve fitted as the initial condition by using the result from the previous time step. The results show that the discrepancies are small in both cases. In case 03, bigger errors occur in the channel downstream, which is believed due to the effects of downstream back-water in the experiments. Since longer time steps were taken in the later stage of the test, the calculated centerline also has bigger errors in larger time steps. Compared to the curved channel cases, the results of case 13 in Fig. 50 show relatively bigger errors. The disagreements are more obvious in the latter time steps. Since the initial plan form of case 13 is an initial curved bend connecting a straight reach, large migration rate and phase lag occur around the connection which has a large curvature change as C_1 and C_2 in Fig. 46(b). Errors from both the estimations of amplitude (A_m) and phase lag (θ_m) in the first three hours accumulate with time so as to affect the calculations in the later time steps. The results show that the approach is capable of duplicating the migration and deformation of a curved channel with an initially symmetric plan form and the bend development of a straight channel with an initial curved bend.

In order to further validate the proposed approach, the prediction equations are applied to several natural rivers. Four sites of four rivers in Texas are selected in the current study. These four sites are Guadalupe River at US 59, Trinity River at FM 787, Nueces River at US 90, and Brazos River at SH 105. It is suggested by TxDOT (Texas Department of Transportation) that these four sites are where the channel migration has been significant and has led to major

maintenance problems in bridge crossings. For each site, aerial photos and topographic maps over the past decades are collected and superimposed together to indicate the direction and enduring progress of river meander. River daily flowrate and other flow properties such as mean velocity *U*, water depth *h*, channel width *W* and the Froude number *Fr* are obtained from the nearest USGU gauge station. Since the channel slope and cross section information are unavailable to the author, uniform flow properties are assumed in the whole site.

The simulation starts from curve fitting the channel centerline of 1959 and iterates the calculation with a daily time step. A critical velocity of the site is assumed first and the result is compared with the centerline coordinate of 1981. If large discrepancy occurs, a new critical velocity is assumed again until a small error is obtained. A critical velocity (U_c = 0.60 m/s) which has a smallest error is found for the site and the result is shown in Fig. 55(a). The calculation then continues with this critical velocity and stops after it reaches 1995. Figs. 55(b) and (c) are the results of the simulation in 1988 and 1995. The results show that the prediction equations are applicable to simulate river centerline migration. The resulting channel plan forms in these three years are quite close to the recorded centerlines.

The simulation starts from curve fitting the earliest available river centerline and iterates the calculation with a daily time step. Since there's no information about the river soil properties available, a critical velocity of each site is assumed. The simulation result is then compared with the centerline of next recorded year. If large discrepancy occurs, a new critical velocity is assumed again until a small error is obtained. Fig. 51 is the aerial photo of Guadalupe River at site US 59. Several meander loops can be seen in the upstream and downstream of the bridge crossing. The river bankline and centerline evolution can be tracked from the topographic map from 1959 to 1995 as shown in Fig. 52. The nearest USGS gauge station around the site is USGS 08176500 and the daily flowrate and other hydraulic properties are recorded as Figs. 53

and 54. A critical velocity (U_c = 0.60 m/s) which has a smallest error in the centerline of 1981 is found and the result is shown in Fig. 55(a). The simulation then continues with this critical velocity and proceeds to the other two years: 1988 (Fig. 55(b)) and 1995 (Fig. 55(c)). The results show that the prediction equations are applicable to simulate river centerline migration. The resulting channel centerlines of these three years are in good agreement with the recorded centerlines.

Another set of aerial photo and topographic map at the same site of Guadalupe River at US 59 is also used in the simulation. Figs. 56 and 57 represent a small and close-up area around US 59 in Figs. 51 and 52. The simulation starts from the centerline of 1959 in Fig. 57(b) with the same soil critical velocity and flow properties at USGS 08176500. The calculated centerlines are shown in Fig. 58. Comparing the results in Figs. 55 and 58, it can be seen that both simulations provide satisfactory channel centerline migration estimations. The discrepancies from the actual channel records, especially in 1995, are expected from the uniform flow properties assumed in the simulations. The results at the same site of Guadalupe River with two different scales of topographic maps indicate that the scale effect of different topographic maps on the prediction equations and the simulation is minimal. Figs. 59-73 are the topographic maps, daily records of flow properties, and the simulation results of the other three rivers. The nearest gauge stations to the sites are USGS 08110200 of Brazos River, USGS 08066500 of Trinity River and USGS 08108700 of Nueces River, respectively. The soil critical velocities of the three sites are 0.55, 0.65, and 0.45 m/s in the above order. The simulations show that satisfactory results are also obtained for the channel centerline meander migration in these three rivers. Note here the channel downstream had been straightened out in Nueces River after 1969. The river plan form in 1995 is much different from the previous years.

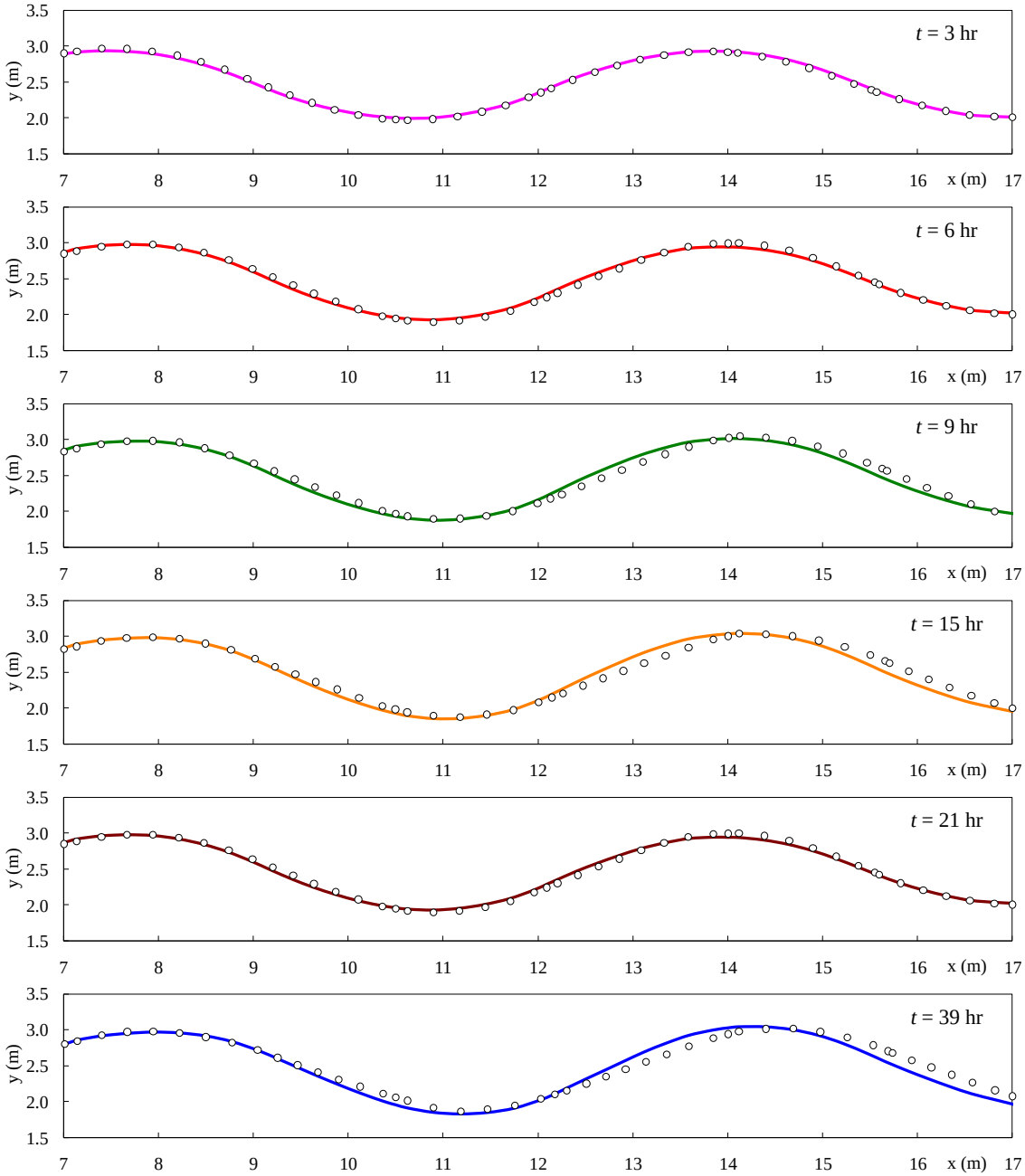

Fig. 49. Channel centerline simulations of case 03, ○ measurements; — 3 hr; — 6 hr; — 9 hr; — 15 hr; — 21 hr; — 39 hr

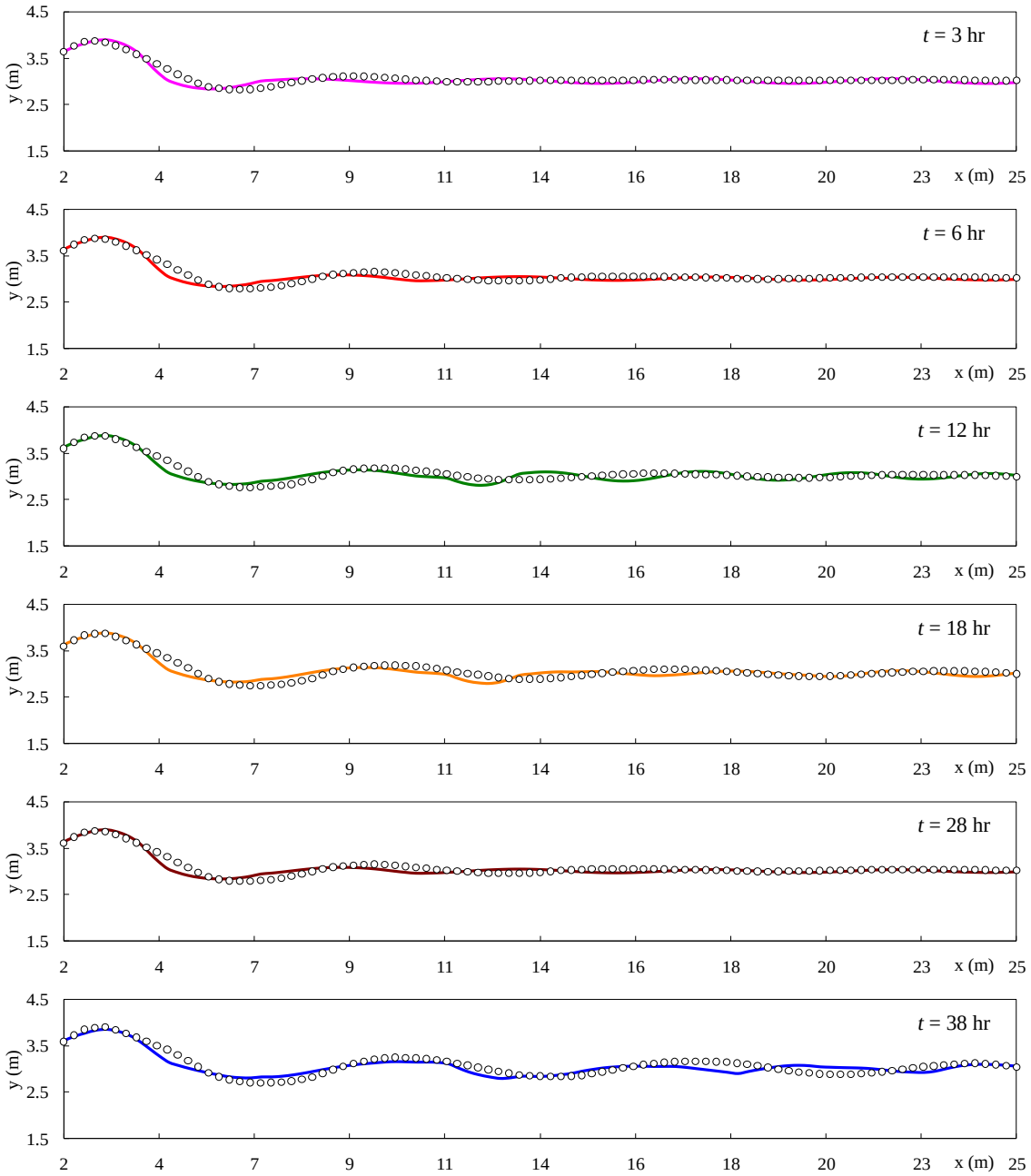

Fig. 50. Channel centerline simulations of case 13, ○ measurements; — 3 hr; — 6 hr; — 12 hr; — 18 hr; — 28 hr; — 38 hr

Fig. 51. Aerial photo of Guadalupe River at US 59 (1) (after Google Map)

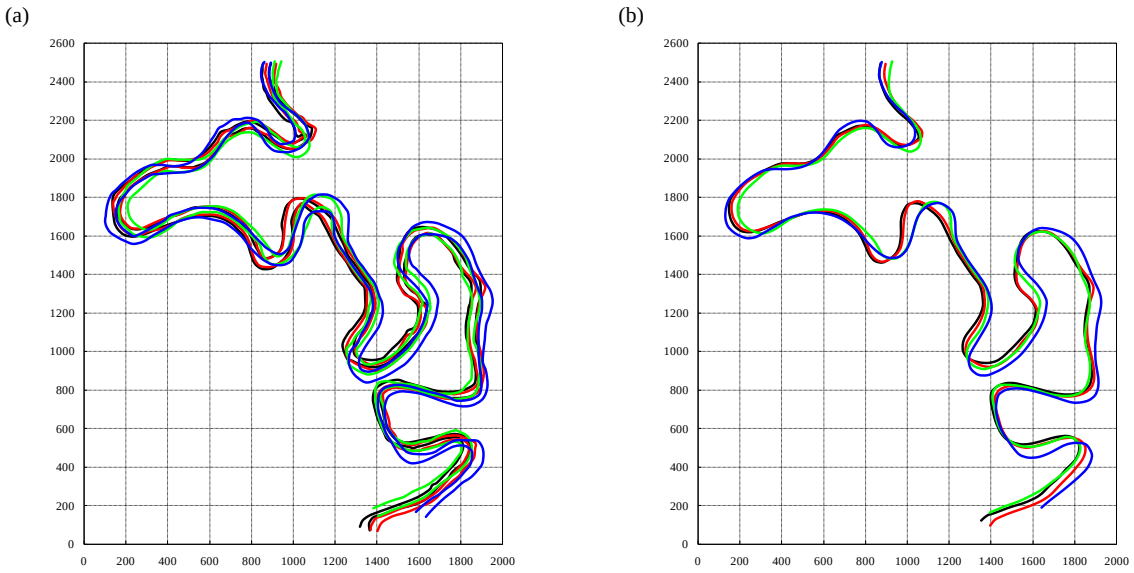

Fig. 52. (a) Banklines; (b) centerlines of Guadalupe River at US 59 (1), ━ 1959; ━ 1981; ━ 1988; ━ 1995

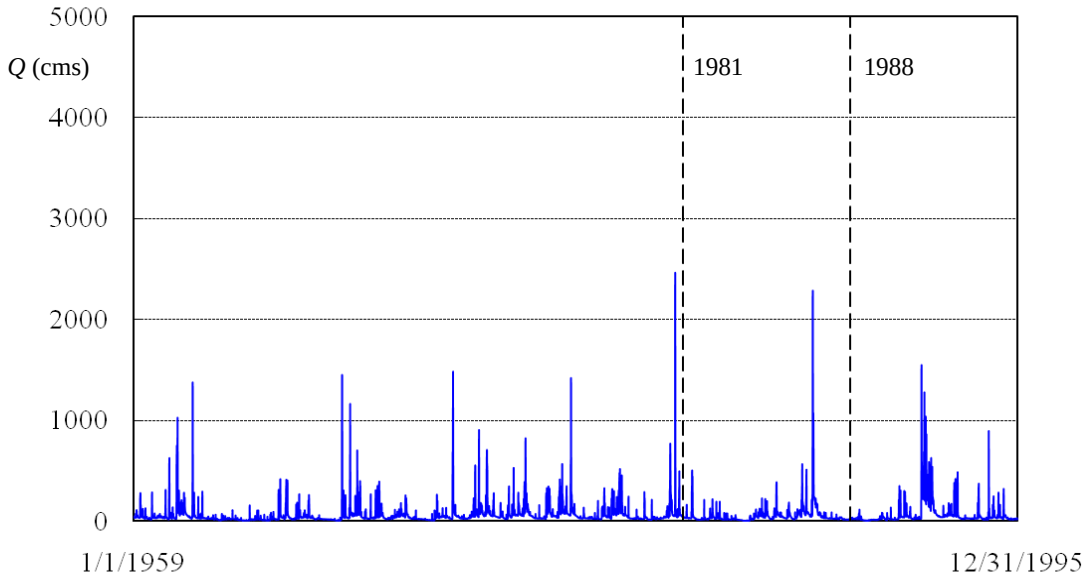

Fig. 53. Daily flowrate records at USGS 08176500

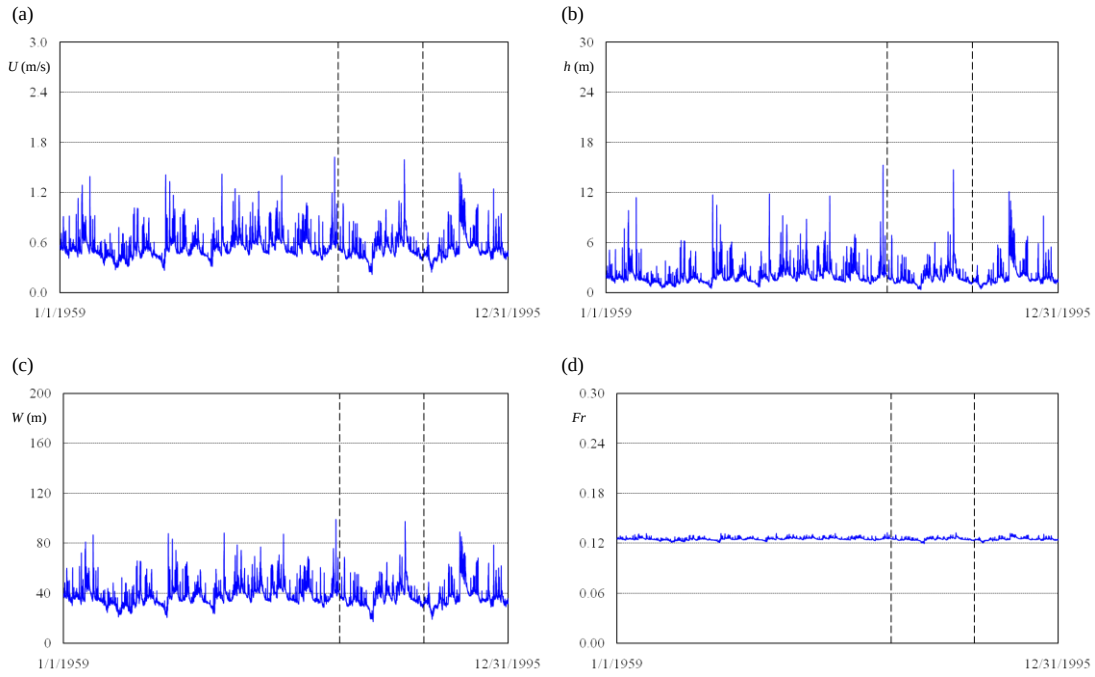

Fig. 54. Flow properties: (a) mean velocity *U*; (b) water depth *h*; (c) channel width *W*; (d) Froude number *Fr* at USGS 08176500

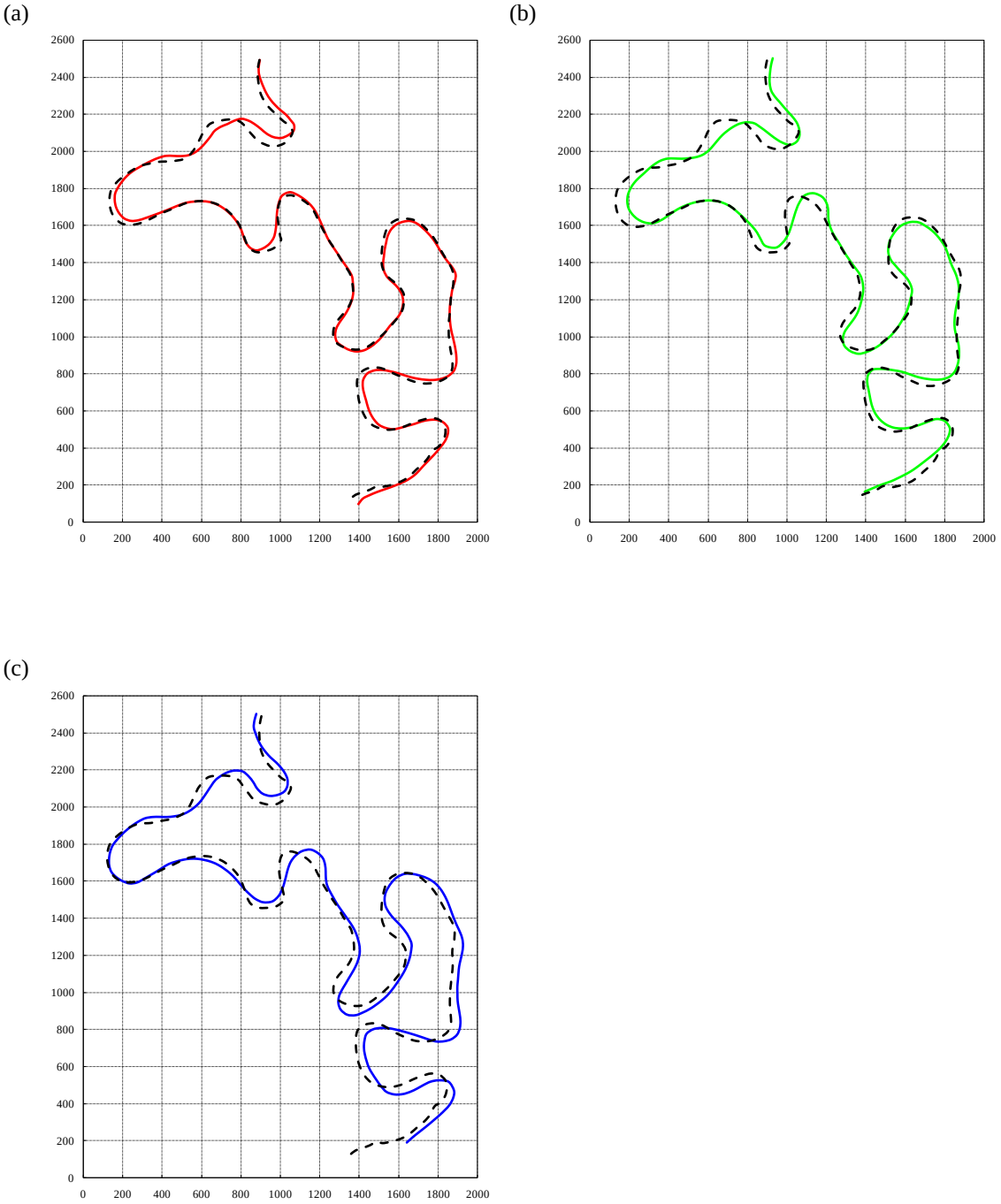

Fig. 55. Centerline simulations of Guadalupe River at US 59 (1), — 1981; — 1988; — 1995; -- simulation results

Fig. 56. Aerial photo of Guadalupe River at US 59 (2) (after Google Map)

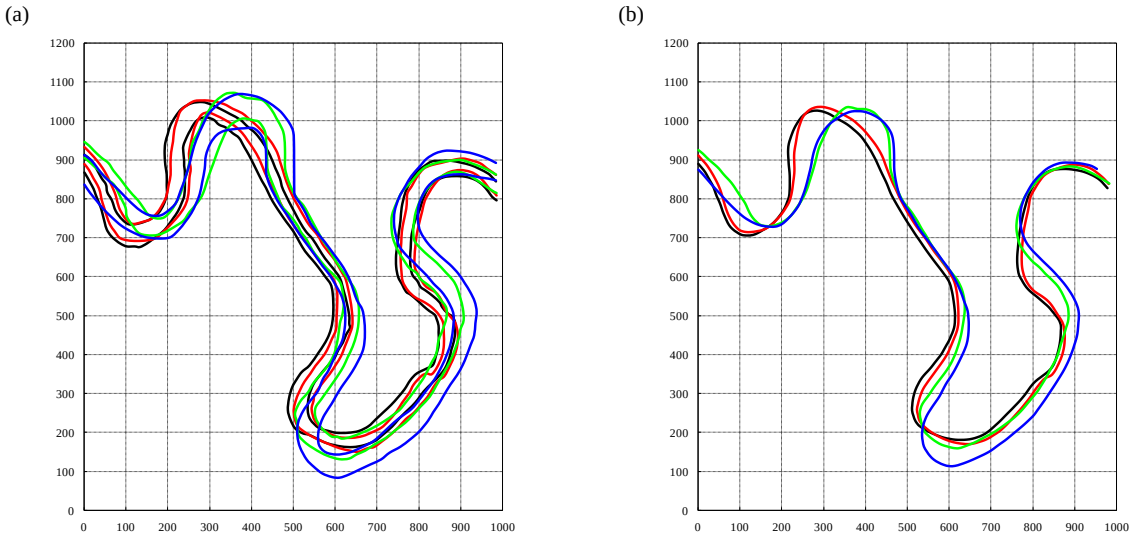

Fig. 57. (a) Banklines; (b) centerlines of Guadalupe River at US 59 (2), ─ 1959; ─ 1981; ─ 1988; ─ 1995

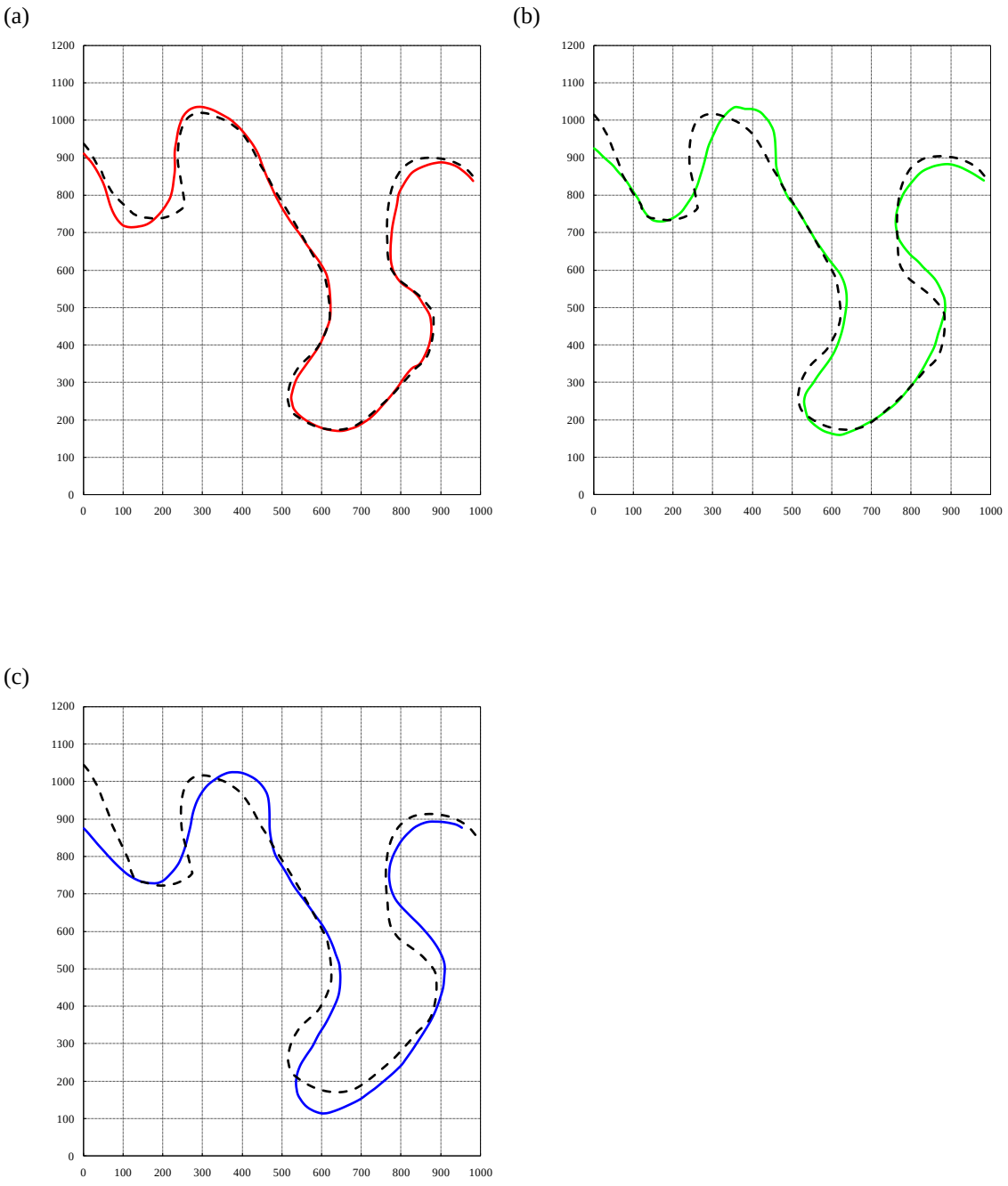

Fig. 58. Centerline simulations of Guadalupe River at US 59 (2), — 1981; — 1988; — 1995; -- simulation results

Fig. 59. Aerial photo of Trinity River at FM 787 (after Google Map)

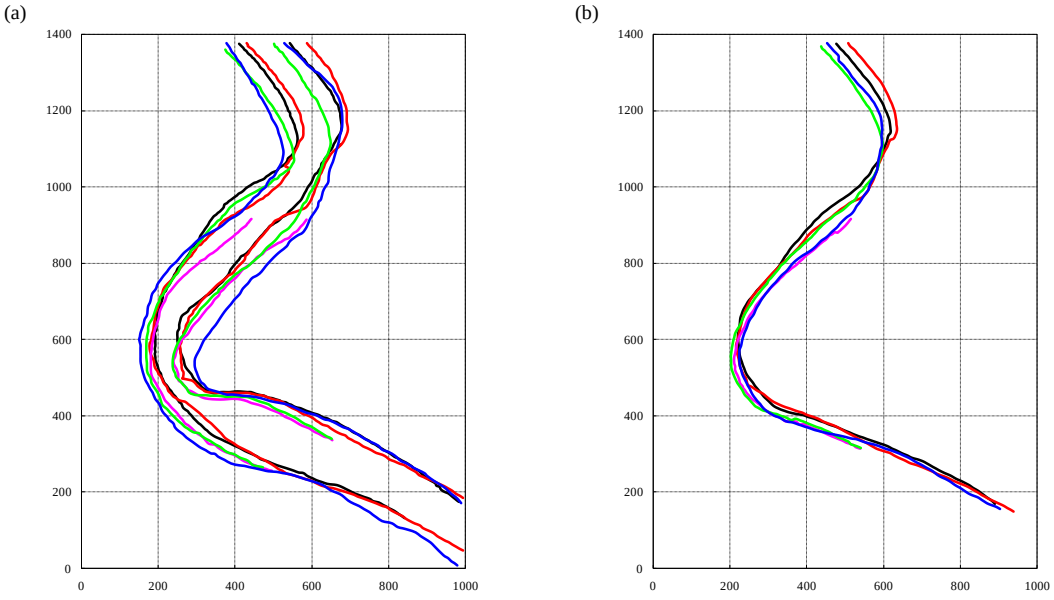

Fig. 60. (a) Banklines; (b) centerlines of Trinity River at FM 787, ─ 1971; ─ 1976; ─ 1983; ─ 1988; ─ 1999

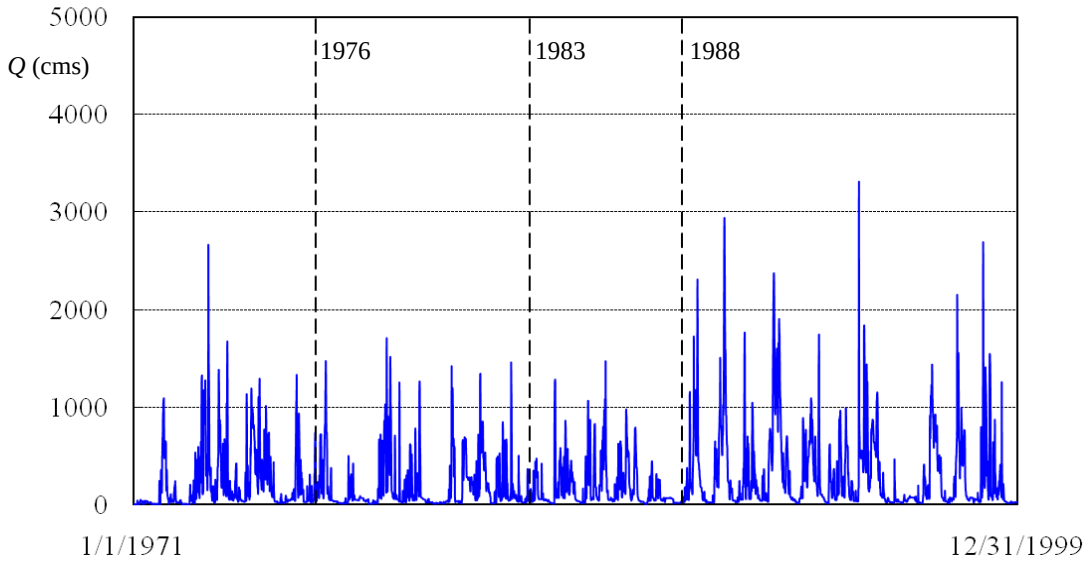

Fig. 61. Daily flowrate records at USGS 08066500

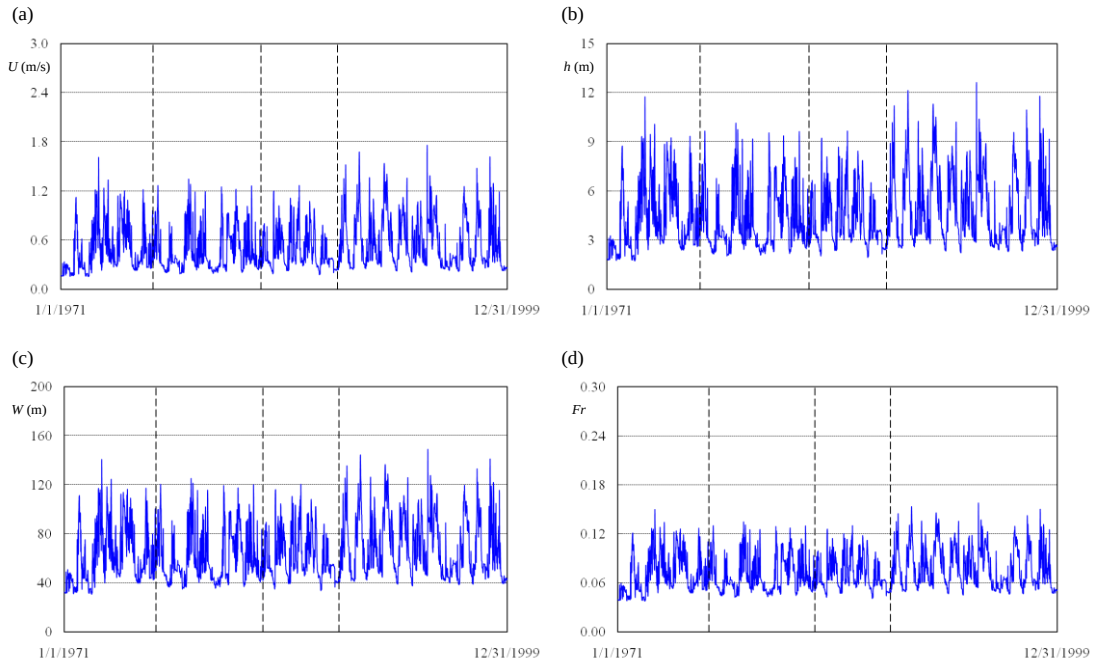

Fig. 62. Flow properties: (a) mean velocity *U*; (b) water depth *h*; (c) channel width *W*; (d) Froude number *Fr* at USGS 08066500

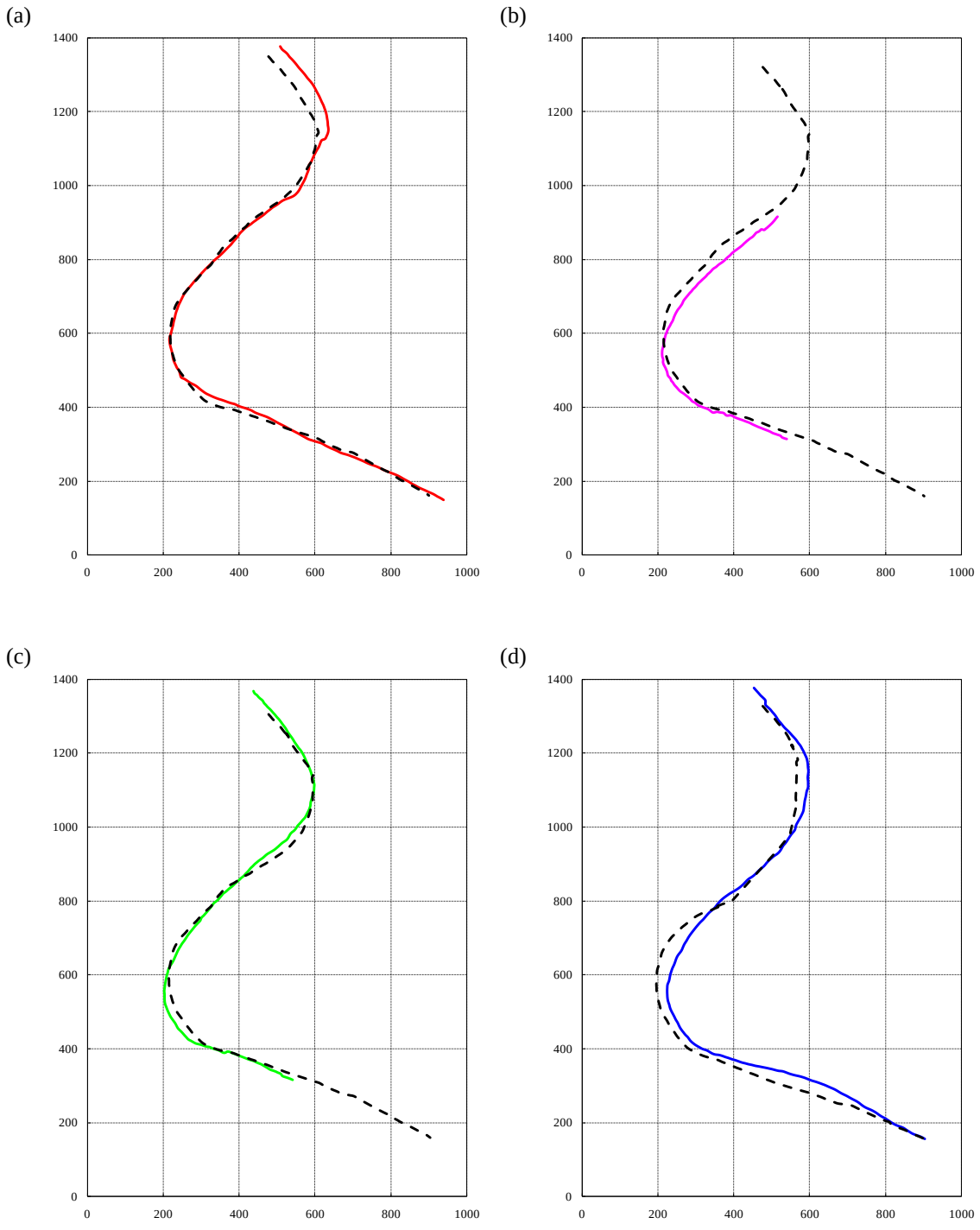

Fig. 63. Centerline simulations of Trinity River at FM 787, — 1976; — 1983; — 1988; — 1999; -- simulation results

Fig. 64. Aerial photo of Brazos River at SH 105 (after Google Map)

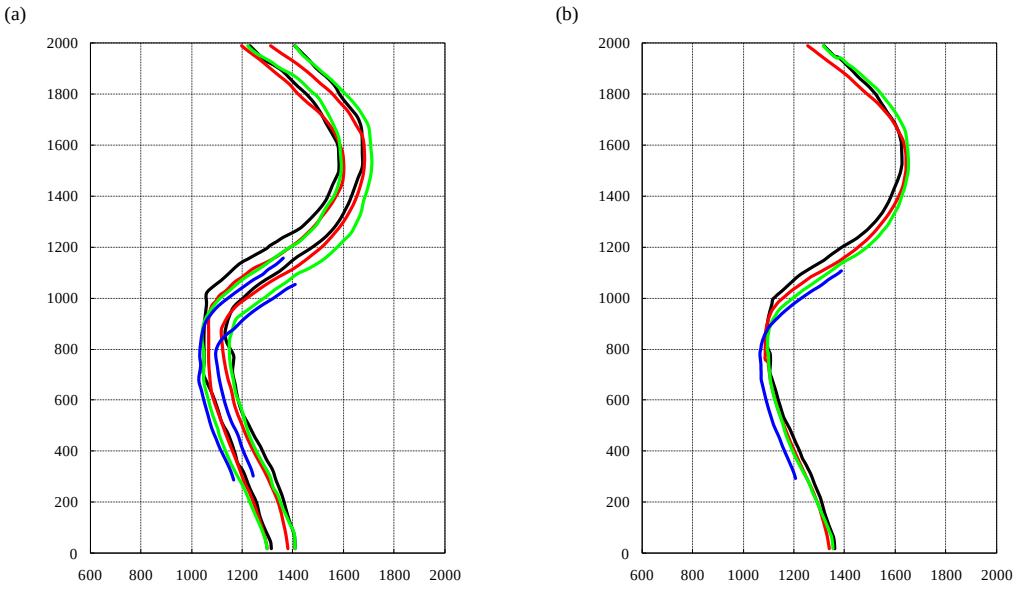

Fig. 65. (a) Banklines; (b) centerlines of Brazos River at SH 105, ▬ 1981; ▬ 1988; ▬ 1995; ▬ 1999

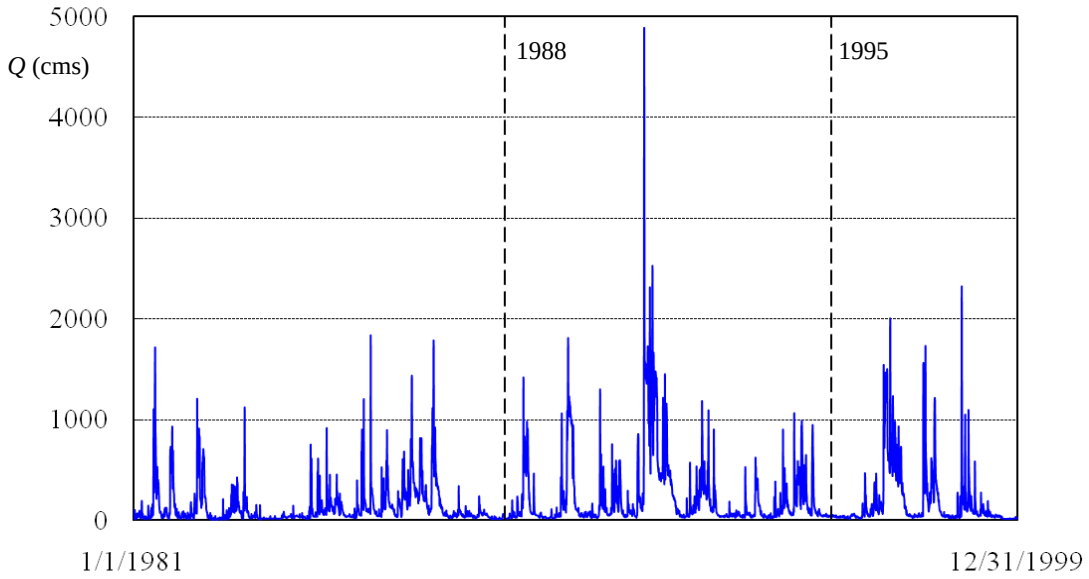

Fig. 66. Daily flowrate records at USGS 08110200

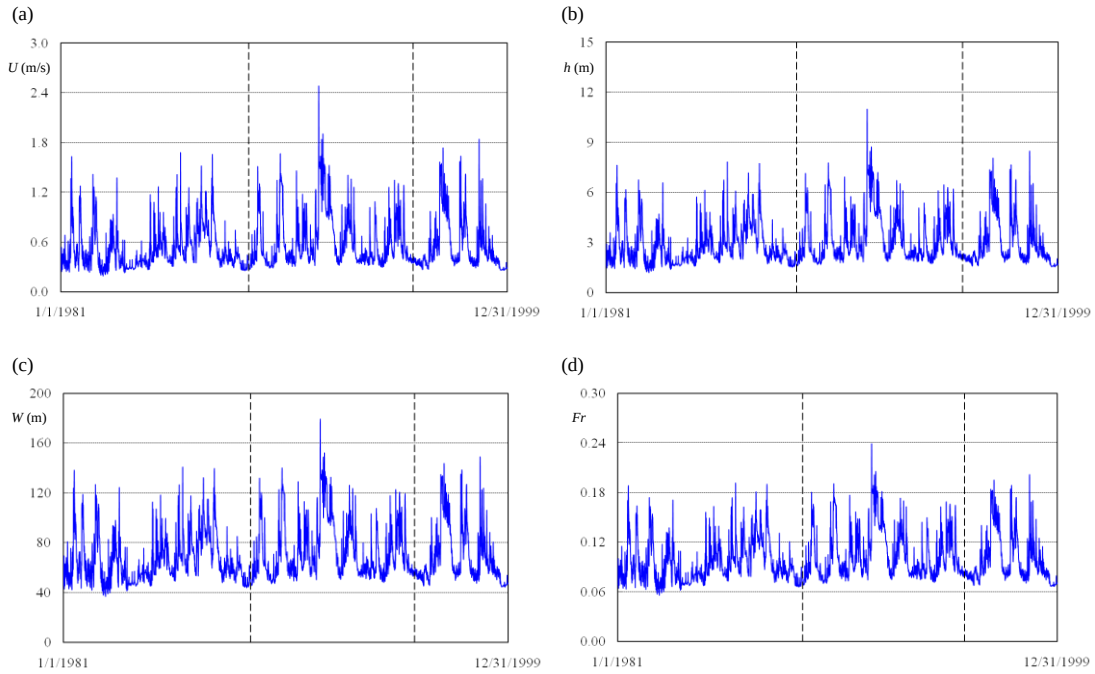

Fig. 67. Flow properties: (a) mean velocity *U*; (b) water depth *h*; (c) channel width *W*; (d) Froude number *Fr* at USGS 08110200

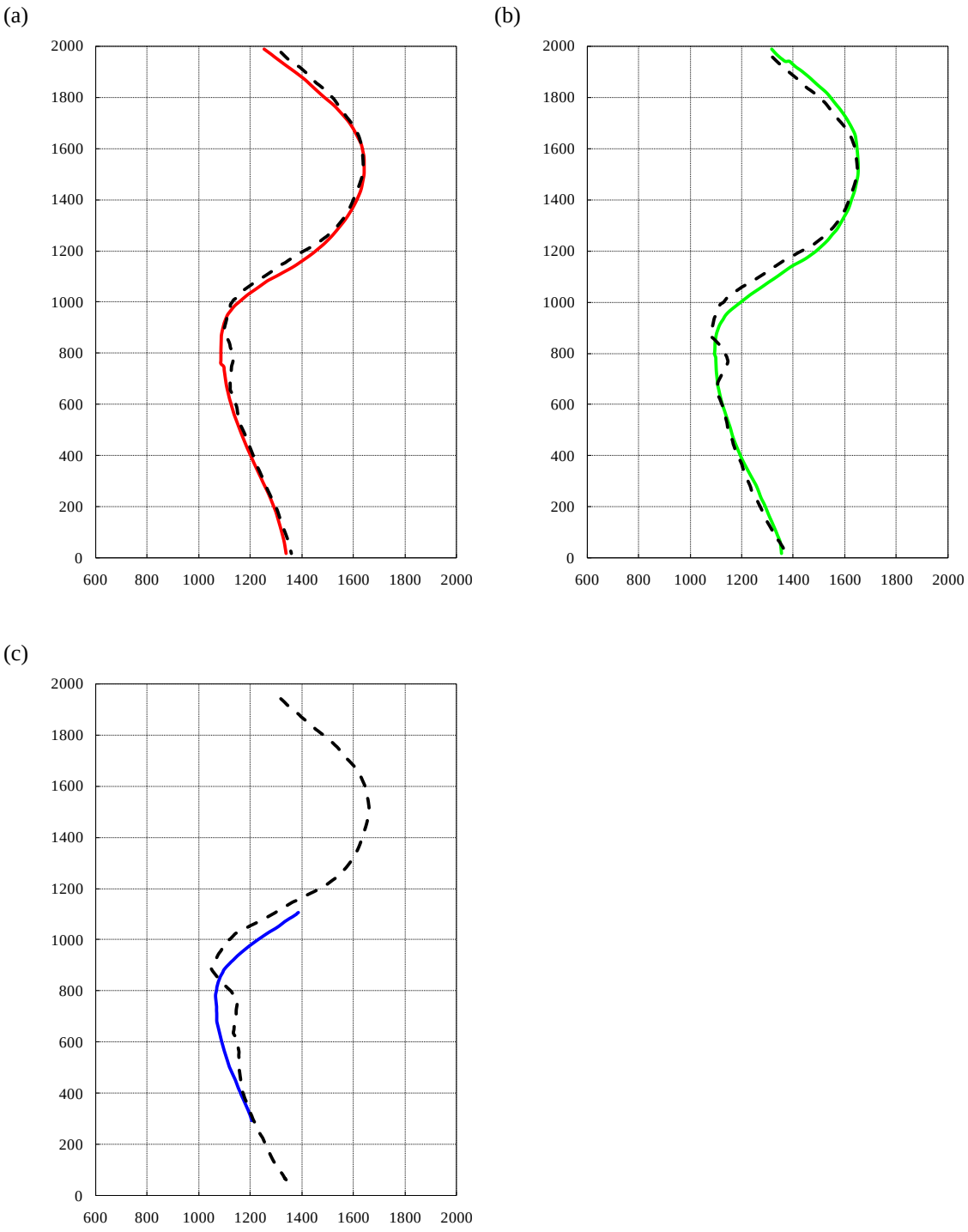

Fig. 68. Centerline simulations of Brazos River at SH 105, — 1988; — 1995; — 1999; -- simulation results

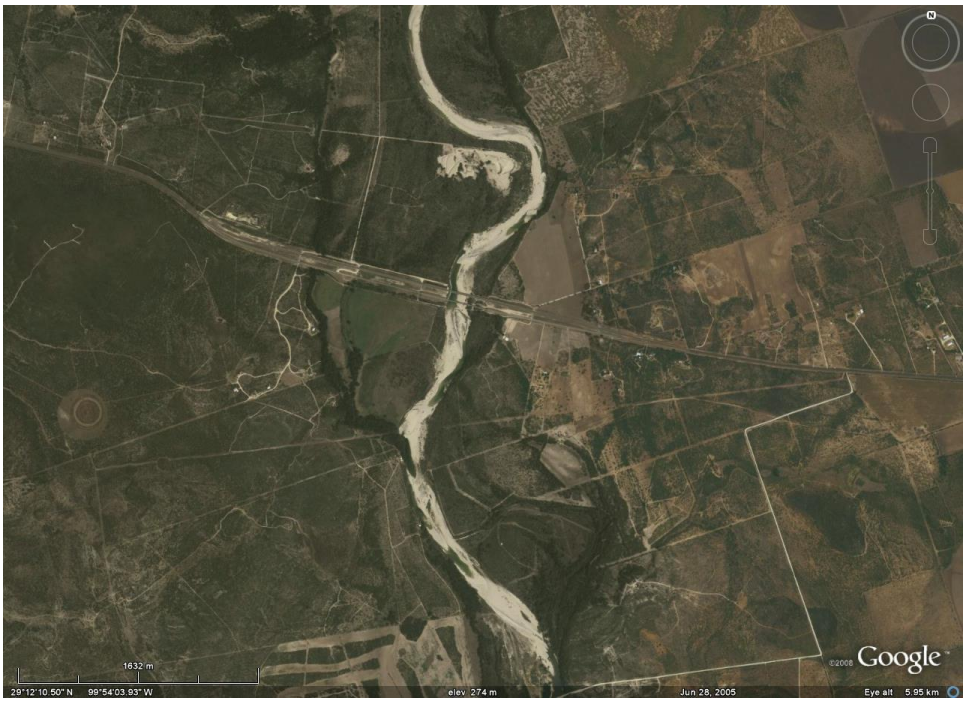

Fig. 69. Aerial photo of Nueces River at US 90 (after Google Map)

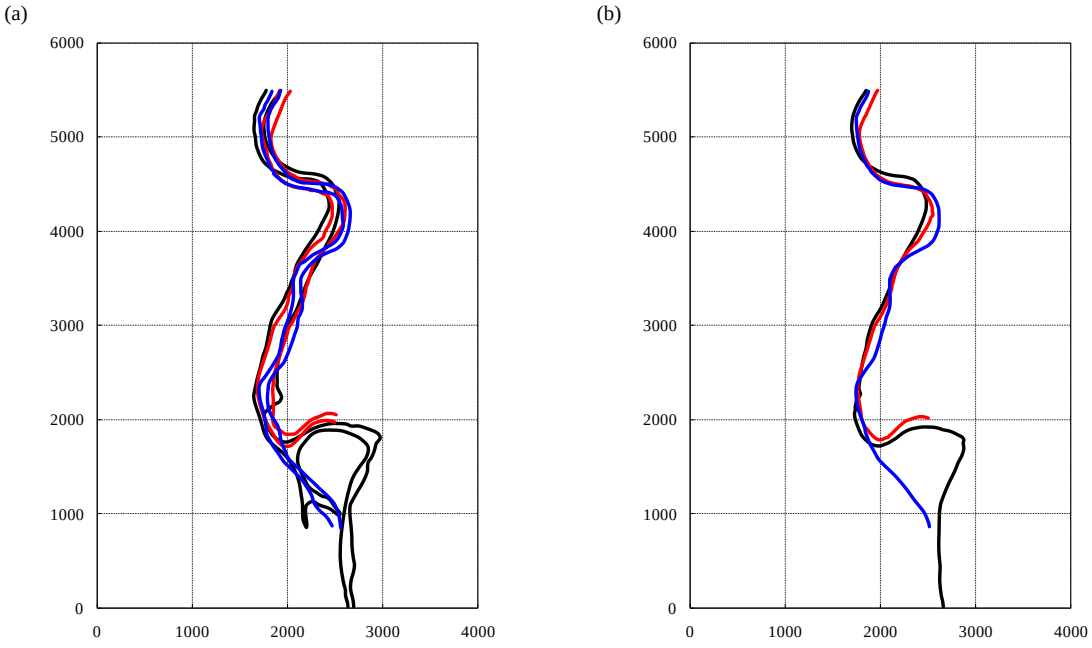

Fig. 70. (a) Banklines; (b) centerlines of Nueces River at US 90, — 1958; — 1969; — 1995

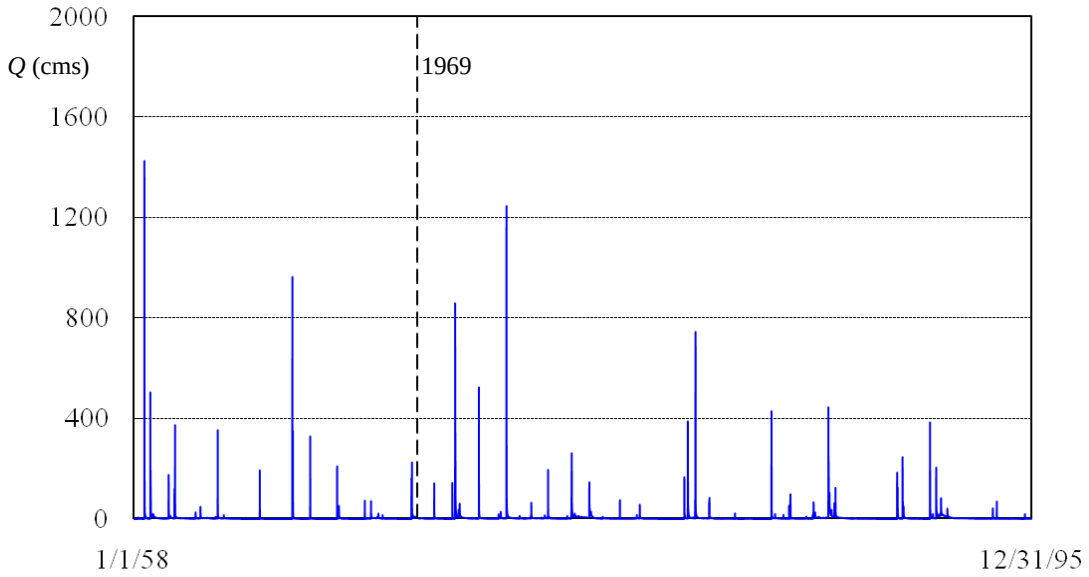

Fig. 71. Daily flowrate records at USGS 08108700

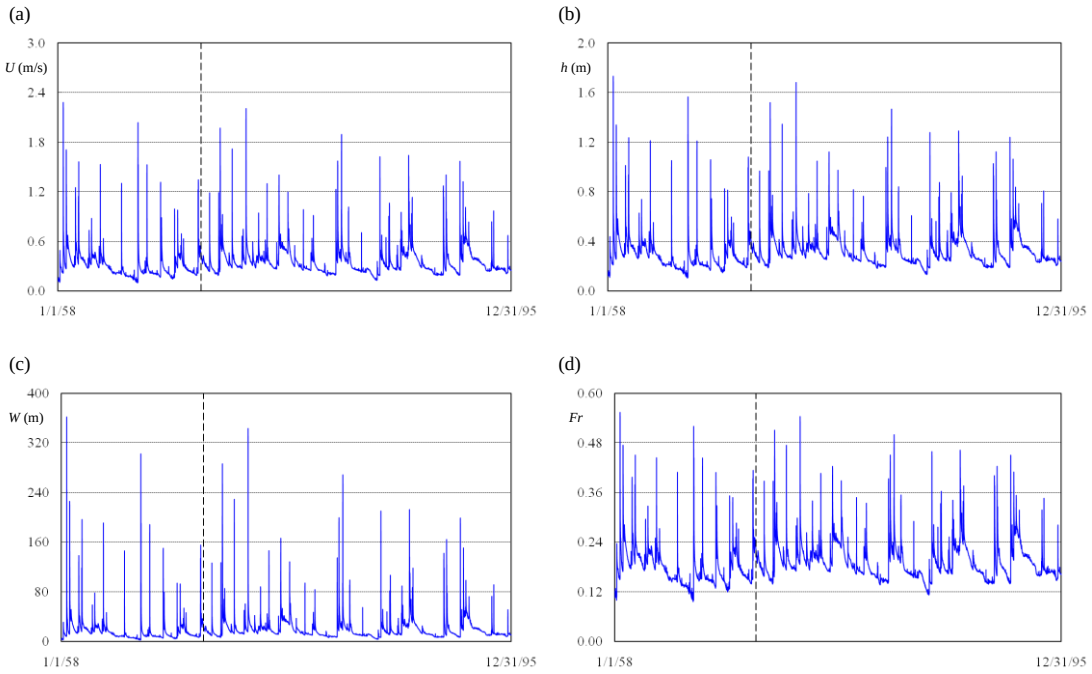

Fig. 72. Flow properties: (a) mean velocity *U*; (b) water depth *h*; (c) channel width *W*; (d) Froude number *Fr* at USGS 08108700

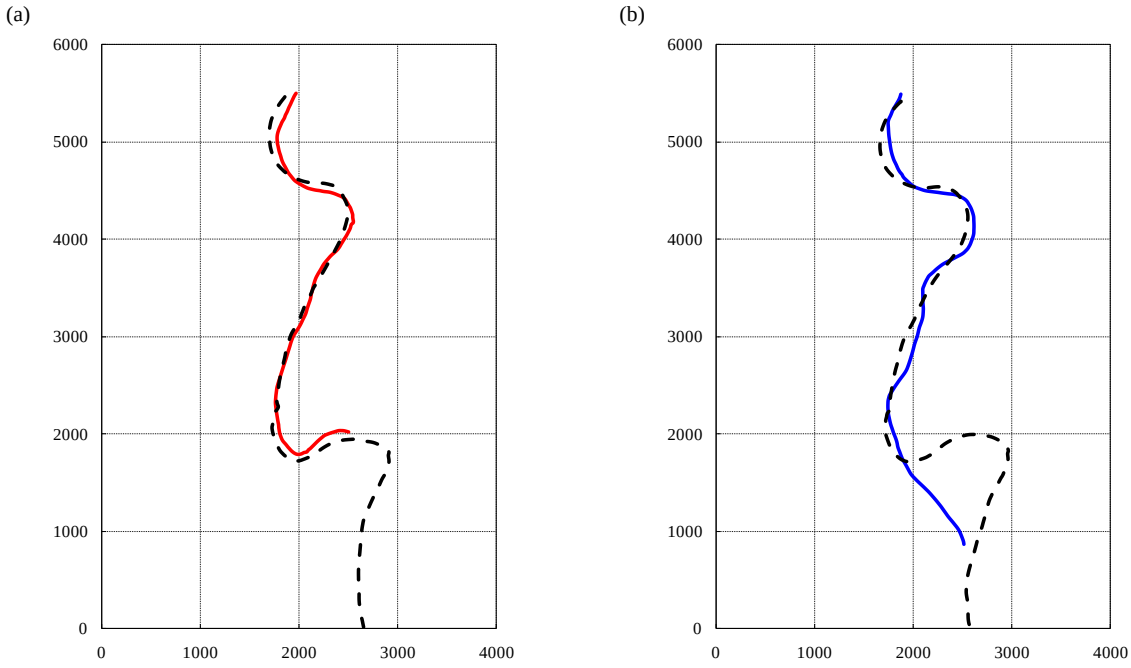

Fig. 73. Centerline simulations of Nueces River at US 90, — 1969; — 1995; -- simulation results

CHAPTER VI

CONCLUSIONS AND FUTURE STUDIES

6.1 Conclusions

This study investigated channel meander migration through large-scale physical model. The migration distance and migration rate of channel bankline and centerline of a sand channel were tested through laboratory experiment. From the dimensional analysis, channel migration distance and rate were affected by radius of curvature to width ratio R/W, band angle Φ, water depth to width ratio h/W and the excess Froude number βFr-Frc. A critical velocity of soil U_c, in stead of critical Shields parameter, was used to represent the soil resistance against flow erosion. Twelve curved and one straight channels with a trapezoidal cross section were molded on the sand bed. By varying the parameters, five different R/W ratios, four different Φ angles and four different flowrates Q were tested. Channel bankline, cross sectional profiles and several hydraulic properties of each time step were measured in the tests.

The morphological behavior of a curved channel under a constant flowrate was examined from both the spatial and temporal aspects. The results show that large migration occurs beyond the outer bank apex and a phase lag exists between the bankline migration and the channel curvature. The channel plan form becomes asymmetric as the migration progresses and the migration is found to contain lateral expansion and downstream translation components. The lateral expansion increases the channel meander width/belt, while the downstream translation stretches the channel length. It is also seen that both banks of the channel undergoes a similar but alternate migration. The temporal variations of the bankline movements has a relatively large migration distance within a short time in the beginning of the test. The bankline migration rate is high and the channel sinuosity also increases rapidly. The migration rate then decreases

gradually as the test proceeds. At the end of the test, the bankline ceases to shift and the channel plan form attains an equilibrium state.

The migration of the channel centerline swings between the two banks and oscillates along the initial channel. The centerline migrates in two opposite moving directions upon the intersection of two consecutive centerlines, which has a zero migration rate. From the bend entrance to the intersection, the centerline moves in centripetal direction, whereas, it moves in centrifugal direction beyond the intersection to the exit of the bend. The channel cross sectional profiles show that the deep pools are formed alternately at the channel outer banks, and point bars are developed in the channel crossings between two curved bends. The thalweg moves sinuously in a path deep in the bends separated by shallow crossings. Due to the phase lag of the thalweg to the channel curvature, the bank erosion and bankline migration also have a phase lag to the channel plan form. This explains the downstream crossings had larger bank migration than the preceded outer bank apexes.

The experimental measurements show that the bankline migration process can be formulated using a hyperbolic function. From the hyperbolic model, the initial migration rate $\dot{M}_i$ and the maximum migration distance M_{max} are fitted with Gaussian distributions. By performing a correlation analysis among the coefficients in the Gaussian distributions and the three controlling parameters, the results show that $\dot{M}_i$ and M_{max} reach a maximum magnitude at $R/W = 4$. For channels with a large bend angle, $\dot{M}_i$ and M_{max} are relatively small and exhibit a bi-modal distribution, and the bankline migration is more uniform and symmetric. Effects due to the hydraulic condition are examined through the excess Froude number. The results show that the initial migration rate $\dot{M}_i$ is in proportion to the Froude number; the channel bankline has a greater initial migration rate with a larger Froude number. However, the channel plan form and the final equilibrium displacement M_{max} are independent of the Froude number.

A prediction method for the channel centerline migration rate and distance is also developed in this study. The intersection of two consecutive centerlines is the inflection point of the migration rate and also the outcome of the channel plan form to the asymmetric migration rate. The phase lag between each inflection point and the bend entrance denotes the degree of translation and rotation in channel morphologic change and is found to be independent of bend curvature and bend angle. The ratio of the phase lag to bend angle decreases as the bend length increases, indicating the tendency of channel straightening in shorter bend with a small curvature. The migration curve length between two successive inflection points is very close to the bend length for curved bends with moderate curvature.

The centerline migration rate exhibits a growth and decay pattern between two successive inflection points and is modeled with a sine function. In a channel with initially symmetric curved bends, the amplitude of migration rate decreases from channel upstream to downstream and also subside with time, showing that a surge of large migration rate propagates towards channel downstream. On the other hand, the migration rate develops with additional loops and propagates from the upstream curved bend on the channel straight reach. The propagation transmits "faster" than the channel curvature as the numbers of the additional loops are more than the numbers of curved bends. The migration rate on the initial curved bend is larger in magnitude and persists some distance on the straight reach due to the curvature change. The amplitude drops rapidly further downstream on the additional loops. The migration rate remains a developing status in the straight reach. More additional loops develop on the downstream straight reach, with the amplitude decays sequentially from last loop of the curved bend with an average 20 % ratio. The migration rate gradually decreases to a uniform state after the whole channel becomes sinuous, results in several curved bends with uniform bend widths and lengths in the end of the test.

The phase lag and migration rate is developed as prediction equations with the flume test results in this study. The channel centerline migration of laboratory experiment and four natural rivers are used to test and validate the current approach. The laboratory results show that the approach is capable of duplicating the migration and deformation of both curved channel with an initially symmetric plan form and a straight channel with an initial curved bend. The discrepancies are mostly due to the effects of downstream back-water or the accumulation in errors on the larger curvature change in the beginning of the test. The validation on natural rivers shows that the prediction equations are applicable to simulate river centerline migration. The calculated river centerlines are in good agreement with the recorded centerlines on the topographic maps. The results from two different scales of topographic maps on the same site of Guadalupe River indicate that the scale effect from different topographic maps on the prediction equations and the simulation is minimal.

6.2 Future Studies

River meander migration is a very complicated phenomenon in nature. It includes the interactions between fluid flow, sediment transport and bank erosion. Different researches focus on different aspects so as different shortage in explanation and prediction of river meander migration. This study first uses a pre-described hyperbolic function to estimate the migration distance of a channel bankline. This method is established on the assumption that channel bankline migration will reach equilibrium under a constant flowrate. Although it's unlikely to have a constant flow rate in real rivers, the hyperbolic function along with the initial migration rate and the maximum migration distance is still a sufficient and convenient tool for predicting channel migration distance. Since flowrate is always varied in natural rivers, further study of this method will be the application on varied flowrate and hydrograph.

The second approach of this study is to predict the channel centerline migration distance through an instantaneous rate. This method normalized the centerline migration rate with river primary mean velocity. The need of a precise streamwise mean velocity distribution affects the accuracy of the prediction and raises the threshold for the data quality demands. The increment of the time step is also a main concern since the migration process is not linear in time. Extending the method from a straight channel to meander bend cut-off will be the next step of this study.

REFERENCES

ASCE Task Committee on Preparation of Sedimentation Manual. (1993). "Closure to 'Sediment transportation mechanics: Initiation of motion.'" *Journal of Hydraulic Division*, 93(5), 297-302.

Briaud, J.-L., Ting, F.C.K., Chen, H.C., Gudavalli, R., Perugu, S., and Wei, G. (1999). "SRICOS: Prediction of scour rate in cohesive soils at bridge piers." *Journal of Geotechnical and Geoenvironmental Engineering*, 125(4), 237-246.

Brice, J. C. (1982). "Stream channel stability assessment." *Report - FHWA/RD-82/021*, Federal Highway Administration, U.S. Department of Transportation, Washington, D.C.

Carson, M. A., and Lapointe, M. F. (1983). "The inherent asymmetry of river meander planform." *Journal of Geology*, 91, 41-45.

Carstens, M. R. (1966). "An analytical and experimental study of bed ripples under water waves." *Quarterly Reports 8 and 9*, School of Civil Engineering, Georgia Institute of Technology, Atlanta, GA.

Chang, H. H. (1984). "Regular meander path model." *Journal of Hydraulic Engineering*, 110(10), 1398-1411.

Chang, H. H. (1988). *Fluvial processes in river engineering*, Wiley, New York.

Corps of Engineers (1970). "Hydraulic design of flood control channels." *EM 1110-2-1601*, Department of Army, Washington, D.C.

Darby, S. E., Alabyan, A. M., and de Wiel, M. J. V. (2002). "Numerical simulation of bank erosion and channel migration in meandering rivers." *Water Resources Research*, 38(9), 1163.

Dietrich, W. E., and Smith, J. D. (1983). "Influence of the point bar on flow through curved channels." *Water Resources Research*, 19(5), 1173-1192.

Duan, J. G. and P. Julien (2005). "Numerical simulation of the inception of meandering channel." *Earth Surface Processes and Landforms*, 30, 1093-1110.

Ferguson, R. I. (1983). "Kinematic model of meander migration." *River Meandering*: *Proceedings of the Conference, Rivers '83*, New Orleans, 942-951.

Fortier, S. and Scobey, F. C. (1926). "Permissible canal velocities." *Transactions ASCE*, 89, No. 1588, 940-984.

Friedkin, J. F. (1945). *A laboratory study of the meandering of alluvial rivers*, War Department, Corps of Engineers, U.S. Army Mississippi River Commission, U.S. Waterways Experimental Station, Vicksburg, Mississippi.

Hasegawa, K. (1981). "Bank erosion discharge based on a non-equilibrium theory." *Proceedings, JSCE*, Tokyo, Japan, 316, 37-50.

Hasegawa, K. (1989). "Universal bank erosion coefficient for meandering rivers." *Journal of Hydraulic Engineering*, 115(6), 414-442.

Hickin, E. J. (1974). "The development of meanders in natural river-channels." *American Journal of Science*, 274(4), 414-442.

Hickin, E. J. (1983). "River channel changes: retrospect and prospect." *Modern and ancient fluvial systems*, International association of sedimentologists special publication, 6, 61-83.

Hickin, E. J., and Nanson, G. C. (1975). "The character of channel migration on the Beatton River, Northeast British Columbia, Canada." *Geological Society of America Bulletin*, 86(4), 487-494.

Hickin, E. J., and Nanson, G. C. (1984). "Lateral migration rates of river bends." *Journal of Hydraulic Engineering*, 110(11), 1557-1567.

Hjulstrom, F. (1935). “Studies of the morphological activity of rivers as illustrated by the River Fyris.” *Bulletin, Geological Institute of Uppsala,* Vol. XXV, Uppsala, Sweden.

Hooke, J. M. (1980). “Magnitude and distribution of rates of river bank erosion.” *Earth Surface Processes*, 5, 143-157.

Howard, A. D., and Knutson, T. R. (1984). “Sufficient conditions for river meandering: A simulation approach.” *Water Resources Research*, 20(11), 1659-1667.

Ippen, T., and Drinker, P. A. (1962). “Boundary shear stresses in curved trapezoidal channels.” *Journal of Hydraulic Division*, 88(5), 143-179.

Ikeda, S., Parker, G., and Sawai, K. (1981). “Bend theory of river meanders. Part I: Linear development.” *Journal of Fluid Mechanics*, 112, 363-377.

Johannesson, H. and Parker, G. (1989). “Linear theory of river meanders.” *River Meandering, Water Resour. Monogr. Ser.*, 12, 181-214.

Keady, D. M., and Priest, M. S. (1977). “The downstream migration rate of river meandering patterns.” *Proceedings, 12th Mississippi Water Resources Conference*, Jackson, Mississippi, 29-34.

Leopold, L. B. (1994). *A view of the river*. Cambridge University Press, Cambridge, U.K., 128.

Mavis, F. T., and Laushey, L. M. (1949). “Formula for velocity at beginning of bed-load movement is reappraised.” *Civil Engineering*, 19, 38-39 & 72.

Mehrota, S. C. (1983). “Permissible velocity correction factors.” *Journal of Hydraulic Engineering*, 109(2), 305-308.

Moura, L., and Kitney, R. (1991). “A direct method for least-squares circle fitting.” *Computer Physics Communications*, 64, 57-63.

Munson, B. R., Young, D. F., and Okiishi, T. H. (2006). *Fundamentals of fluid mechanics*, 5th Ed., Wiley, New York.

Nanson, G. C., and Hickin, E. J. (1983). "Channel migration and incision on the Beatton River." *Journal of Hydraulic Engineering*, 109(3), 327-337.

Nanson, G. C., and Hickin, E. J. (1986). "A statistical analysis of bank erosion and channel migration in western Canada." *Geological Society of America Bulletin*, 97, 497-504.

Nagata, N., Hosoda, T. and Muramoto, Y. (2000). "Numerical analysis of river channel processes with bank erosion." *Journal of Hydraulic Engineering*, 126(4), 243-252.

Nakagawa, H., and Tsujimoto, T. (1980). "Sand bed instability due to bed load motion." *Journal of Hydraulic Division*, 106(12), 2029-2051.

Neill, C. R. (1967). "Mean velocity criterion for scour of coarse uniform bed material." *Proceedings of the 12th Congress*, IAHR, Fort Collins, CO, 46-54.

Odgaard, A. J. (1987). "Streambank erosion along two rivers in Iowa." *Water Resources Research*, 23(7), 1225-1236.

Odgaard, A. J. (1989). "River-meander model. I: Development." *Journal of Hydraulic Engineering*, 115(11), 1433-1450.

Osman, A. M. and Thorne, C. R. (1988). "Riverbank stability analysis. I: Theory." *Journal of Hydraulic Engineering*, 114(2), 134-150.

Parker, G., Sawai, K., and Ikeda, S. (1982). "Bend theory of river meanders. Part II: nonlinear deformation of finite amplitude bends." *Journal of Fluid Mechanics*, 115, 303-314.

Parker, G. (1983). "Theory of meander bend deformation." *River Meandering: Proceedings, Rivers '83 Conference*, New York, 772-732.

Rozovskii, I. L. (1957). "Flow of water fin bends of open channels." The Academy of Sciences of the Ukrainian SSR, translated from Russian by the Israel Program for Scientific Translations, Jerusalem, Israel, 1961.

Thorne, C. R., Zevenbergen, L. W., Pitlick, J. C., Rais, S., Bradley, J. B., and Julien, P. Y. (1985). "Direct measurements of secondary currents in a meandering sand-bed river." *Nature*, 316(6022), 746-747.

Yen, C., and Yen, B. C. (1971). "Water surface configuration in channel bends." *Journal of Hydraulic Division*, 97(2), 303-321.

APPENDIX A

CHANNEL BANKLINE MIGRATION

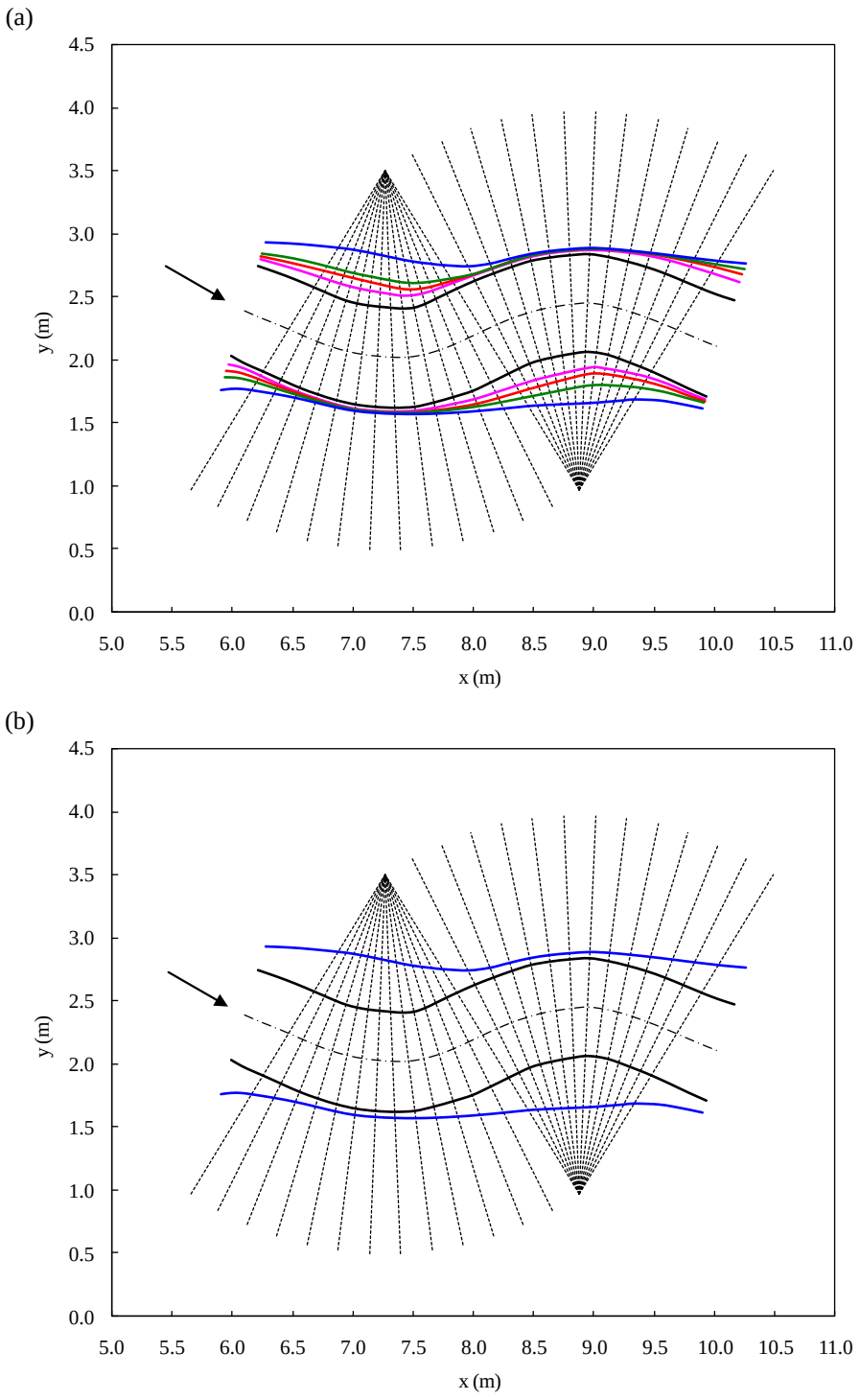

A-1. Channel Bankline Migration of Case 01: (a) — 0 hr; — 3 hr; — 6 hr; — 9 hr; — 18 hr; (b) — 0 hr; — 18 hr

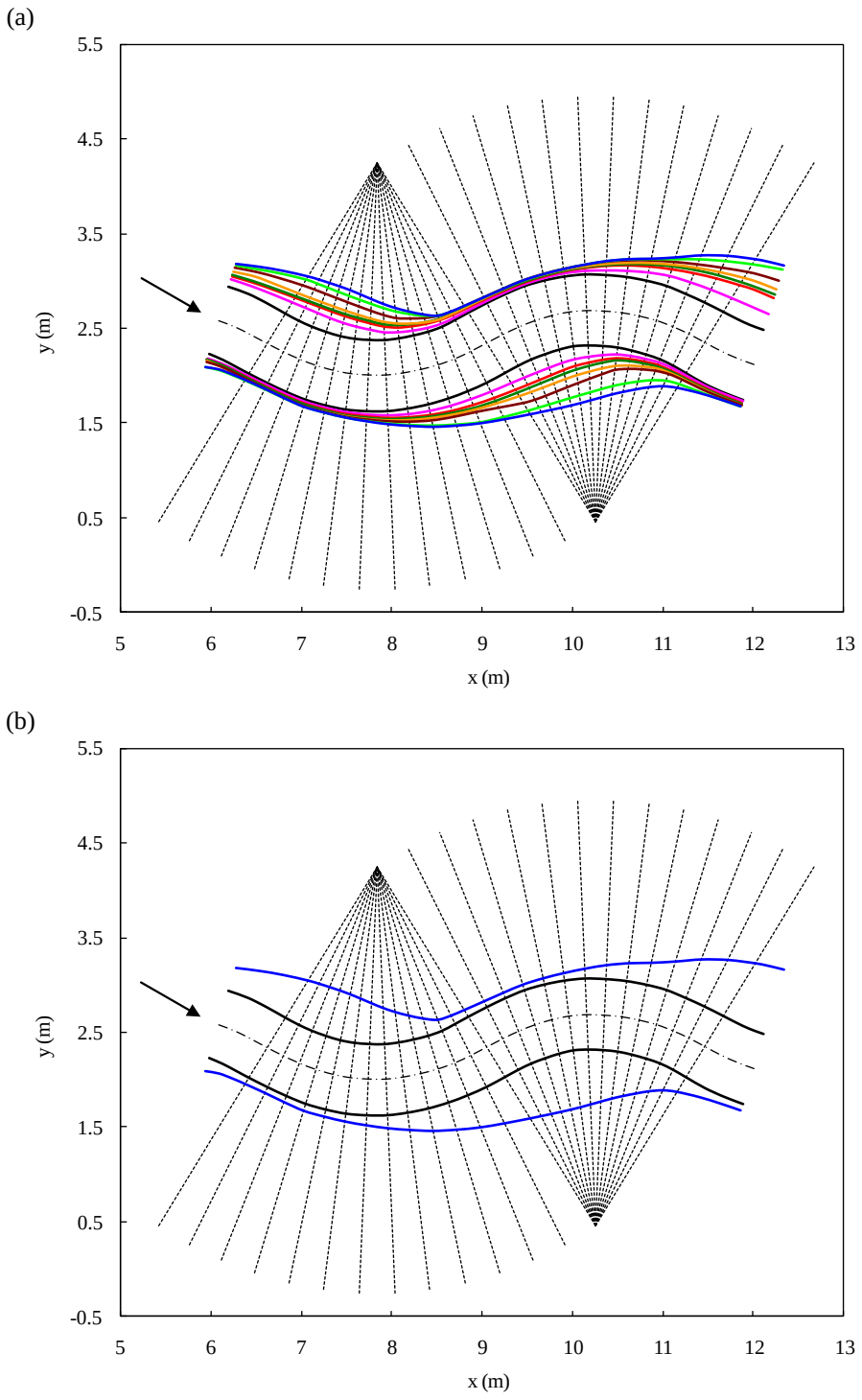

A-2. Channel Bankline Migration of Case 02: (a) — 0 hr; — 3 hr; — 9 hr; — 15 hr; — 24 hr; — 33 hr; — 42 hr; (b) — 0 hr; — 42 hr

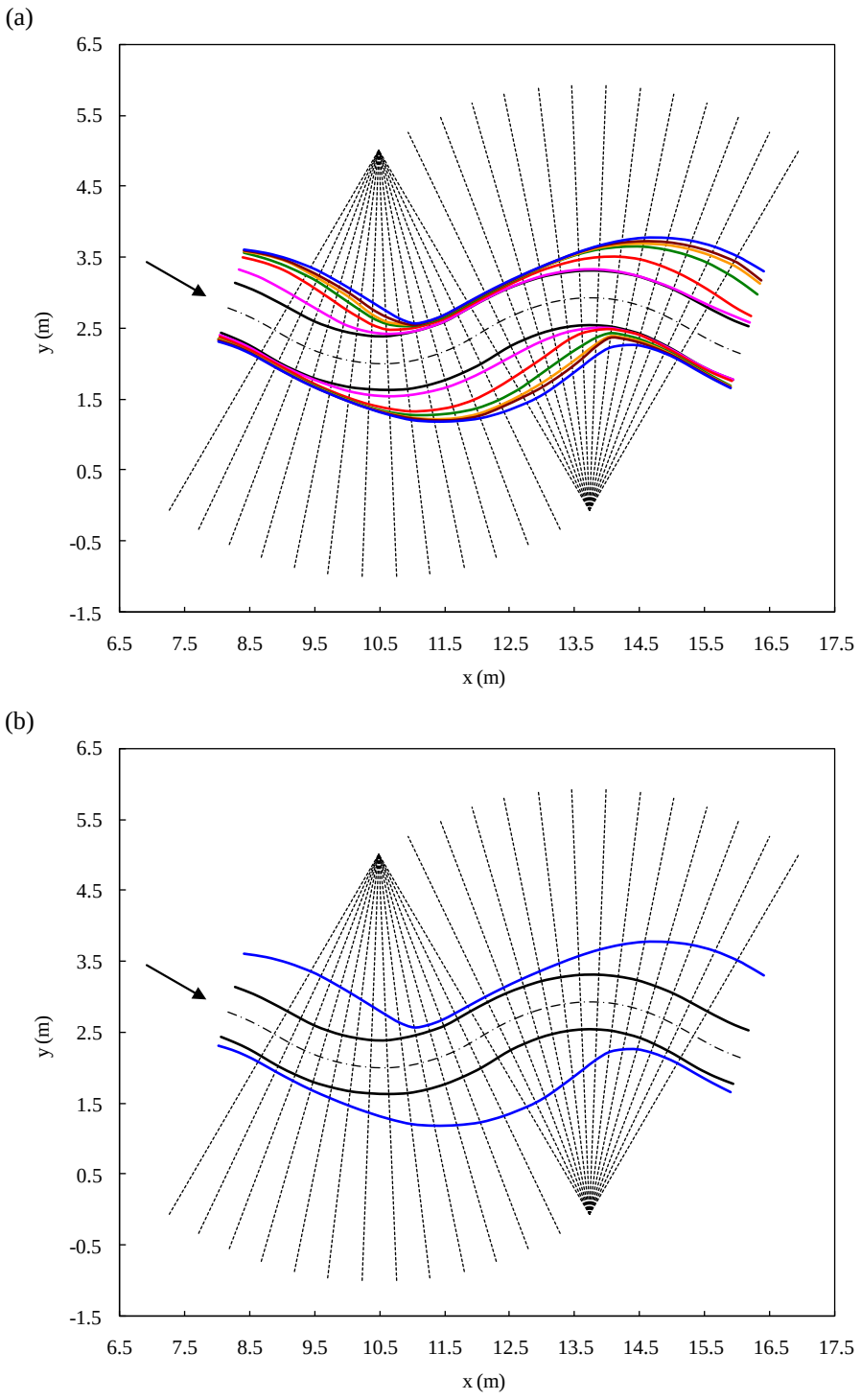

A-3. Channel Bankline Migration of Case 03: (a) — 0 hr; — 3 hr; — 6 hr; — 9 hr; — 15 hr; — 21 hr; — 39 hr; (b) — 0 hr; — 39 hr

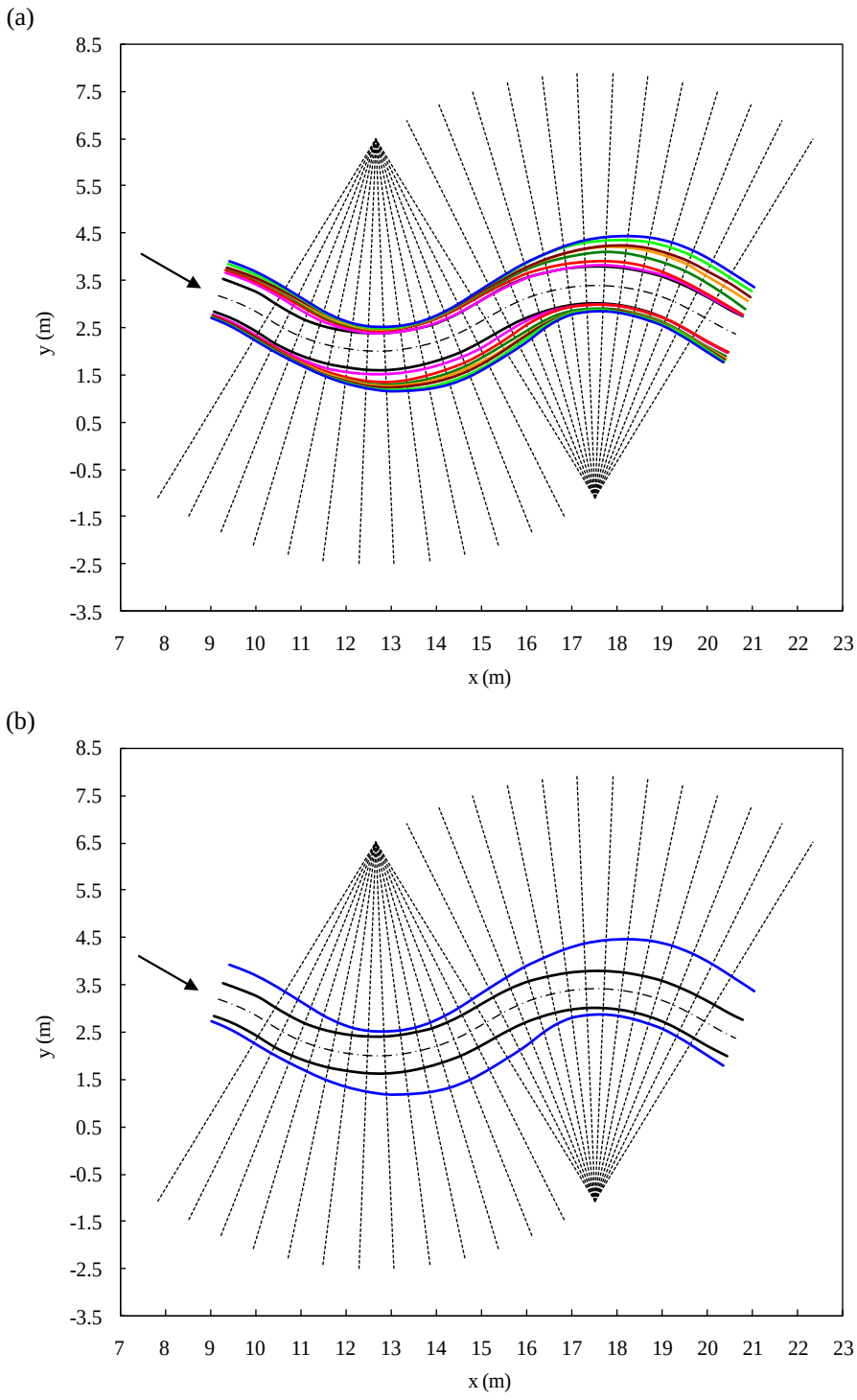

A-4. Channel Bankline Migration of Case 04: (a) — 0 hr; — 3 hr; — 6 hr; — 9 hr; — 15 hr; — 22 hr; — 34 hr; — 45 hr; (b) — 0 hr; — 45 hr

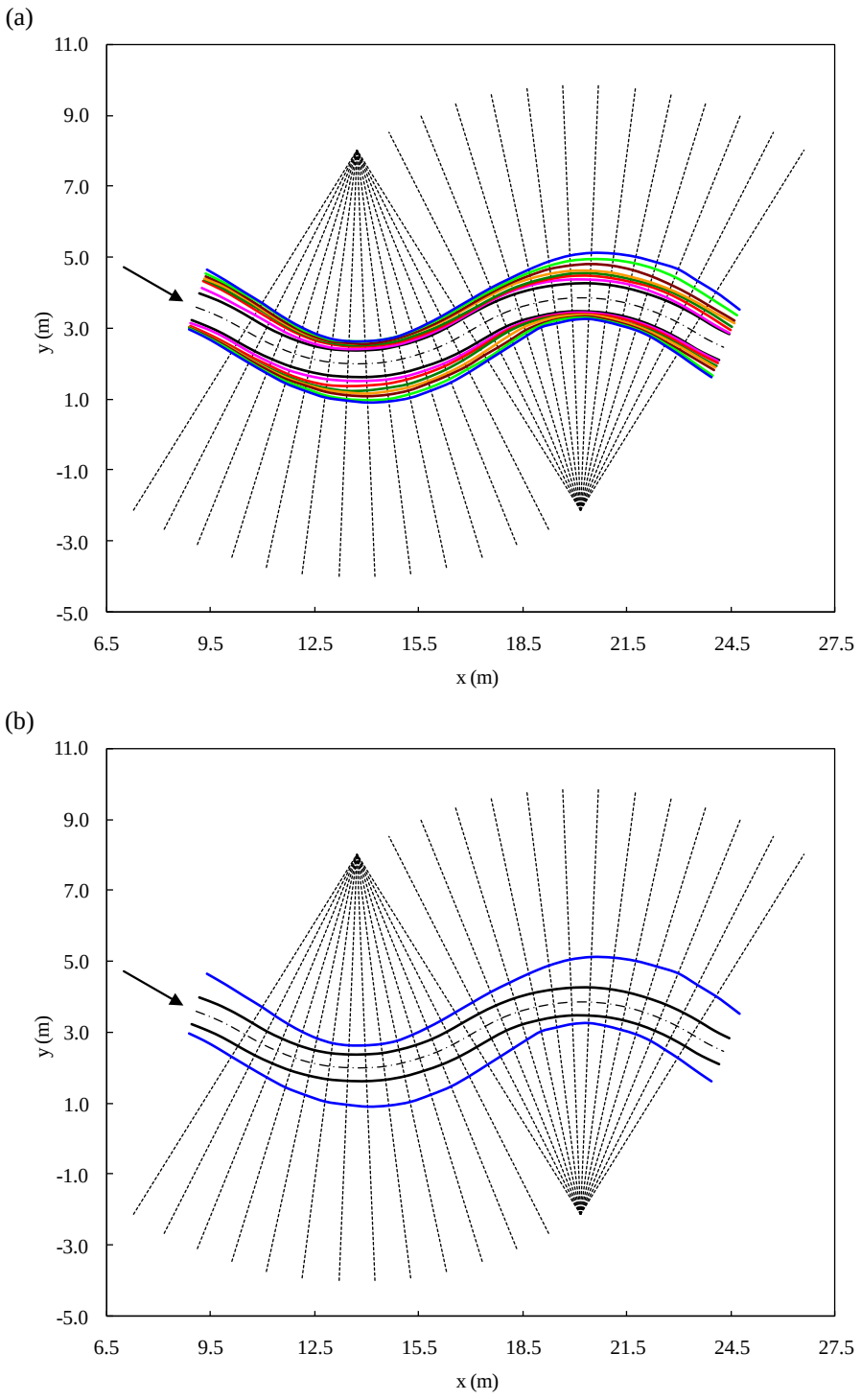

A-5. Channel Bankline Migration of Case 05: (a) — 0 hr; — 3 hr; — 6 hr; — 9 hr; — 15 hr; — 24 hr; — 42 hr; — 66 hr; (b) — 0 hr; — 66 hr

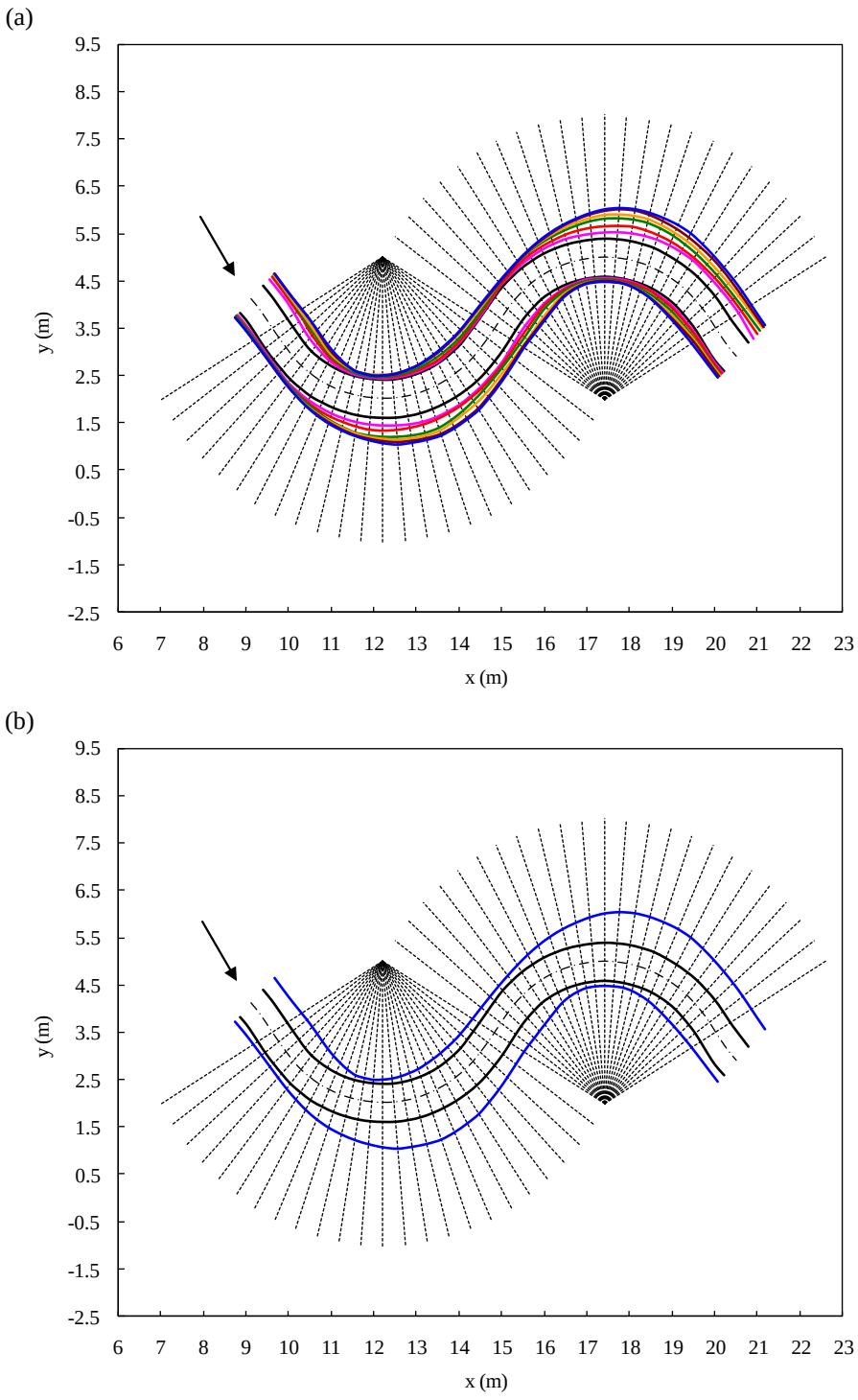

A-6. Channel Bankline Migration of Case 06: (a) — 0 hr; — 3 hr; — 6 hr; — 12 hr; — 18 hr; — 24 hr; — 30 hr; (b) — 0 hr; — 30 hr

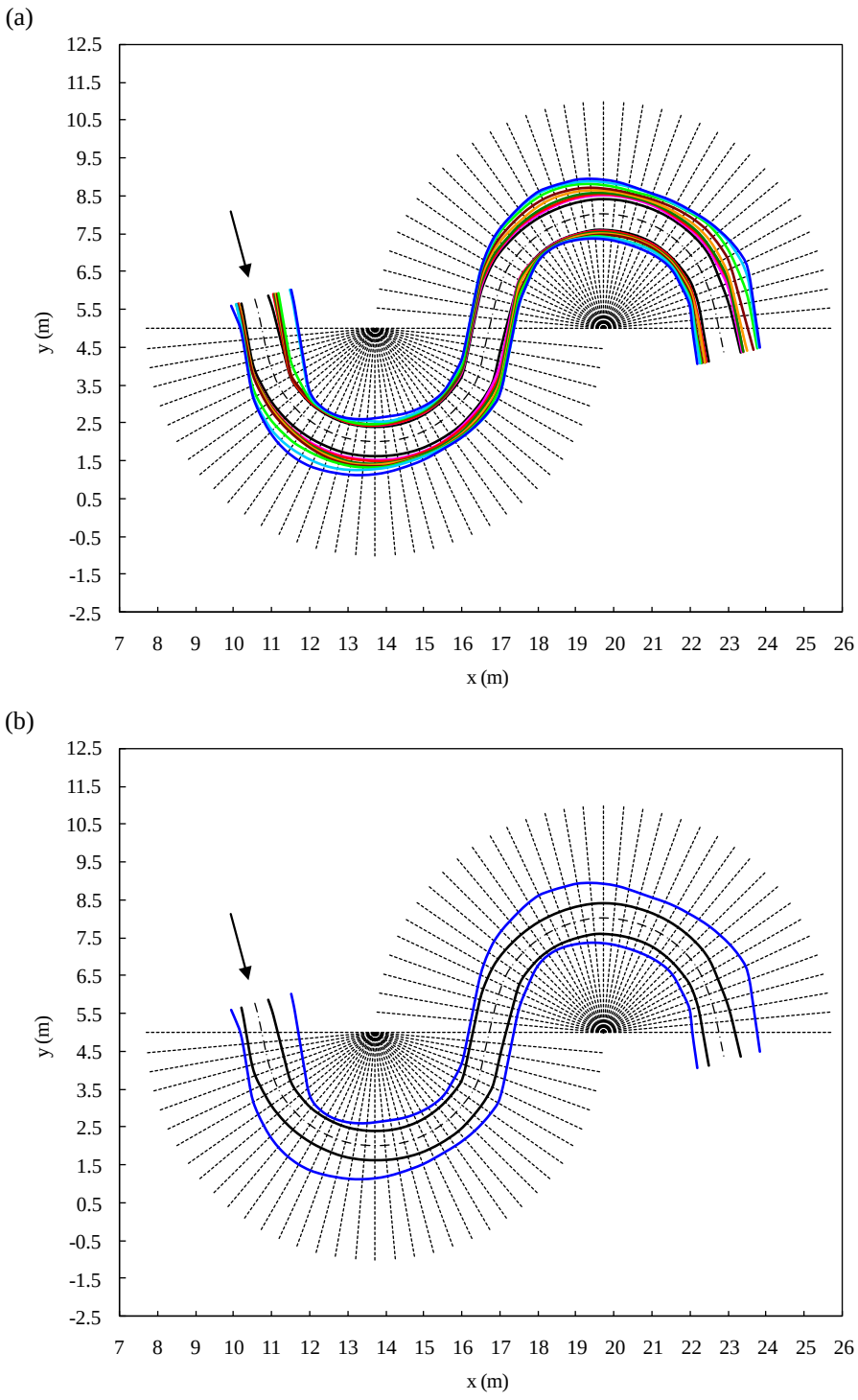

A-7. Channel Bankline Migration of Case 07: (a) — 0 hr; — 3 hr; — 6 hr; — 15 hr; — 24 hr; — 36 hr; — 48 hr; — 66 hr; — 86 hr; (b) — 0 hr; — 86 hr

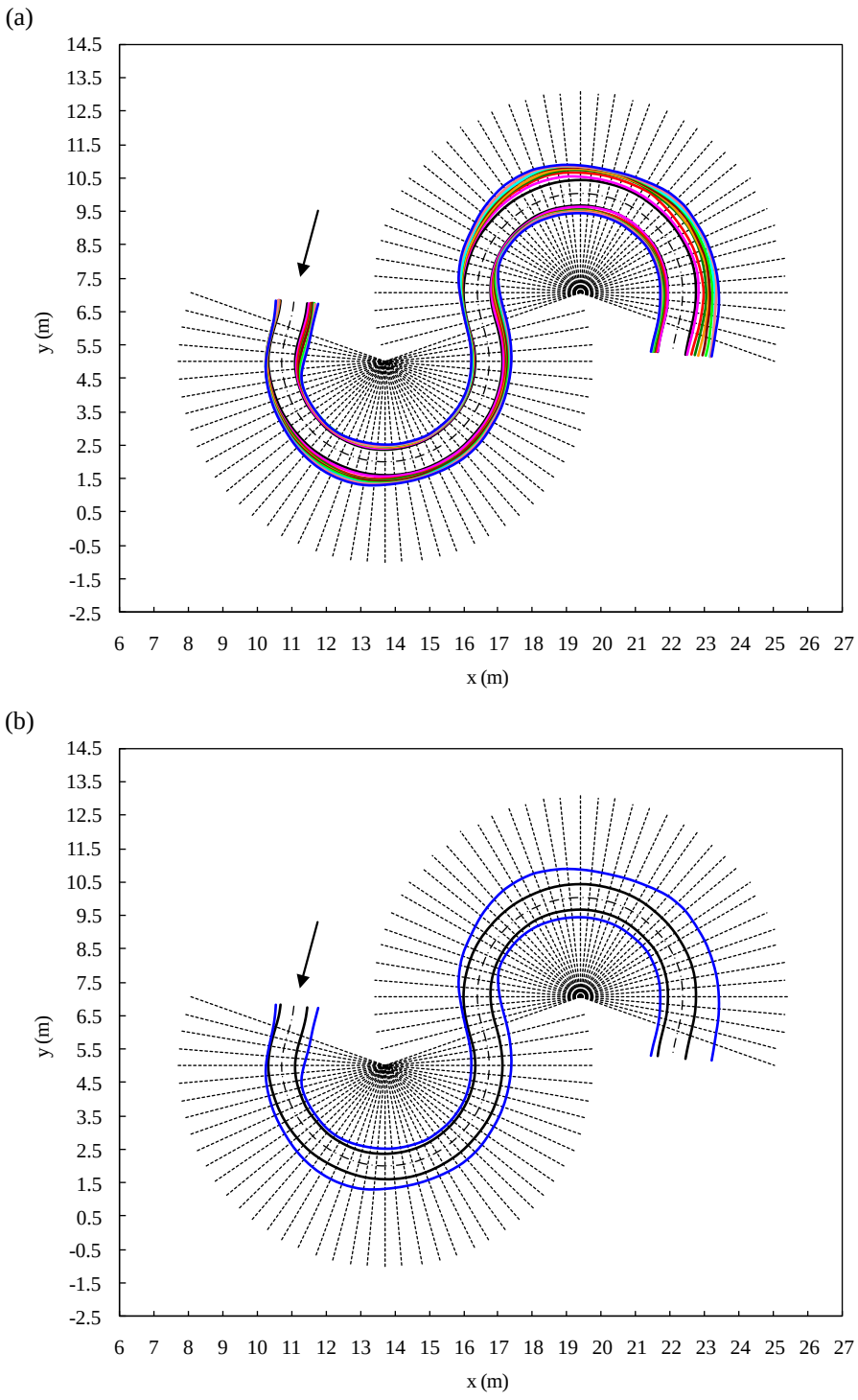

A-8. Channel Bankline Migration of Case 08: (a) — 0 hr; — 3 hr; — 9 hr; — 18 hr; — 30 hr; — 48 hr; — 69 hr; — 96 hr; — 123 hr; — 147 hr; (b) — 0 hr; — 147 hr

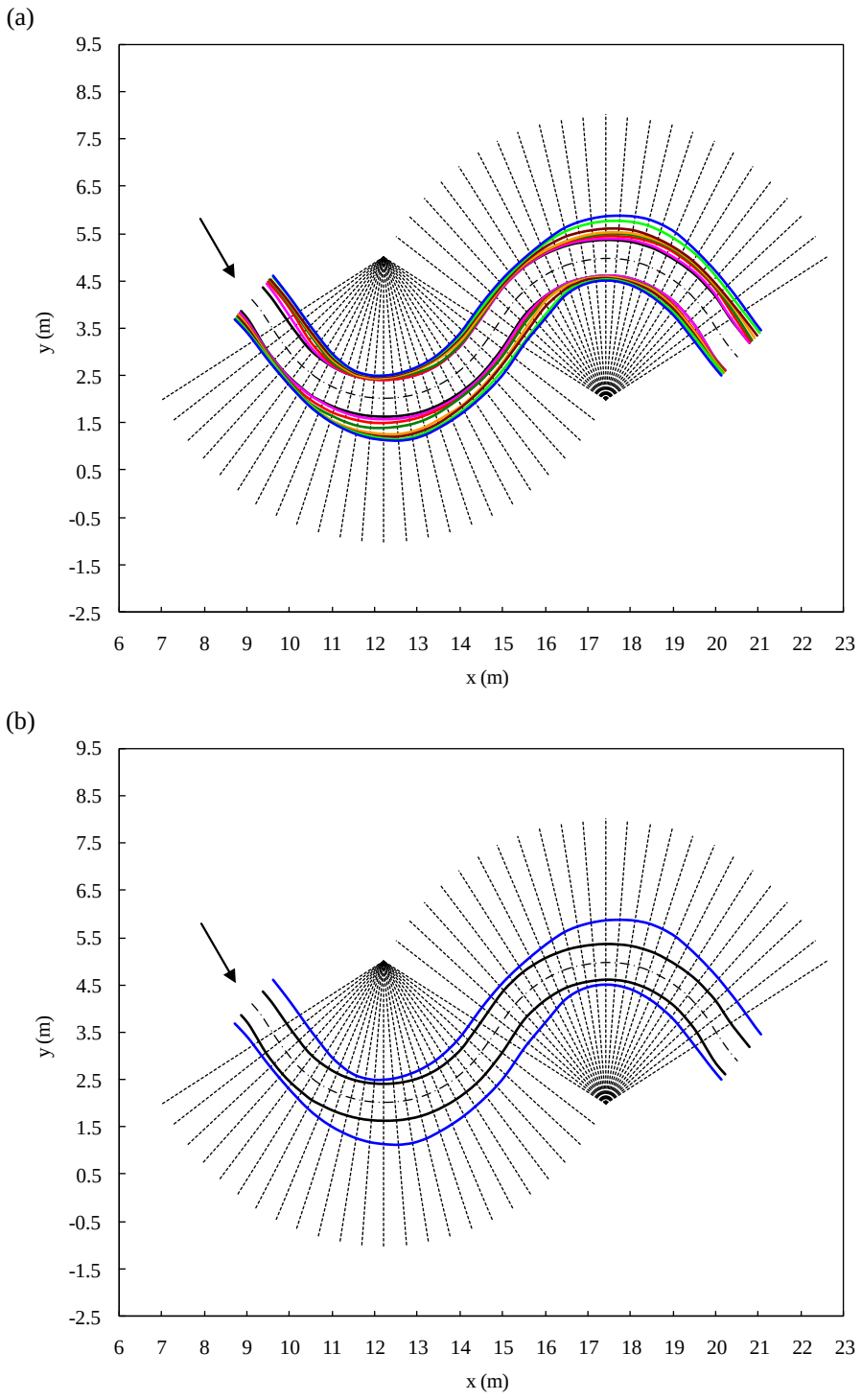

A-9. Channel Bankline Migration of Case 09: (a) — 0 hr; — 4 hr; — 10 hr; — 16 hr; — 24 hr; — 32 hr; — 44 hr; — 56 hr; (b) — 0 hr; — 56 hr

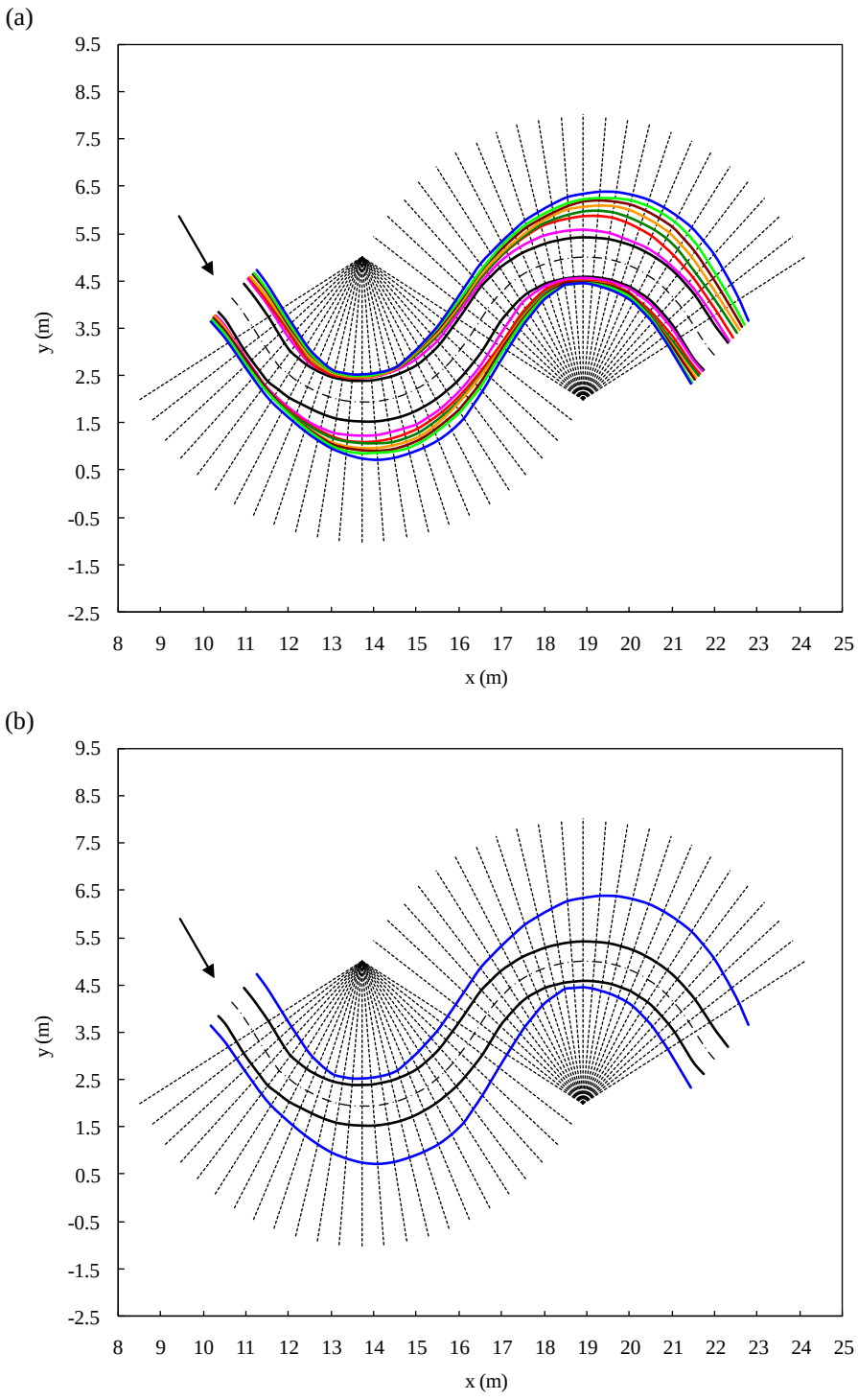

A-10. Channel Bankline Migration of Case 10: (a) — 0 hr; — 3 hr; — 6 hr; — 9 hr; — 15 hr; — 21 hr; — 27 hr; — 39 hr; (b) — 0 hr; — 39 hr

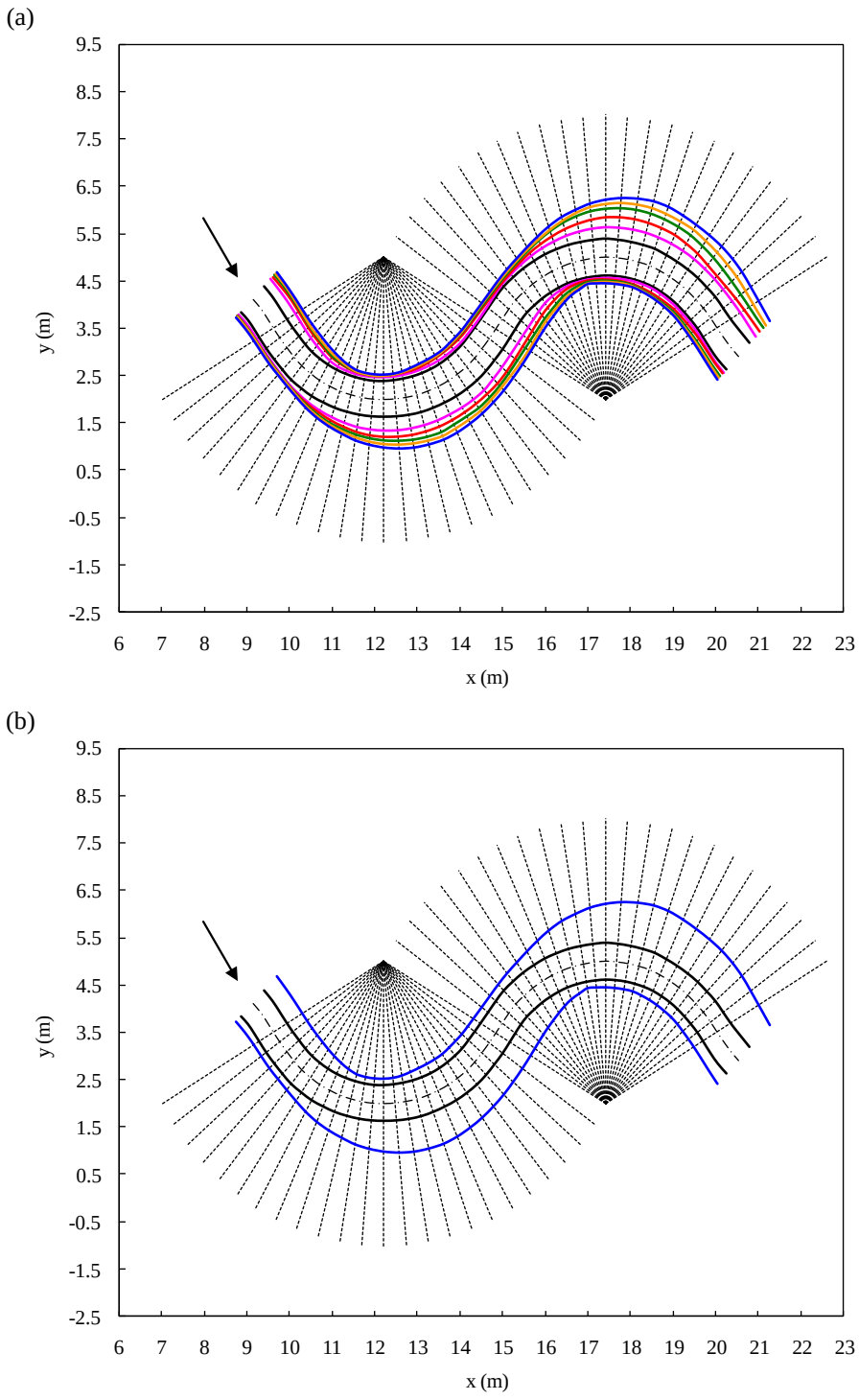

A-11. Channel Bankline Migration of Case 11: (a) — 0 hr; — 2 hr; — 5 hr; — 9 hr; — 14 hr; — 23 hr; (b) — 0 hr; — 23 hr

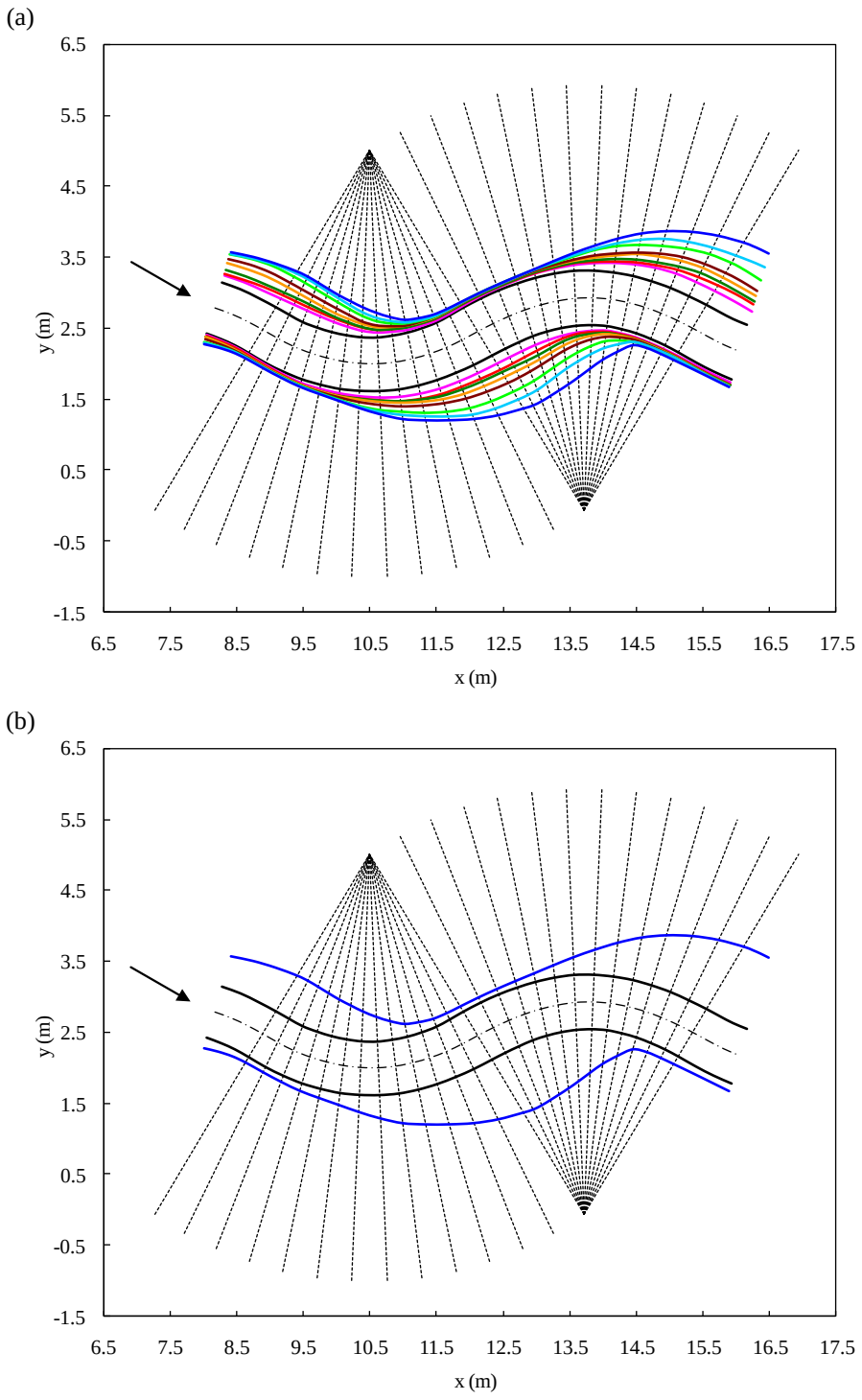

A-12. Channel Bankline Migration of Case 12: (a) — 0 hr; — 3 hr; — 6 hr; — 9 hr; — 15 hr; — 21 hr; — 33 hr; (b) — 0 hr; — 33 hr

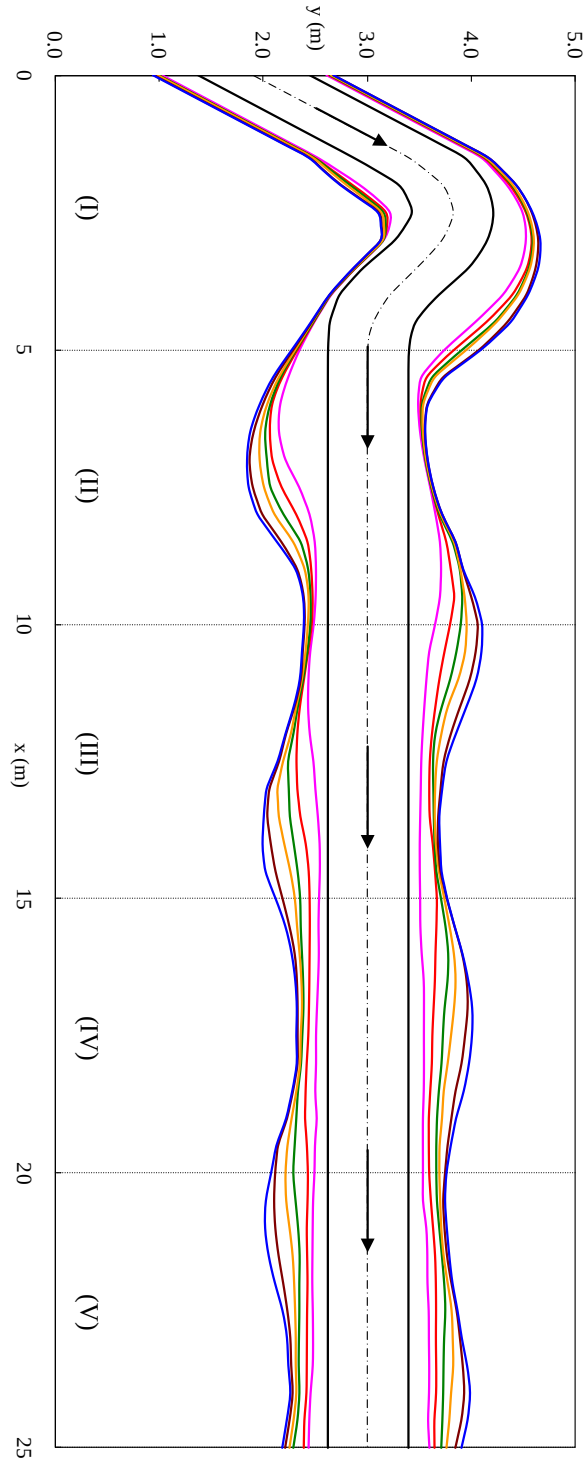

A-13. Channel Bankline Migration of Case 13: — 0 hr; — 3 hr; — 6 hr; — 12 hr; — 18 hr; — 28 hr; — 38 hr

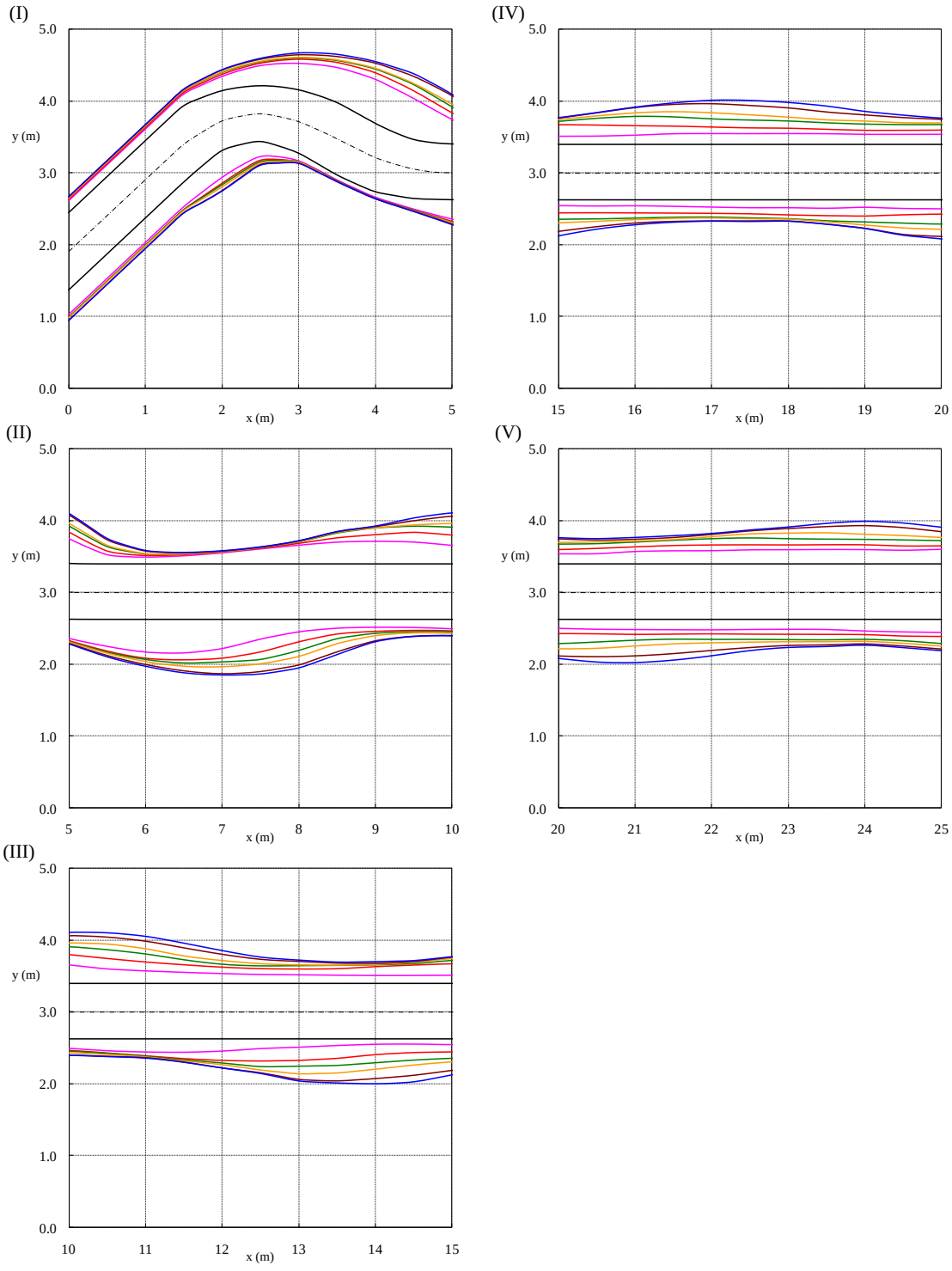

A-13. (Continued)

APPENDIX B

CHANNEL CENTERLINE MIGRATION

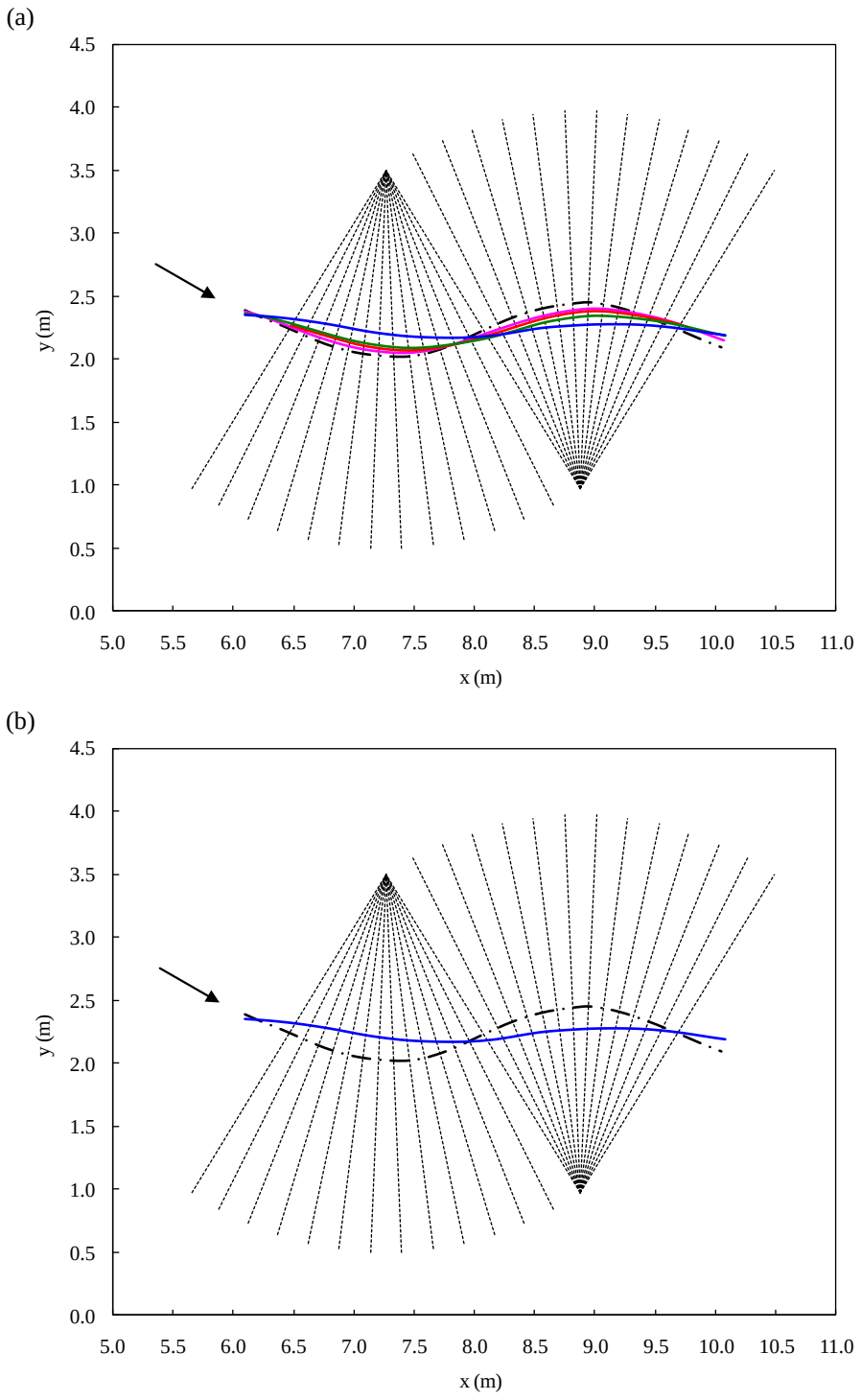

B-1. Channel Centerline Migration of Case 01: (a) — 0 hr; — 3 hr; — 6 hr; — 9 hr; — 18 hr; (b) — 0 hr; — 18 hr

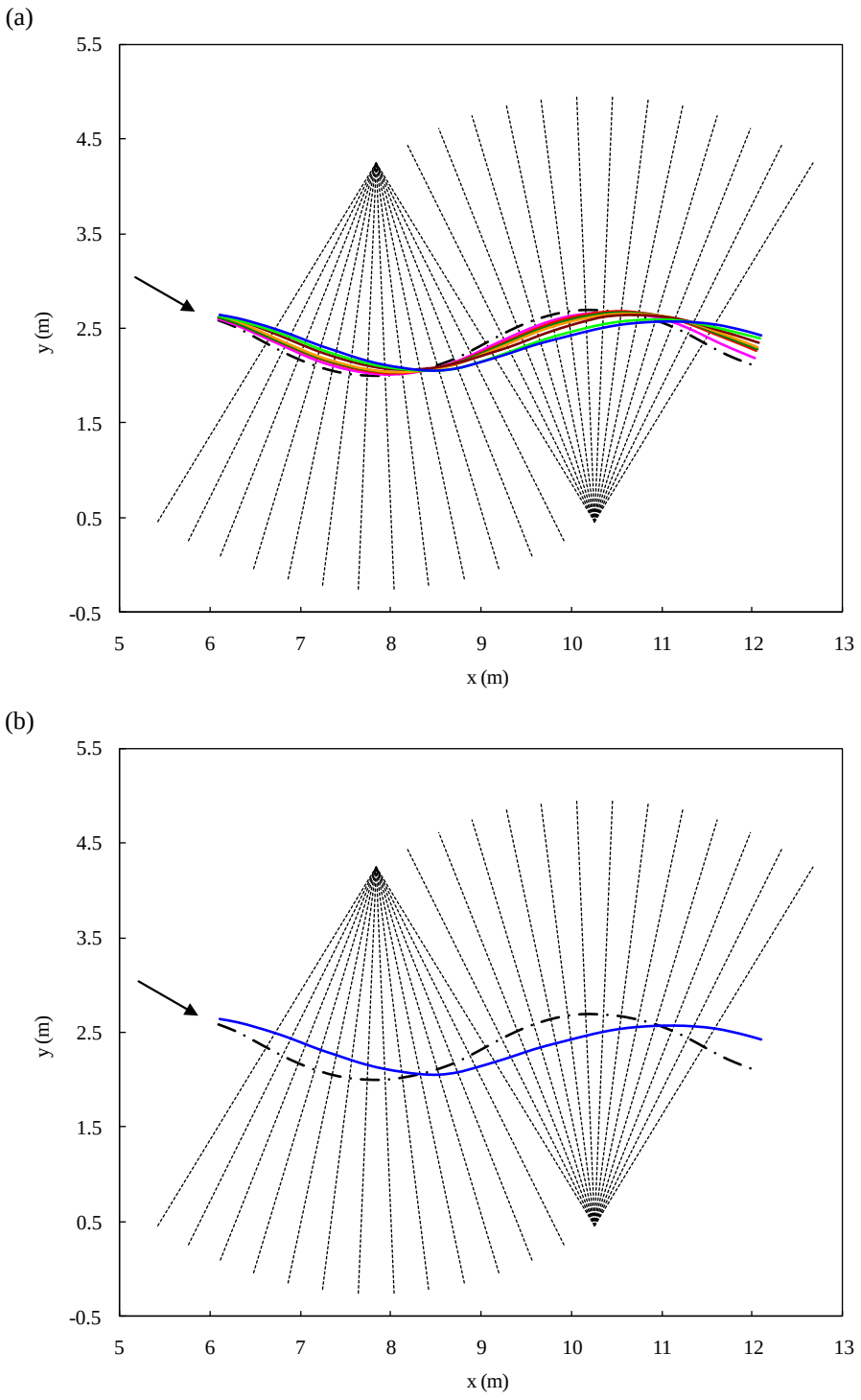

B-2. Channel Centerline Migration of Case 02: (a) — 0 hr; — 3 hr; — 9 hr; — 15 hr; — 24 hr; — 33 hr; — 42 hr; (b) — 0 hr; — 42 hr

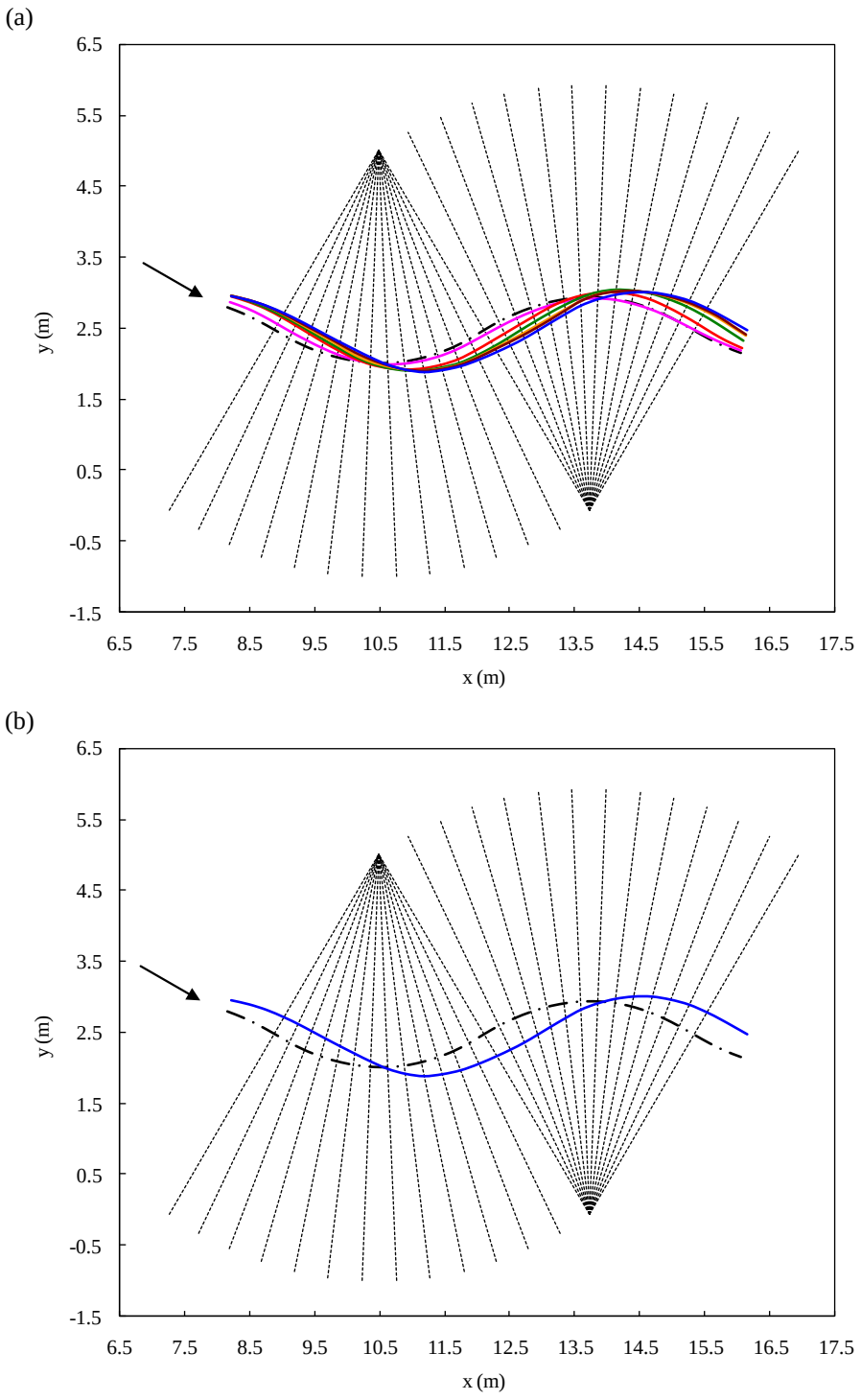

B-3. Channel Centerline Migration of Case 03: (a) — 0 hr; — 3 hr; — 6 hr; — 9 hr; — 15 hr; — 21 hr; — 39 hr; (b) — 0 hr; — 39 hr

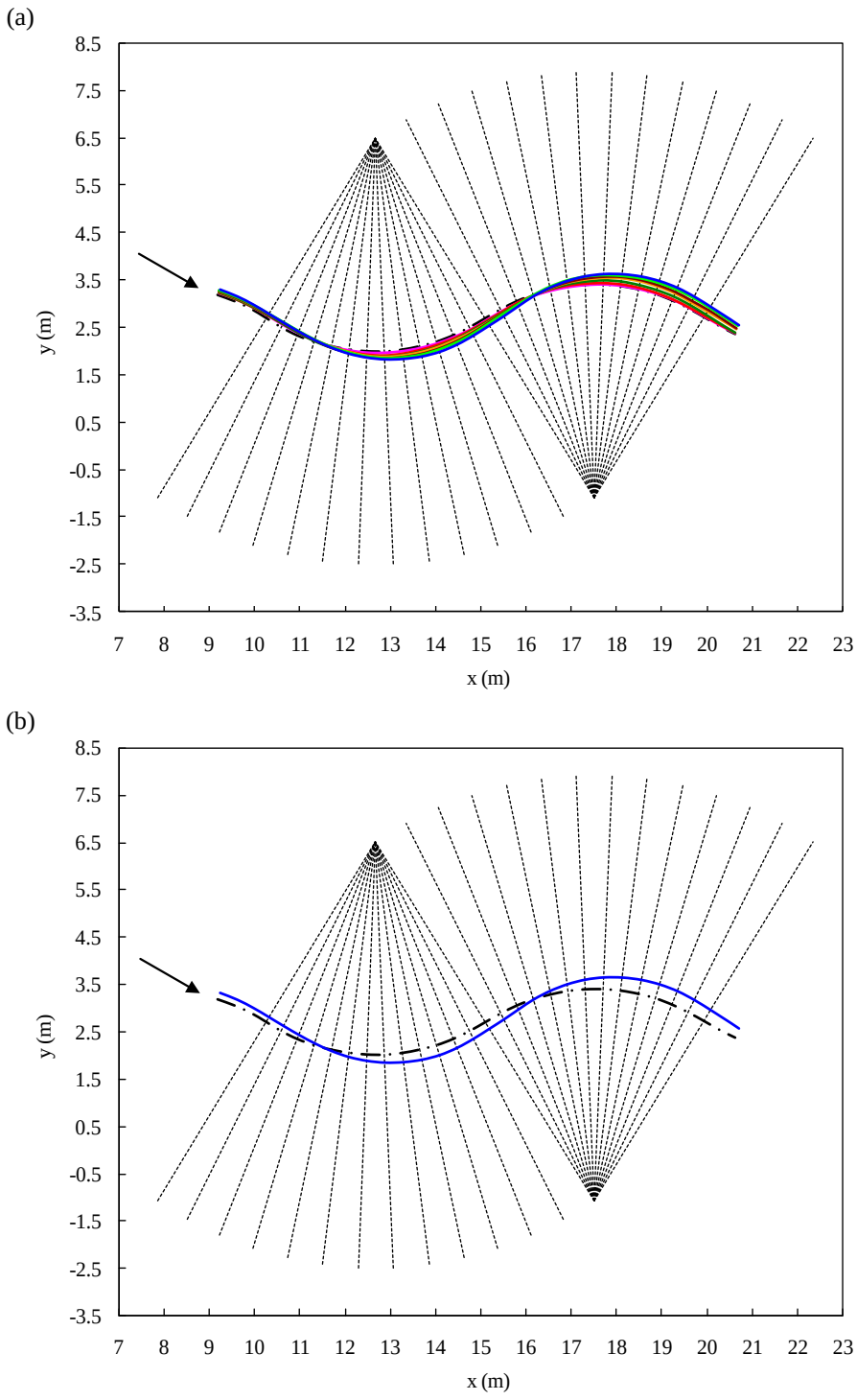

B-4. Channel Centerline Migration of Case 04: (a) — 0 hr; — 3 hr; — 6 hr; — 9 hr; — 15 hr; — 22 hr; — 34 hr; — 45 hr; (b) — 0 hr; — 45 hr

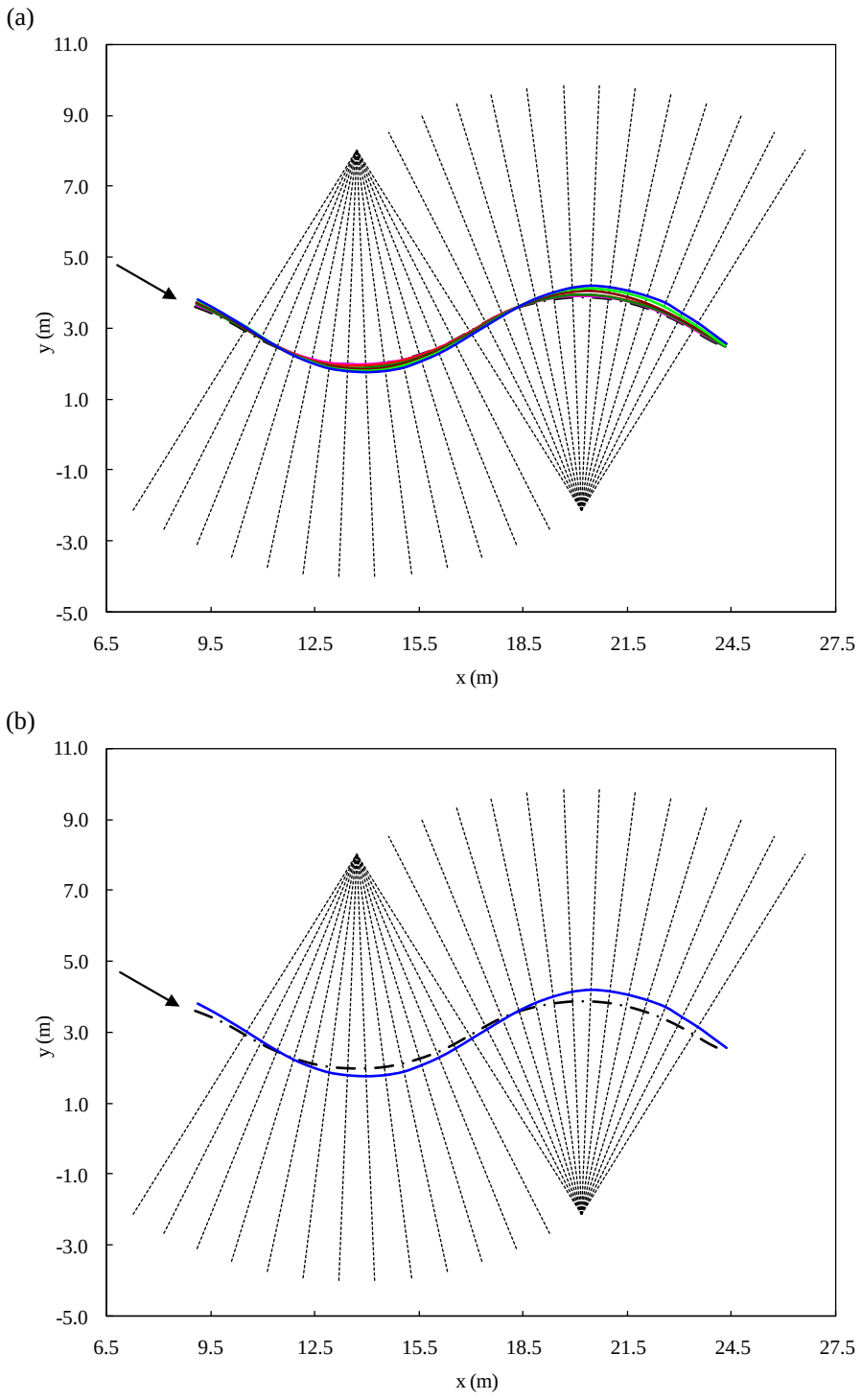

B-5. Channel Centerline Migration of Case 05: (a) — 0 hr; — 3 hr; — 6 hr; — 9 hr; — 15 hr; — 24 hr; — 42 hr; — 66 hr; (b) — 0 hr; — 66 hr

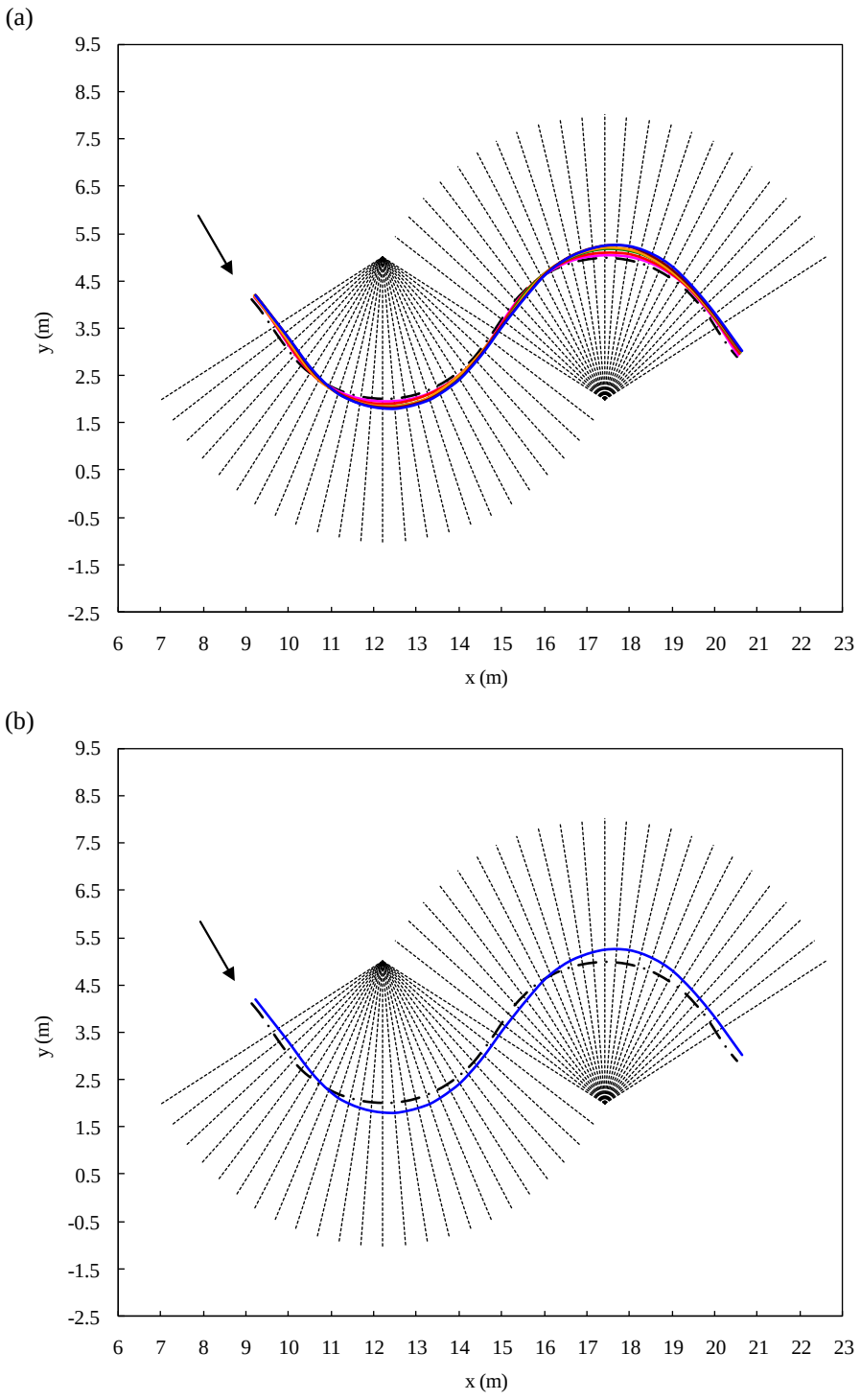

B-6. Channel Centerline Migration of Case 06: (a) — 0 hr; — 3 hr; — 6 hr; — 12 hr; — 18 hr; — 24 hr; — 30 hr; (b) — 0 hr; — 30 hr

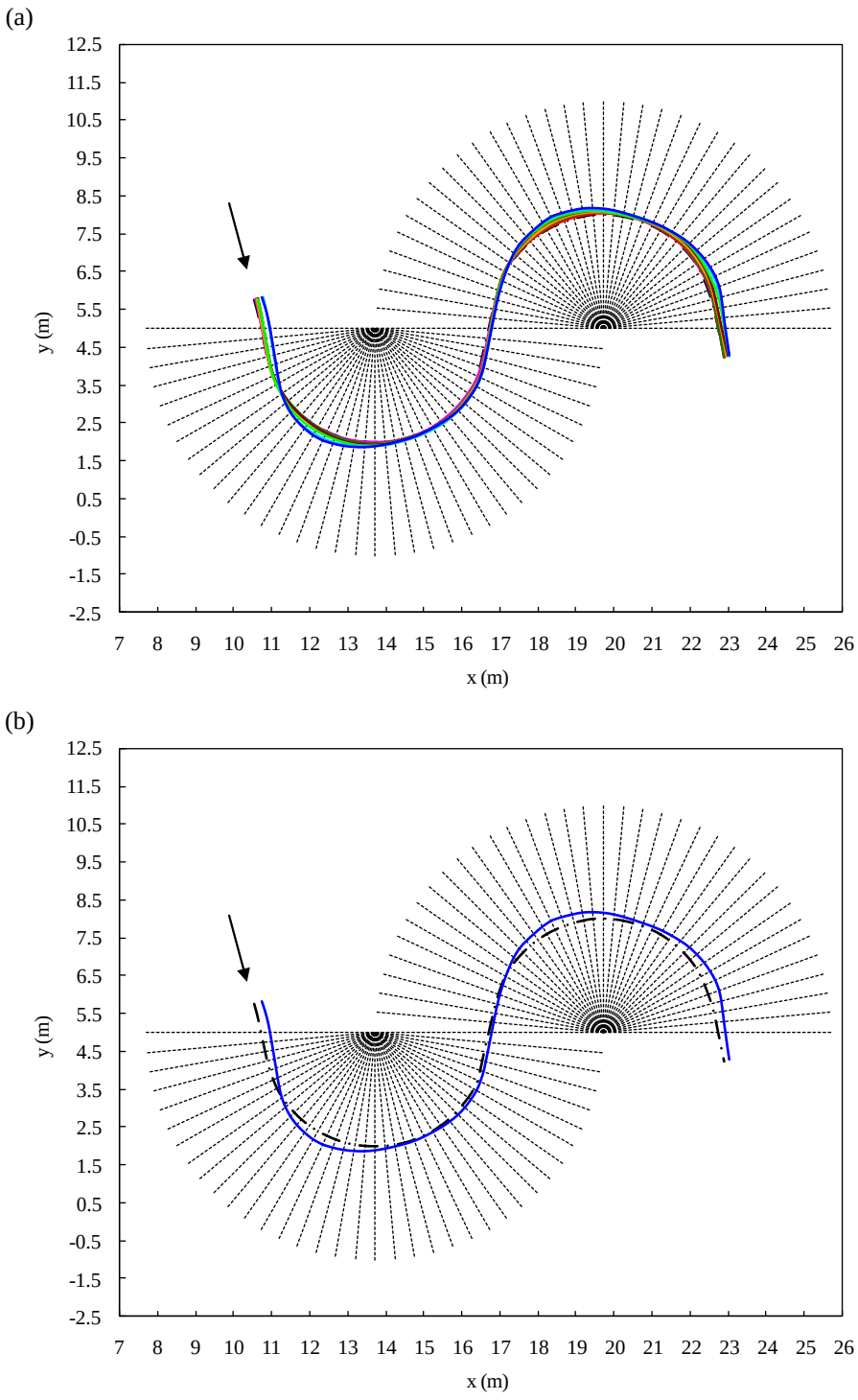

B-7. Channel Centerline Migration of Case 07: (a) — 0 hr; — 3 hr; — 6 hr; — 15 hr; — 24 hr; — 36 hr; — 48 hr; — 66 hr; — 86 hr; (b) — 0 hr; — 86 hr

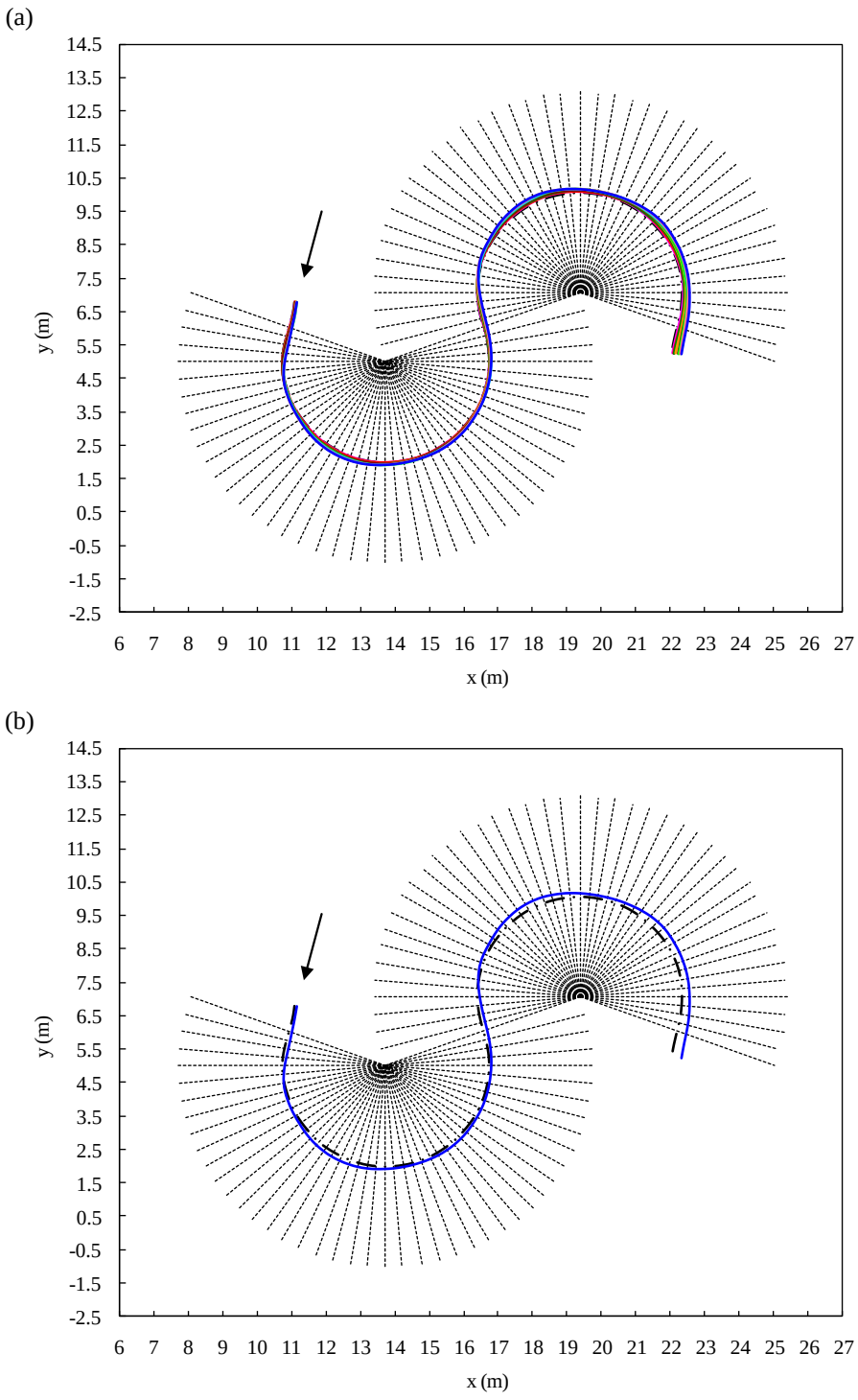

B-8. Channel Centerline Migration of Case 08: (a) — 0 hr; — 3 hr; — 9 hr; — 18 hr; — 30 hr; — 48 hr; — 69 hr; — 96 hr; — 123 hr; — 147 hr; (b) — 0 hr; — 147 hr

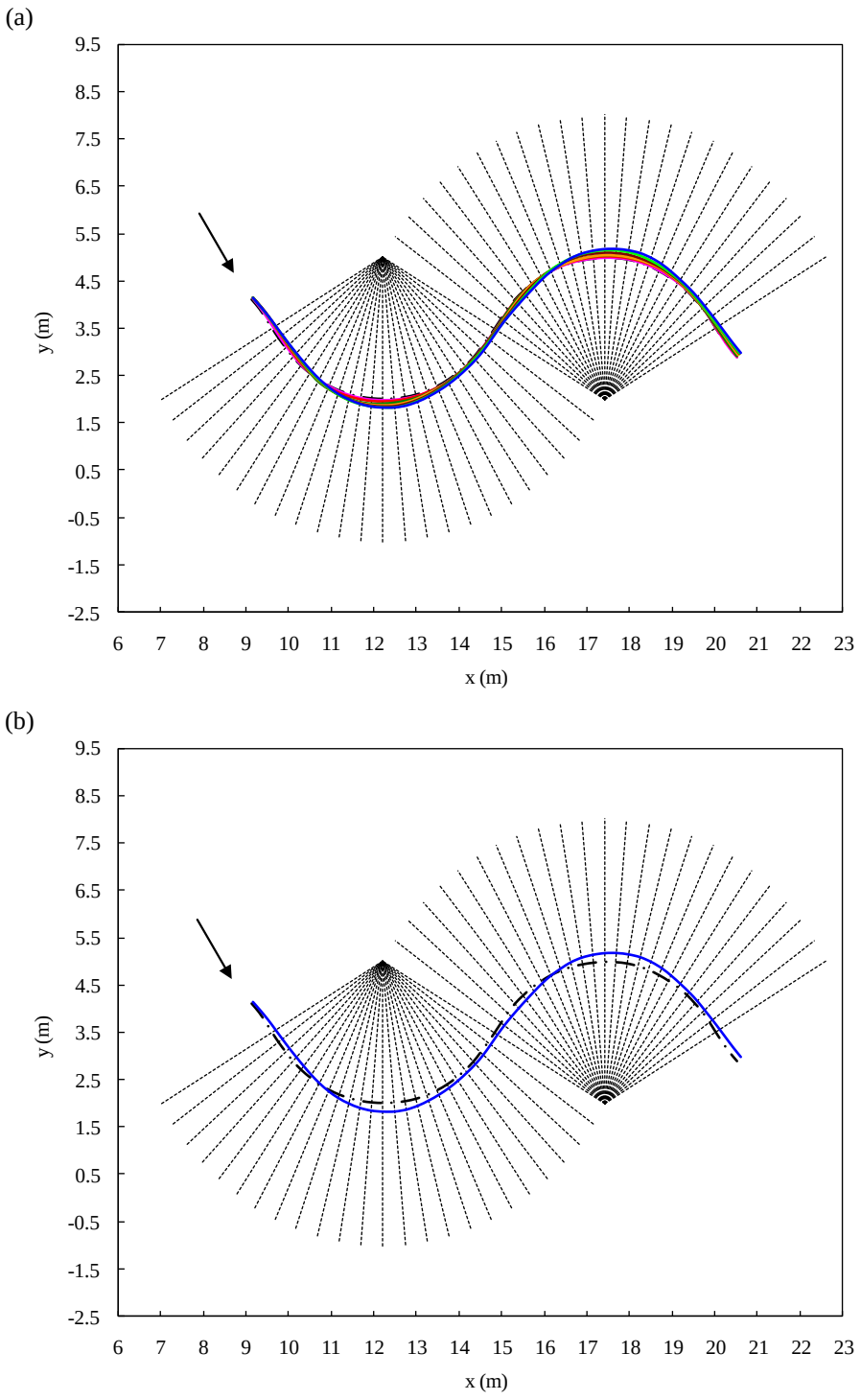

B-9. Channel Centerline Migration of Case 09: (a) — 0 hr; — 4 hr; — 10 hr; — 16 hr; — 24 hr; — 32 hr; — 44 hr; — 56 hr; (b) — 0 hr; — 56 hr

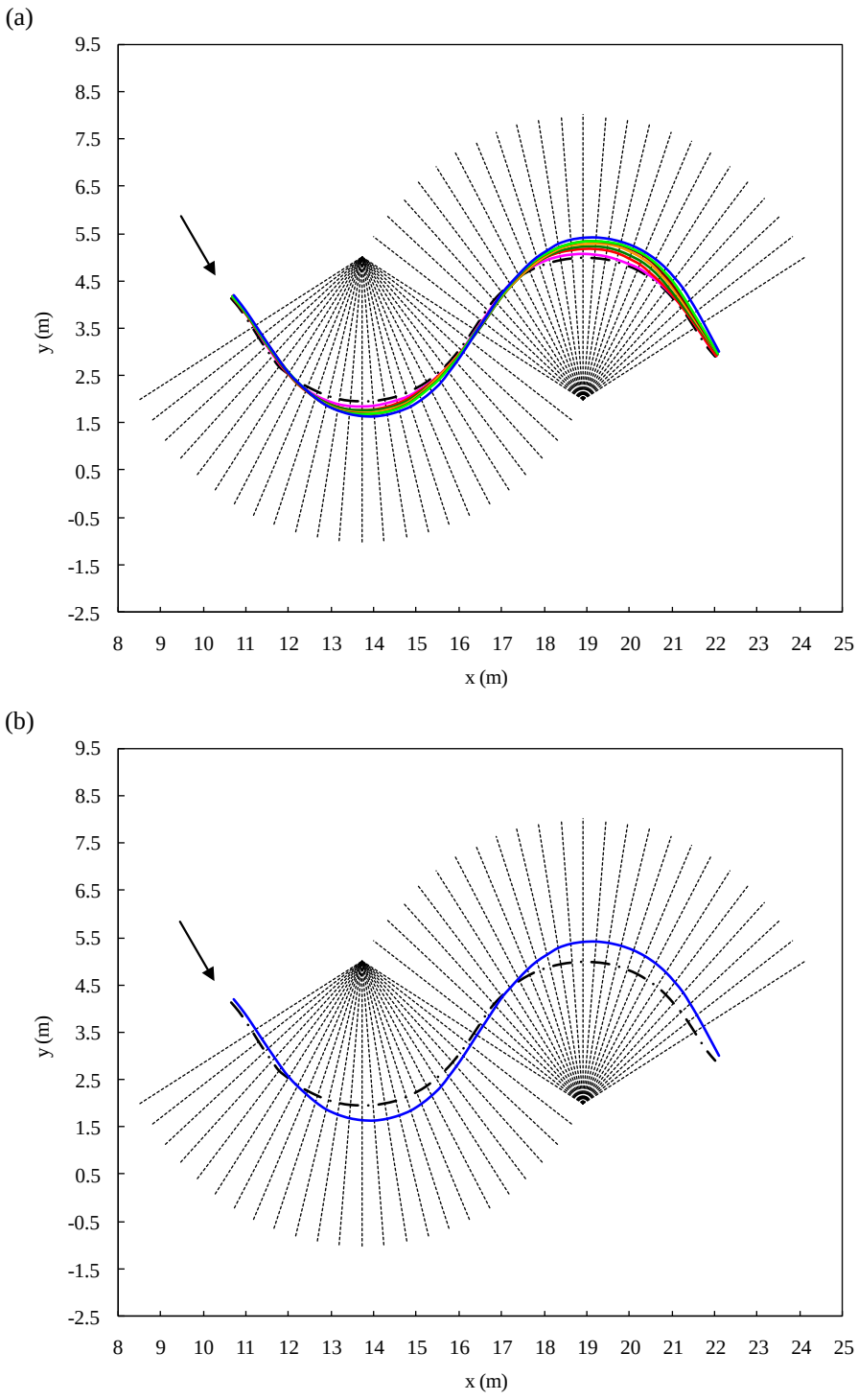

B-10. Channel Centerline Migration of Case 10: (a) — 0 hr; — 3 hr; — 6 hr; — 9 hr; — 15 hr; — 21 hr; — 27 hr; — 39 hr; (b) — 0 hr; — 39 hr

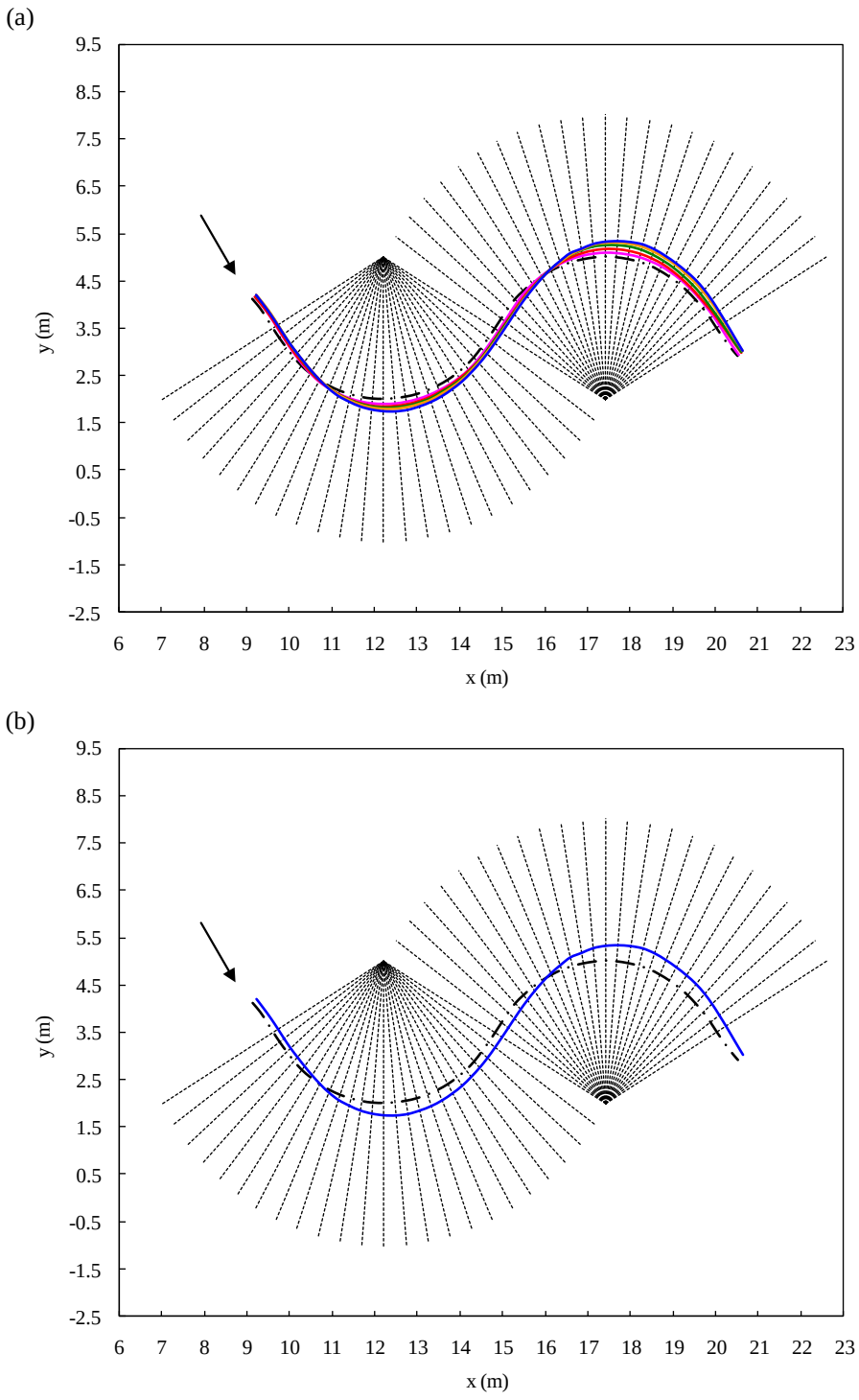

B-11. Channel Centerline Migration of Case 11: (a) — 0 hr; — 2 hr; — 5 hr; — 9 hr; — 14 hr; — 23 hr; (b) — 0 hr; — 23 hr

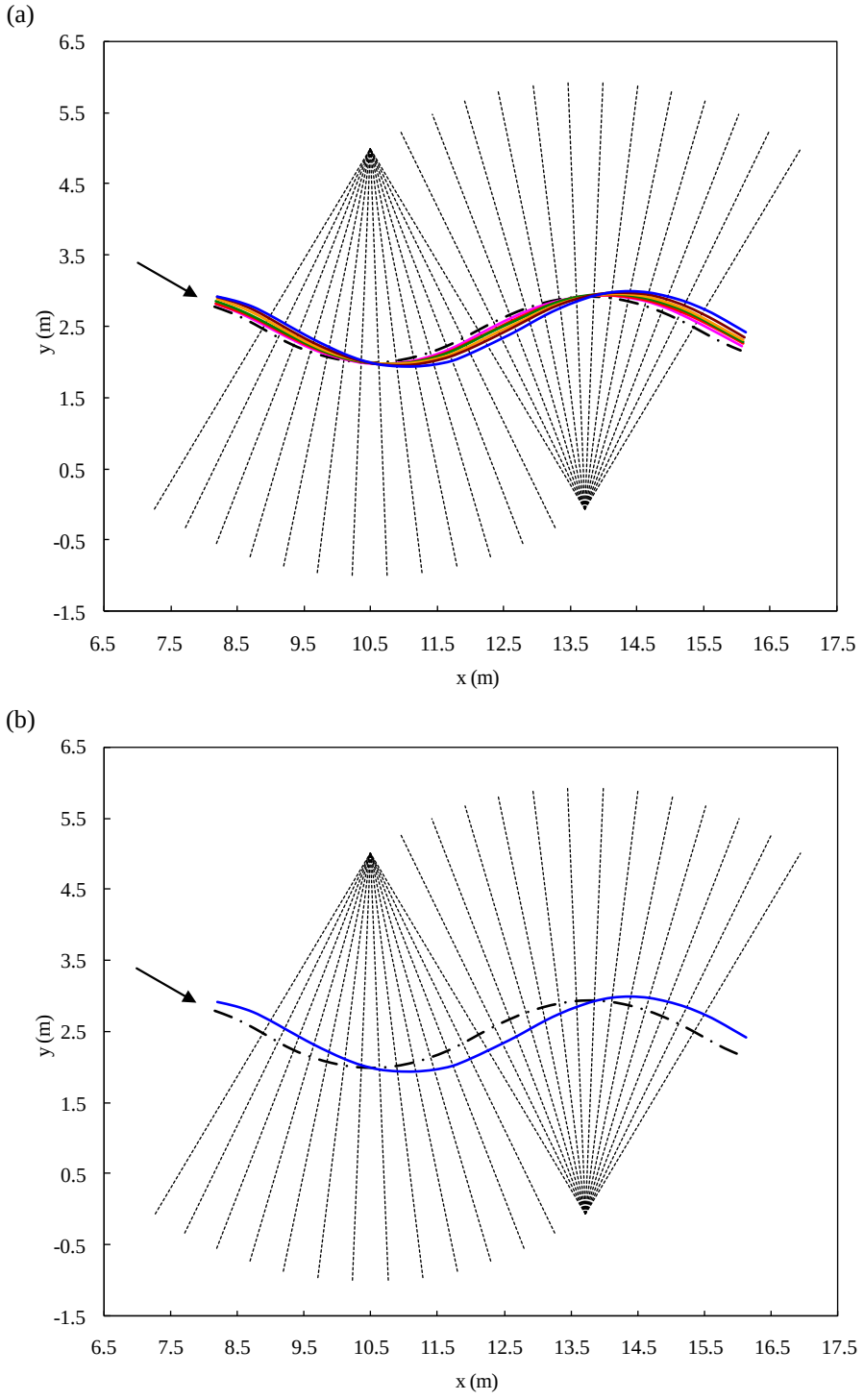

B-12. Channel Centerline Migration of Case 12: (a) — 0 hr; — 3 hr; — 6 hr; — 9 hr; — 15 hr; — 21 hr; — 33 hr; (b) — 0 hr; — 33 hr

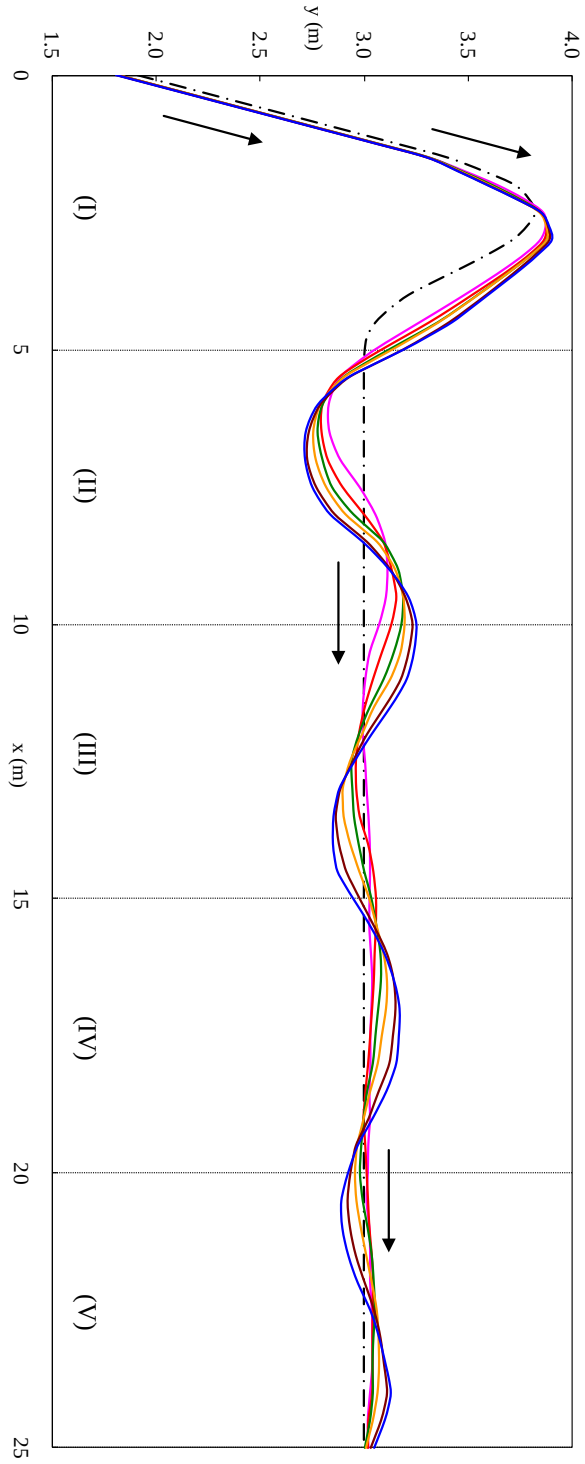

B-13. Channel Centerline Migration of Case 13: — 0 hr; — 3 hr; — 6 hr; — 12 hr; — 18 hr; — 28 hr; — 38 hr

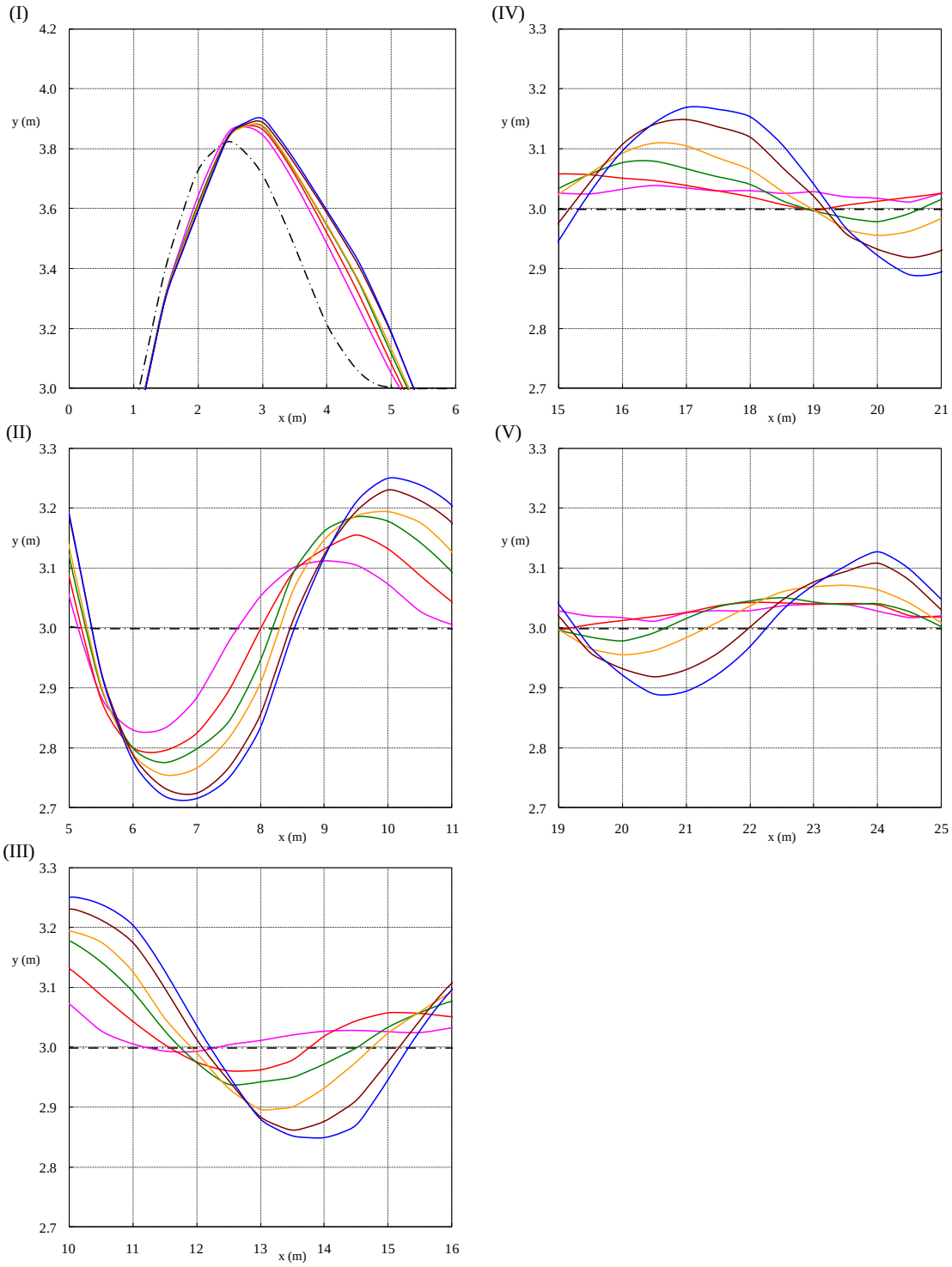

B-13. (Continued)

APPENDIX C

CROSS SECTION PROFILES

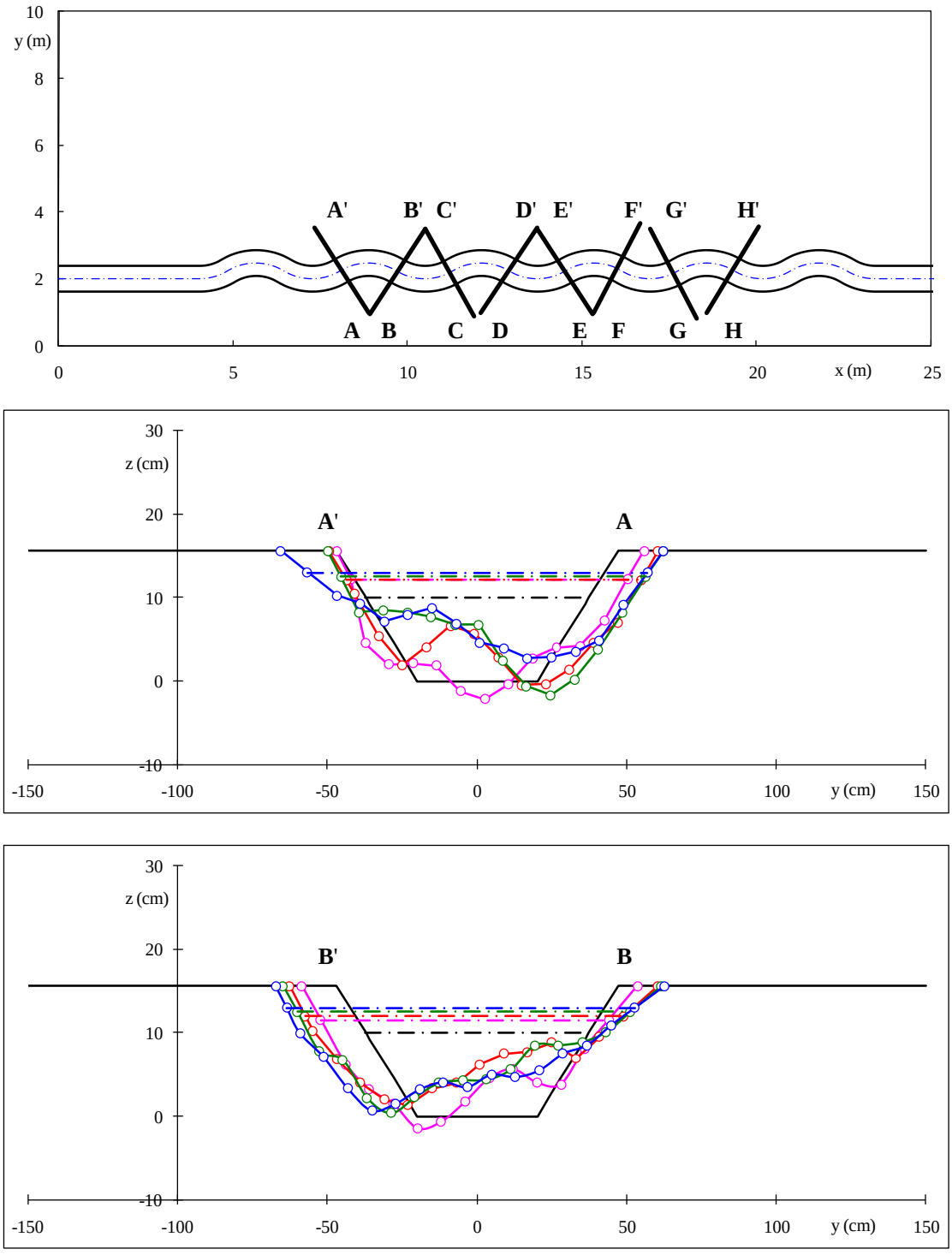

C-1. Channel Cross Section Profiles of Case 01: ○ measurements; ━ 0 hr; ━ 3 hr; ━ 6 hr; ━ 9 hr; ━ 18 hr

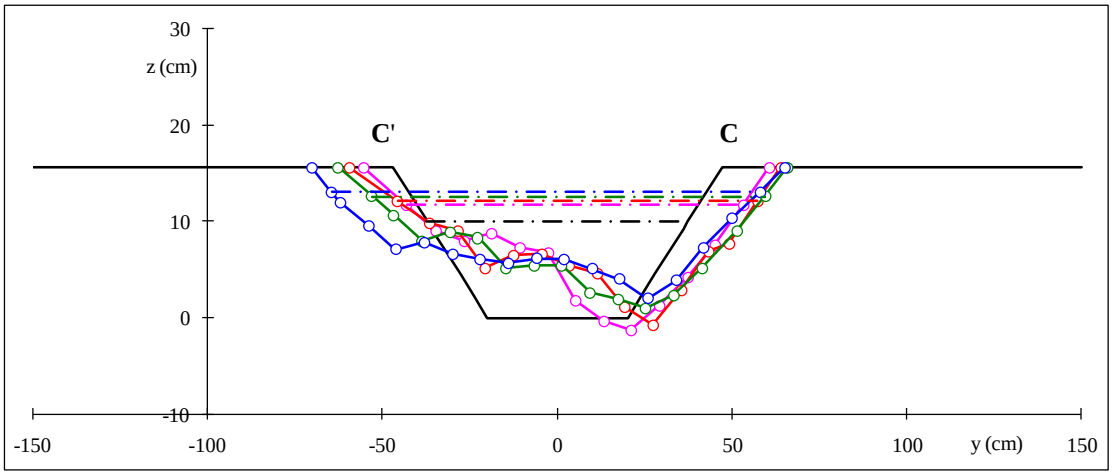

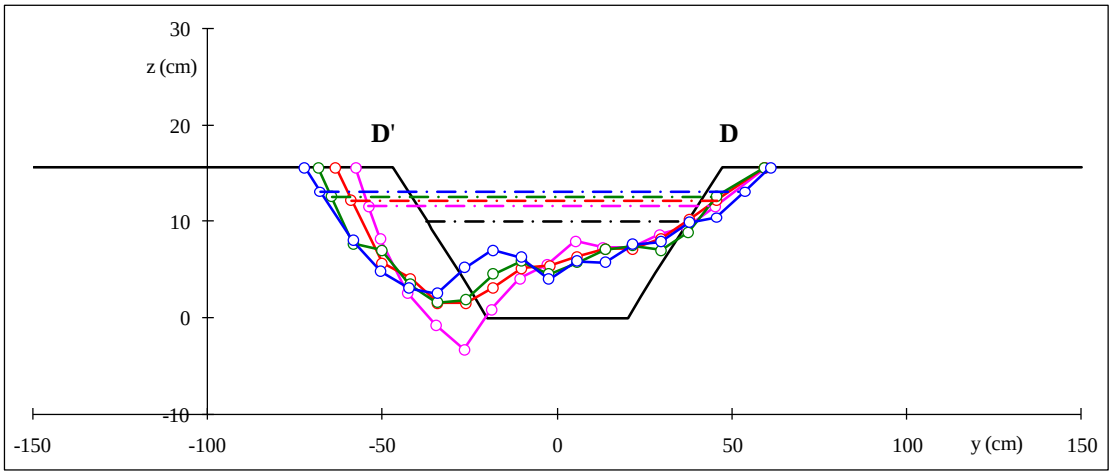

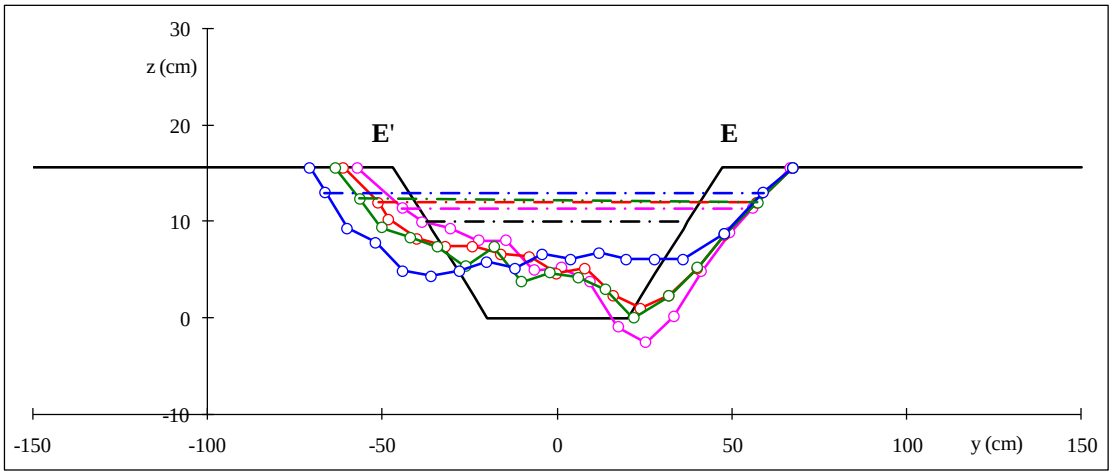

C-1. (Continued)

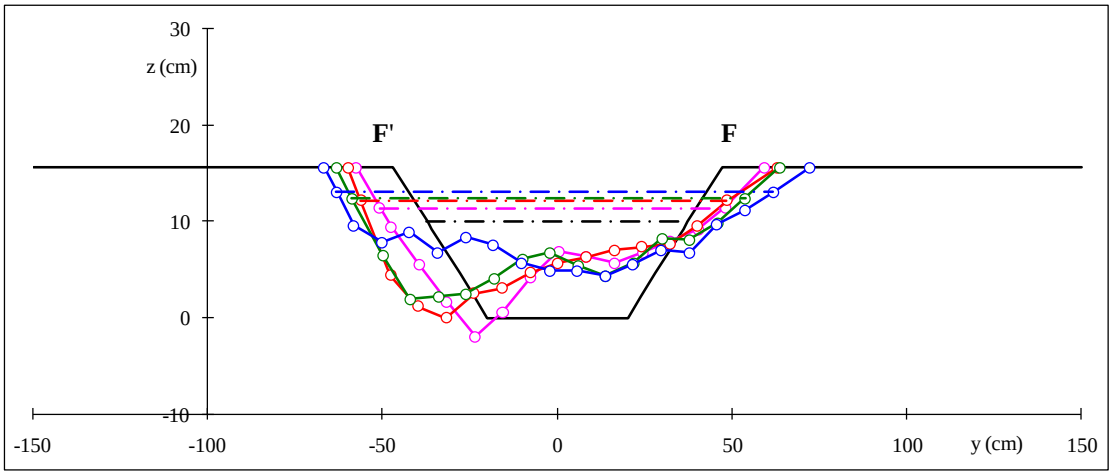

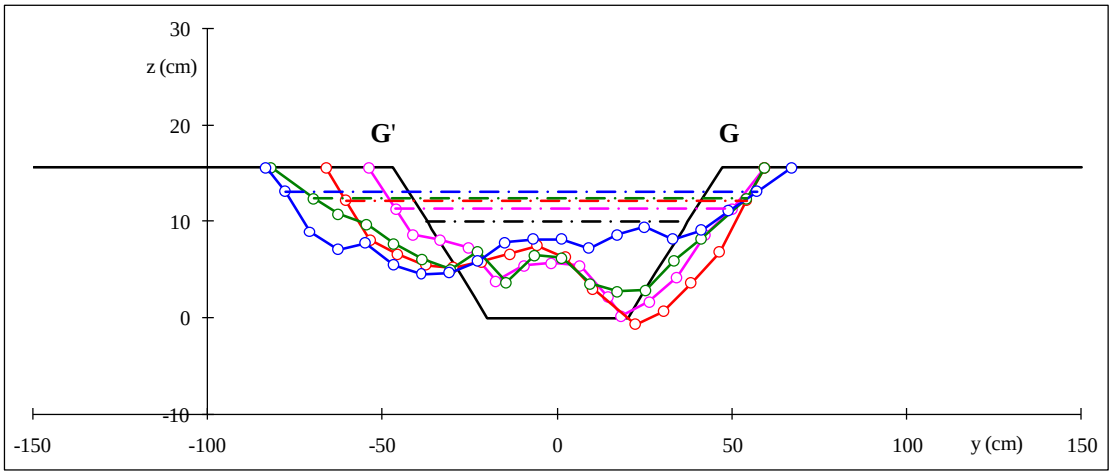

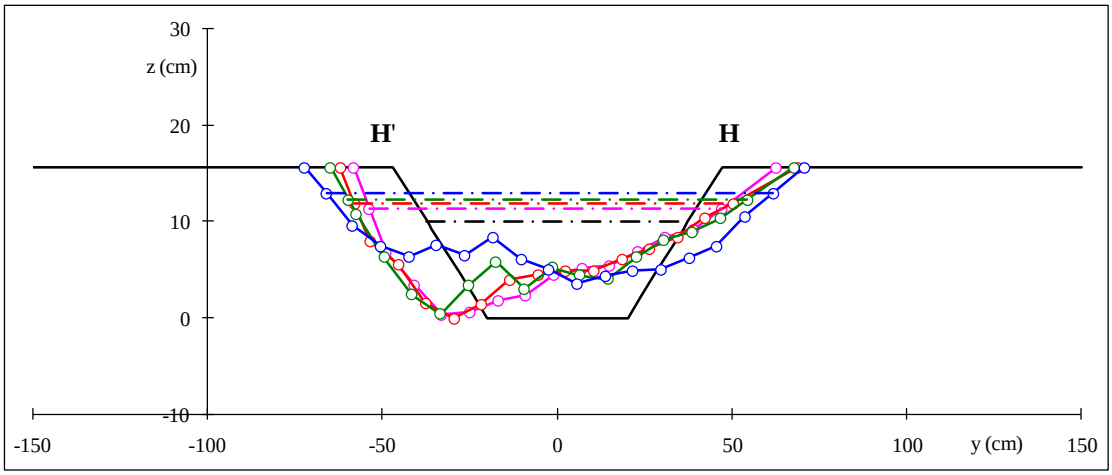

C-1. (Continued)

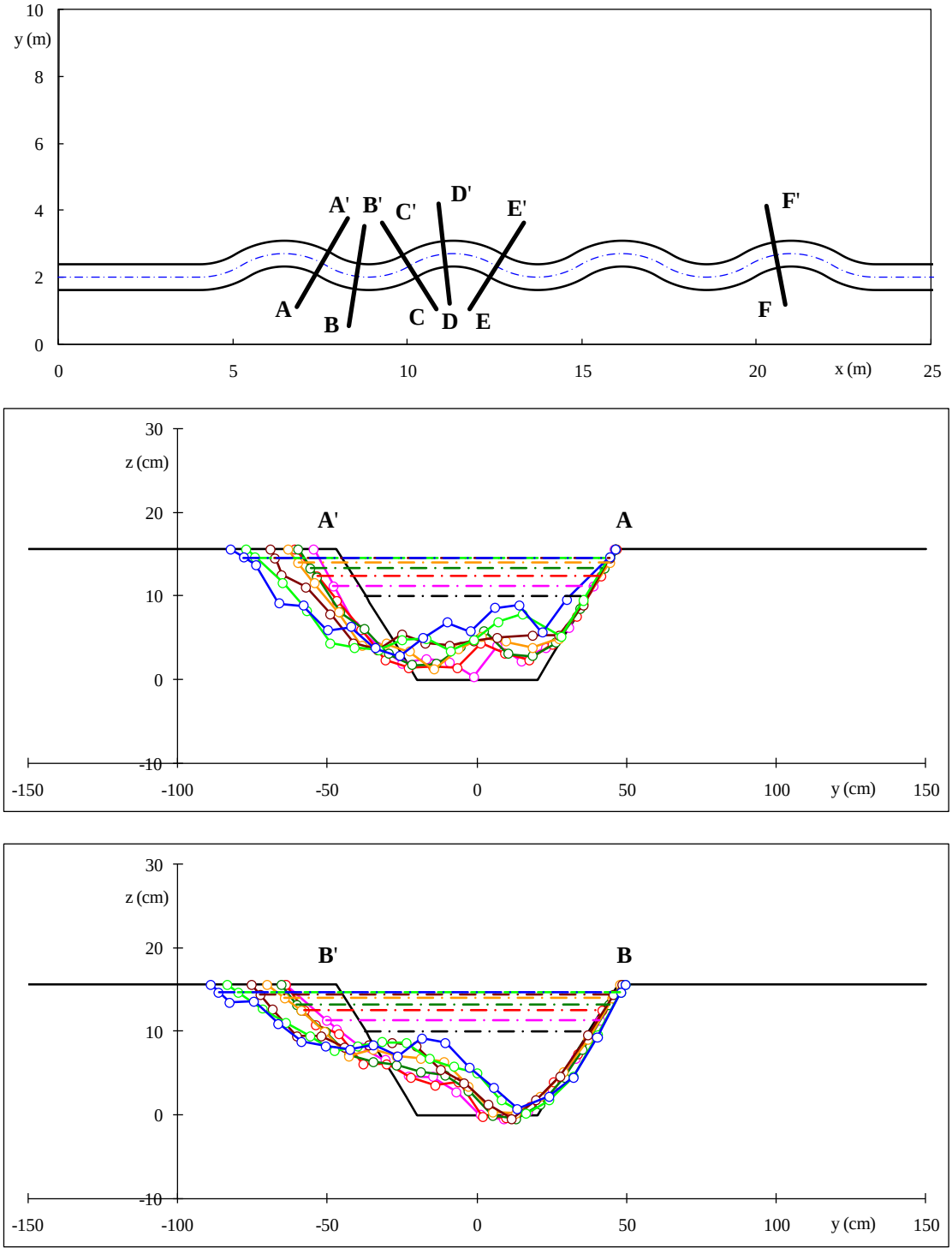

C-2. Channel Cross Section Profiles of Case 02: ○ measurements; — 0 hr; — 3 hr; — 9 hr; — 15 hr; — 24 hr; — 33 hr; — 42 hr

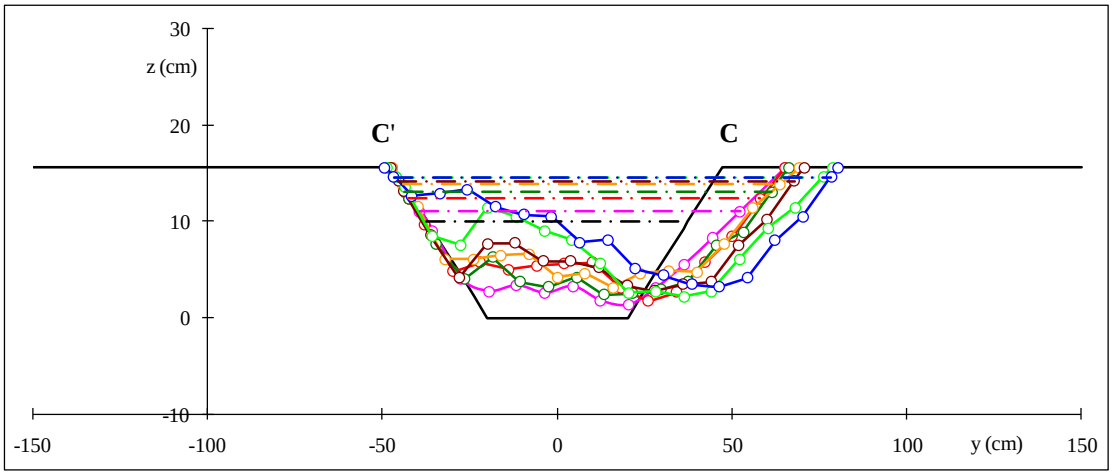

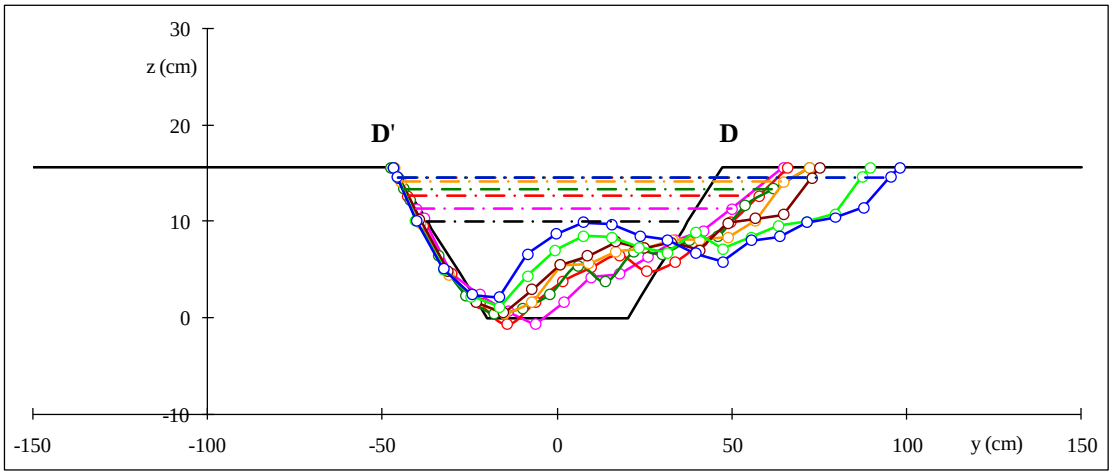

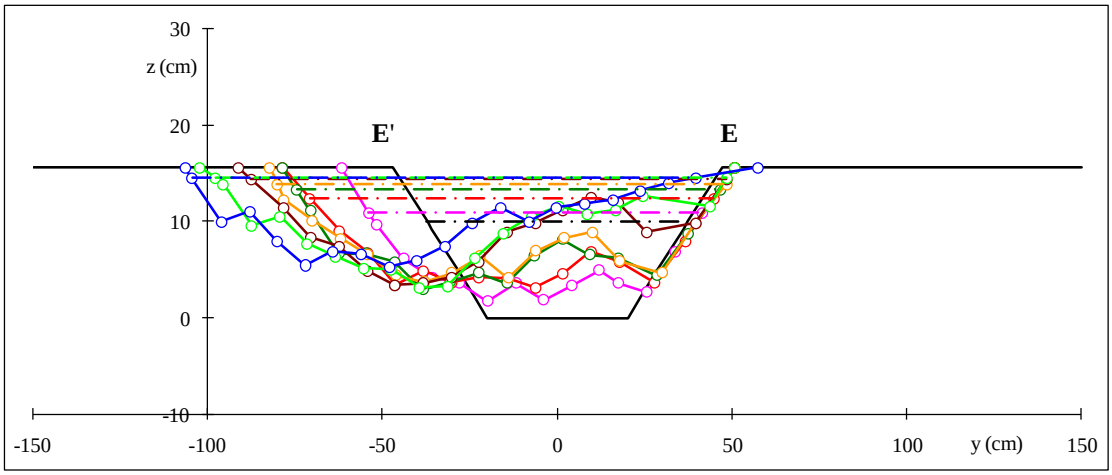

C-2. (Continued)

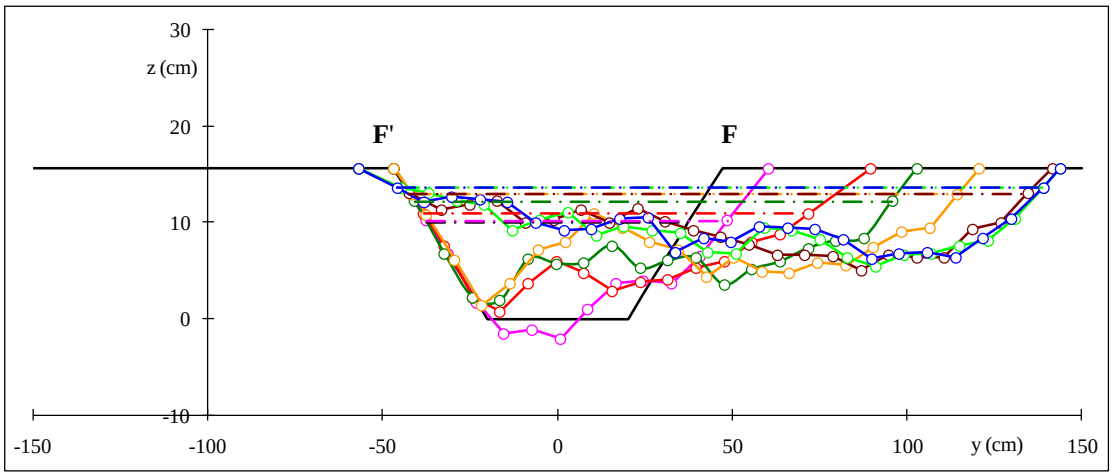

C-2. (Continued)

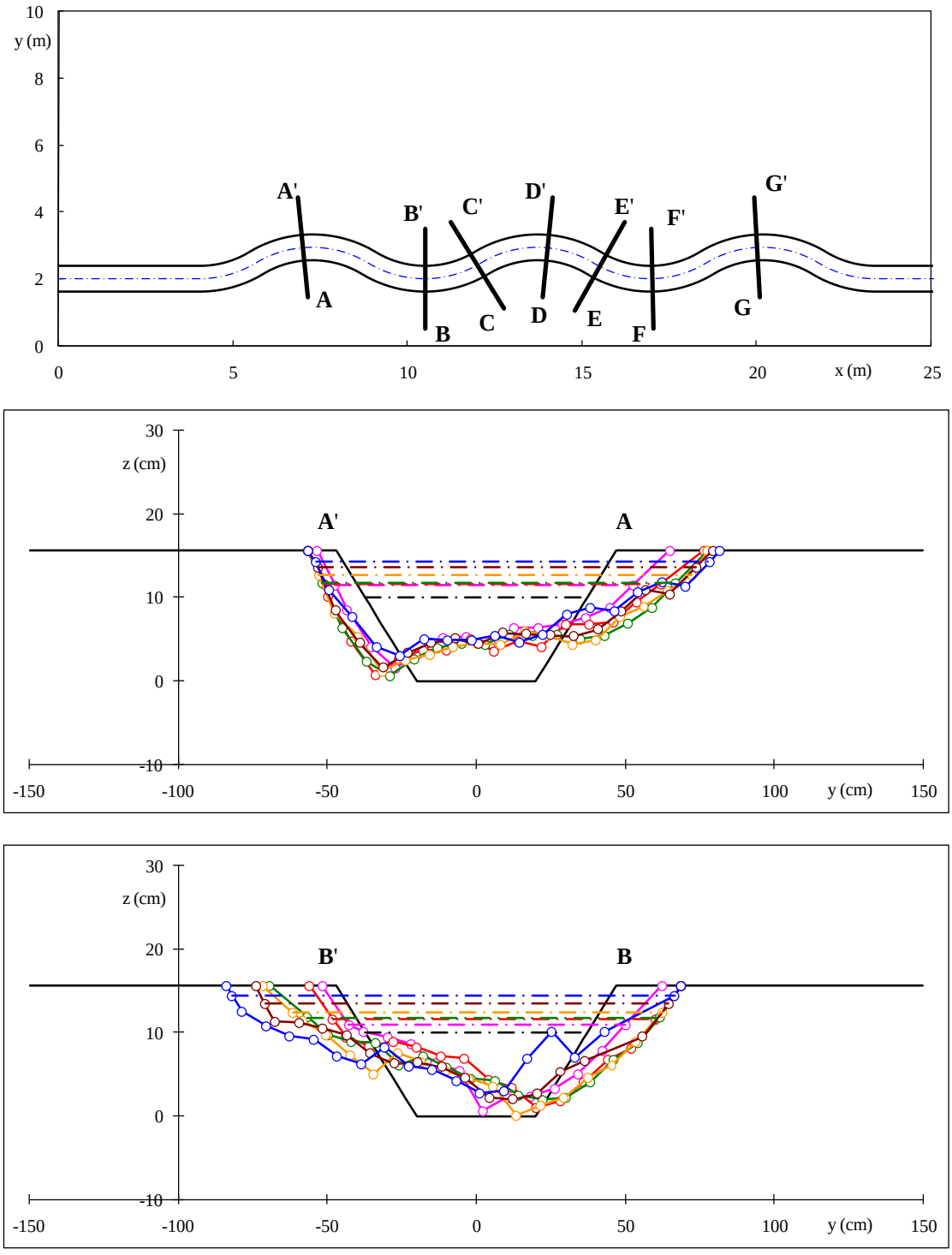

C-3. Channel Cross Section Profiles of Case 03: ○ measurements; — 0 hr; — 3 hr; — 6 hr; — 9 hr; — 15 hr; — 21 hr; — 39 hr

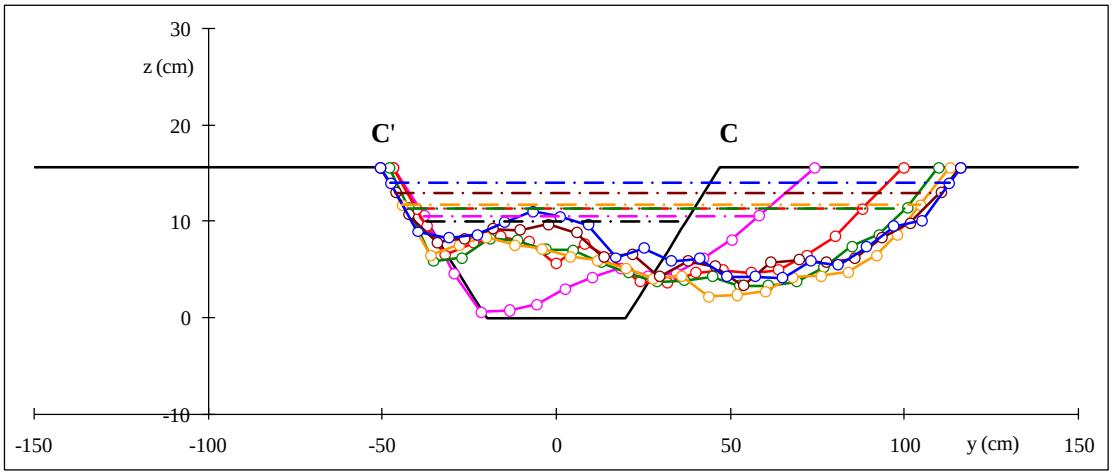

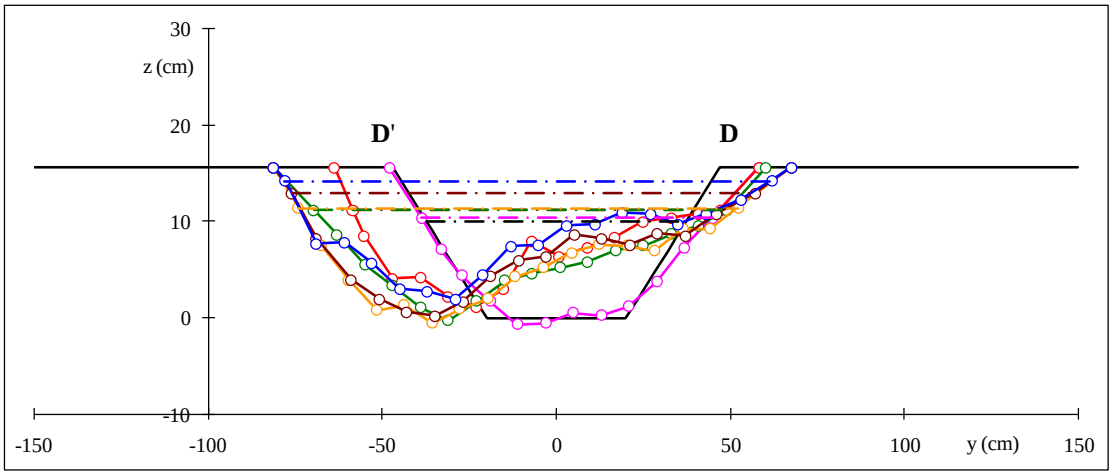

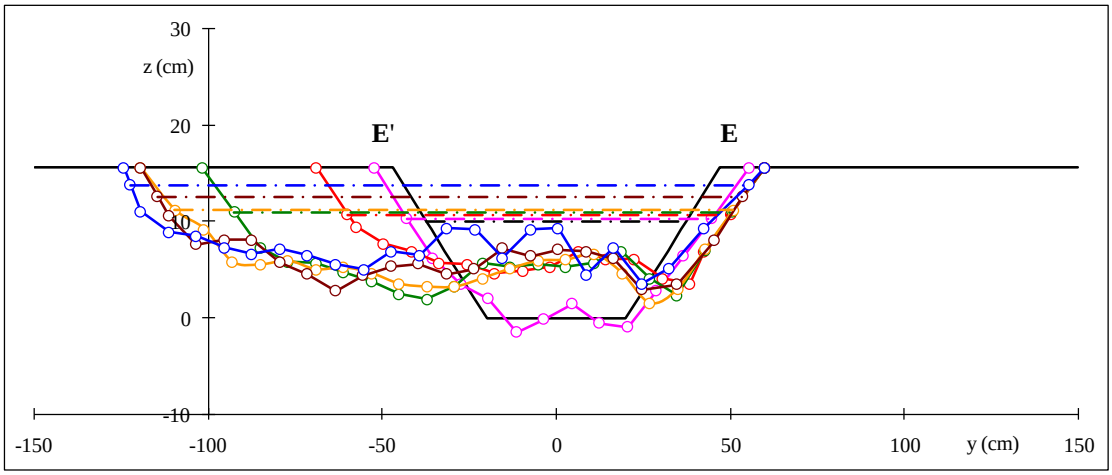

C-3. (Continued)

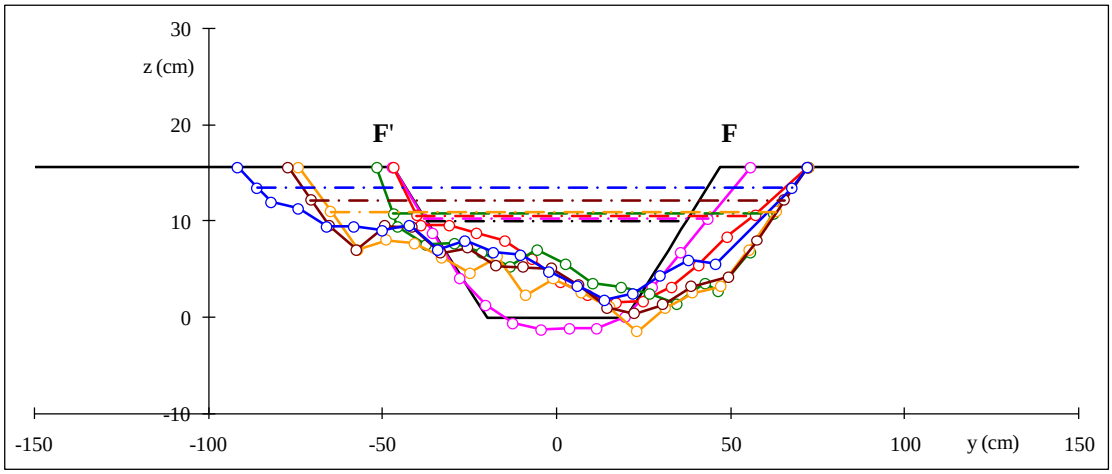

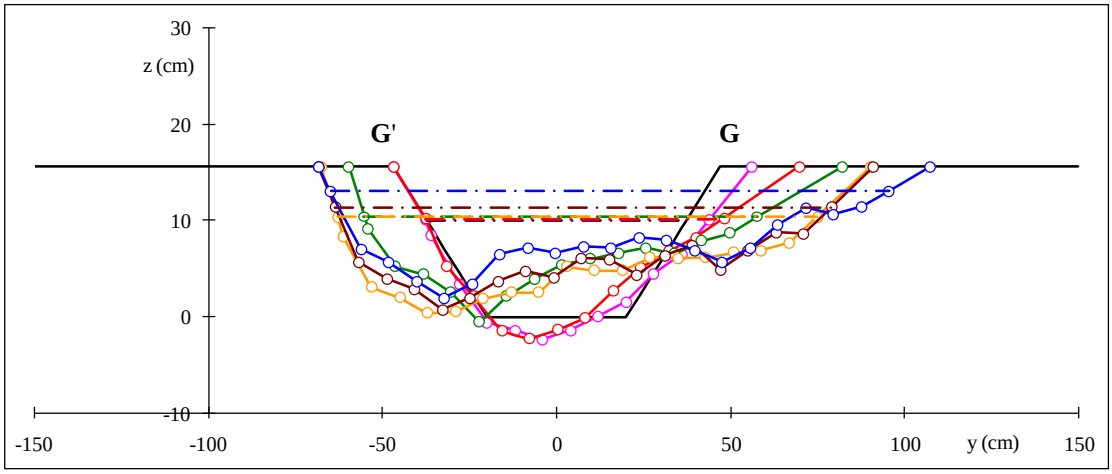

C-3. (Continued)

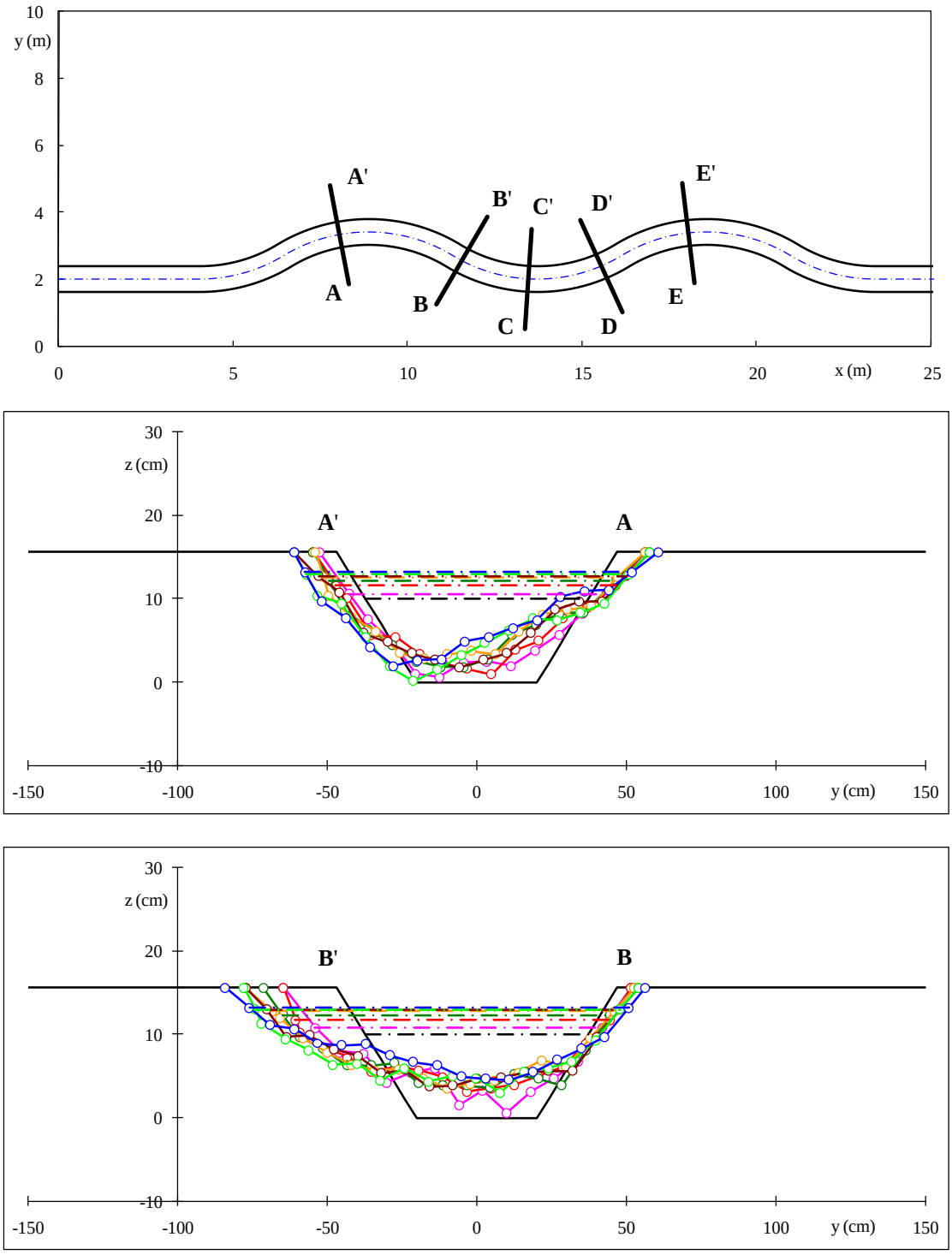

C-4. Channel Cross Section Profiles of Case 04: ○ measurements; — 0 hr; — 3 hr; — 6 hr; — 9 hr; — 15 hr; — 22 hr; — 34 hr; — 45 hr

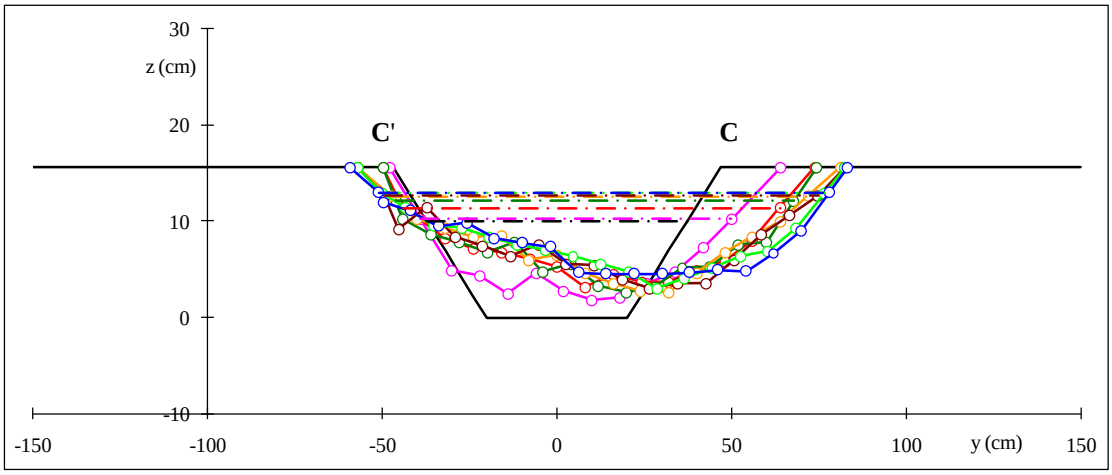

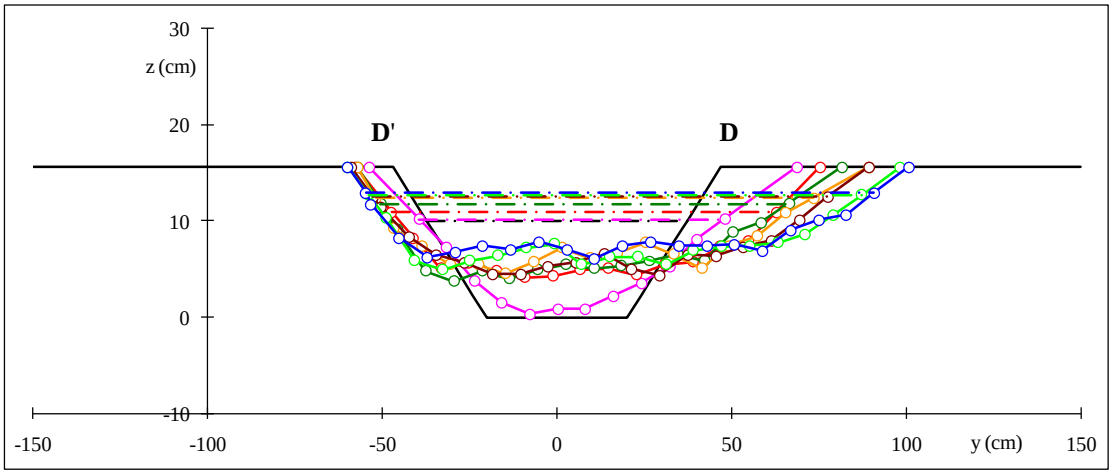

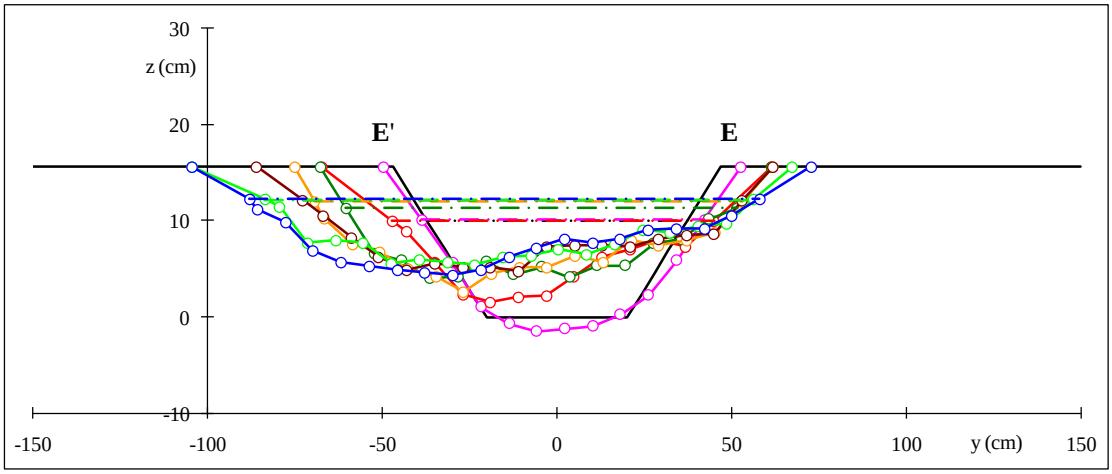

C-4. (Continued)

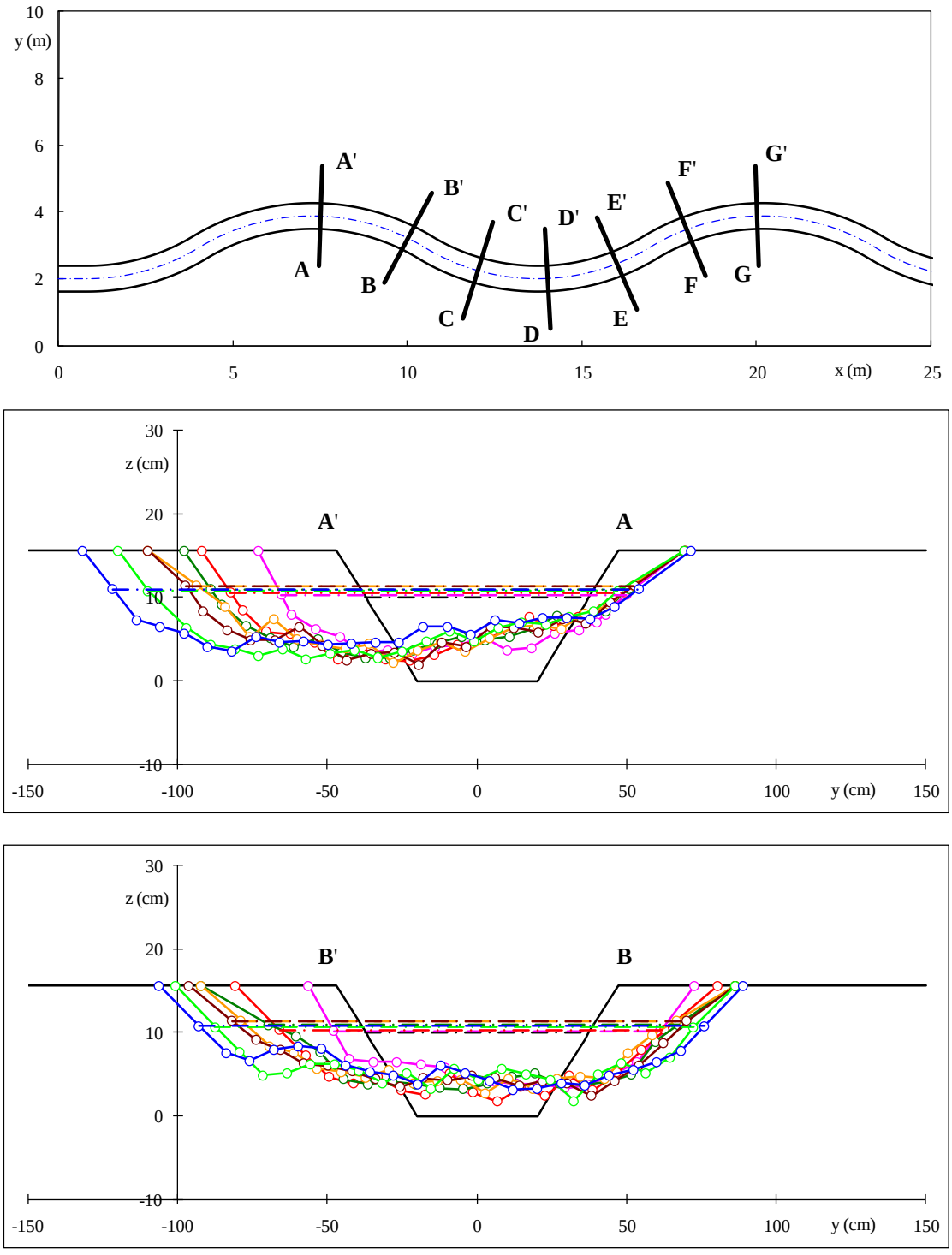

C-5. Channel Cross Section Profiles of Case 05: ○ measurements; — 0 hr; — 3 hr; — 6 hr; — 9 hr; — 15 hr; — 24 hr; — 42 hr; — 66 hr

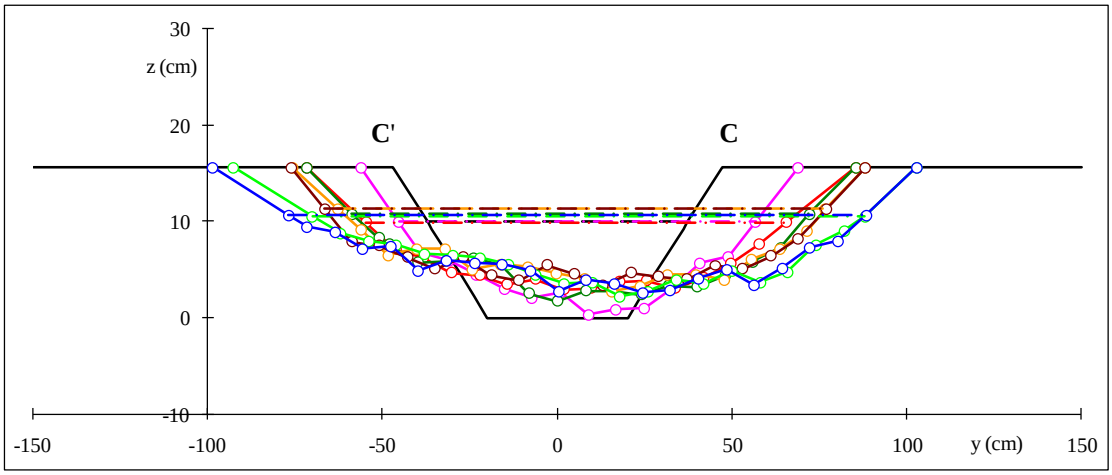

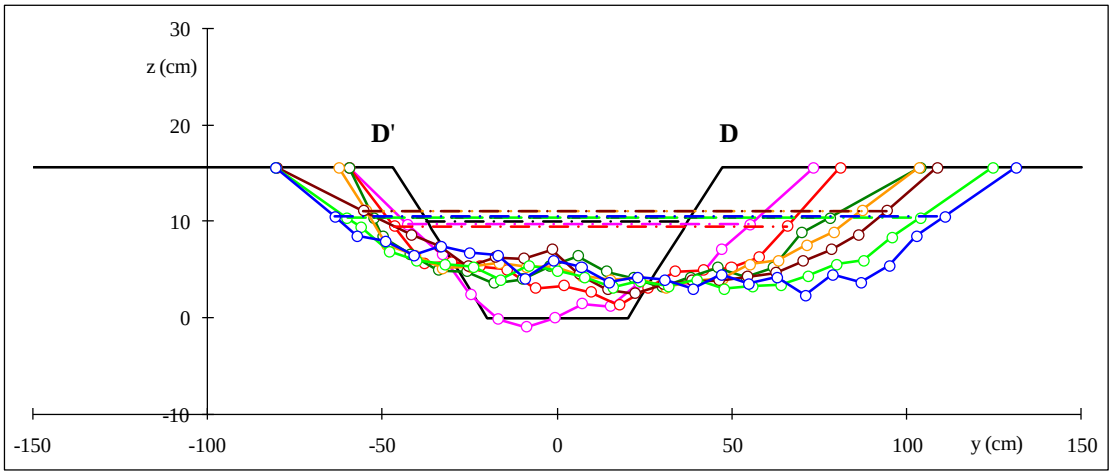

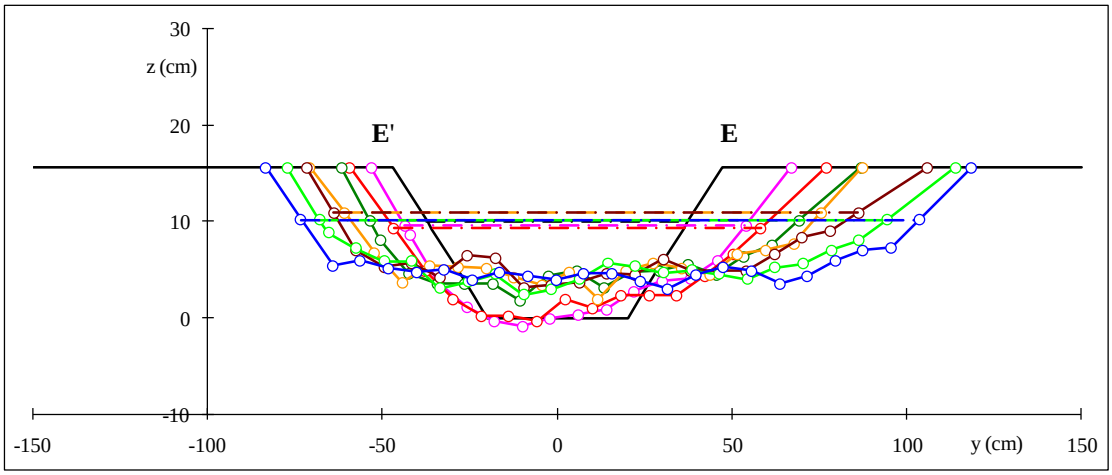

C-5. (Continued)

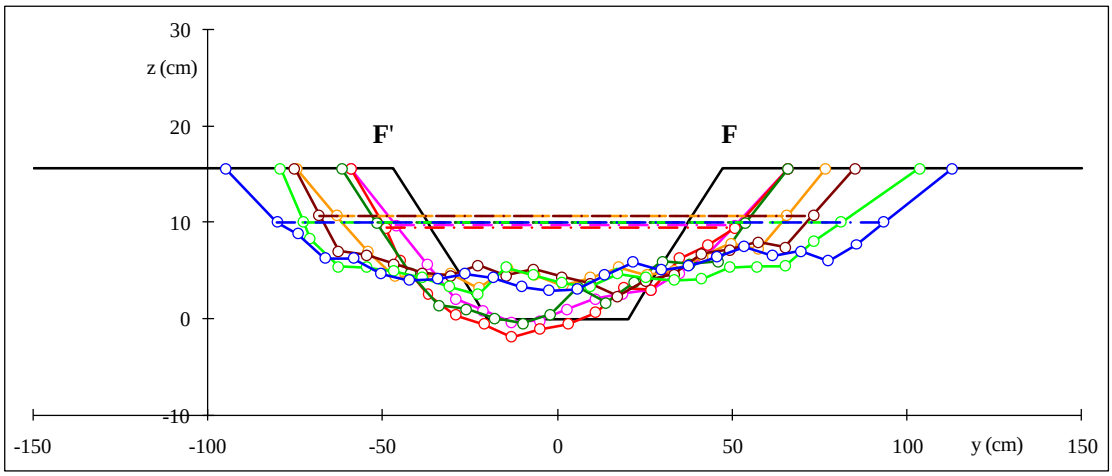

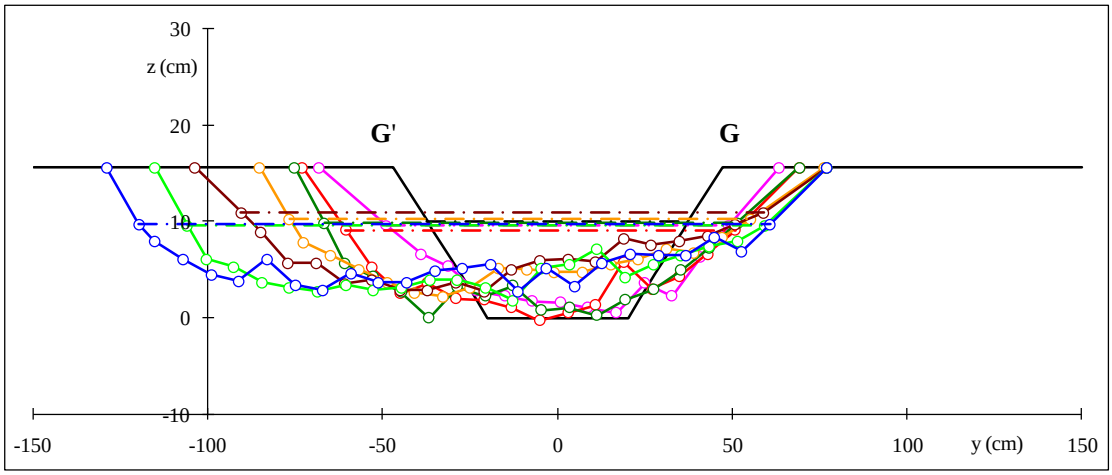

C-5. (Continued)

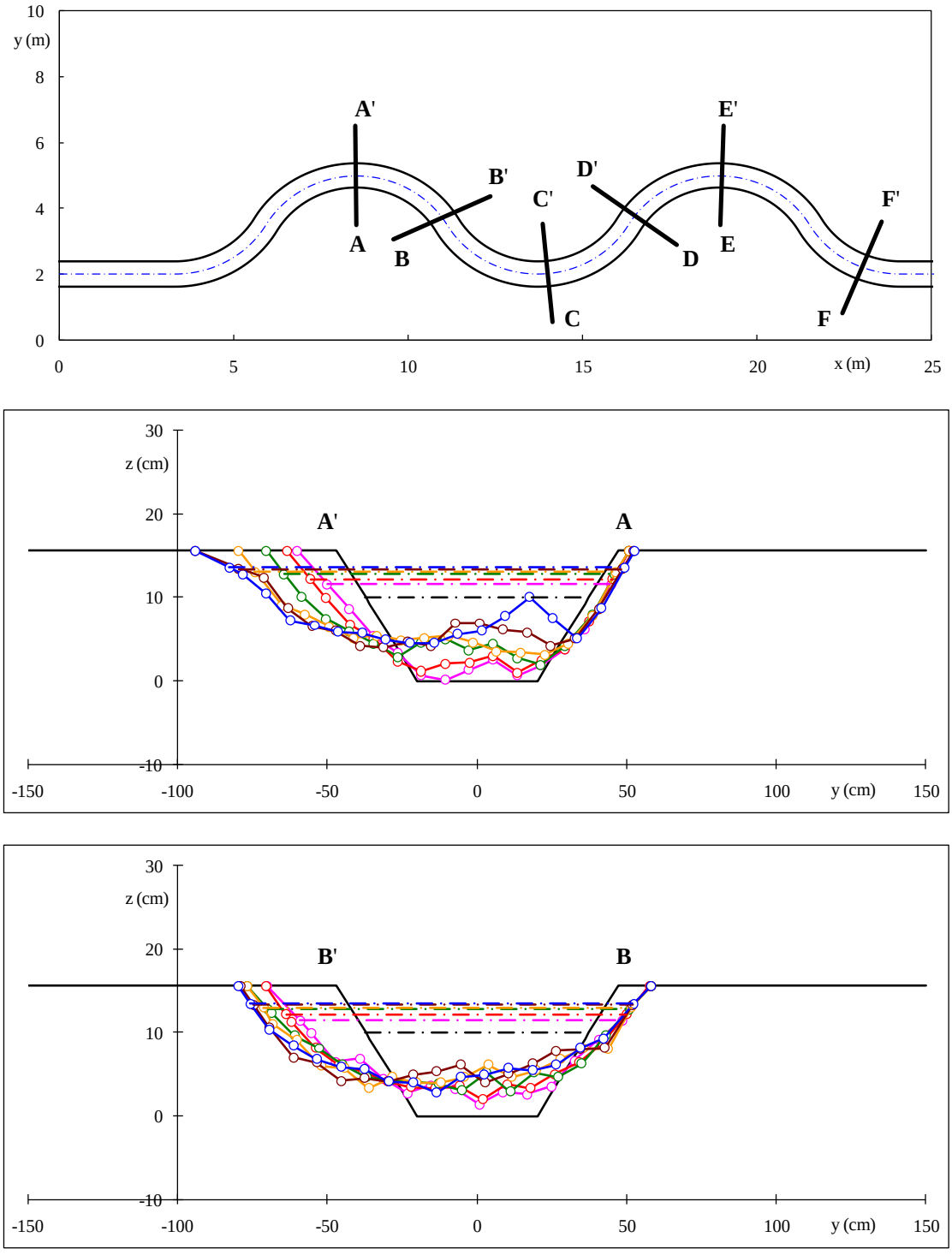

C-6. Channel Cross Section Profiles of Case 06: ○ measurements; — 0 hr; — 3 hr; — 6 hr; — 12 hr; — 18 hr; — 24 hr; — 30 hr

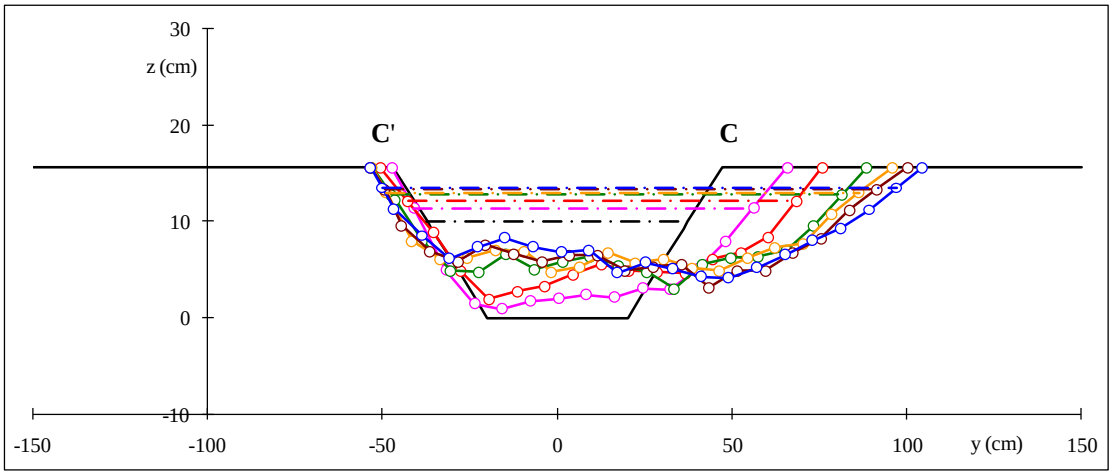

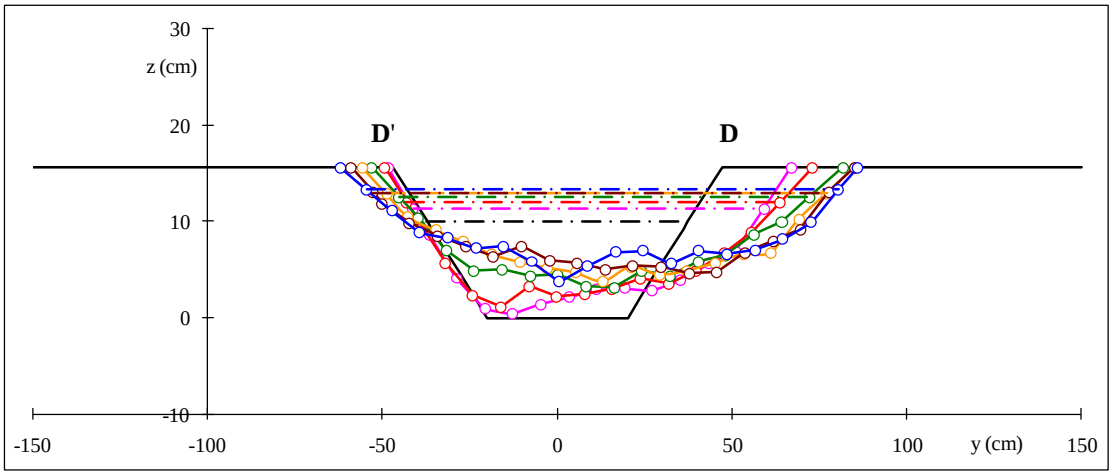

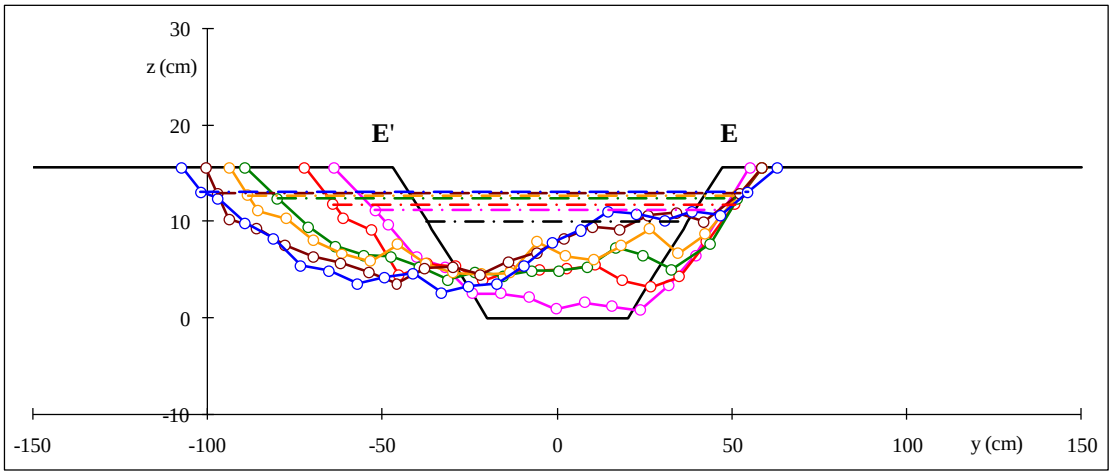

C-6. (Continued)

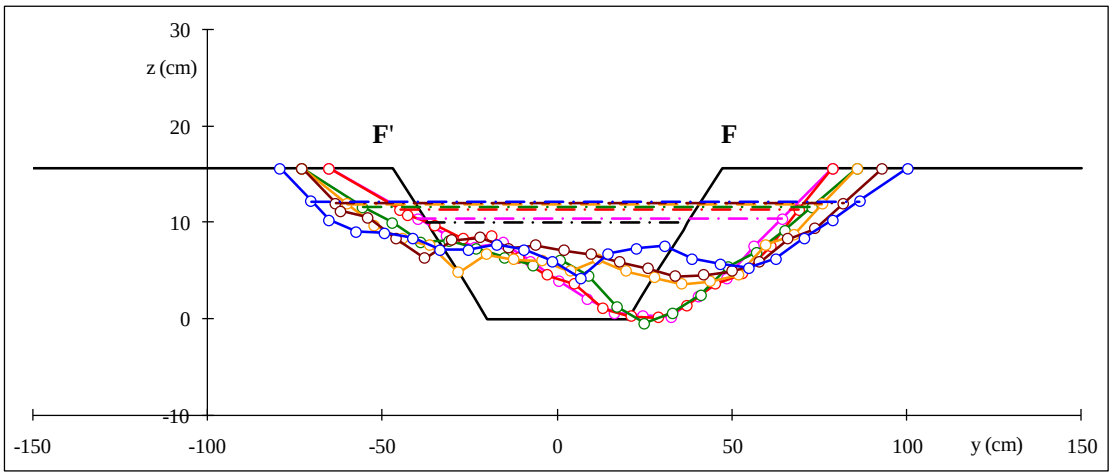

C-6. (Continued)

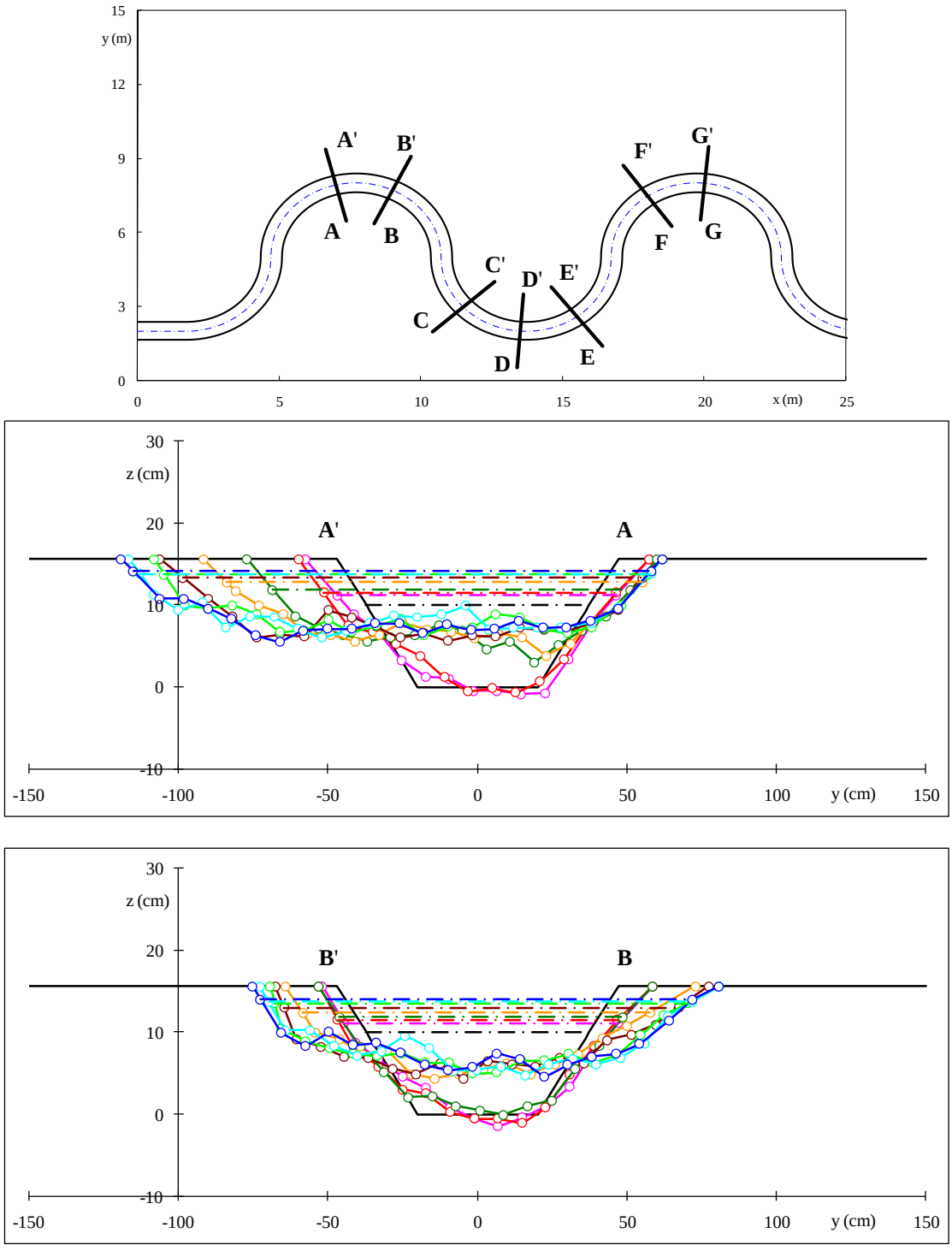

C-7. Channel Cross Section Profiles of Case 07: ○ measurements; — 0 hr; — 3 hr; — 6 hr; — 15 hr; — 24 hr; — 36 hr; — 48 hr; — 66 hr; — 86 hr

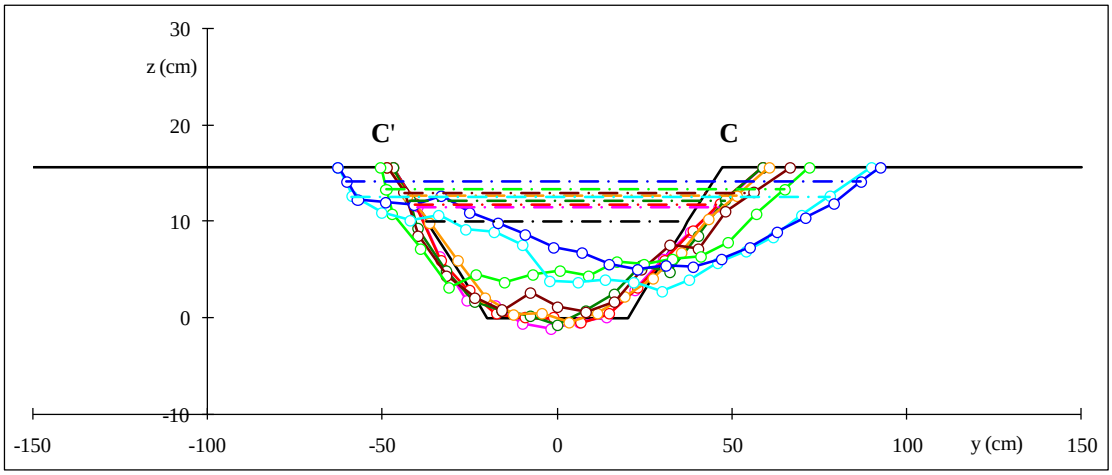

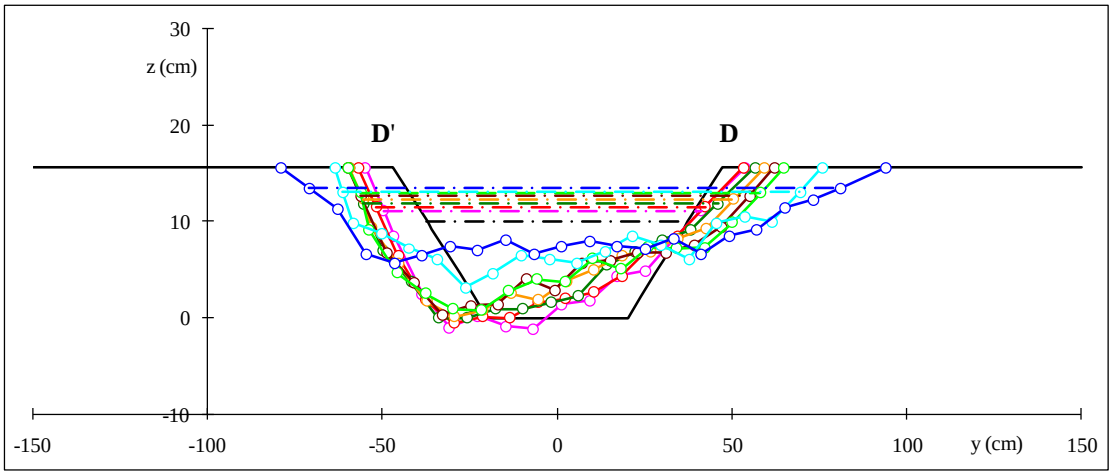

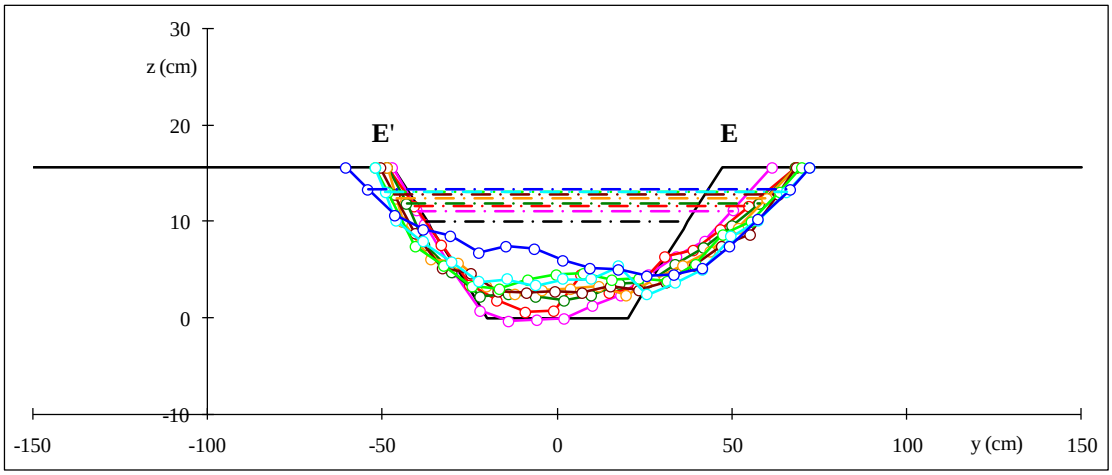

C-7. (Continued)

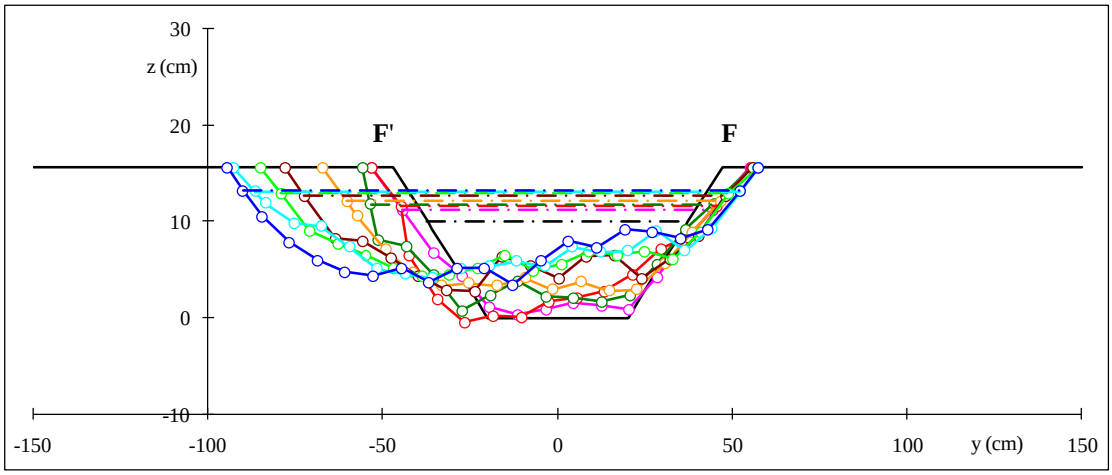

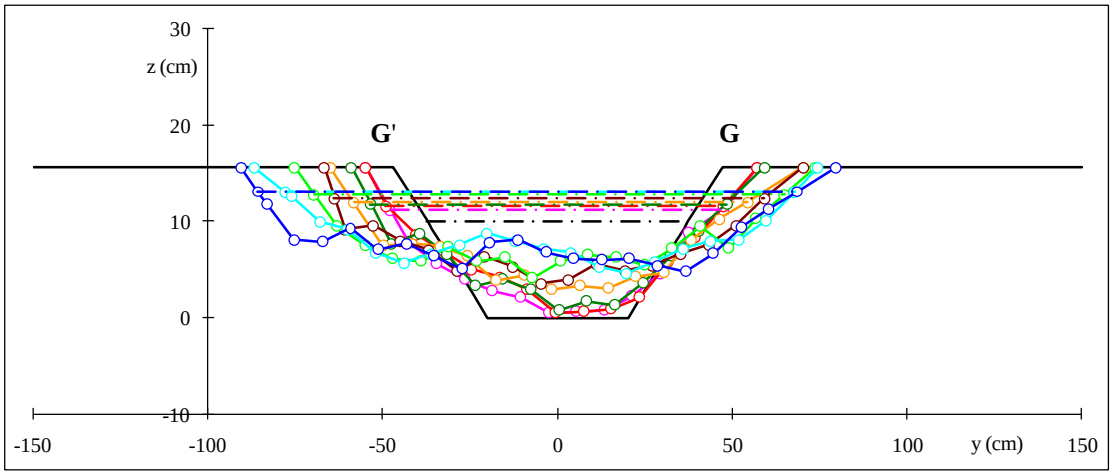

C-7. (Continued)

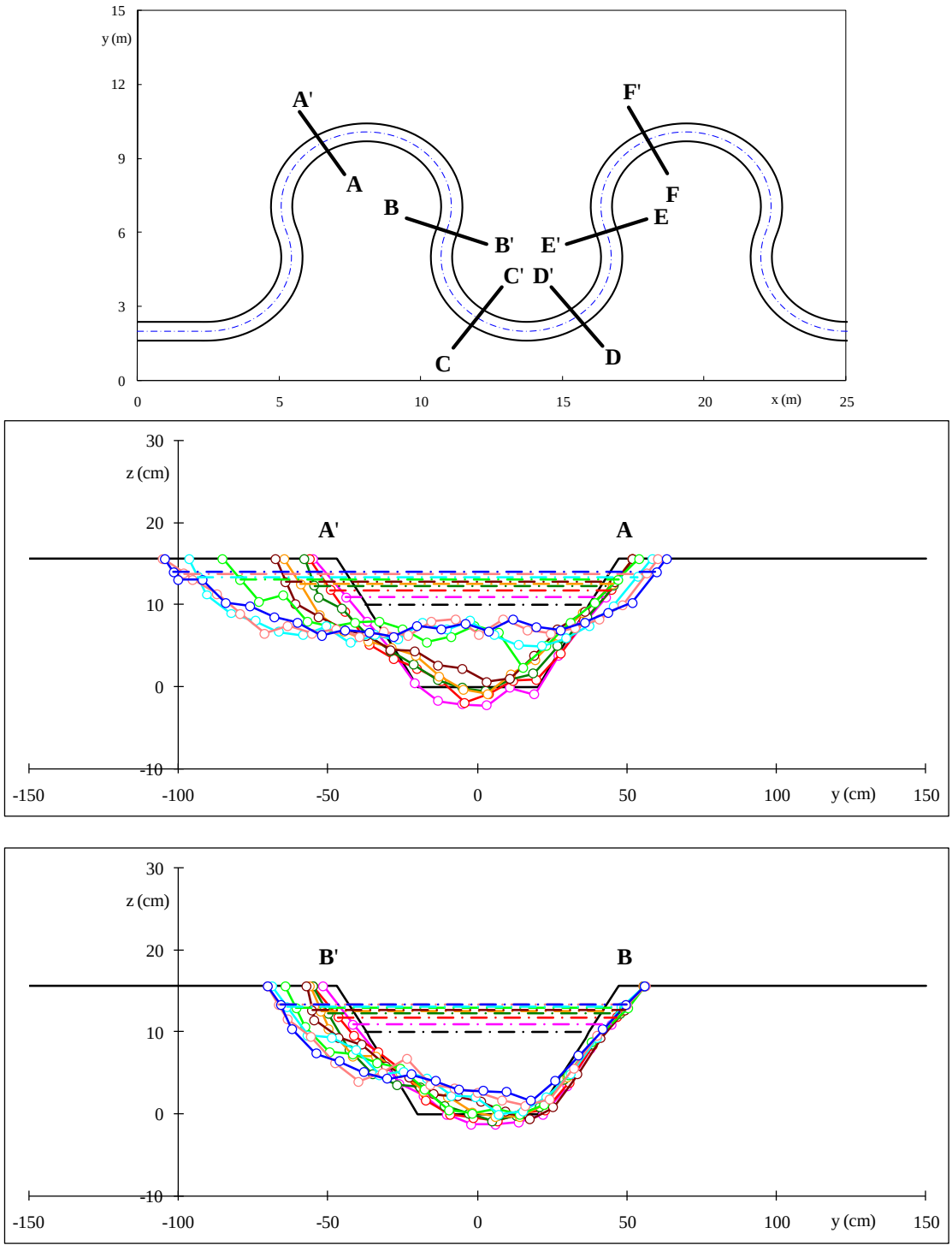

C-8. Channel Cross Section Profiles of Case 08: ○ measurements; — 0 hr; — 3 hr; — 9 hr; — 18 hr; — 30 hr; — 48 hr; — 69 hr; — 96 hr; — 123 hr; — 147 hr

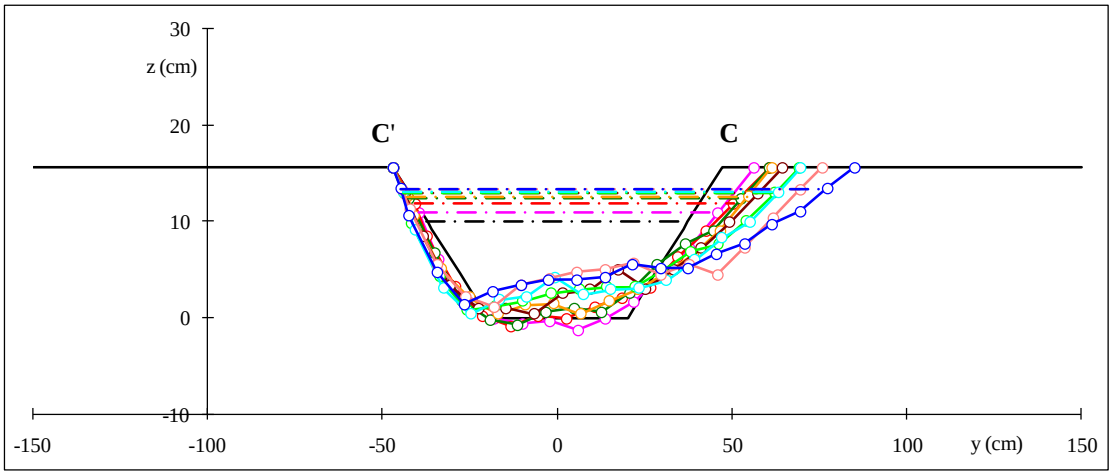

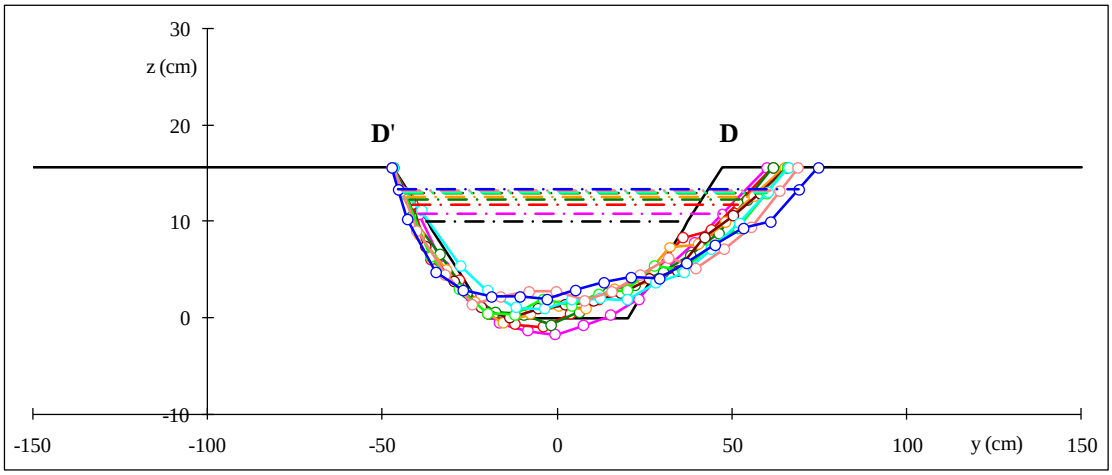

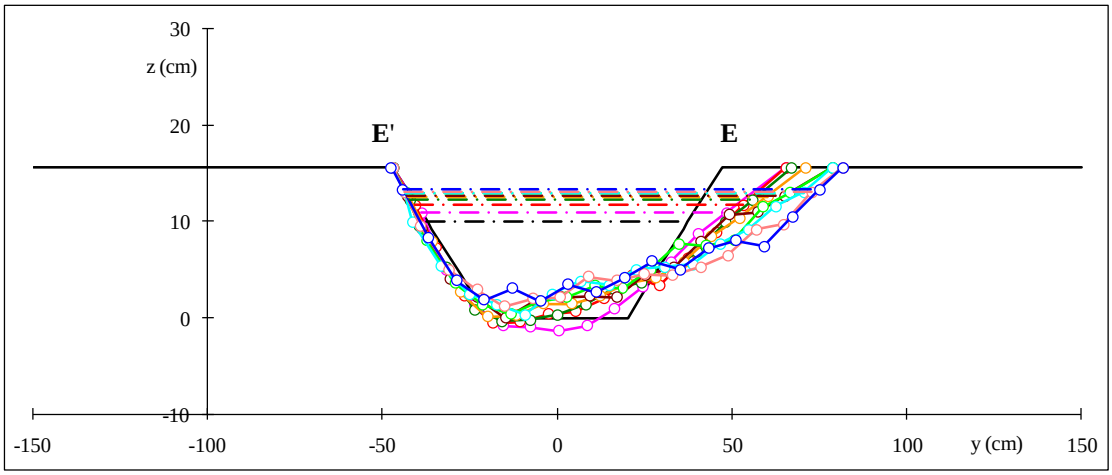

C-8. (Continued)

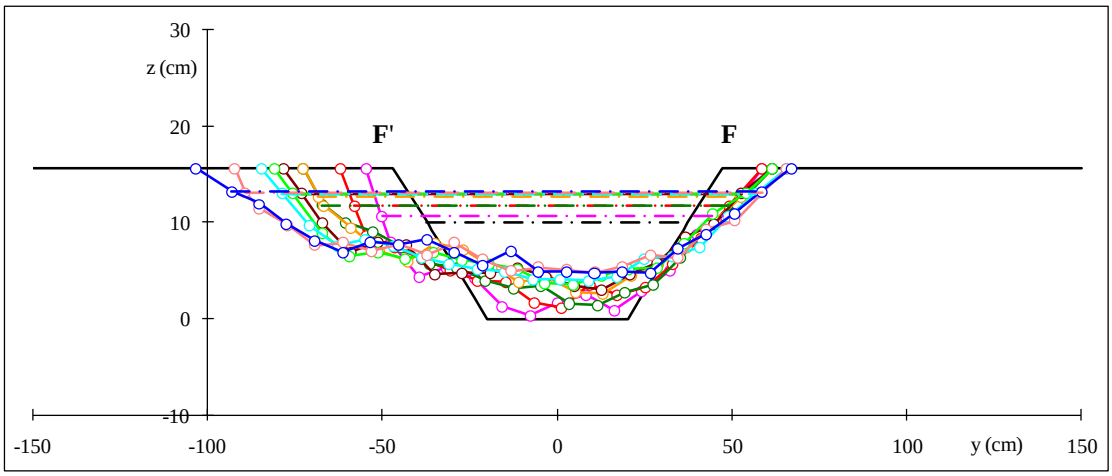

C-8. (Continued)

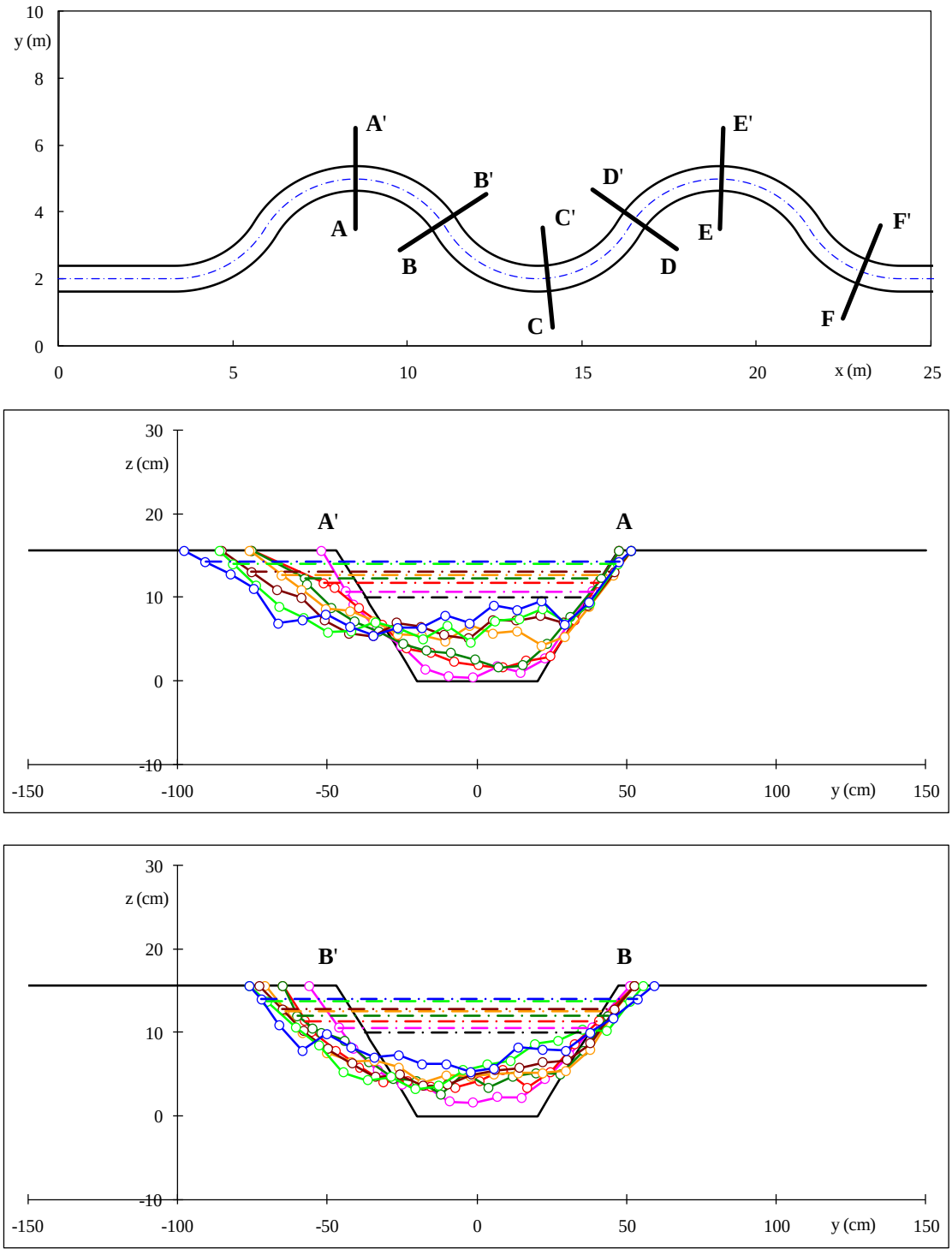

C-9. Channel Cross Section Profiles of Case 09: ○ measurements; ━ 0 hr; ━ 4 hr; ━ 10 hr; ━ 16 hr; ━ 24 hr; ━ 32 hr; ━ 44 hr; ━ 56 hr

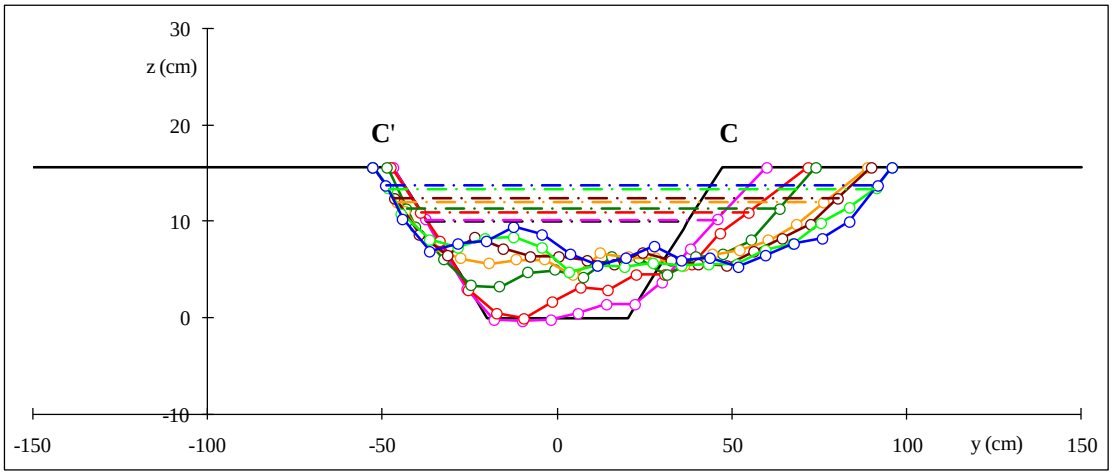

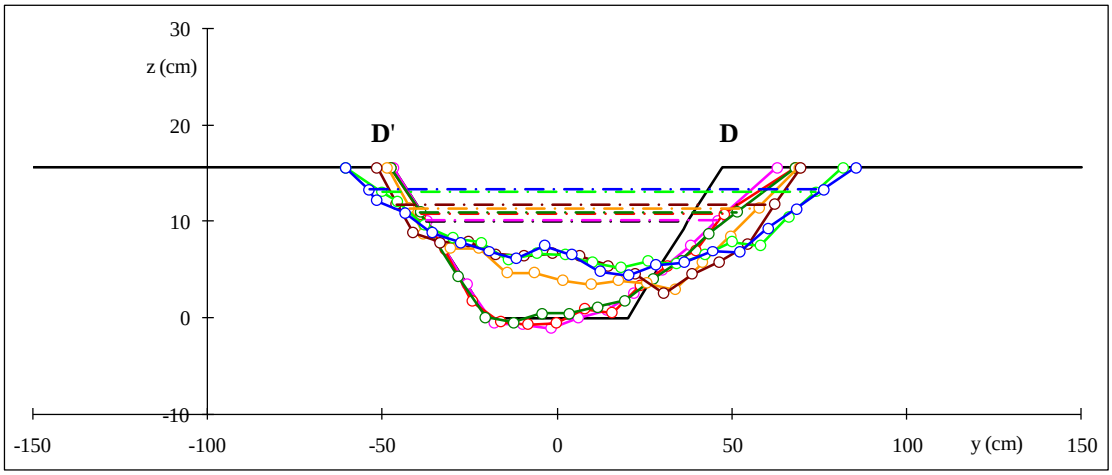

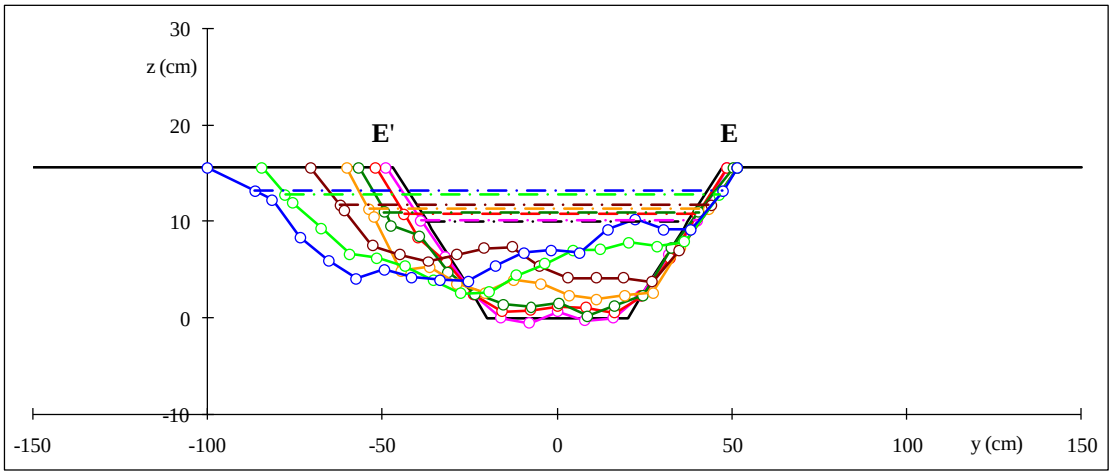

C-9. (Continued)

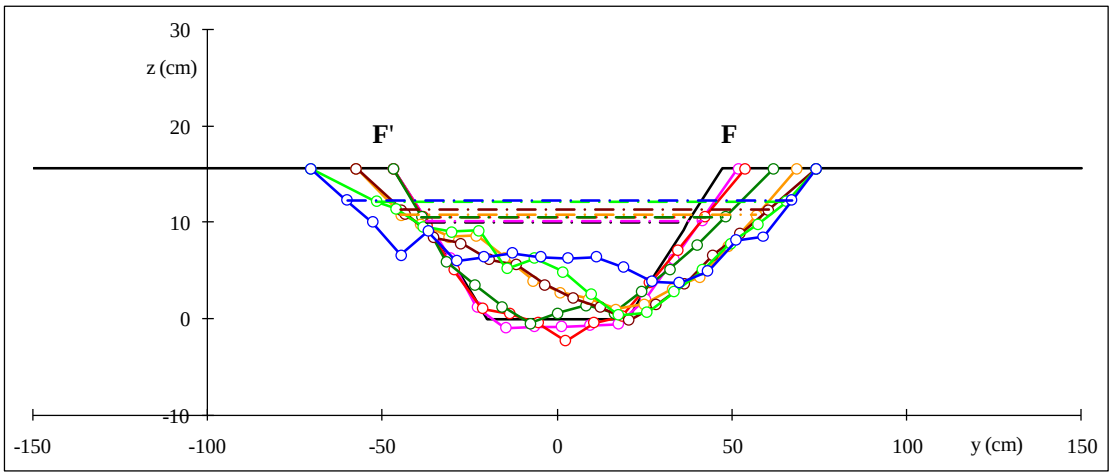

C-9. (Continued)

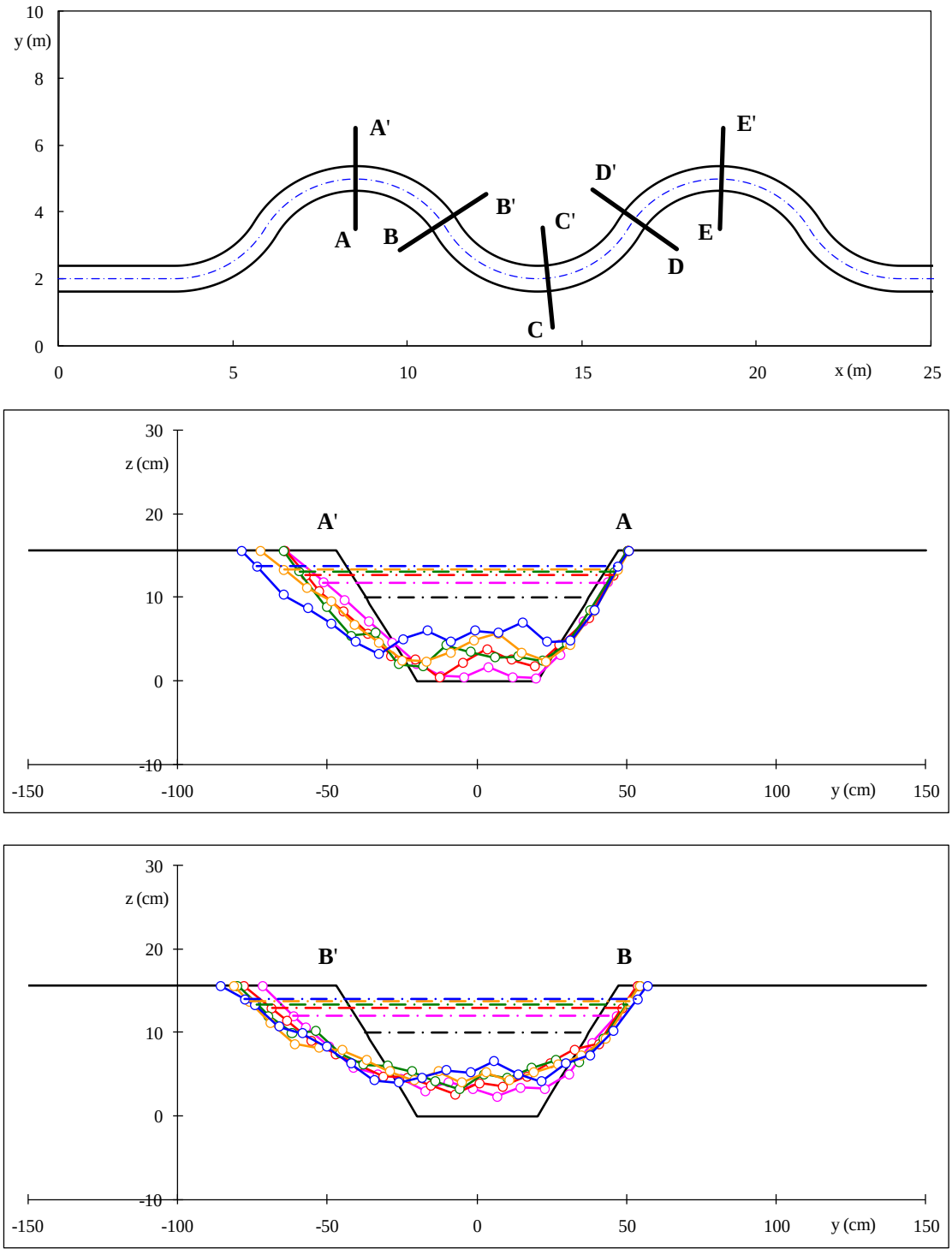

C-10. Channel Cross Section Profiles of Case 11: ○ measurements; — 0 hr; — 2 hr; — 5 hr; — 9 hr; — 14 hr; — 23 hr

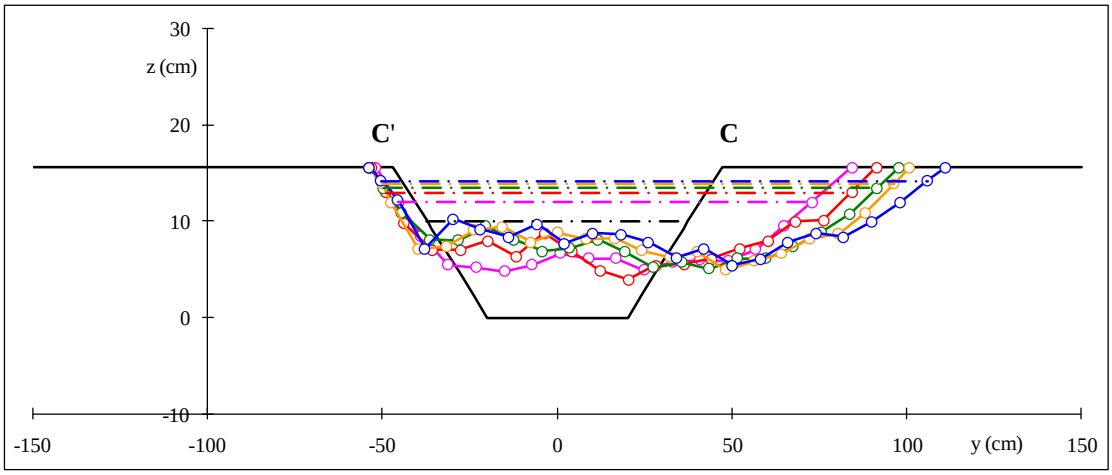

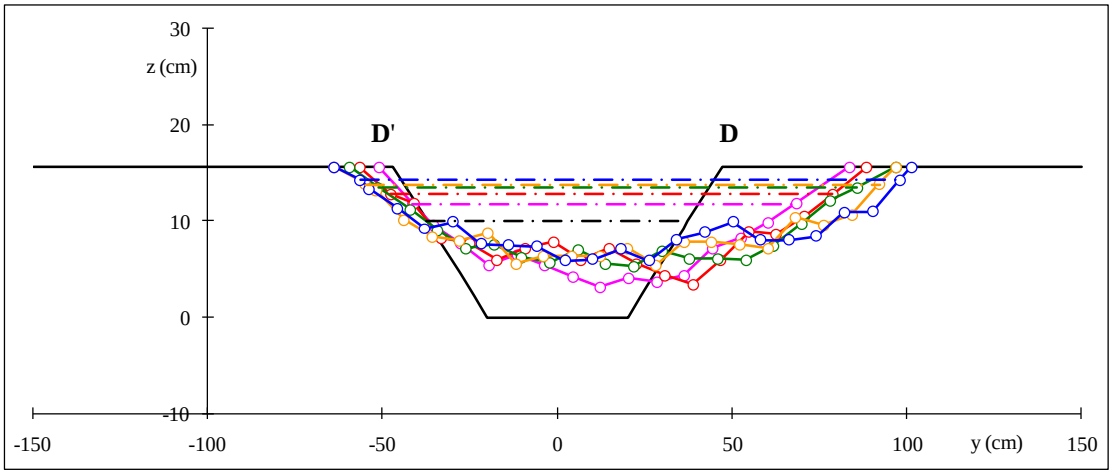

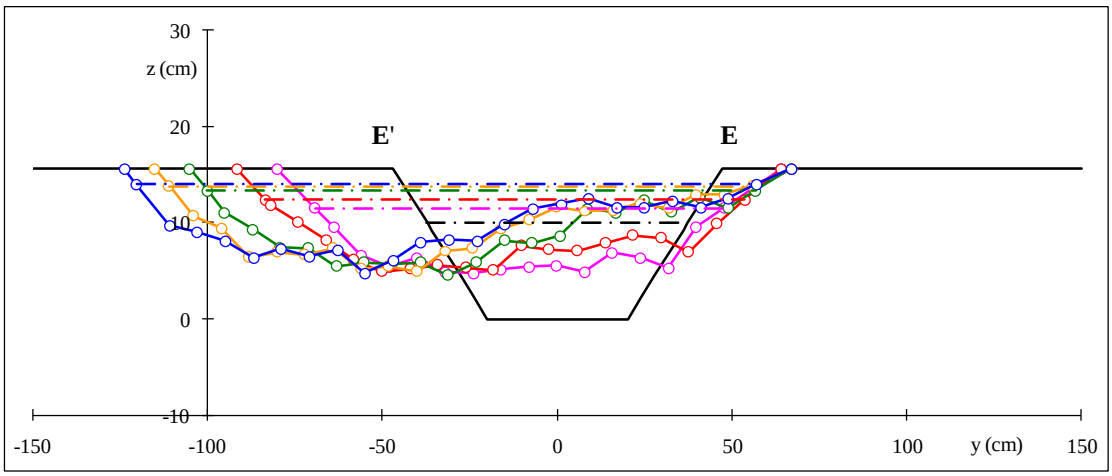

C-10. (Continued)

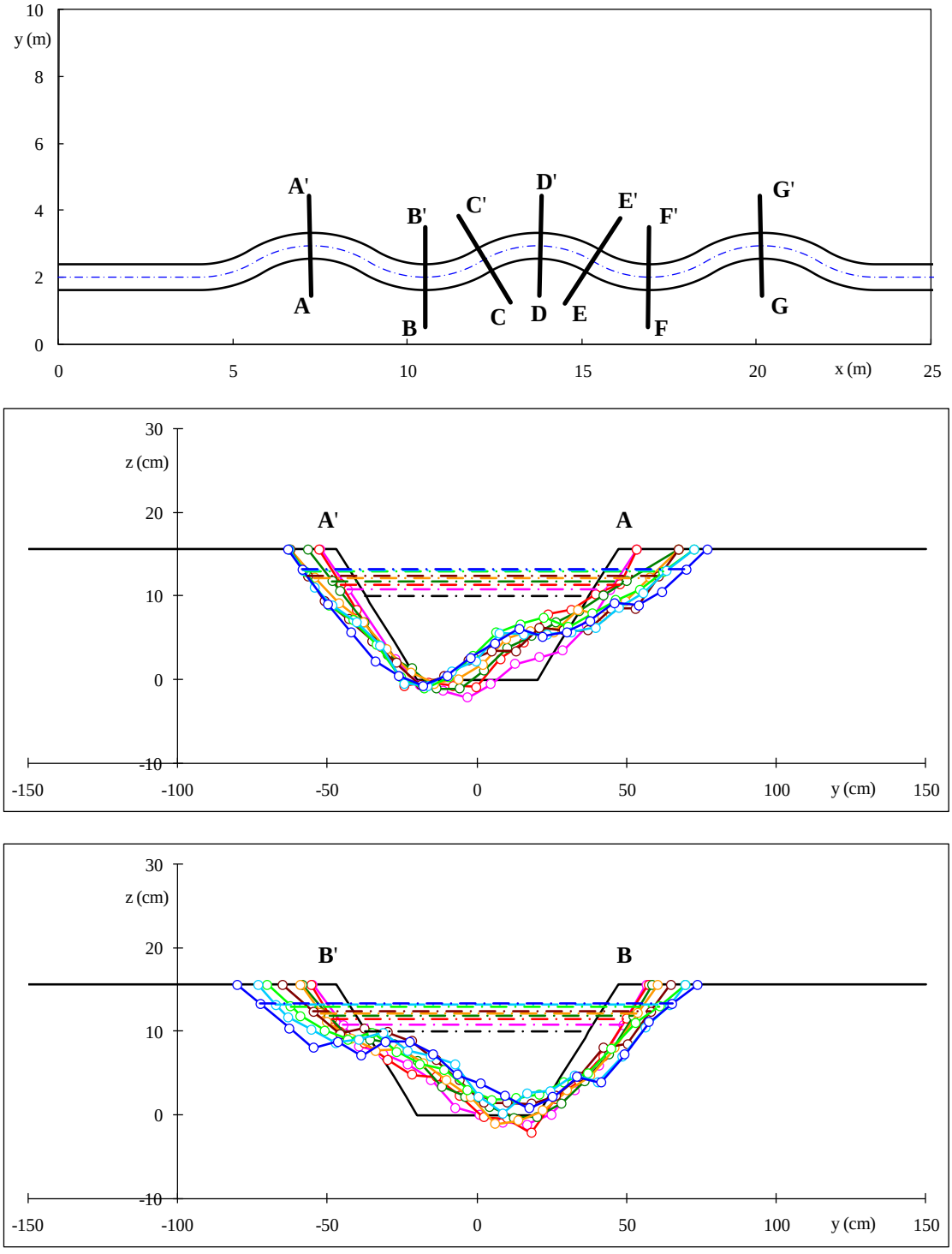

C-11. Channel Cross Section Profiles of Case 12: ○ measurements; — 0 hr; — 3 hr; — 6 hr; — 9 hr; — 15 hr; — 21 hr; — 33 hr

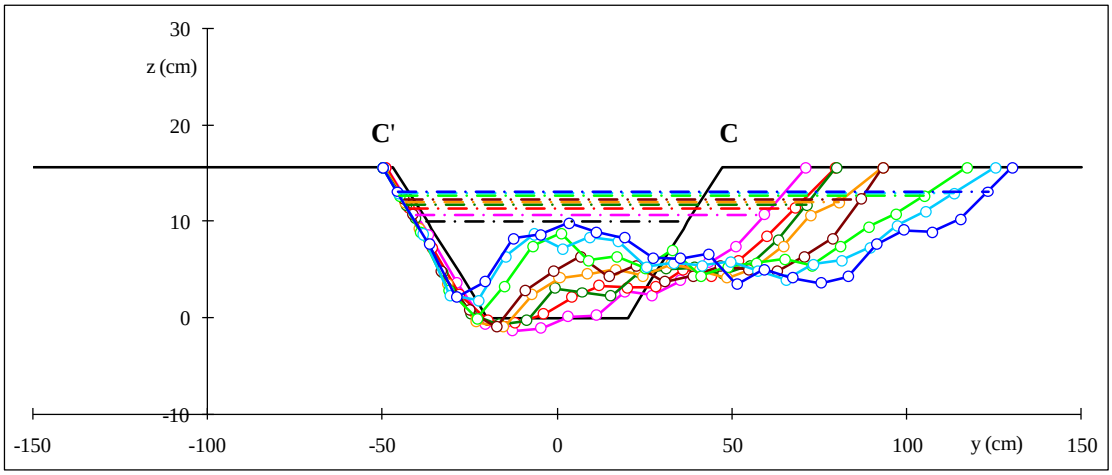

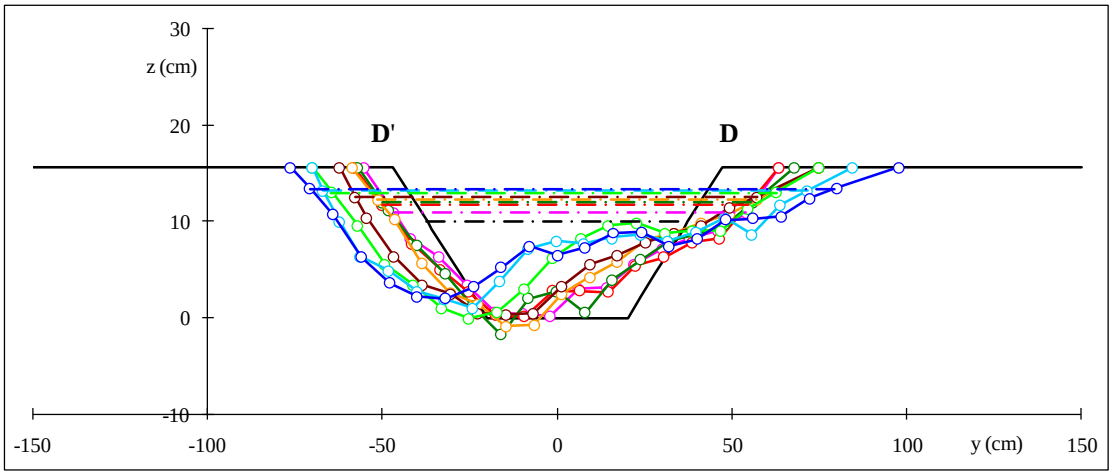

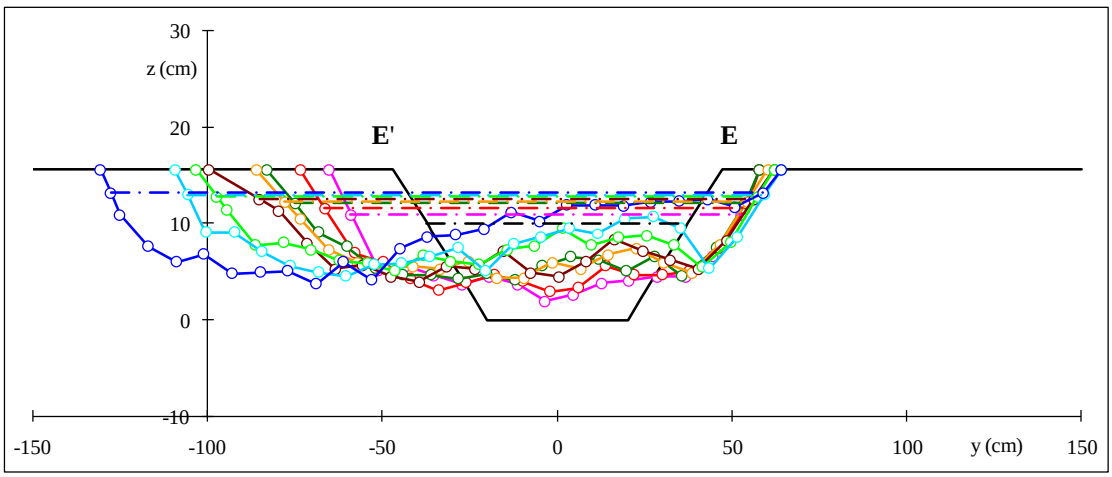

C-11. (Continued)

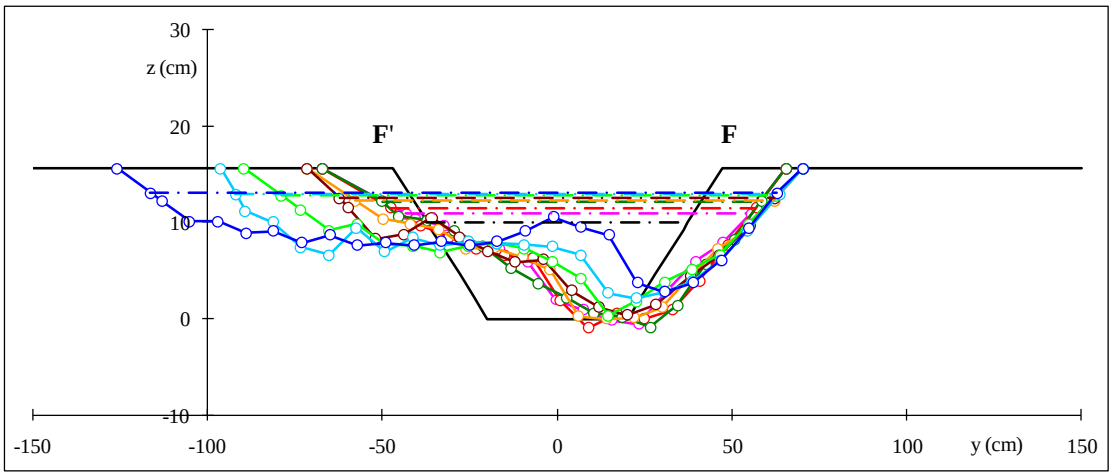

C-11. (Continued)

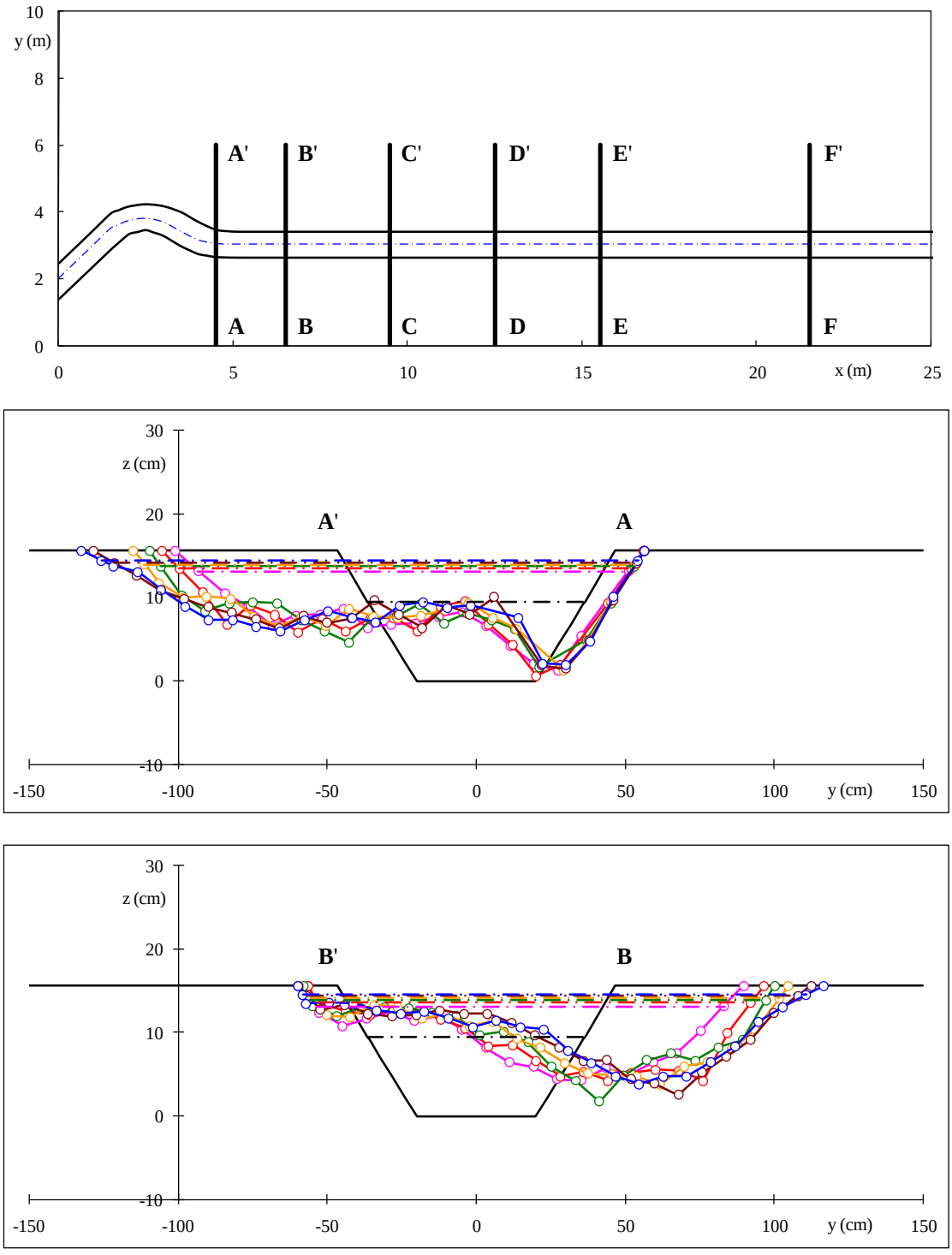

C-12. Channel Cross Section Profiles of Case 13: ○ measurements; — 0 hr; — 3 hr; — 6 hr; — 12 hr; — 18 hr; — 28 hr; — 38 hr

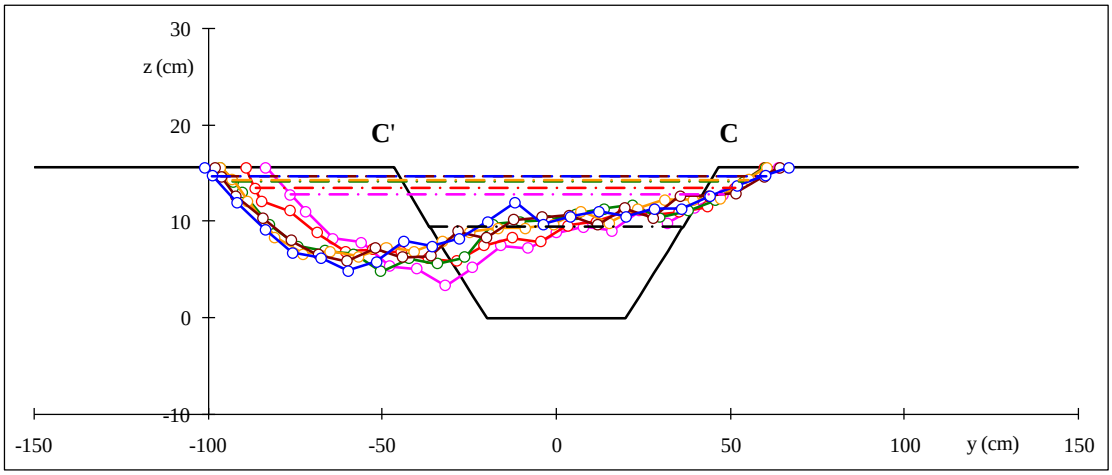

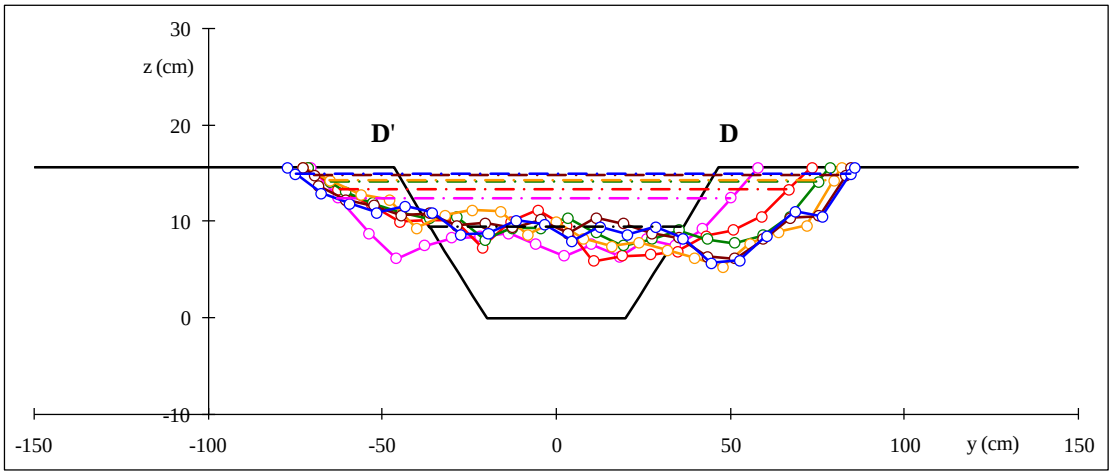

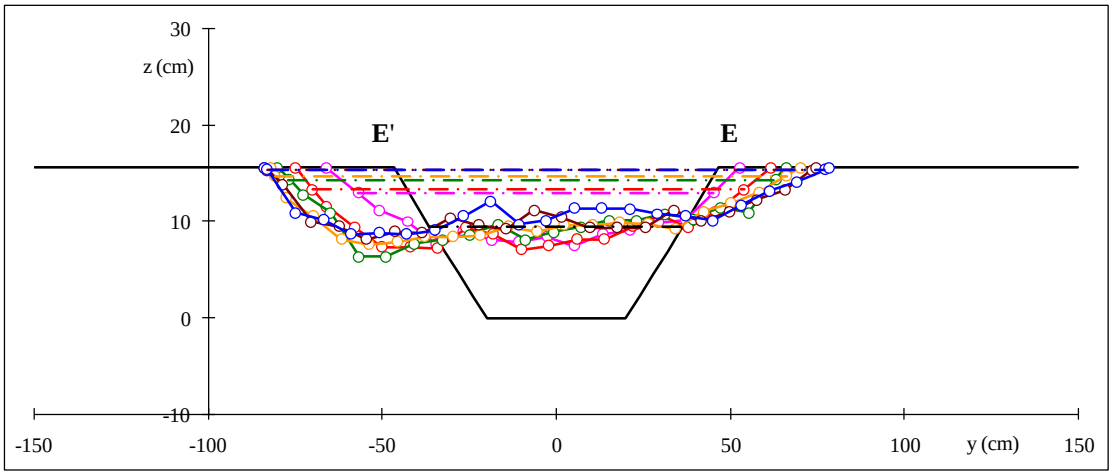

C-12. (Continued)

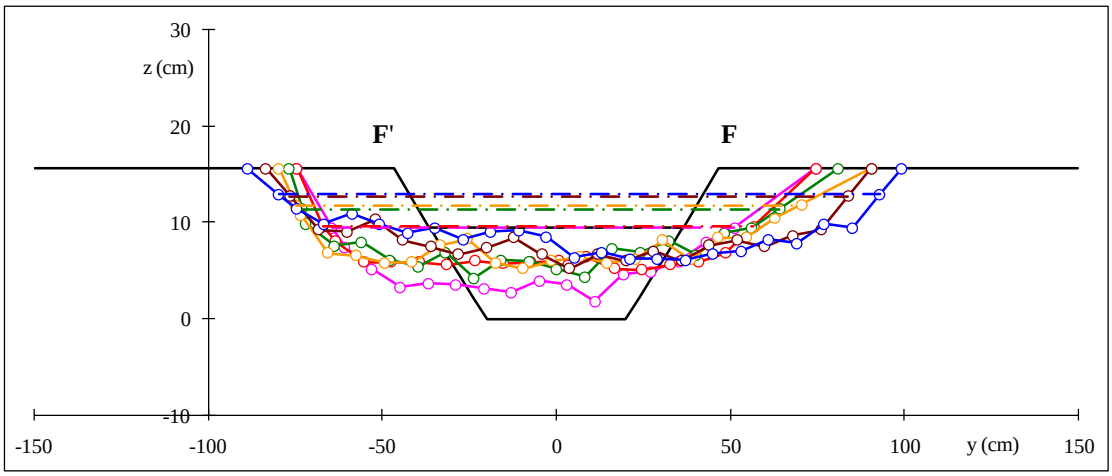

C-12. (Continued)

APPENDIX D

CROSS SECTION MEASUREMENTS

(a)

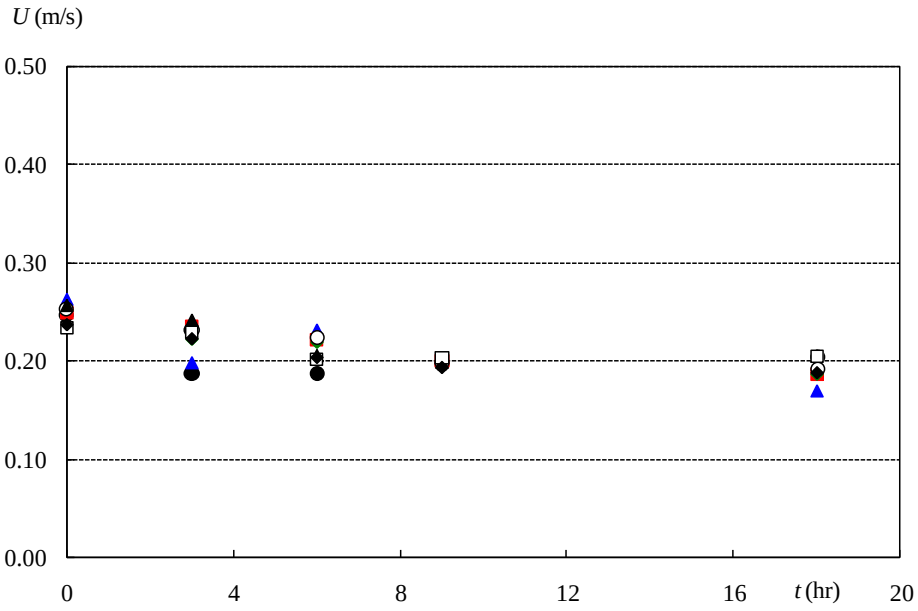

(b)

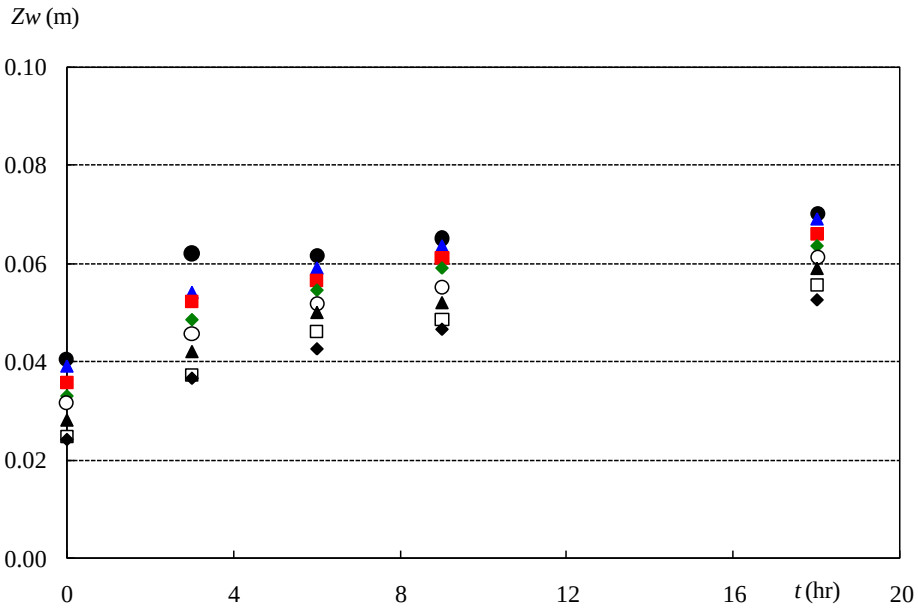

D-1. (a) Mean velocity *U*; (b) water elevation *Zw*; (c) water depth *h*; (d) Froude number *Fr* measurements of case 01, ● section A; ▲ section B; ■ section C; ♦ section D; ○ section E; ▲ section F; □ section G; ♦ section H

(c)

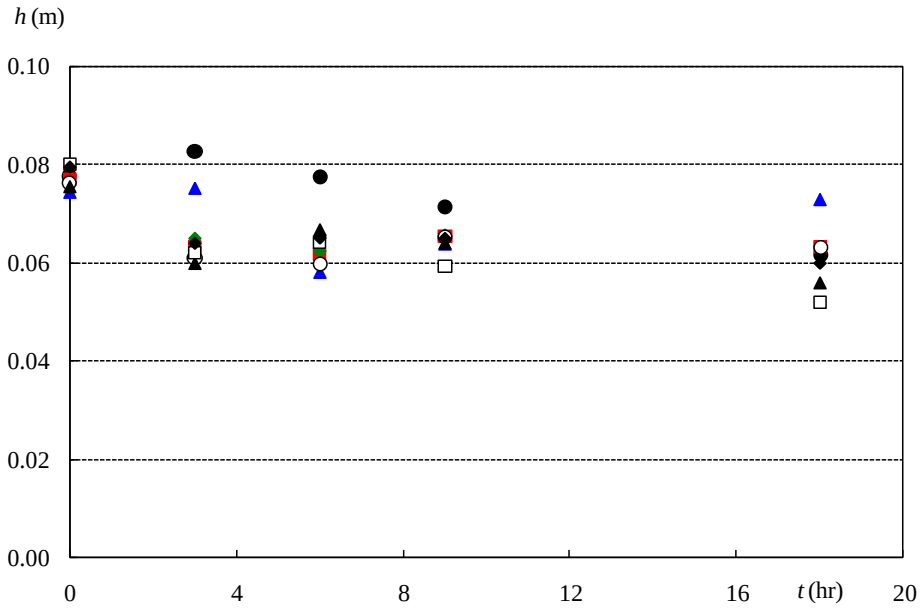

(d)

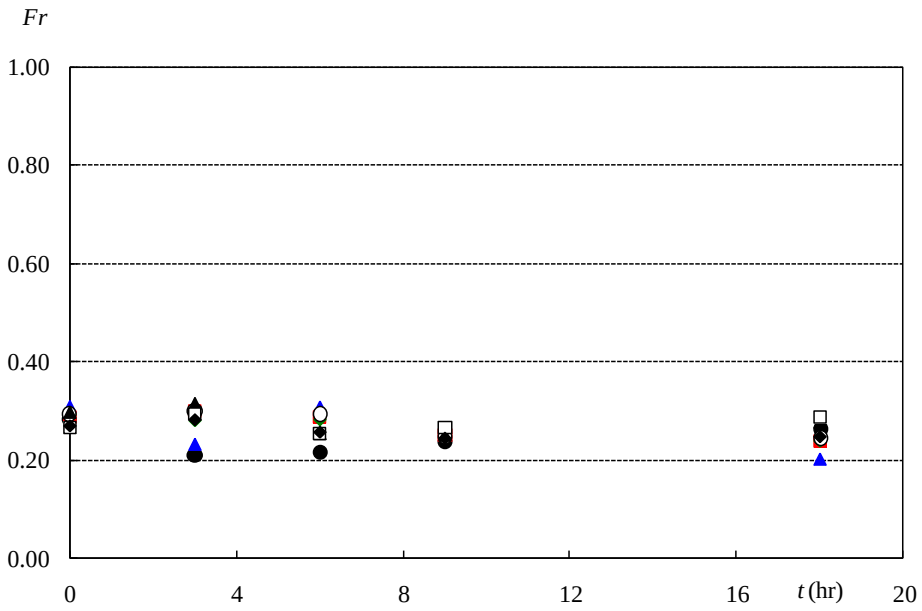

D-1. (Continued)

(a)

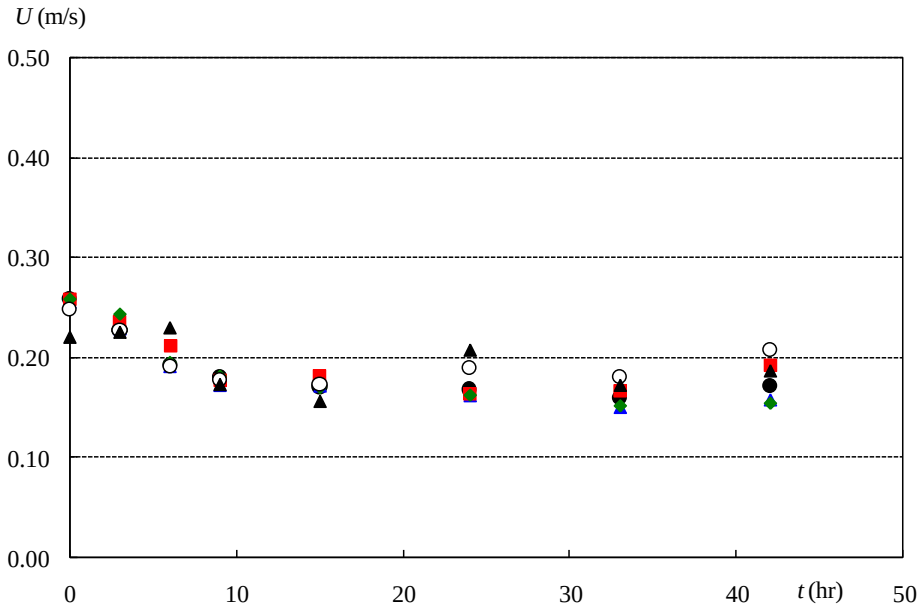

(b)

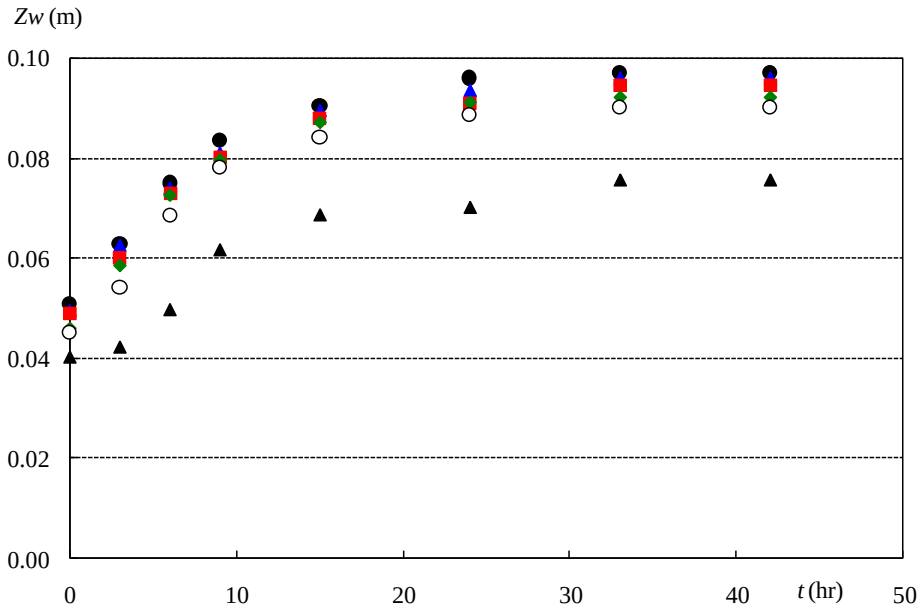

D-2. (a) Mean velocity *U*; (b) water elevation *Zw*; (c) water depth *h*; (d) Froude number *Fr* measurements of case 02, ● section A; ▲ section B; ■ section C; ♦ section D; ○ section E; ▲ section F

(c)

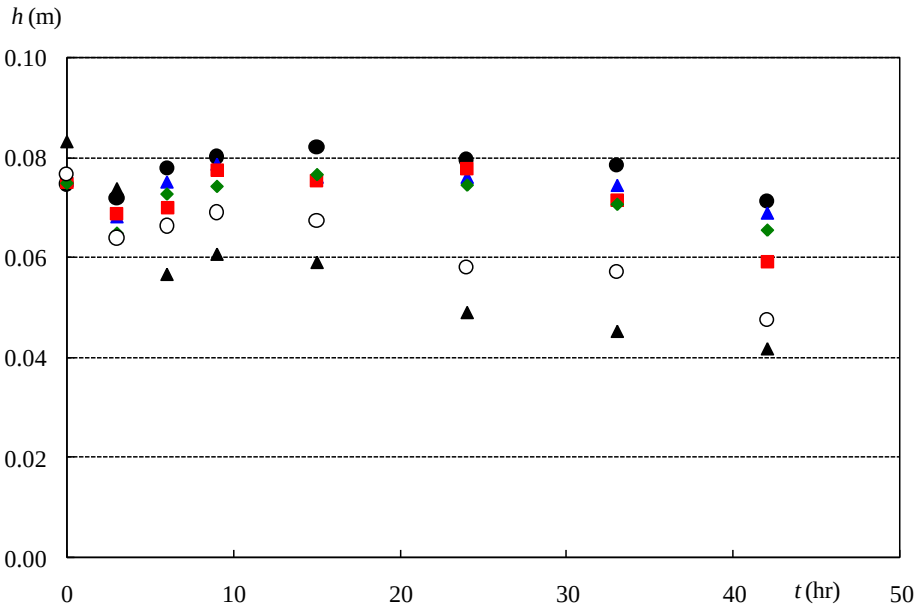

(d)

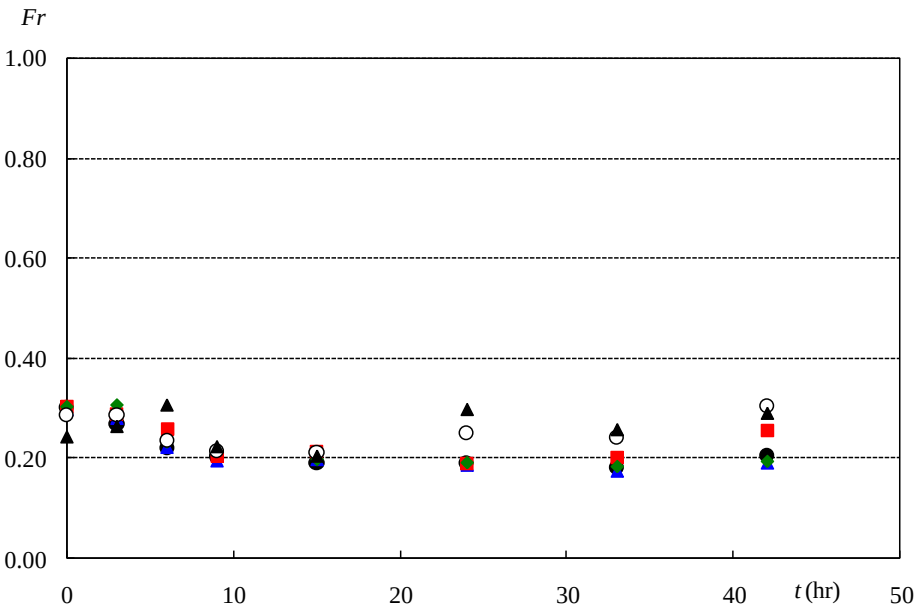

D-2. (Continued)

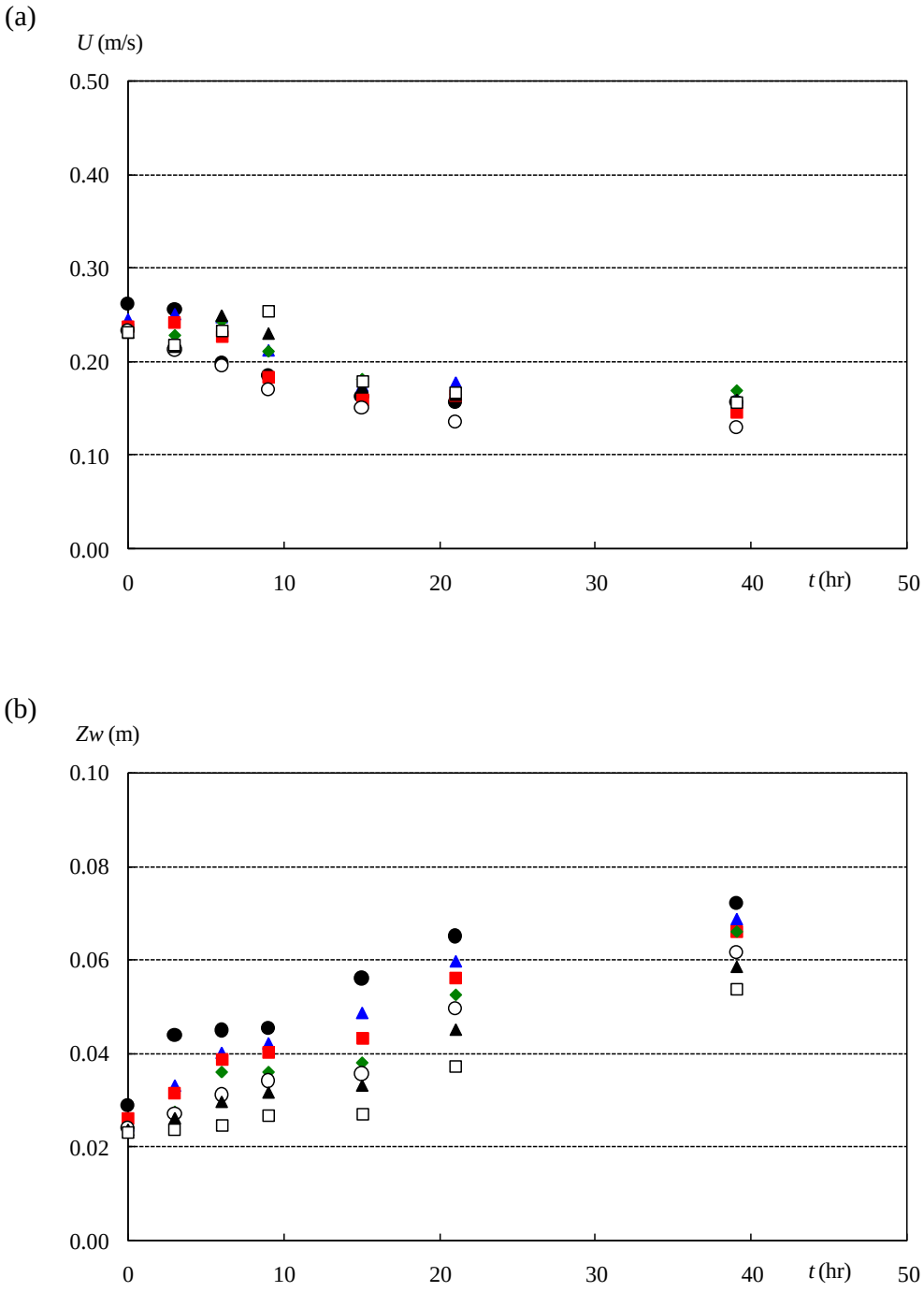

D-3. (a) Mean velocity *U*; (b) water elevation *Zw*; (c) water depth *h*; (d) Froude number *Fr* measurements of case 03, ● section A; ▲ section B; ■ section C; ♦ section D; ○ section E; ▲ section F; □ section G

(c)

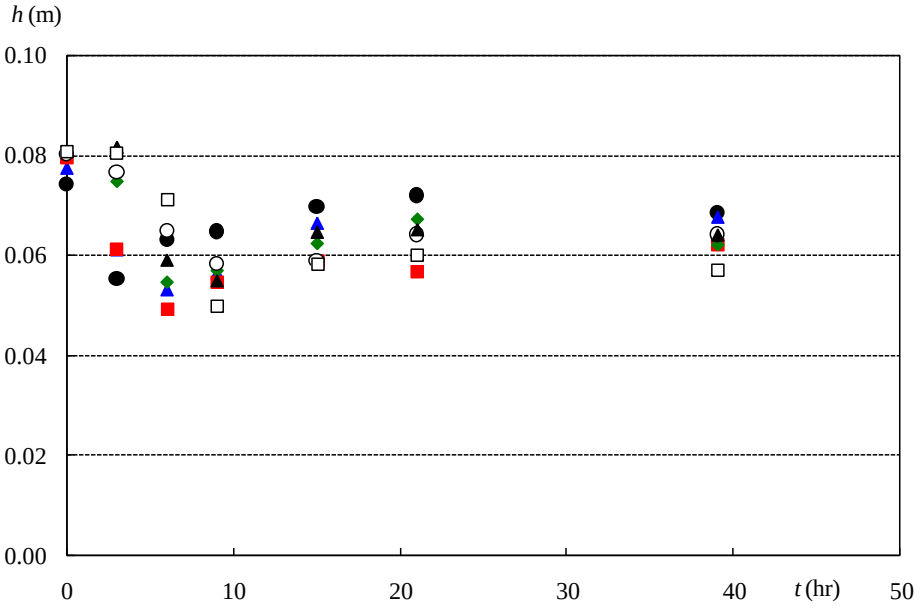

(d)

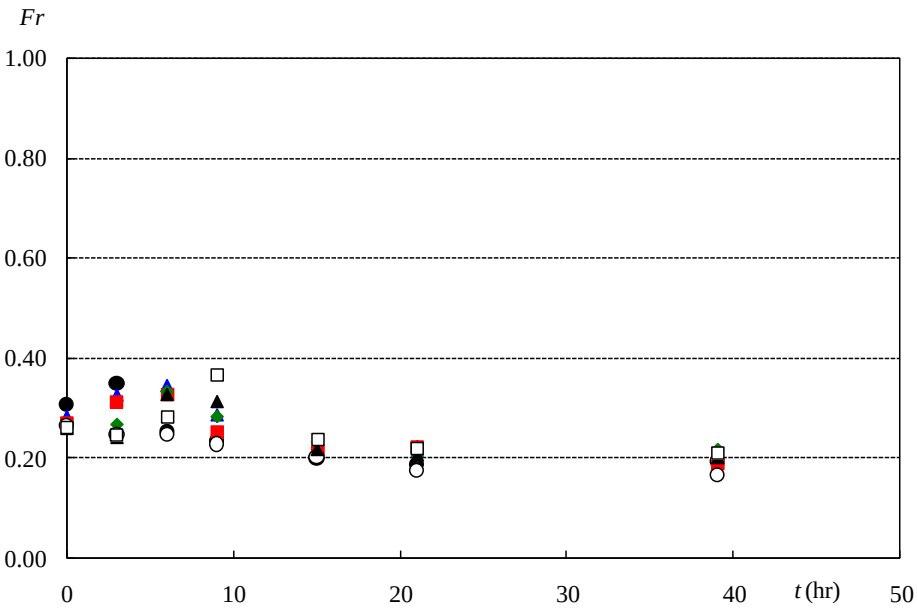

D-3. (Continued)

(a)

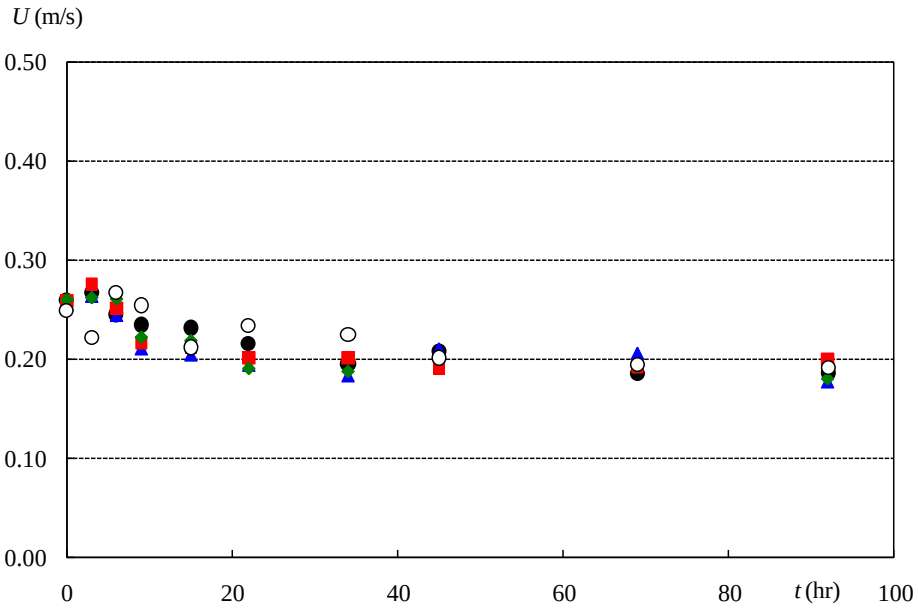

(b)

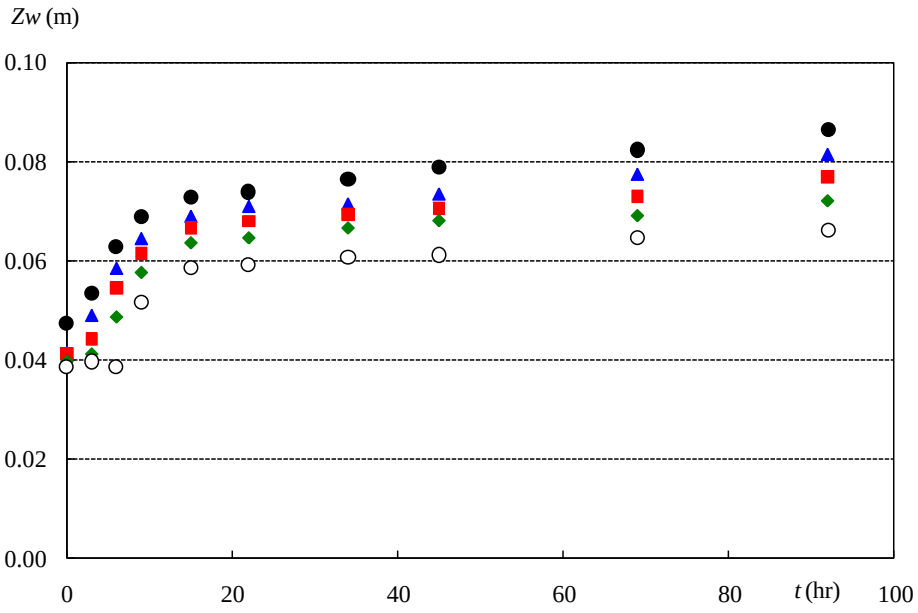

D-4. (a) Mean velocity *U*; (b) water elevation *Zw*; (c) water depth *h*; (d) Froude number *Fr* measurements of case 04, ● section A; ▲ section B; ■ section C; ♦ section D; ○ section E

(c)

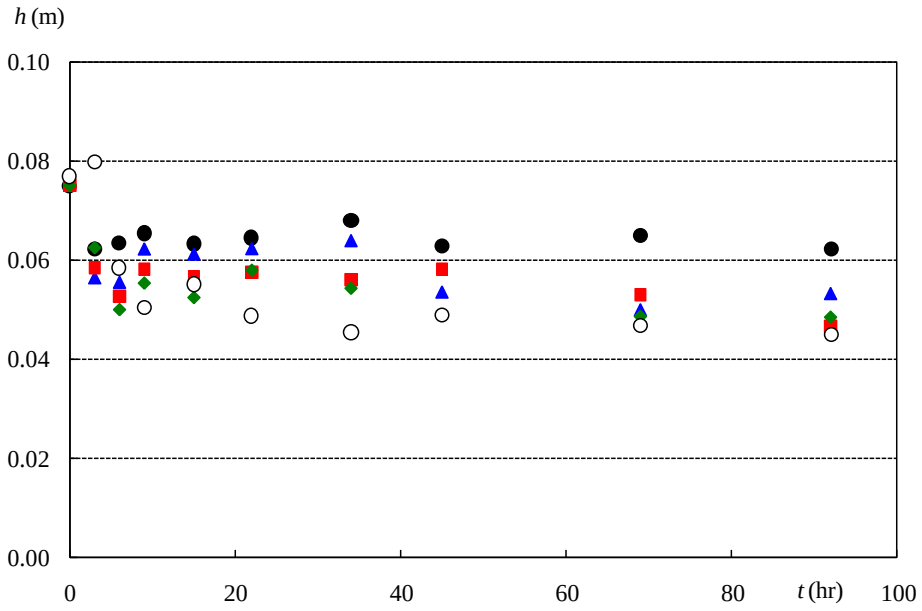

(d)

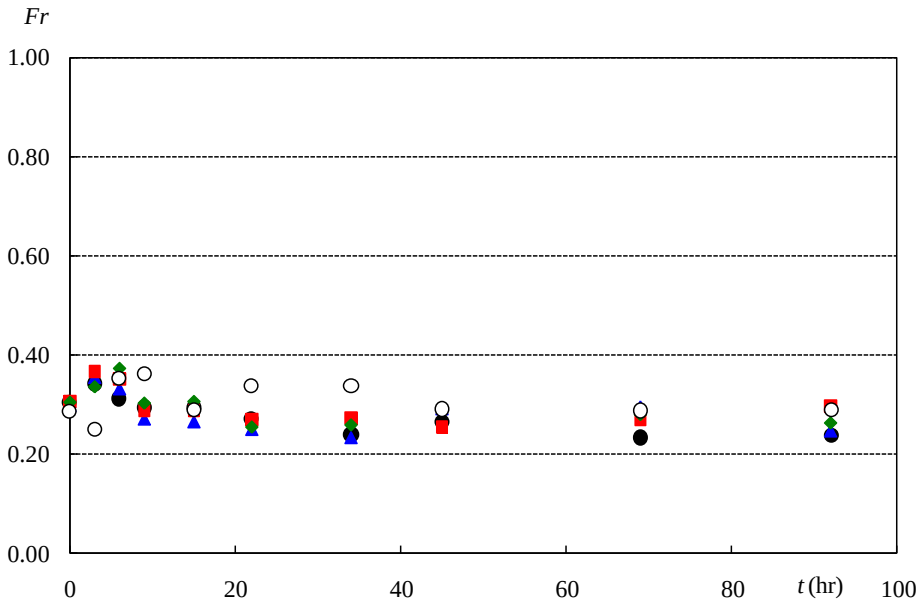

D-4. (Continued)

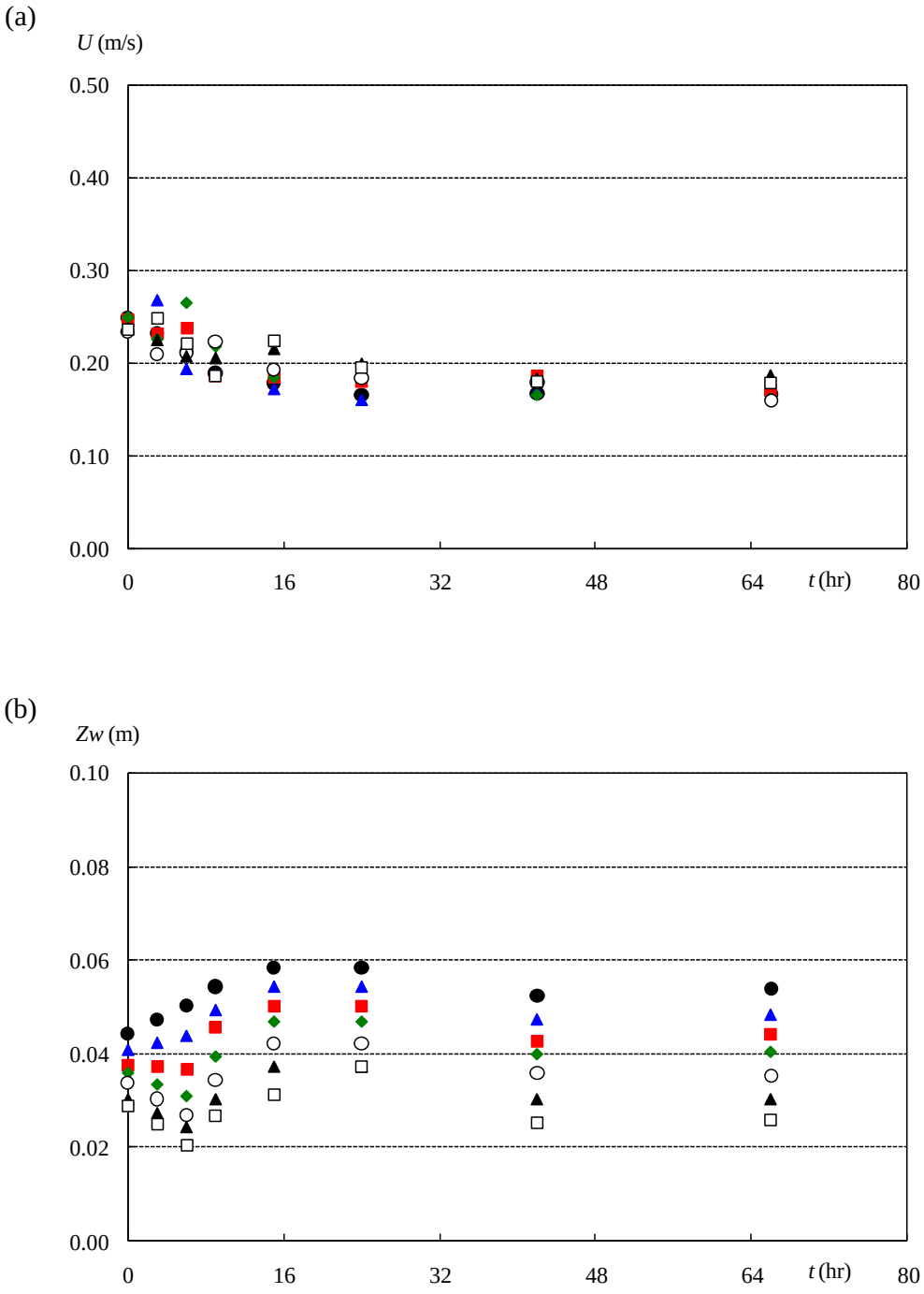

D-5. (a) Mean velocity *U*; (b) water elevation *Zw*; (c) water depth *h*; (d) Froude number *Fr* measurements of case 05, ● section A; ▲ section B; ■ section C; ♦ section D; ○ section E; ▲ section F; □ section G

(c)

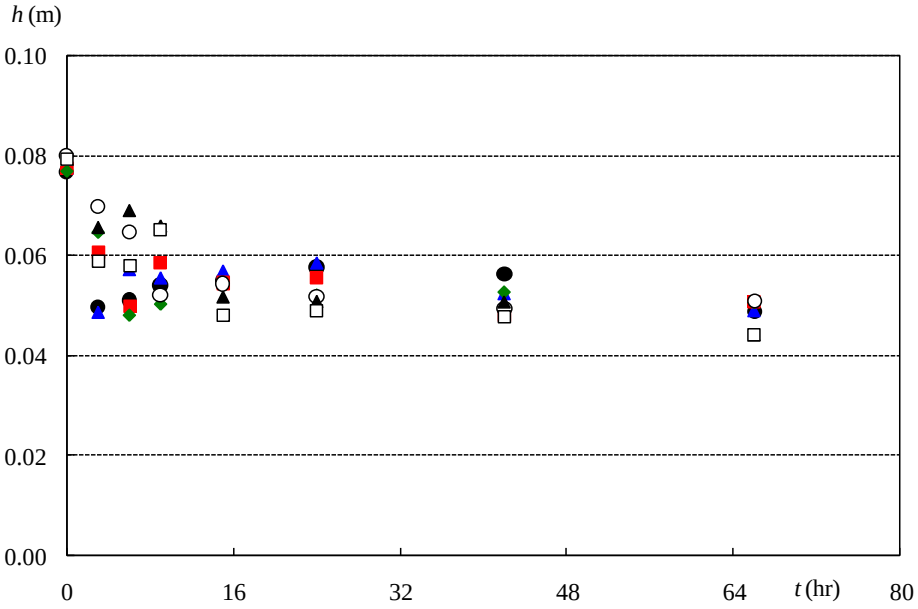

(d)

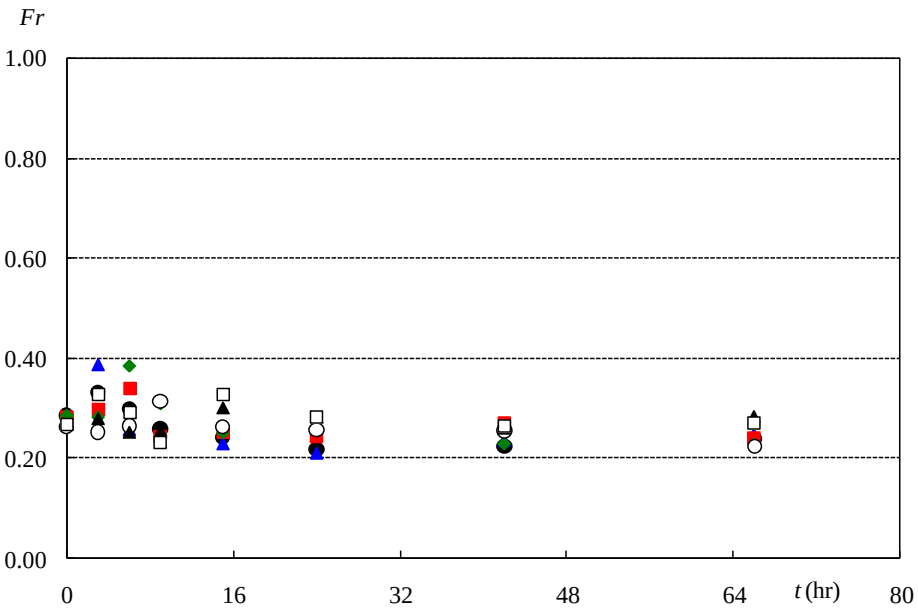

D-5. (Continued)

(a)

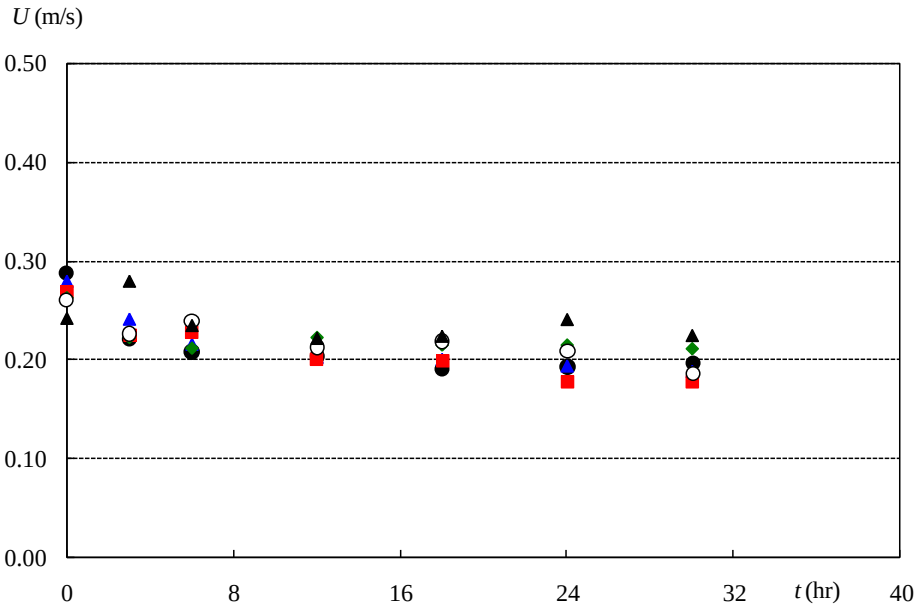

(b)

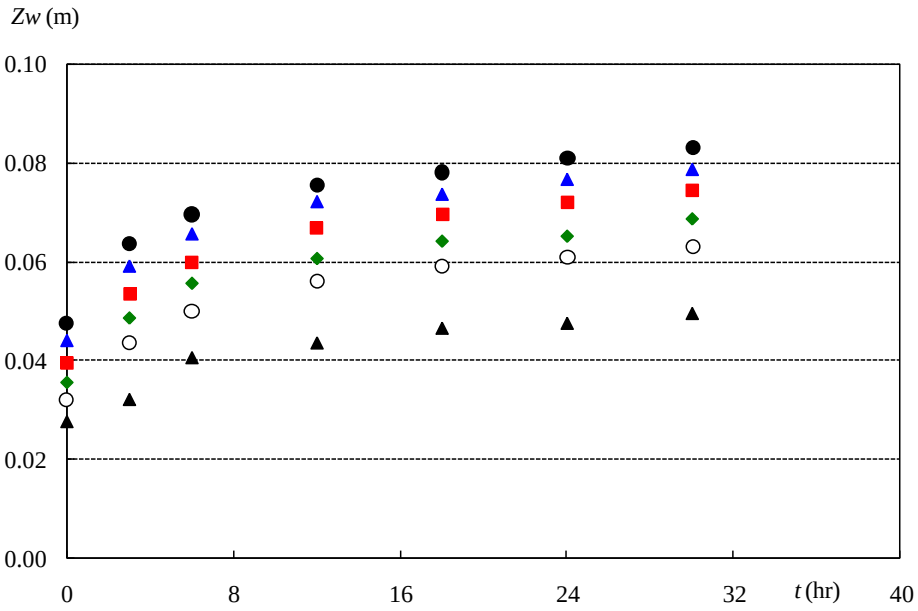

D-6. (a) Mean velocity *U*; (b) water elevation *Zw*; (c) water depth *h*; (d) Froude number *Fr* measurements of case 06, ● section A; ▲ section B; ■ section C; ♦ section D; ○ section E; ▲ section F

(c)

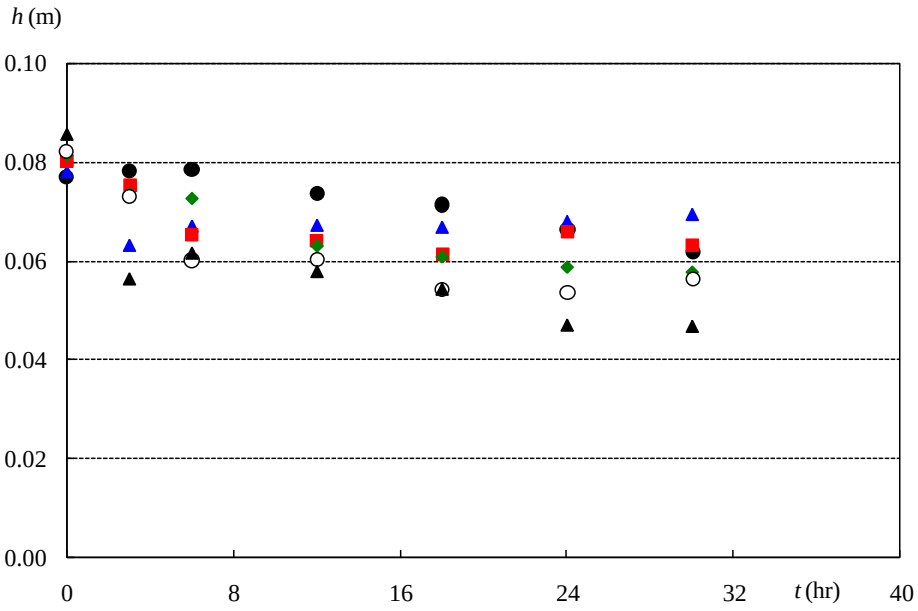

(d)

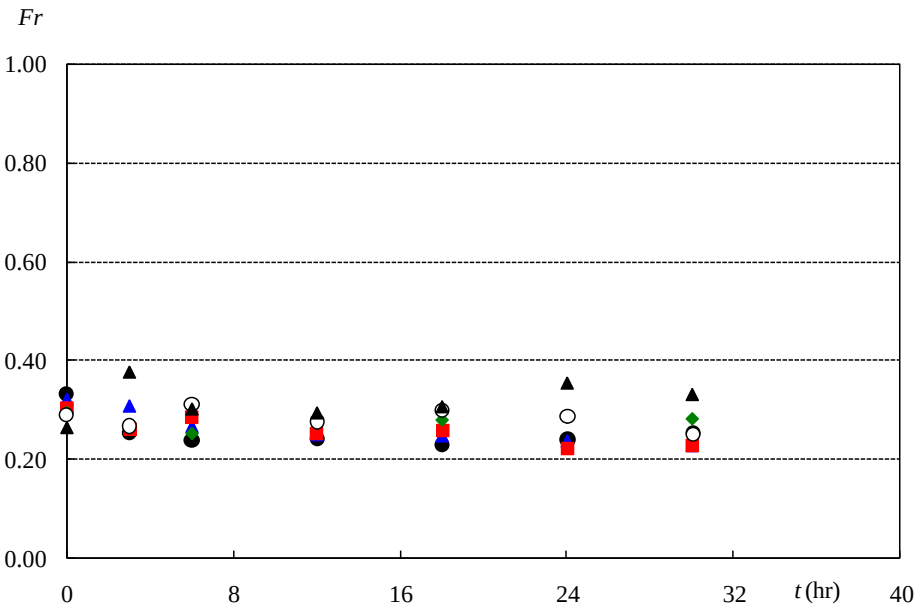

D-6. (Continued)

(a)

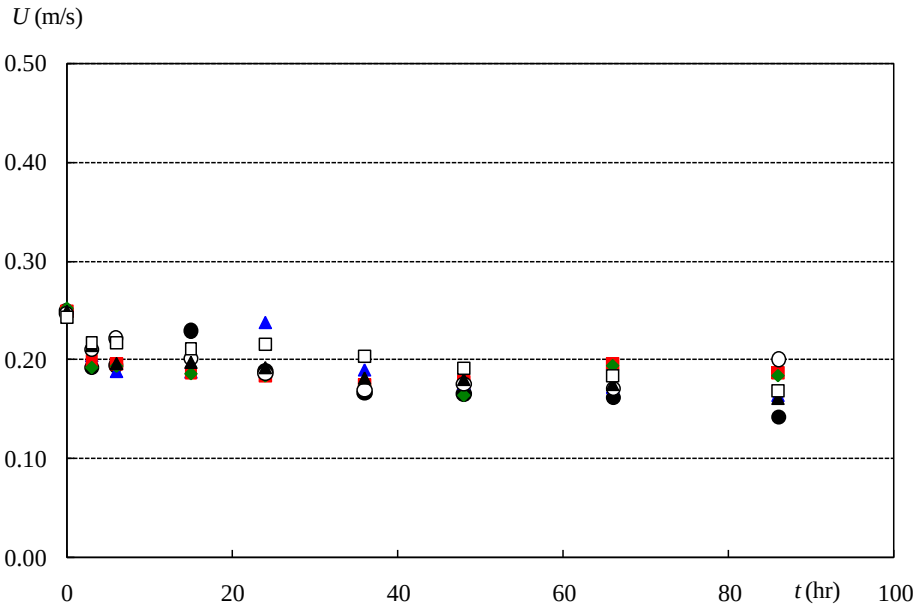

(b)

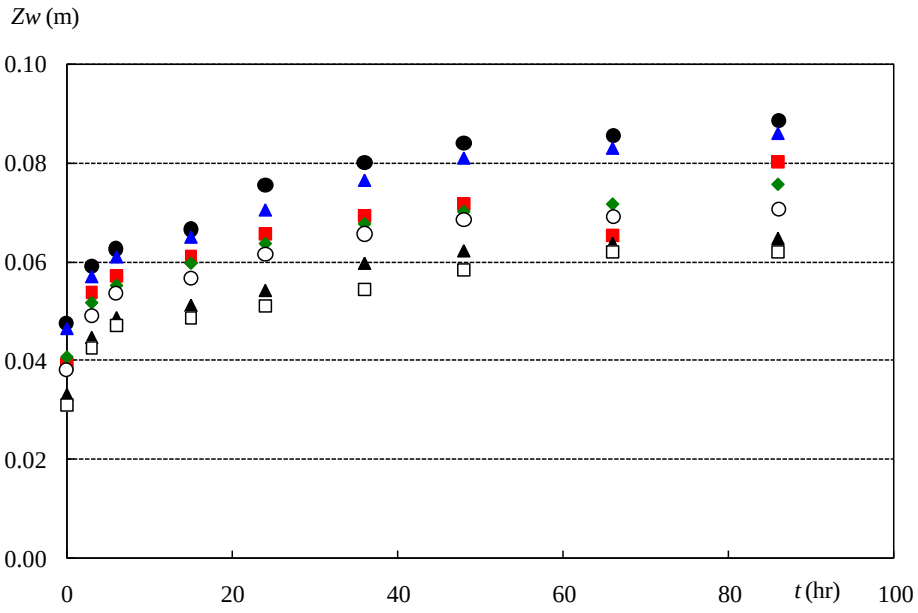

D-7. (a) Mean velocity *U*; (b) water elevation *Zw*; (c) water depth *h*; (d) Froude number *Fr* measurements of case 07, ● section A; ▲ section B; ■ section C; ♦ section D; ○ section E; ▲ section F; □ section G7

(c)

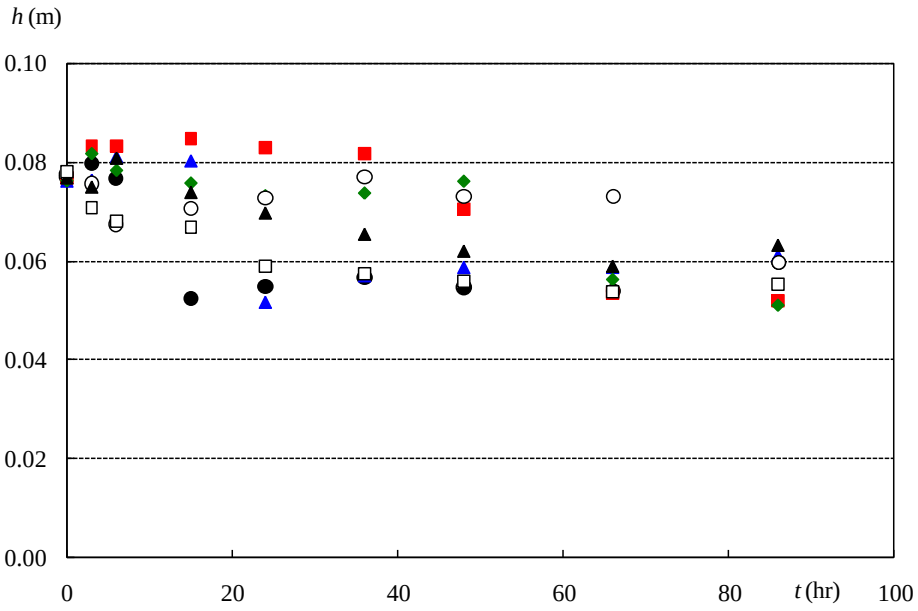

(d)

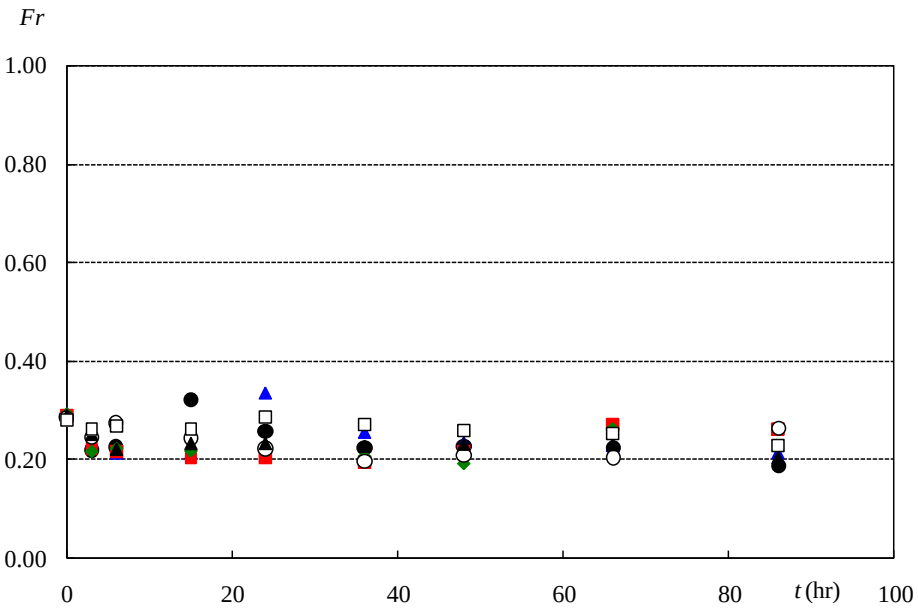

D-7. (Continued)

(a)

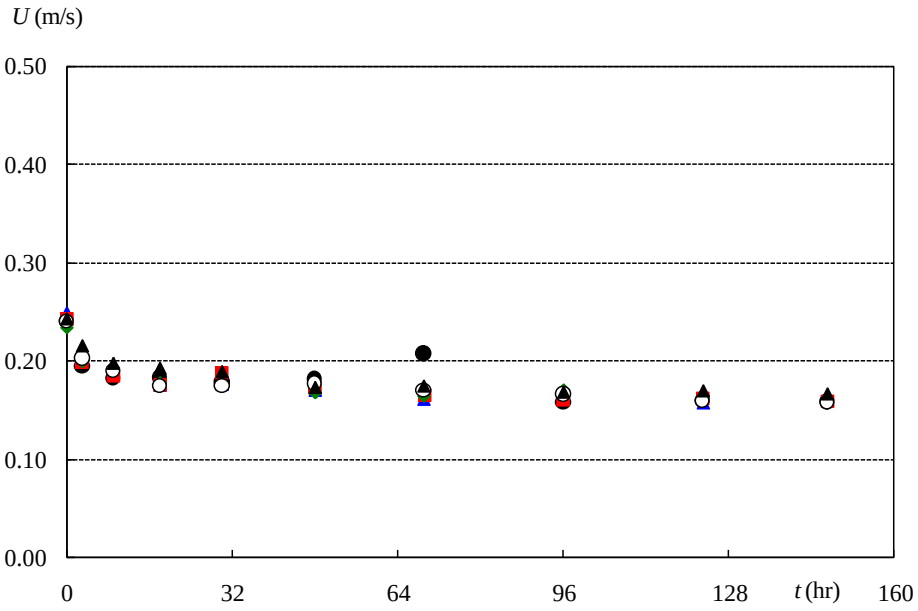

(b)

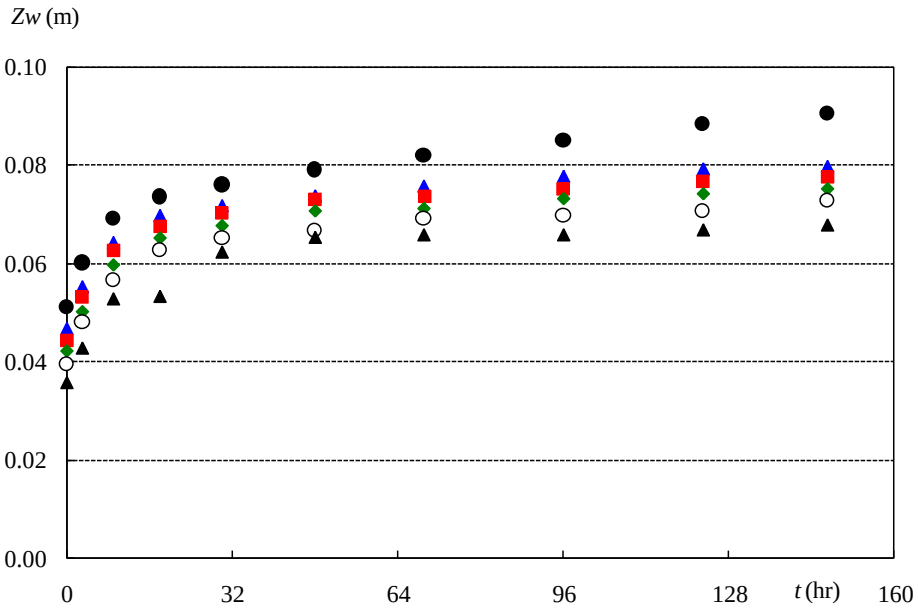

D-8. (a) Mean velocity *U*; (b) water elevation *Zw*; (c) water depth *h*; (d) Froude number *Fr* measurements of case 08, ● section A; ▲ section B; ■ section C; ♦ section D; ○ section E; ▲ section F

(c)

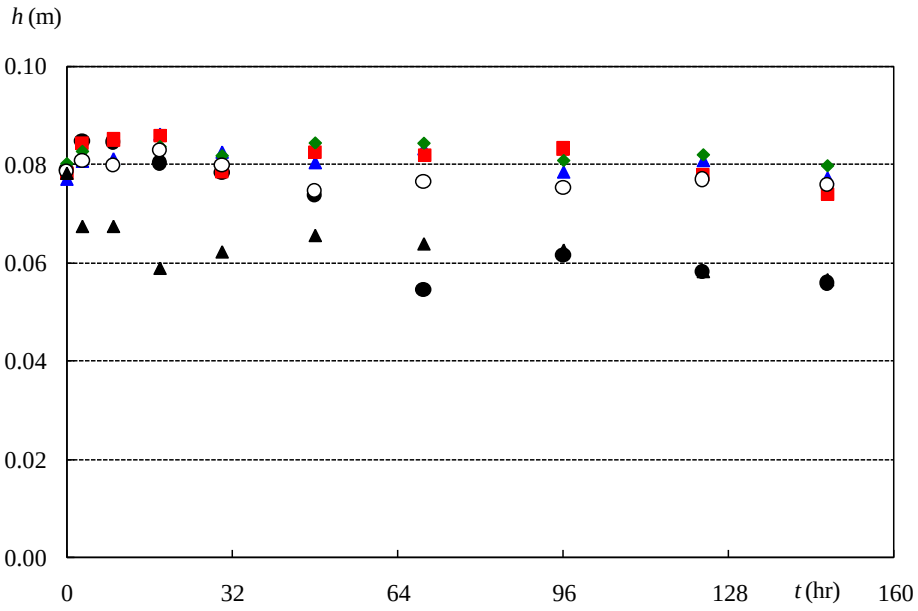

(d)

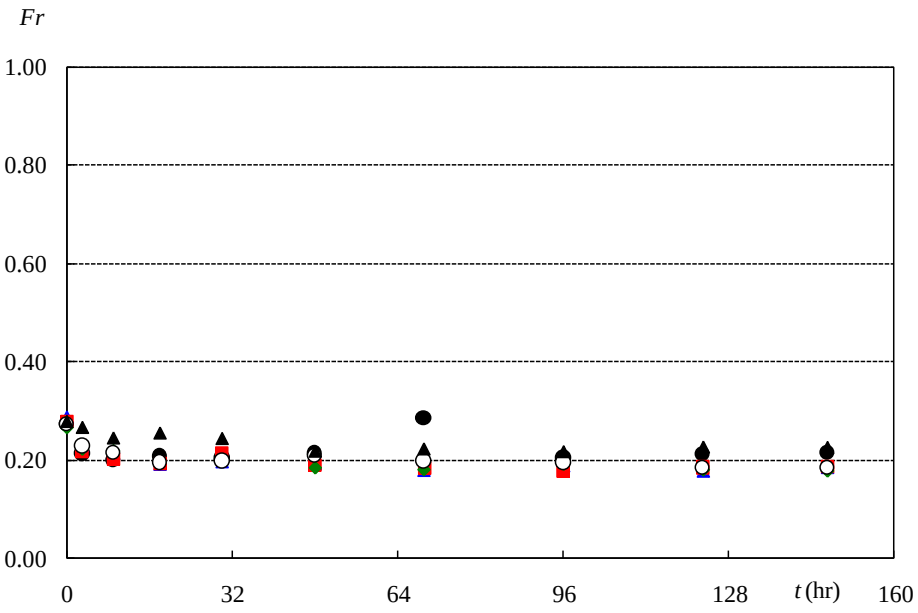

D-8. (Continued)

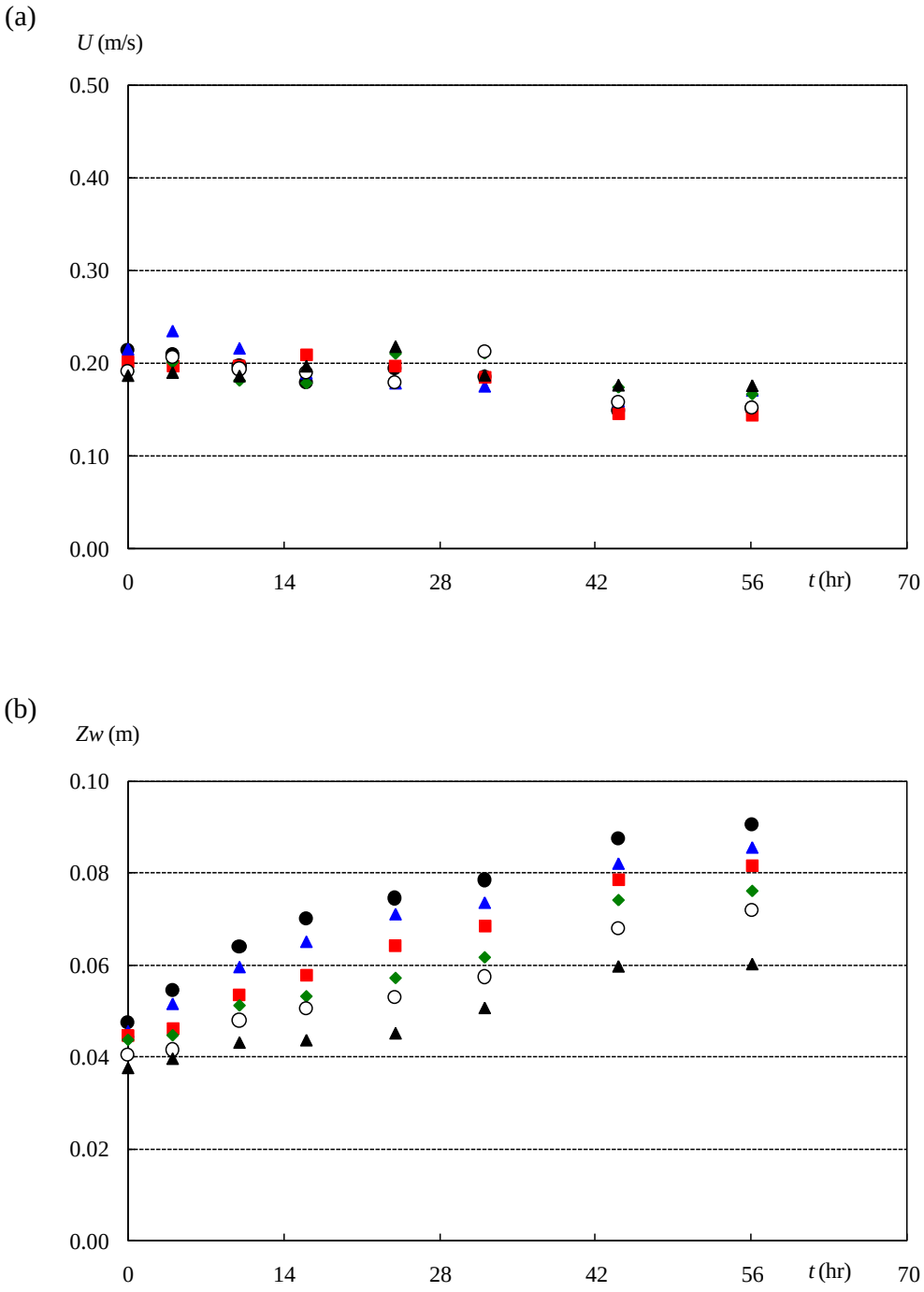

D-9. (a) Mean velocity *U*; (b) water elevation *Zw*; (c) water depth *h*; (d) Froude number *Fr* measurements of case 09, ● section A; ▲ section B; ■ section C; ♦ section D; ○ section E; ▲ section F

(c)

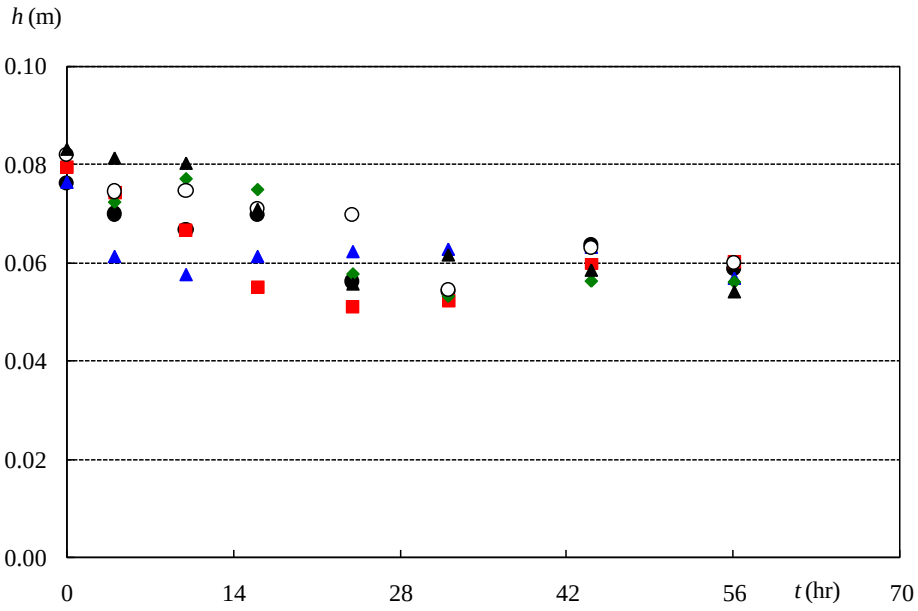

(d)

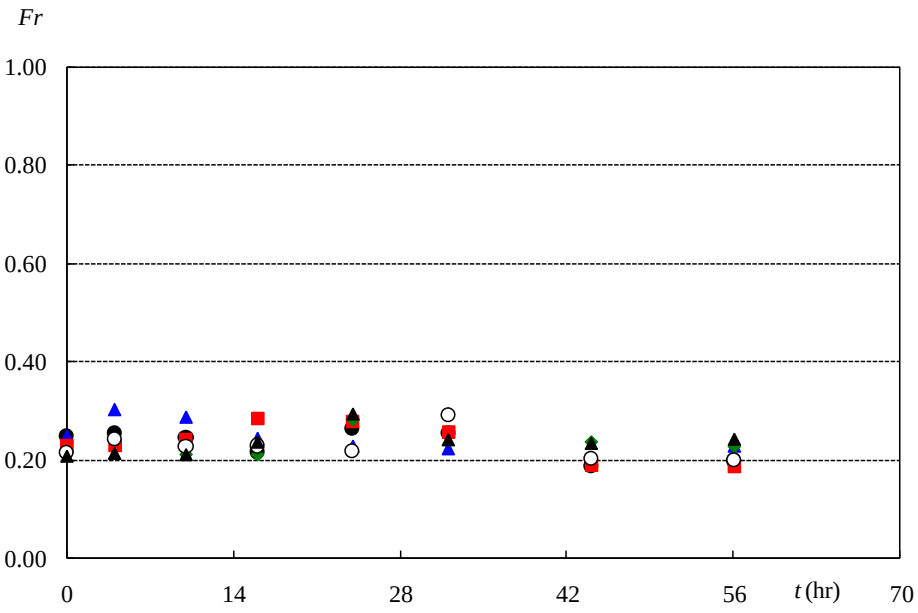

D-9. (Continued)

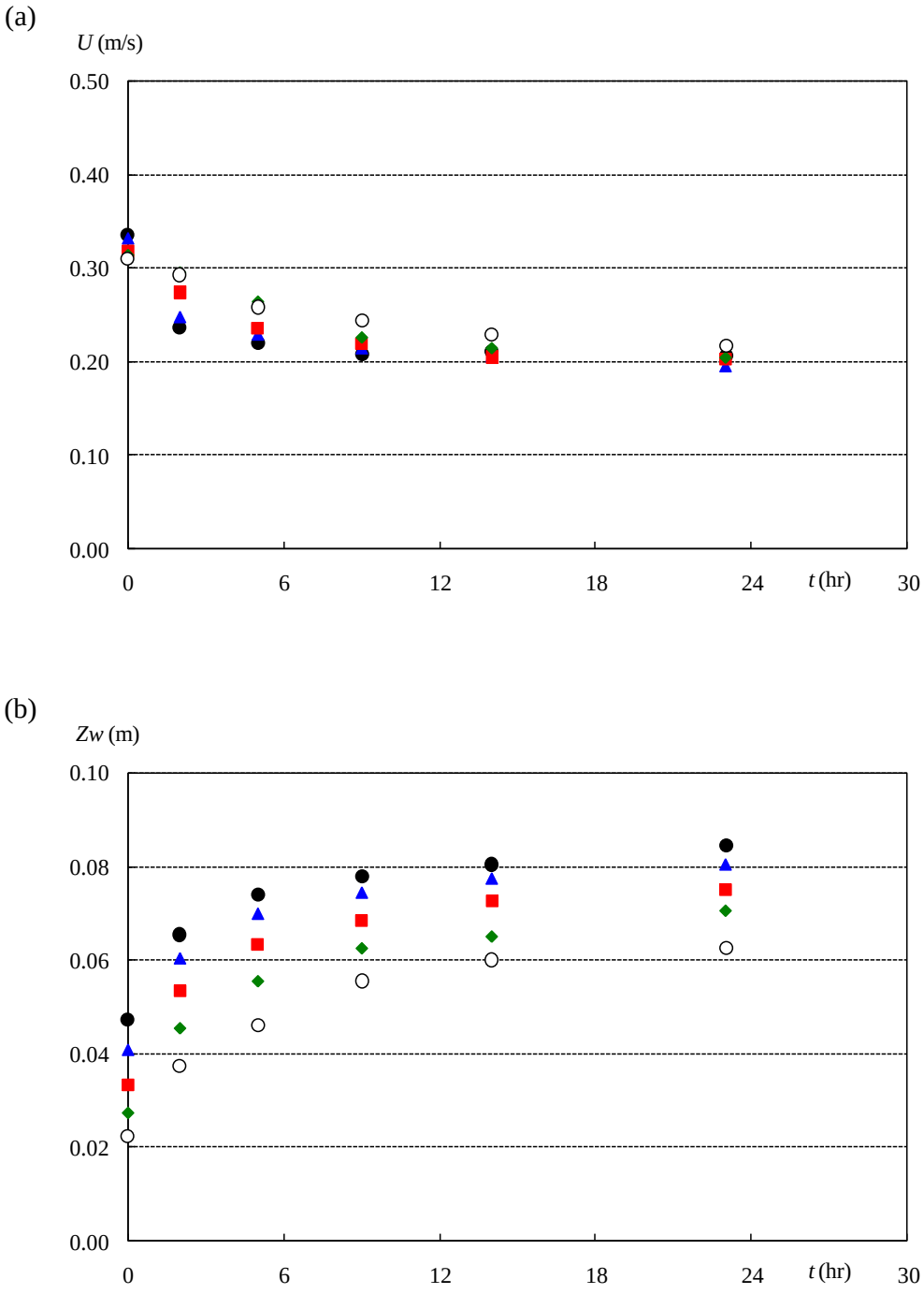

D-10. (a) Mean velocity *U*; (b) water elevation *Zw*; (c) water depth *h*; (d) Froude number *Fr* measurements of case 11, ● section A; ▲ section B; ■ section C; ♦ section D; ○ section E

(c)

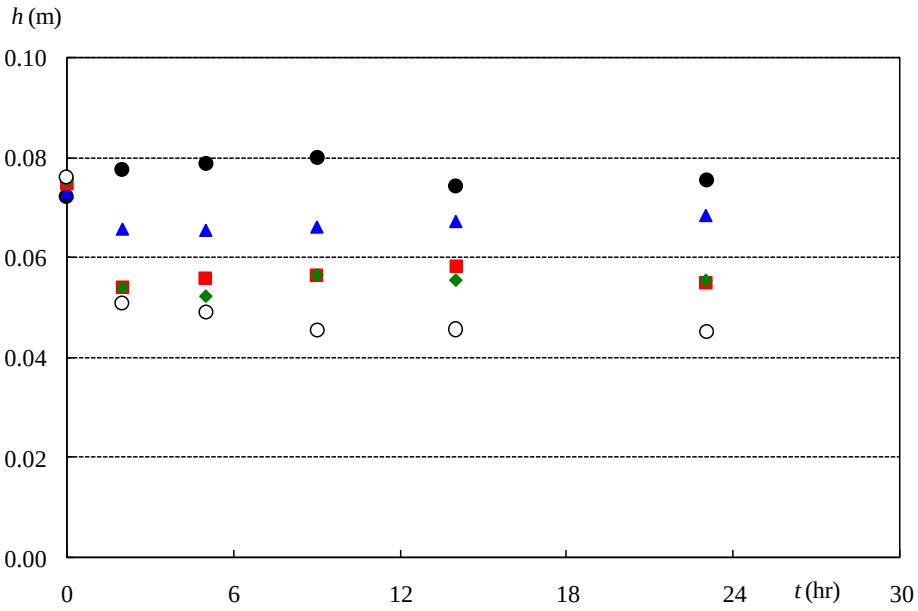

(d)

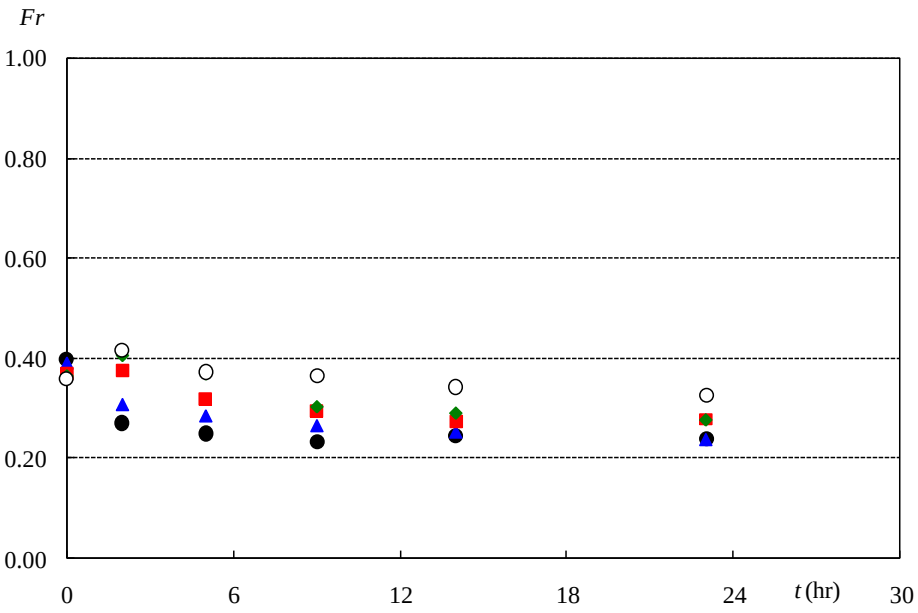

D-10. (Continued)

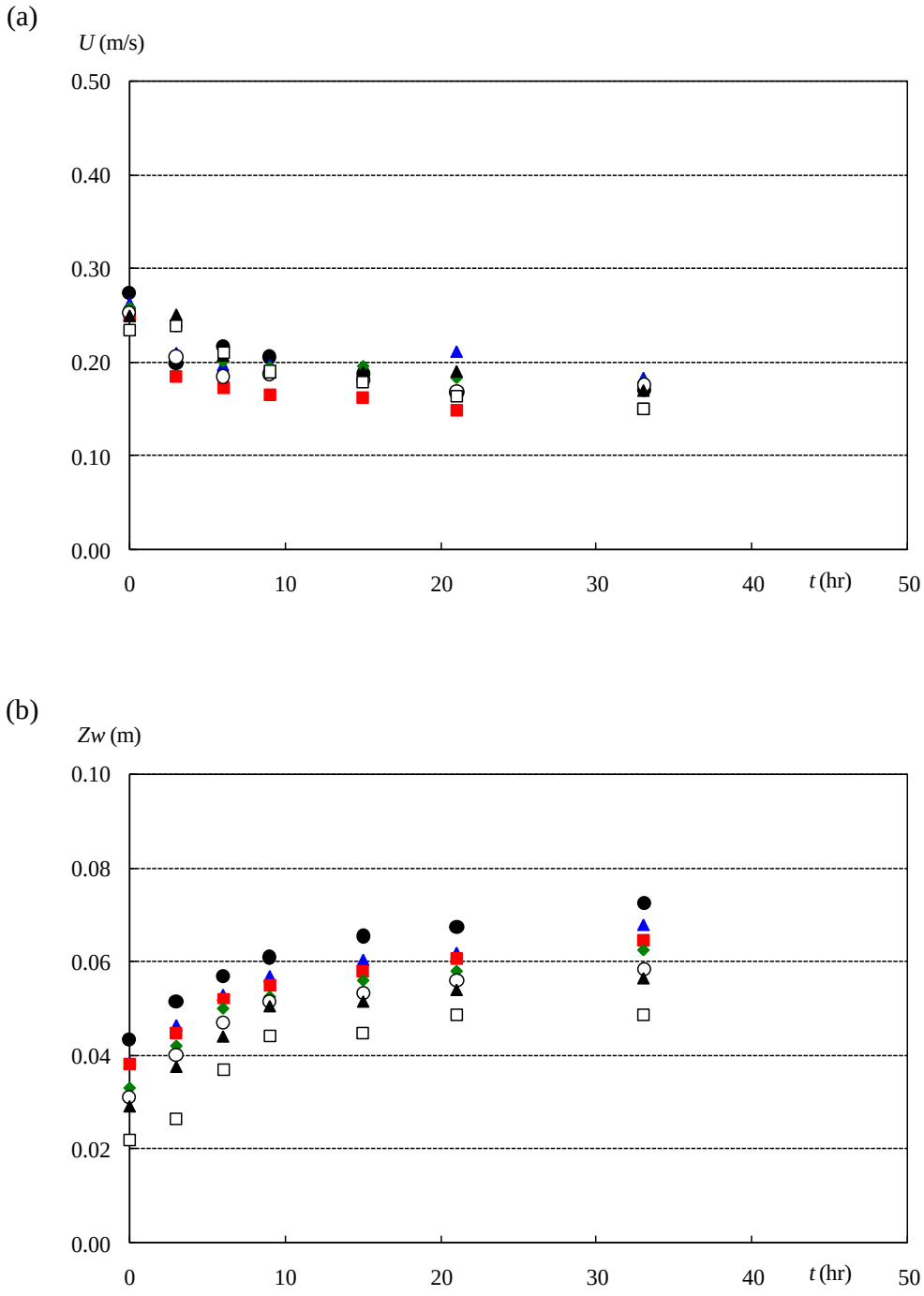

D-11. (a) Mean velocity *U*; (b) water elevation *Zw*; (c) water depth *h*; (d) Froude number *Fr* measurements of case 12, ● section A; ▲ section B; ■ section C; ♦ section D; ○ section E; ▲ section F; □ section G

(c)

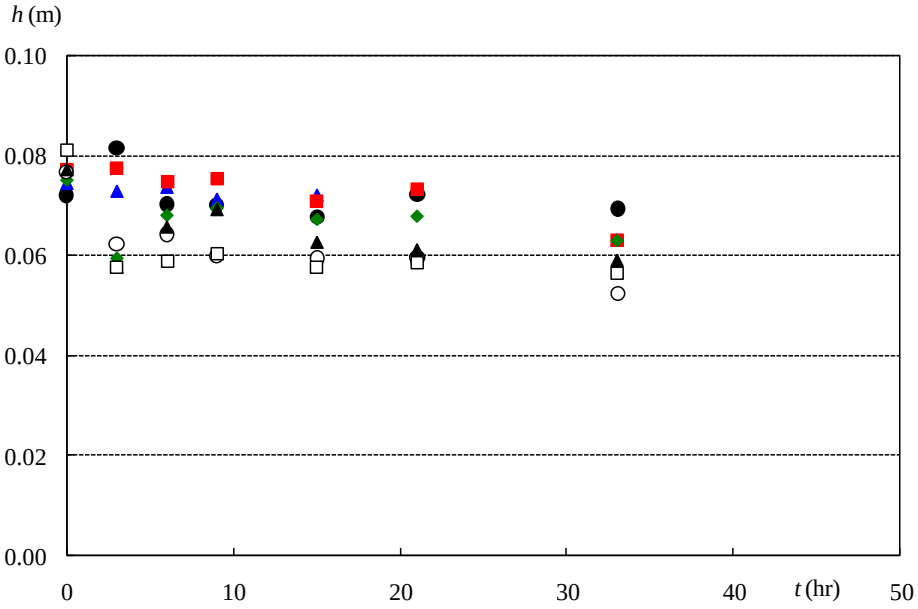

(d)

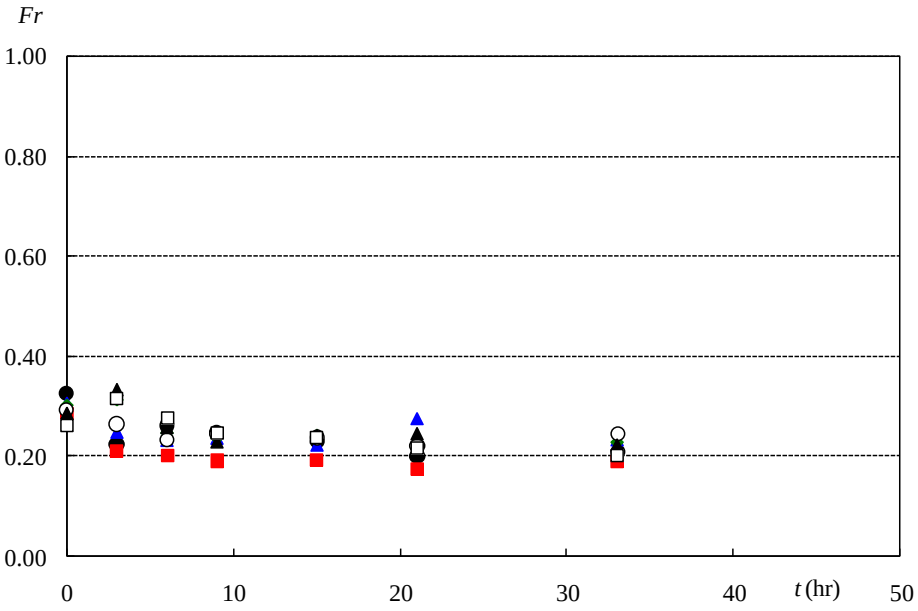

D-11. (Continued)

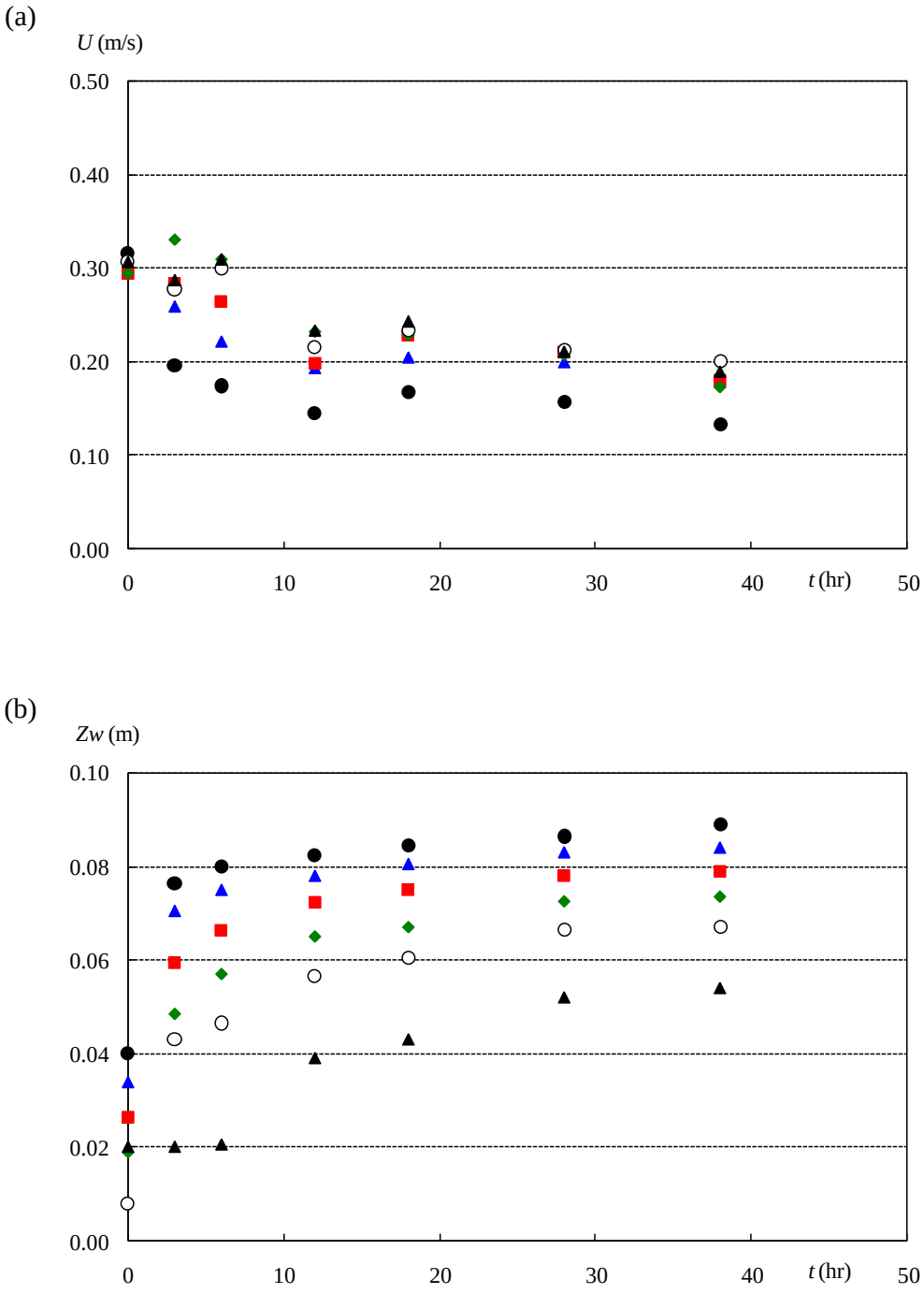

D-12. (a) Mean velocity *U*; (b) water elevation *Zw*; (c) water depth *h*; (d) Froude number *Fr* measurements of case 13, ● section A; ▲ section B; ■ section C; ♦ section D; ○ section E; ▲ section F

(c)

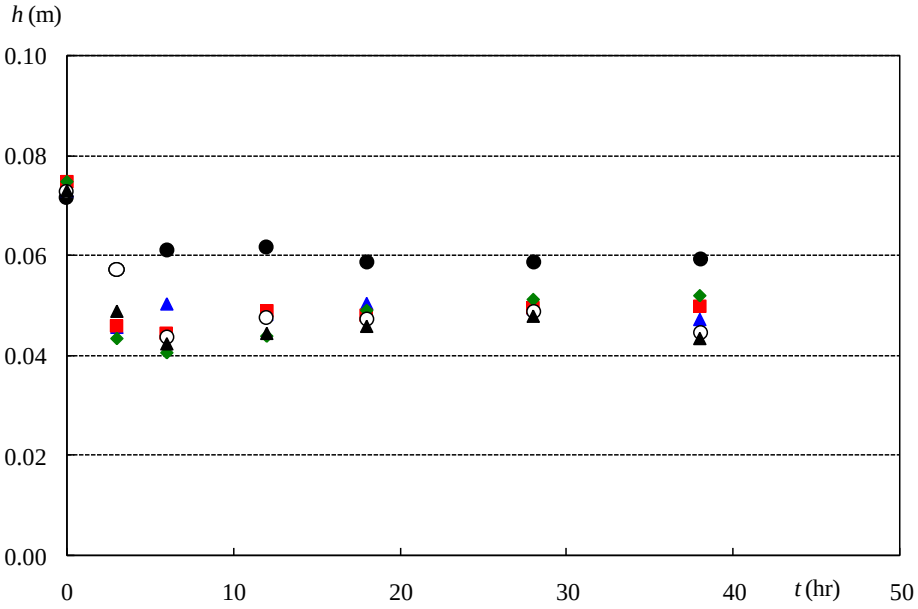

(d)

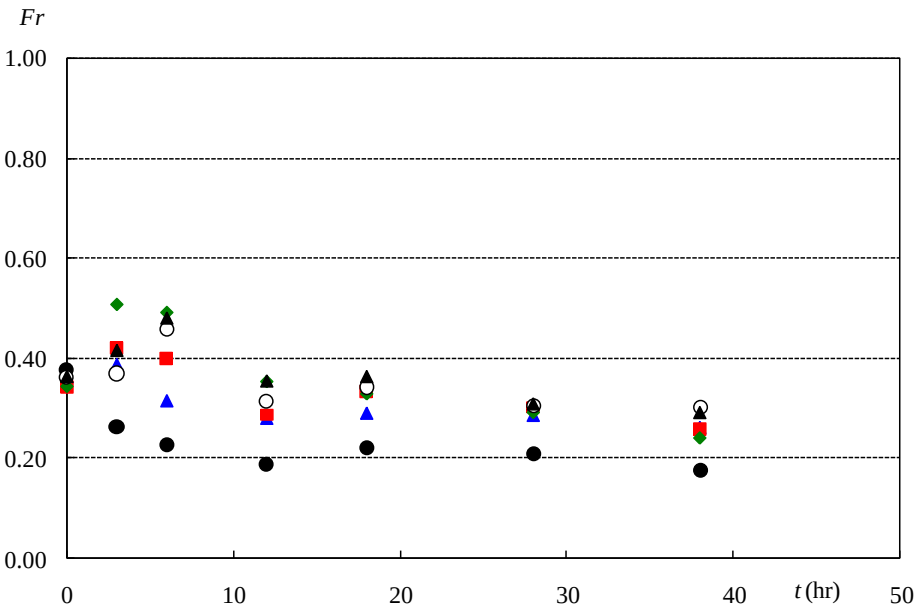

D-12. (Continued)

VITA

Po-Hung Yeh received his Bachelor of Science degree in water resources and environmental engineering from Tamkang University at Tamsui, Taiwan in 1994, and his Master of Science degree in civil engineering from National Chung Hsing University at Taichung, Taiwan in 1996. He entered the Ocean Engineering program of Civil Engineering at Texas A&M University in September 2002 and received his Doctor of Philosophy degree in August 2009. His research interests include sediment transport, hydraulic engineering, river and coastal engineering.